Global Positioning System Measurements of Crustal Deformation Across the Pacific-North American Plate Boundary in Southern California and Northern Baja, Mexico

by

Richard A. Bennett

B.S. Geophysics, *Summa Cum Laude*, University of California, Riverside, 1990.

Submitted to the Department of
Earth, Atmospheric, and Planetary Sciences
in partial fulfillment of the requirements
for the degree of
Doctor of Philosophy in Geophysics

at the

MASSACHUSETTS INSTITUTE OF TECHNOLOGY

February, 1996

Signature of Author.....
Earth Resources Laboratory and the
Department of Earth, Atmospheric, and Planetary Sciences
October 18, 1995

Certified by.....
Professor Thomas A. Herring
Department of Earth, Atmospheric, and Planetary Sciences
Thesis Supervisor

Accepted by.....
Professor Thomas H. Jordan
Department Head
Department of Earth, Atmospheric, and Planetary Sciences

Global Positioning System Measurements of Crustal Deformation Across the Pacific-North American Plate Boundary in Southern California and Northern Baja, Mexico

by

Richard A. Bennett

Submitted to the Department of Earth, Atmospheric, and Planetary Sciences
on October 18, 1995 in partial fulfillment of the requirements
for the degree of
Doctor of Philosophy

Abstract

The Pacific-North American plate boundary in southern California and northern Baja, Mexico undergoes a complex transition from crustal spreading in the Gulf of California to right-lateral transform motion along the San Andreas and associated fault systems. Historically, this has been one of the most seismically active segments of the plate boundary. We use GPS observations collected during the period from 1986 to 1995 to investigate the nature of ongoing crustal deformation in this complicated region and to estimate the contemporary rate of Pacific-North American relative plate motion. By allowing for episodic deformation associated with earthquakes, the time evolution of GPS coordinate estimates reveals a steady-state crustal deformation signal. By enlisting a simple block model to explain both the distribution and sum of deformation across the plate boundary, we use the horizontal components of the estimated secular site velocities to infer deep slip rates of 26 $\pm$ 2 mm/yr, 9 $\pm$ 2 mm/yr, 7 $\pm$ 2 mm/yr, and 7 $\pm$ 2 mm/yr for the San Andreas, San Jacinto, Elsinore, and San Clemente faults respectively. We also infer rates of 35 $\pm$ 2 mm/yr and 42 $\pm$ 1 for the Imperial and Cerro Prieto faults, and a total Pacific-North America relative plate motion rate of 49 $\pm$ 3 mm/yr. Our results are highly consistent with both geologic estimates for long term slip rates and previous space geodetic results, and are statistically consistent with, though slightly larger than, the NUVEL-1A plate motion estimate. We detect no systematic trends in the residual velocity field. We cannot reject the hypothesis that Pacific-North American relative plate motion is

accommodated across a finite set of discrete, relatively narrow shear zones which lie below fault systems known to have undergone significant Quaternary offset. Neither can we reject the elastic Poisson Earth hypothesis.

Coseismic surface deformation associated with the M_w 6.1, April 23, 1992, Joshua Tree earthquake is well represented by estimates of geodetic monument displacements at 20 locations independently derived from Global Positioning System and trilateration measurements. We apply a Tikhonov regularization operator to these estimates to infer a slip distribution yielding a geodetic moment estimate of 1.7×10^{18} N m with corresponding maximum slip around 0.8 m which compares well with independent and complementary information including seismic moment and source time function estimates and main shock and aftershock locations. From empirical Green's function analyses, a rupture duration of 5 s is obtained which implies a rupture radius of 6–8 km. Most of the inferred slip lies to the north of the hypocenter, consistent with northward rupture propagation. Stress drop estimates are in the range of 2–4 MPa. In addition, predicted Coulomb stress increases correlate remarkably well with the distribution of aftershock hypocenters; most of the aftershocks occur in areas for which the mainshock rupture produced stress increases larger than about 0.1 MPa. In contrast, predicted stress changes are near zero at the hypocenter of the M_w 7.3, June 28, 1992, Landers earthquake which nucleated about 20 km beyond the northernmost edge of the Joshua Tree rupture. Based on aftershock migrations and the predicted static stress field, we speculate that redistribution of Joshua Tree-induced stress perturbations played a role in the spatio-temporal development of the earthquake sequence culminating in the Landers event.

Thesis supervisor: Thomas A. Herring
Title: Associate Professor of Geophysics

Acknowledgment

I do not think that I would have attempted this ambitious enterprise were it not for the warm allusions, relentless encouragement, and sincere enthusiasm of my good friend and father-in-law David Ocumpaugh. I would also like to thank my undergraduate professors Shawn Biehler and Tien-Chang Lee at the University of California, Riverside for an inspiring and most enjoyable introduction to geophysics.

I will never forget the excitement I experienced after being invited to attend MIT by Professor M. Nafi Toksöz. Nafi provided me the opportunity to work and learn within a top-notch research environment for which I am truly grateful. Nafi also introduced me to Rob Reilinger. Rob had the foresight and gumption to instigate and maintain the STRC GPS network, and was kind enough to allow me the opportunity to work on this exciting project. He was always willing to provide sound advice and a good GPS observation story. He also taught me the art of writing papers and proposals.

My learning curve has never sloped more steeply than during the periods in which I was afforded the opportunity to emulate two scientists at MIT who are undeniably deserving of the title mentor: Tom Herring and Bill Rodi. Tom Herring, who I tacitly adopted as my thesis advisor, was always willing to share his knowledge. Tom has amazing skill with data and no one can fail to appreciate his insight into the subtleties of analysis. His hands on and personal approach to teaching makes his classes a main attraction in the EAPS department at MIT. Bill Rodi is one of the highlights of the Earth Resources Laboratory. He is friendly, humorous, highly intelligent, and growing more knowledgeable with each day; everything that a scientist should be. Bill has proven to be a reliable source of inspiration, encouragement, and advice, as well as an excellent teacher. Over the last five years, he has contributed immensely to my education.

I have also greatly benefited from interacting with Bob King and Brad Hager. Bob is arguably the most patient scientist in the whole of MIT. He was always willing to spend long hours combing over the details, identifying and illuminating the significance of each systematic residual. Bob can teach more about the GPS in a single hour in front of a computer, than can be gleaned from any stack of text books given any amount of time. He is also a great writer. His thorough and thoughtful editorial comments have substantially improved every draft that I have been fortunate enough to have had him read. Brad Hager seemed to have known what my thesis would be about before I did and much of the thesis' content is directly attributable to very informative conversations with him. He always knew just the right questions to ask.

I owe a debt of gratitude to numerous people involved in the collection and dis-

semination of the STRC data (a lot of people!). In particular, I would like to thank John Beavan, Lewis Gilbert, Javier Gonzalez, Shawn Larsen, and Bill Young for their contributions to the project. I am also grateful to Danan Dong, Egill Hauksson, Ken Hudnut, Yingping Li, and Simon McClusky for kindly providing ideas, data, and/or the results of their research.

The Earth Resources Laboratory is equipped with a first-rate staff. I would like to thank Sara Brydges, Naida Buckingham, Chuck Doll, Liz Henderson, Jane Maloof, Al Taylor, and Sue Turbak for their kind help over the years. I would also like to thank Joe Matarese and Ted Charratte for helping to keep the computers up and running time and again.

I have had the pleasure of meeting many interesting people over the last five years. Specifically, I would like to thank Matthijs Haartsen and Matthias Imhof for their interest in everything under the sun and their companionship. Craig Schultz plays a mean game of racket ball. Michel Bouchon kindly shared his interest in earthquakes and his knowledge. I have been lucky enough to have worked among both the EAPS students on the sixth floor of the Green building and at the ERL.

I am most grateful to my family. My grandparents Ginny and Welito provided financial and emotional support without which I would never have had this opportunity. I would also like to thank my parents for emphasizing the importance of education. In particular, I would like to thank my mother for her sense of humor and good character. Special thanks to my brother Cody for flying out to Boston to visit year after year. I owe the greatest debt of gratitude to my wife and best friend Susan who has proven to be the most tolerant and understanding person the world will ever know. Her love and support provide me with an unequaled source of strength. Finally, I would like to share my deepest appreciation for our two sons Josh and Paul whose wisdom and curiosity serve as a beacon for happiness and health.

The work for this thesis was funded by a fellowship from Chevron, grants from the Society of Exploration Geophysicists, grants from the United States Geological Survey under the National Earthquake Hazards Reduction Program, and a grant from NASA through the Carnegie Institution of Washington.

Contents

Chapter 1

Introduction

Precise estimates of Earth's surface deformation provide invaluable information about the external forces and internal processes acting on and within the planet. A complete description of these geodynamic phenomena is indeed one of the primary objectives of "space-based" geodesy. With the advent of the Global Positioning System (GPS), such measurements are directly obtainable. From the local fault-crossing scale typical of trilateration studies, to the more global scales typical of Very Long Baseline Interferometry (VLBI), GPS affords a unique opportunity to investigate a broad spectrum of deformation with precisions of the order of millimeters.

The social and economic importance of crustal deformation studies is evident. Despite improvements in structural design in many areas of the world, earthquakes are responsible for, on average, about 10,000 deaths per year [*Waverly Person, National Earthquake Information Center, personal communication*, 1994]. While the loss of life is clearly the most important issue, property damage is also of concern. The 1995 Kobe, Japan, and the 1994 Northridge, California, earthquakes, which together amassed billions of dollars in damage, provide recent examples. Though empirical evi-

dence is equivocal [e.g., *Kagan and Jackson*, 1991; *Nishenko and Sykes*, 1993; *Jackson and Kagan*, 1995], the theories of plate tectonics and elastic rebound lead one to conclude that earthquakes tend to occur in seismic gaps. Measuring the patterns and rates of deformation along and across active fault zones is, therefore, an important step toward identifying constraints useful for earthquake damage mitigation. Furthermore, earthquake potential in areas characterized by sparse and/or scarce seismicity which are not readily amenable to statistical studies may be estimated from geodetic measurements of regional strain rates [e.g., *Ward*, 1994].

Subsurface earthquake rupture is not directly observable. Nevertheless, GPS measurements of coseismic surface deformation can provide relatively detailed approximations to subsurface rupture patterns. This is important because geodetic images of fault slip greatly facilitate understanding of the earthquake source, particularly in conjunction with independent and complementary types of information such as precise aftershock locations, and source time function estimates. Furthermore, since coseismic and post-seismic stress patterns depend largely on the distribution of earthquake slip, such images may be instrumental in monitoring changes in earthquake potential.

This thesis is concerned with GPS measurements of crustal deformation in and around the diffuse, intercontinental plate boundary zone known as the Salton Trough. Constituting one of the most seismically active segments of the Pacific-North American plate boundary, the Salton Trough imports a complex transition between crustal spreading in the Gulf of California and right-lateral transform motion along the San Andreas and associated fault systems. Detailed knowledge of the contemporary style of tectonic deformation occuring throughout this region may lead to improved understanding of continental tectonic processes and may assist earthquake hazard assessment in southern California and northern Mexico.

1.1 Objectives

The primary objectives of this thesis are to reduce and analyze new Global Positioning System (GPS) measurements in southern California and northern Baja, Mexico and to infer the spatial and temporal details of the crustal deformation field along and across the Pacific-North American plate boundary. Toward this end, we make the following original contributions:

- Analysis of seventeen GPS experiments, seven of them new, involving nearly 120 stations in southern California and northern Baja during the period from 1986 to 1995. Estimates of both GPS site velocities and earthquake displacements, obtained with the GAMIT/GLOBK software, are reported.
- Development of inference procedures for geophysical interpretation of GPS estimates of interseismic and coseismic crustal deformation based on the principles of inversion theory and statistics.
- Geodetic investigation of the nature of contemporary interseismic crustal deformation in southern California and northern Baja, Mexico.
- Geodetic investigation of the 1992 M_w 6.1 Joshua Tree, southern California earthquake.

1.2 Overview

We begin in Chapter 2 with an analysis of the 1988 to 1995 Salton Trough-Riverside County (STRC) GPS experiments. Combining the results of these analyses with those representing a set of ten additional GPS experiments (1986-1993), we infer the crustal deformation field for the period from 1986 to 1995. We then explore some

of the tectonic implications of our geodetic results with the aid of an elastic block model. In Chapter 3, we develop an inversion methodology for interpretation of geodetic measurements of coseismic surface displacements. Finally, in Chapter 4, we use this methodology to investigate the 1992 M_w 6.1 Joshua Tree, southern California, earthquake and some of its implications regarding the occurrence of the 1992 M_w 7.4 Landers, southern California, earthquake. Chapters 3 and 4 have been published as a single paper [*Bennett et al.*, 1995], while Chapter 2 is to be submitted. Consequently, some degree of redundancy and notational inconsistency is sure to be found between these two parts of the thesis.

Chapter 2

Interseismic accommodation of Pacific-North American relative plate motion in southern California and northern Baja, Mexico: 1986-1995

Then the earth started to shake and tremble, and to bubble up in places, and the rocks piled up. It was terrible, but that was how they behaved.

Cahuilla Creation Myth, narrative by Joe Lomas (1881-1969), in Cahuilla Texts, Hansjakob Seiler, 1970

2.1 Introduction

In this chapter our main objective is to investigate how the total relative motion between the Pacific and North American plates is partitioned among the fault zones of southern California and northern Mexico. The chapter can roughly be divided into two main parts. In the first part, which includes the remainder of this introductory section, we focus on observations relevant to our objective. We begin with a brief survey of the previous geological and geodetic investigations which have motivated our study, summarizing the observations and results which we hope to build upon. After this introduction, we present analyses of a set of GPS experiments which were performed in southernmost California and northern Baja, Mexico for the period 1986-1995. From these experiments, we infer the GPS deformation field, which appears to consist of a superposition of episodic earthquake displacements and steady-state interseismic velocities. We are able to recover both components of the deformation signal for many sites in the network. In the second part of this chapter, we use the estimated velocity field to investigate the distribution of relative plate motion. Our approach to the problem is to enlist a simple model to serve as a source of plausible hypotheses regarding the nature of the deformation field across the plate boundary. Our objective in taking this approach is to test and refine the manifold of geological and geodetic estimates reported in the literature.

2.1.1 The Pacific-North American plate boundary

Sometime around 30 Ma, the ancestral East Pacific Rise collided with the trench that then separated the North American and Farallon plates [*Atwater,* 1970] bringing the Pacific and North American plates into contact. Although the details of the early evolution of this boundary are hazy, by about 20 Ma the existence of a right-lateral

proto-San Andreas transform near the present-day continental borderland is probable [e.g., *Tennyson,* 1989]. Eastward migration of the proto-San Andreas transform to its present location and the associated rifting of the Gulf of California appear to be as recent as 5 Ma [e.g., *Sedlock and Hamilton,* 1991].

The NUVEL-1A global plate motion model [*DeMets et al.,* 1990; 1994] predicts Pacific-North American relative motion across southern California of 46 $\pm$ 1 mm/yr. This estimate represents plate motions averaged over the last three million years. It is the ongoing motions of these plates that drives the contemporary accumulation of elastic strain within the plate boundary and is, therefore, ultimately responsible for earthquakes throughout the region.

However, it has long been recognized that the San Andreas fault in southern California is not the sole boundary between the Pacific and North American plates [e.g., *Atwater,* 1970]. Instead, relative motion is accommodated here across a series of sub-parallel fault zones which, in effect, stretch the deforming "boundary zone" over hundreds of kilometers. This is in contrast to the relatively narrow and fairly well defined ocean-like ridge-transform signatures of the plate boundary through the Gulf of California. While the spatial diffusion of deformation northward from the Gulf of California can be attributed to the subduction of the ancestral East Pacific Rise [e.g., *Atwater,* 1970; *Dickson and Snyder,* 1979], such behavior is typical of the contrasting styles of continental and oceanic crustal deformation which is, in turn, attributed to rheological differences between continental and oceanic lithosphere [e.g., *Thatcher,* 1995]. This complex transition from crustal spreading in the Gulf of California to the right-lateral transform systems of southern California occurs within the Salton Trough. Just how contemporary relative plate motion is accommodated across this complex zone is a question ideally addressed by GPS measurements. Geological and seismological observations also provide important constraints.

2.1.2 Seismicity and Quaternary faulting

The southernmost San Andreas fault, in contrast to its behavior elsewhere in California, has remained dormant throughout the historical period, not having ruptured since about 1680 [*Sieh,* 1986]. However, paleoseismic evidence indicates that this segment has maintained an average recurrence interval of about 300 years over the past 2,000 years [*Sieh,* 1986]. Geological slip rate estimates range between 10 and 35 mm/yr [*Keller et al.,* 1982] with the mean rate estimated at 25 ± 4 mm/yr [*Weldon and Sieh,* 1985].

The San Jacinto fault zone, on the other hand, exhibits relatively high rates of seismicity, having produced at least six moderate earthquakes during the last century. Geological slip rate estimates are in the range of 2 to 15 mm/yr with the average estimated at 10 ± 2 mm/yr [*Wesnouski,* 1986 *and references therein*]. One 40 km long segment of the fault, the Anza seismic gap, is characterized by a deficiency in historic rupture, and by a quiescent, 20 km subsegment bounded by relatively high rates of seismicity [*Sanders and Kanamori,* 1984].

Approximately 40 km southwest of the San Jacinto fault, the Elsinore fault zone constitutes yet another important component of the Pacific-North American plate boundary. Long-term slip rate estimates along this fault zone are in the range of 1-9 mm/yr with average rate near 4 mm/yr [*Wesnouski,* 1986 *and references therein*]. Moderate levels of diffuse seismicity are associated with this fault zone.

The area in the vicinity of the Superstition Hills, Superstition Mountain, and Imperial fault zones, including the Brawley Seismic Zone, is generally characterized by very high rates of diffuse seismicity. Yet little geologic or seismic information constrains the long-term slip behavior of these structures. Nevertheless, several large earthquakes, the most notable of which are the 1940 and 1979 Imperial Valley earth-

quakes and the 1987 Superstition Hills earthquake sequence, testify to the area's great seismic potential.

In the Mexicali Valley, northern Mexico, high rates of seismicity similar to those found in the Brawley Seismic Zone characterize what is known as the Mexicali Seismic Zone which connects the right-stepping Cerro Prieto and Imperial faults. Using seismic moment estimates of the last four M > 6 earthquakes along this fault zone, *Frez and Gonzalez* [1991] estimate the slip rate along the Cerro Prieto to be about 53 mm/yr. However, they included a factor of 1.3 in their calculation to account for all seismicity of lesser magnitude. Without this factor of 1.3, their estimate is 41 mm/yr.

Offshore, in the southern California continental borderlands, bathymetric, seismic reflection, magnetometer, sea beam, and other geophysical data clearly delineate the San Clemente fault zone [*Legg et al.,* 1989], for which long term slip rate estimates are in the range of 0-7 mm/yr [*Humphreys and Weldon,* 1986]. Seismicity along the San Clemente fault is fairly sparse.

To the south, the Agua Blanca fault zone represents a major transverse tectonic element of northern Mexico [*Allen et al.,* 1960]. The Quaternary slip rate for this fault is estimated to be in the range of 2-5 mm/yr [*Hatch and Rockwell,* 1986]. There is no major historic earthquake and very little seismicity associated with this feature [*Frez and Gonzalez,* 1991].

Also in Mexico, near the Laguna Salada fault zone, intermittent uplift of the northwest Sierra Cucapa range throughout the Quaternary is indicative of long term transpressional interactions [*Sylvester and Smith,* 1976]. A minimum long-term slip rate estimate for the Laguna Salada fault of about 1 mm/yr is reported by *Mueller and Rockwell* [1991]. Unlike the Agua Blanca fault zone, however, relatively high rates of seismicity are associated with the Laguna Salada fault system [*Frez and Gonzalez,* 1991].

It was long ago observed that moderate to large historic earthquakes tend to occur along major through going faults having extensive Quaternary displacements [*Allen et al.,* 1965][1]. Yet not all fault zones having undergone large Quaternary displacement have demonstrated their potential in the relatively short historic record. While the full relationship between seismicity and long-term fault behavior may not yet be completely revealed, what can be said regarding contemporary fault behavior? And on a larger scale, how does the contemporary rate of Pacific North American plate motion compare with the three million year average represented by plate models such as NUVEL-1A? Geodetic measurements are beginning to provide the answers.

2.1.3 Previous geodetic work

Conventional measurements.

Conventional geodetic measurements including leveling, triangulation, and trilateration have been collected frequently over the last sixty years in southern California. These data have been used to investigate deformation throughout the southern California region and have provided many important results [e.g., *Savage and Prescott,* 1976; *Thatcher,* 1979; *Snay et al.,* 1982; *Reilinger,* 1984; *Reilinger and Larson,* 1986; *Savage et al.,* 1986; *Savage et al.,* 1987; *Snay and Drew,* 1988; *Larsen and Reilinger,* 1991; *Lisowski et al.,* 1991, *Savage et al.,* 1993; *Johnson,* 1993; *Johnson et al.,* 1994; *Gilbert et al.,* 1994; *Savage and Lisowski,*, 1995; *Savage and Lisowski,*, 1995; *Savage,* 1995]. These results include 1) a ratio of slip rate to locking depth for the northern San Jacinto fault of about 1.2×10^{-6}/yr [*Savage and Prescott,* 1976], 2) unusually large strain rates (steep velocity gradients) along the southernmost San Jacinto fault

[1]This observation does not imply that large earthquakes should not occur along structures which are not known to have undergone large Quaternary displacements. In fact, the 1992 Landers earthquake serves as a reminder of this possibility.

[*Thatcher,* 1979; *Lisowski et al.,* 1991; *Johnson et al.,* 1994], 3) highly variable rates of deformation across the Imperial Valley ranging from 35 to 82 mm/yr, possibly indicative of postseismic effects associated with the 1940 Imperial Valley earthquake [e.g., *Thatcher,* 1979; *Snay et al.,* 1982; *Snay and Drew,* 1988], 4) temporally uniform strain accumulation along the San Andreas fault [*Savage et al.,* 1986; *Savage et al.,* 1987; *Savage et al.,* 1993; *Savage and Lisowski,*, 1995; *Savage and Lisowski,*, 1995; *Savage,* 1995], 5) extension near the eastern knot of the bend in the San Andreas [*Lisowski et al.,* 1991; *Savage et al,* 1993, *Johnson et al.,* 1994], 6) steady state, interseismic deformation across the Imperial Valley of 37 $\pm$ 1 mm/yr [*Lisowski et al.,* 1991], 7) steep gradients in the southern California velocity field over the San Andreas, San Jacinto and to a lesser extent, the Elsinore faults [*Lisowski et al.,* 1991], and 8) extremal bounds on the average slip rates of the San Andreas, San Jacinto, and Elsinore faults of 11-23 mm/yr, 7-25 mm/yr, and 0.3-17 mm/yr (95% confidence) respectively. In general, conventional geodetic measurements provide slip rates for major strike slip faults that are consistent with the long-term geologic estimates, possibly indicating that the observed deformation is largely elastic and likely to be recovered in future earthquakes [e.g., *Lisowski et al.,* 1991]. *Larsen and Reilinger* [1991] demonstrate that leveling and other geophysical information suggest that the fault configuration in the vicinity of the Brawley Seismic Zone is much younger than the 5 Ma age of the Salton Trough. *Gilbert et al.* [1994] conclude from observations of the principal directions of strain that the geodetic measurements favor deformation models involving predominantly vertical zones of shear which extend well below the brittle-ductile transition.

In northern Mexico, observation campaigns have been conducted but with less intensity [e.g., *Darby et al.,* 1984; *Kasser et al.,* 1987]. *Savage et al.,* [1994] present results from their analysis of a trilateration network crossing the Laguna Salada fault, Baja California. They observe extension above the fault and report that it is difficult to explain this observation using a model representing normal displacements on the

Laguna Salada fault without adopting unusual values for the dip of the fault plane.

Space geodetic measurements.

While plate motion models and space geodetic measurements are statistically consistent, geodetic rates estimated along specific plate boundaries, such as the Pacific-North American, are consistently slightly faster. The contemporary rate of total Pacific-North American relative plate motion, for example, has been estimated from VLBI data to be near 47-48 mm/yr across California [e.g., *Kroger et al.,* 1987; *Ward,* 1990; *Argus and Gordon,* 1990]. *Feigl et al.* [1993] use a combination of VLBI and GPS measurements to estimate Pacific-North America relative motion (site VNDN with respect to North America) at 46.7 $\pm$ 0.3 mm/yr across southern California. *Argus and Heflin* [1995] estimate plate motions using GPS measurements from a global network of stations and obtain a rate of 53 $\pm$ 3 mm/yr of Pacific-North American motion across the same section of the plate boundary. Similarly, *Dixon et al.* [1991] used the GPS to estimate that up to 47 $\pm$ 7 mm/yr relative motion is accommodated across the southern Gulf of California.

GPS measurements also provide results comparable to those from smaller scale conventional geodetic measurements. For example, *Larsen and Reilinger* [1992] analyze GPS data collected in the Imperial Valley during the period between 1986 and 1989. They infer between 52 $\pm$ 9 mm/yr and 59 $\pm$ 10 mm/yr relative motion across the valley. The first rate represents motion estimated from two epochs of GPS measurements spanning one year after the occurrence of the 1987 Superstition Hills earthquake sequence (1988-1989), while the second rate represents motion inferred from two epochs of GPS data spanning a two year period which includes the event (1986-1988). They estimate relative motion between two sites (BLAC, PIN1) on either side of the southernmost San Andreas fault of 14 $\pm$ 8 mm/yr.

The most comprehensive space geodetic study of the southern California region to date was reported by *Feigl et al.* [1993]. They combine GPS and VLBI data to infer the velocity field in central and southern California. They find significant rates of shortening across the eastern Santa Barbara Channel, the Ventura Basin, the Los Angeles basin, and the Santa Maria Fold and Thrust Belt. They estimate that 23 $\pm$ 2 mm/yr of relative motion is accommodated between sites BLAC and PIN1 about the southernmost San Andreas. Their results also provide evidence to suggest that the San Clemente fault could accommodate an appreciable amount of the total Pacific-North American relative plate motion [also see *Larson,* 1993].

Finally, *Farina et al.* [1994] provide evidence from GPS measurements in northern Baja California, Mexico, for a minimum slip rate of 6 mm/yr along the Agua Blanca fault.

2.2 GPS data analyses

In this section, we address the first of our primary objectives. We detail our GPS data analyses beginning with a description of the individual Salton Trough–Riverside County experiments (1988-1995) and their reductions. We then present a multi-experiment analysis involving a total of seventeen experiments (1986-1995) from which we infer the GPS deformation field. The results of this section form the basis of the tectonic investigations making up the remainder of the thesis.

2.2.1 The Salton Trough-Riverside County GPS experiments

Between 1988 and 1995, a consortium of university groups and government agencies [2] performed a series of GPS experiments in the Salton Trough with the goal of refining estimates of the present-day rates and patterns of crustal deformation along and across the individual faults composing the Pacific-North American plate boundary in southern California and northern Mexico (Table 2.1). Though experiments began with a re-occupation of a GPS network established in 1986 by the National Geodetic Survey in the Imperial Valley, the network has steadily grown and now extends from the San Bernadino Mountains east of Los Angeles, to the Gulf of California in northern Mexico, and from the Pacific Ocean to the California-Arizona border (Figure 2-1). We loosely refer to the ensemble of experiments conducted here during this period as the Salton Trough-Riverside County (STRC) experiments. Of the total of 117 stations observed during these campaigns, over 50 have been occupied with sufficient redundancy over the last eight years to precisely determine their velocities despite the occurrence of the 1992 Joshua Tree and Landers earthquakes. (Table 2.2).

Each of the STRC experiments consists of a set of observation sessions during which groups of stations simultaneously recorded the phase and pseudo-ranges of GPS satellite signals. Experiments through 1989 were conducted using Texas Instruments receivers and antennae. The remaining experiments were conducted using an assortment of receiver and antenna types including Ashtech, Rogue, Texas Instruments, and Trimble (Table 2.1).

[2]The STRC consortium includes: California Institute of Technology, Centro de Investigacion Cientifica y de Educacion Superior de Ensenada, Jet Propulsion Laboratory, Lamont-Doherty Earth Observatory, Lawrence Livermore National Laboratory, Massachusetts Institute of Technology, National Geodetic Survey, New Mexico State University, Riverside County Flood Control and Water Conservation District, San Bernadino County Survey, Unidad Municipal de Protection Civil de Mexicali, Universidad Nacional de Mexico, University of California at Riverside, University of California at San Diego, University Navstar Consortium, University of Nevada, University of Texas at Dallas, U.S. Geological Survey, and U.S. Army Range Support Directorate Optical Division.

The GPS measurements themselves consist of carrier phases and, when available, P-code pseudo-ranges recorded every 30 seconds[3]. Sessions typically lasted for 6 to 8 hours, yielding of the order of 800 epochs of measurement. For a typical experiment involving around 20 stations per session, of the order of a million measurements were recorded. When a sufficient amount of good global tracking data was available, it too was included in our analyses.

We analyzed the data from each experiment using the GAMIT/GLOBK software [*King and Bock,* 1995] following the two-step processing procedure outlined by *Feigl et al.* [1993]. In the first step, we analyzed each of the individual observation sessions within each experiment. In the second step, we combined the data in a multi-experiment analysis. Both steps of this procedure can be further be divided into an analysis of the quality of the observations, and a rigorous determination of parameter estimates.

To begin, we used GPS phase and pseudo-range[4] observations for each session to estimate station coordinates, satellite orbital parameters, integer phase biases, and four parameters belonging to a piece-wise constant function representing atmospheric zenith delay. Antenna phase center variation models were applied. We edited the data using the GAMIT preprocessor AUTCLN [*Herring,* 1995; *King and Bock,* 1995], restricting data alterations to unweighting of obvious outliers and recompensation of cycle slips owing to losses of lock.

Once the GAMIT analyses of the observation sessions were complete, and before preparing the data for the second stage of processing, we performed a repeatability study to assess the quality of each experiment. Using the GLOBK Kalman filter

[3]Though some measurements were collected at 15 second intervals, these data were decimated to 30 seconds for processing. Data from the Joshua Tree experiments were recorded every two minutes.

[4]GAMIT uses pseudo-range measurements only in data editing and to determine receiver clock offsets.

[*Herring,* 1995], session by session series of quasi-independent baseline component estimates were obtained for each experiment by imposing global constraints (pertaining to the experiment as a whole) on the orbital parameters and usually a small set of well known tracking station coordinates while otherwise allowing the STRC site coordinates to vary freely from session to session. A detailed description of the orbital constraint models (the orbital state transition equations) used by the GLOBK software is provided in Appendix A. We analyzed the weighted root-mean-square scatter about the weighted means of these baseline component series to assess the precisions of the experiments. The results are presented in Appendix B.

Next, in preparation for the second stage of processing, we used GLOBK to combine parameter estimates and their variance-covariance information from each of the individual GAMIT analyses making up each experiment. That is, we estimated a single vector of site coordinates and a variance-covariance matrix representative of each experiment. In forming these individual experiment combinations, all site coordinate constraints were freed to avoid distorting results derived from them during the next stage of processing. Earth rotation parameters (X and Y polar motion and UT1) were estimated as freely varying stochastic processes.

2.2.2 The GPS deformation field

Once the STRC experiment combinations were created, we performed a multi-experiment analysis using GLOBK to estimate the GPS velocity field. In addition to the seven STRC experiments described above, we included nine of the experiment combinations discussed by *Feigl et al.* [1993][5]. These experiments cover roughly the same time pe-

[5]The particular subset of experiments from *Feigl et al.* that we consider here are numbered 0 (1986), 10 (1988), 13 (1989), 14 (1989), 16 (1989), 18 (1990), 20 (1991), SB1 (1991), and VB2 (1992).

riod as the STRC experiments (1986-1992), and extend GPS coverage across the southern California continental borderlands. The subset of data that we used from these experiments consists of measurements from local sites BLUF, BRSH, MONU, NIGU, PIN1 (including PINY tie), PVER, SIO1 (including SIO2 tie), and YUMA in addition to the tracking stations discussed below. We also included an experiment combination representing the 1993 Inter County survey which contains GPS observations from several STRC stations[6]. The local sites observed during this experiment that we used are listed in Table 2.2. We have, then, a total of 17 vectors of site coordinate estimates, h_k, and variance-covariance matrices, H_k, representing 17 different epochs, t_k, in the period from 1986 to 1995[7].

To assess the nature of the deformation field represented by this set of estimates, we used GLOBK to compute a time series of site coordinates, x_k, referred to a temporally uniform, North America fixed reference frame. Earth rotation parameters were also estimated. This frame was defined by constraining the coordinates and velocities (Table 2.4) of California site Mojave and a small set of global trackers[8] outside of California at values determined by *Feigl et al.* [1993] from a combination of VLBI and GPS data. The constraints that we applied are listed in Table 2.3. Because we are estimating both velocities and episodic displacements, we restrict our analyses to sites that were observed at least three times[9]. In order to tie experiments with little or no tracking data to the reference frame, we forced seven of the local sites (NIGU,

[6]This experiment was conducted by the United States Geological Survey, Pasadena, CA. The GAMIT analyses from which the particular experiment combination that we incorporate was created from were performed by S. McClusky, Massachusetts Institute of Technology, Cambridge, MA.

[7]In the GAMIT/GLOBK jargon, each of these site coordinate vector/variance-covariance matrix pairs is stored in an "h-file".

[8]The trackers that we use to define the reference frame are: Algonquin, Fairbanks, Ft. Davis, Kokee, Penticton, Pietown, Richmond, St. John's, Yarragadee, and Yellowknife.

[9]We make exceptions for sites IPE0, LPUR, SM01, and VA01 all located in northern Mexico and observed only during the 1993 and 1995 STRC campaigns, site ENDA also located in northern Mexico and observed only during the 1989 GEOMEX and 1993 STRC campaigns, and site YUMA located near the California-Arizona border just north of the USA-Mexico border and observed only during the 1986 TREX and 1993 STRC campaigns.

PIN1, BLAC, ENDD, SIO1, YUMA, SFBC) to conform to linear in time motion (excepting the earthquake deformation) and constrained their vertical motions at the 5 mm/yr level. In Appendix C, we present the evolution of site coordinate estimates determined in this frame.

The occurrence of the 1992 Landers earthquake is apparent in the horizontal components of many of the site coordinate histories. For many sites, abrupt deviations from an otherwise well behaved trend, coincident with the epoch of the earthquake, amount to a significant fraction of the total motion observed over the time spanned by the experiments. In order to recover the more temporally uniform components of the crustal deformation signal, therefore, we must account for displacements associated with this event. In Appendix C, we observe that, after applying appropriate episodic (i.e. step-function) displacement corrections at the epoch of the earthquake, the dominant horizontal component of the GPS signals appear to be linear.

Interpretation of the vertical components is less clear. We expect the vertical signal associated with tectonic motions to be relatively small. However, the time series for a few of the sites exhibit large apparent vertical motions. Given these anomalies and since our primary interest is in the horizontal components of motion, we do not attempt to fit the vertical motions using the constant velocity/episodic earthquake displacement model.

From our set of seventeen measurements (h_k, H_k), we estimated one global set of horizontal site coordinates, x, displacements at the epoch of the Landers event, constant site velocities, v, and earth rotation parameters (as well as their joint variance-covariance matrix, C). These parameters all refer to the same uniform reference frame discussed above with the following exceptions: The constraints imposed for the coordinates and velocities of the global tracking stations were loosened by a factor of two relative to those used in the time series solution (Table 2.3) to avoid unnecessary

propagation of fiducial errors into the site velocity estimates; The vertical components of all local sites' coordinates were free to evolve as in the time series solution so as to decouple the horizontal and vertical motions and hence avoid possibly projecting vertical errors into the estimates for horizontal velocity.

The Landers earthquake sequence adds significant uncertainty to the estimation of horizontal velocities for STRC sites, particularly for the northern part of the network. Indeed, as examination of the time series in Appendix C corroborates, estimation of accurate velocities was hampered for most of the STRC sites prior to incorporation of the data from the 1995 survey. Based on preliminary modeling, we believe the effects of Landers to be significant ($\sim$ 5 mm) as far south as 32° north latitude, roughly 250 km away from the epicenter [e.g., *Bennett et al.,* 1994]. Accordingly, to infer interseismic site velocities from our data, we accounted for coseismic displacements associated with the earthquake by allowing for episodic jumps in the coordinate estimates for all sites within 500 km of the earthquake epicenter. These jumps were constrained by propagating spatially correlated noise processes into the parameter variance-covariance matrix between measurement epochs bracketing earthquakes. The structure of the noise processes is such that the standard deviations of the allowable coordinate jumps decay in proportion to the inverse-square of the distance from the earthquake scaled according to the magnitude of the event [see *Herring,* 1995]. This reflects the expected attenuation of the actual earthquake displacement signal [e.g., *Aki and Richards*, 1980]. For sites located near the epicenter, observations before and after the event were effectively uncoupled; the effective variances of the coordinate jumps were at the level of tens of centimeters for these sites. Since we ignored earthquake displacement radiation patterns, the episodic jump constraints may be overly conservative for sites located along nodal directions.

The chi-square per degree of freedom for the GLOBK run in which we estimated site velocities is 5.1. We therefore scaled the formal uncertainty estimates by a factor

of 2.3. In appendix C, the estimated horizontal velocities and earthquake displacements are shown superimposed on the time series of site coordinates discussed above. Velocity estimates computed relative to site ENDD (Figure 2-2; Table 2.5) provide an approximate sense of the velocity field in a North America fixed frame of reference[10]. Landers earthquake displacement estimates are listed in Table 2.6 and shown in Figure 2-3.

Prerequisite to a thorough understanding of the error estimates for GPS site velocities is an understanding of the temporal and spatial characteristics of the error spectra of the GPS position estimates themselves. Unfortunately, this information is not readily available. Rescaling the formal uncertainties by the square root of the chi-square per degree of freedom, as we have done, should provide valid estimates, *a posteriori*, provided that the noise spectrum is flat between durations of months to several years. However, comparative analyses of short and long term GPS position repeatability [cf., *Feigl et al.,* 1993] suggest that systematic components of error associated with experiment combinations may be commensurable to the short term scatters, implying that the noise power is concentrated at low frequencies. Indeed, our estimated variance scale factor of 2.3 is about twice the average short term normalized root-mean-square scatter (Appendix B), suggestive of systematic errors of about this same level. The uncertainties in the velocity estimates for stations observed only two or three times could be significantly larger than that reflected by the square root of chi-square per degree of freedom, particularly those which were significantly affected by the Landers earthquake. While our error estimates are not calibrated by comparison with independent geodetic measurements such as VLBI, rescaling by a factor of two to three appears to be typical of this type of GPS analysis [e.g., *Dong,* 1993; *Feigl et al.,* 1993; *Oral,* 1994].

[10]The error ellipses shown represent uncertainties in the ENDD frame and are not representative of other relative rates among different pairs of sites which, due to correlations between nearby sites, could potentially be significantly more accurate depending on the site pair considered.

2.3 Geodetic allotment of Pacific-North American relative plate motion

The GPS derived velocity field is clearly dominated by right-lateral shear (Figure 2-2), potentially masking more subtle, presumably more interesting tectonic motions. Nevertheless, we draw the following general conclusions from the ENDD fixed reference frame prior to reducing the velocity field by removing the effects of a deformation model. First, there are no significant relative motions among sites located beyond about 30 km northeast of the San Andreas and Imperial faults in southern California and the Cerro Prieto fault in northern Mexico. If stations here are moving with respect to North America, they do so roughly as a rigid unit. Possible accumulated deformational motion across this region associated with the plate boundary structures or other sources is less than about 5 mm/yr. Second, the steepest velocity gradients are clearly over the San Andreas, Imperial, and Cerro Prieto faults, delineating the primary structures of the Pacific-North American plate boundary. Third, the total deformation across the network as indicated by the relative motions between sites BLUF and ENDD (47 $\pm$ 5 mm/yr) and between sites LLCO and ENDD (48 $\pm$ 5 mm/yr)[11] compares well with rates inferred from the NUVEL-1A global plate motion model, and previous space geodetic measurements. These observations suggest that the network spans the width of the plate boundary zone.

2.3.1 Geophysical interpretation of GPS geodetic inferences

In order to assess further the implications of our geodetic results, we employ a model in order to reduce the geodetic velocity field. That is, we wish to interpret the

[11]The uncertainties reported here reflect the 68% confidence level after rescaling the formal uncertainties by 2.3.

collection of 2-vector estimates of the horizontal velocities for each station within the context of a geophysical theory. The geodetic analyses presented above provide us with estimates of the motions of the geodetic monuments of the network in a particular realization of the North America fixed reference frame together with their error variance-covariance matrix. The full variance-covariance matrix contains all of the information pertaining to the accuracies of the baseline vectors and their rates.

To begin, we notice that the velocity estimate for the ith station, denoted v_i, can be written as

$$v_i = v_{i,NA} + e_i, \tag{2.1}$$

where the errors e_i are related to the velocity error variance-covariance matrix V by $\sigma^2 V_{ij} = \mathrm{E} e_i e_j^T$ (E is the expectation operator)[12], and $v_{i,NA}$ is the "true" velocity of station i in the North America fixed frame. Finally, σ^2 is an unknown scale factor to be determined.

The motion of the ith station can also be expressed in another reference frame specific to a tectonic model, represented by the vector $A_i m$, as

$$v_{i,0} = A_i m. \tag{2.2}$$

In this notation, $A_i m$ is a 2-vector representing the hypothetical velocity of the ith geodetic station. The $2 \times M$ matrix A_i maps an M-dimensional model parameter vector m to velocities $v_{i,0}$ with respect to some convenient or "natural" model coordinate system.

Clearly, any such model frame can be related to the North America fixed frame by an expression of the form

$$v_{i,NA} = v_{i,0} + v_{0,NA}. \tag{2.3}$$

[12] V is extracted from the larger GLOBK parameter estimate error variance-covariance matrix C after rescaling to reflect *a posteriori* errors.

We thus have

$$v_i = A_i m + n + e_i, \tag{2.4}$$

where, to simplify the notation, we have introduced the 2-vector n to represent the inter-frame translation $v_{0,NA}$.

For an N station network, the N 2-vector estimates of horizontal velocity can be expressed together concisely as

$$v = Am + Bn + e, \tag{2.5}$$

where

$$v = (v_1, \ldots, v_N), \tag{2.6}$$

$$e = (e_1, \ldots, e_N), \tag{2.7}$$

$$Am = (A_1 m, \ldots, A_N m), \tag{2.8}$$

and

$$B = \begin{bmatrix} 1 & 0 \\ 0 & 1 \\ -- & -- \\ \vdots & \vdots \\ -- & -- \\ 1 & 0 \\ 0 & 1 \end{bmatrix}, \quad N \text{ partitions.} \tag{2.9}$$

Given v and V, we wish to obtain an estimate of m. We begin by normalizing the system of equations by the Cholesky square root, L, of V (i.e., $V = LL^T$). The resulting normalized system is denoted as

$$\hat{v} = \hat{A}m + \hat{B}n + \hat{e}, \tag{2.10}$$

where $\hat{v} = L^{-1}v$, $\hat{A} = L^{-1}A$, $\hat{B} = L^{-1}B$, and $\hat{e} = L^{-1}e$, such that $\hat{V} = \mathrm{E}\hat{e}\hat{e}^T/\sigma^2$ becomes the $2N$ dimensional identity matrix.

We define the functional Ψ as

$$\Psi(m,n) = \|\hat{v} - \hat{A}m - \hat{B}n\|^2. \tag{2.11}$$

To optimally eliminate the nuisance parameter n from the problem, we orthogonally project the system onto the $2N$-2 dimensional null space of $\hat{B}^\dagger \equiv (\hat{B}^T\hat{B})^{-1}\hat{B}^T$ by minimizing *a priori* with respect to n. In doing so we obtain

$$\Psi(m,\tilde{n}) = \|\hat{v}' - \hat{A}'m\|^2, \tag{2.12}$$

where $\hat{v}' = \hat{P}\hat{v}$, $\hat{A}' = \hat{P}\hat{A}$, and $\hat{P} = I - \hat{B}\hat{B}^\dagger$. $\hat{P}$ is an orthogonal projection operator.

We arrive at the least squares estimate

$$\tilde{m} = (\hat{A}'^T\hat{A}')^{-1}\hat{A}'^T\hat{v}'. \tag{2.13}$$

by minimizing (2.12) with respect to m.

Since Ψ/σ^2 is chi-square distributed, that is

$$\mathrm{E}\Psi = \sigma^2(2N - 2 - M), \tag{2.14}$$

we may estimate σ^2 as

$$\tilde{\sigma}^2 = \Psi(\tilde{m},\tilde{n})/(2N - 2 - M). \tag{2.15}$$

The error variance-covariance matrix is then estimated as

$$\mathrm{E}\tilde{m}\tilde{m}^T = \tilde{\sigma}^2(\hat{A}'^T\hat{A}')^{-1}. \tag{2.16}$$

It is not difficult to show that the residual, or reduced, velocity field, r, can be computed as

$$r = Pv - PA\tilde{m}, \tag{2.17}$$

where the weighted projection operator P is formed from the orthogonal $\hat{P}$ by

$$P = L\hat{P}L^{-1}. \tag{2.18}$$

2.3.2 A block model

We are now ready to address our second primary objective, namely, to infer the distribution of crustal deformation in southern California and northern Baja from the GPS derived velocity field. Toward this end, we adopt a simple elastic block model similar to that of *Matsu'ura et al.* [1986] and apply the inversion procedure described above.

The deformation model that we use consists of a set of elastic Poisson blocks in contact along vertical planar boundaries. From the surface to some depth, the blocks are welded together. Below this "locking depth", they are free to slide past one another. The blocks are assumed to extend to infinite depth. For non-trivial locking depths, temporally uniform relative motions among the blocks results in the temporally uniform accumulation of elastic strain within the blocks. When the stresses thus induced exceed the strength of one of the welded contacts, abrupt elastic rebound will return the adjacent blocks to a state of reduced strain. The velocity field predicted on the surface of the blocks can be considered as the superposition of temporally uniform rigid block motions and the cyclic and spatially variable perturbations due to the accumulation and release of elastic strain.

Our choice of this particular type of deformation model is motivated by the following observations. First, previous geodetic measurements and geological evidence imply that geological slip rates on faults throughout the plate boundary zone appear to be largely constant over tens to millions of years. Therefore strain accumulation appears to be largely elastic, at least as viewed from small aperture networks. Relative plate motions also appear to be fairly constant over similar time scales as determined from geological evidence and space geodetic measurements. Second, steep gradients in the observed southern California and northern Mexico velocity field, and the principal directions of strain accumulation are features well represented by dislo-

cation models. While we do not allow for variation in rheological properties such as possibly occur at the crust/mantle interface, we expect that our simple model should adequately account for most of the observed motion. Furthermore, once the velocity field has been reduced using this simple elastic model, we will have an opportunity to investigate the residual field.

We apply this model to southern California and northern Baja by hypothesizing that the surface of the Earth, as viewed from our GPS network, deforms like a set of five blocks which are in horizontal motion with respect to one another and which are joined along 15 planar surfaces (Figure 2-4). We wish to determine which among the family of crustal deformation hypotheses parameterized by four independent model parameters representing relative motions between the five blocks is most consistent with the GPS velocity field presented in Section 2. This vector of model parameters is

$$m = (m_1, m_2, m_3, m_4), \tag{2.19}$$

where m_1 represents the relative motion between the Pacific (PB) and Peninsular Ranges (PRB) blocks, m_2 represents the relative motion between the PRB and the Riverside block (RB), m_3 represents the relative motion between the RB and the Coachella block (CB), and m_4 represents the relative motion between the CB and the North American block (NAB). The locations and orientations of the block boundaries have been chosen to represent the most tectonically important faults based on the geologic, seismic, and geodetic evidence reviewed in the introductory section of this chapter (Table 2.7). We specified the locking depths appropriate for each fault zone based on depths of seismicity and previous geodetic investigations [e.g., *Savage and Prescott,* 1976; *Thatcher,* 1979; *Doser and Kanamori,* 1986; *Couch et al.,* 1991; *Frez and Gonzalez,* 1991].

The actual calculation of a velocity field can be factored into two main transformations. First, we relate the relative block motions to a slip rate vector $s = (s_1, \ldots, s_{15})$,

representing the 2-vector (horizontal) displacement rates along each of the 15 dislocation surfaces. Each of these displacement rate vectors can be resolved into fault parallel and perpendicular components. The vector s, therefore, contains 30 elements; 2 for each of the 15 displacement rate vectors. Note that the locking depths are meaningful only for the fault parallel components of the displacement rates. Table 2.7 provides the ordering of the 2-vectors of displacement rate in the slip rate vector. The kinematic relationship between relative block motions and fault slip rates is given by the 30×4 fault geometry matrix F

$$
F = \begin{bmatrix}
0 & 0 & \cos(\theta_{SA2} - \theta_{SA1}) & \cos(\theta_{SA2} - \theta_{SA1}) \\
0 & 0 & \sin(\theta_{SA2} - \theta_{SA1}) & \sin(\theta_{SA2} - \theta_{SA1}) \\
0 & 0 & 1 & 1 \\
0 & 0 & 0 & 0 \\
0 & 0 & 0 & \cos(\theta_{SA3} - \theta_{SA4}) \\
0 & 0 & 0 & \sin(\theta_{SA3} - \theta_{SA4}) \\
0 & 0 & 0 & 1 \\
0 & 0 & 0 & 0 \\
0 & 0 & 0 & \cos(\theta_{SA4} - \theta_B) \\
0 & 0 & 0 & \sin(\theta_{SA4} - \theta_B) \\
0 & 0 & 1 & 1 \\
0 & 0 & 0 & 0 \\
0 & 0 & \cos(\theta_I - \theta_M) & \cos(\theta_I - \theta_M) \\
0 & 0 & \sin(\theta_I - \theta_M) & \sin(\theta_I - \theta_M) \\
0 & 1 & 1 & 1 \\
0 & 0 & 0 & 0 \\
0 & 0 & 1 & 0 \\
0 & 0 & 0 & 0 \\
0 & 0 & \cos(\theta_{SJ} - \theta_S) & 0 \\
0 & 0 & \sin(\theta_{SJ} - \theta_S) & 0 \\
0 & 1 & 0 & 0 \\
0 & 0 & 0 & 0 \\
0 & \cos(\theta_E - \theta_{LS}) & 0 & 0 \\
0 & \sin(\theta_E - \theta_{LS}) & 0 & 0 \\
1 & 0 & 0 & 0 \\
0 & 0 & 0 & 0 \\
\cos(\theta_{SC} - \theta_{AB}) & 0 & 0 & 0 \\
\sin(\theta_{SC} - \theta_{AB}) & 0 & 0 & 0 \\
\cos(\theta_{SPM} - \theta_{SC}) & 0 & 0 & 0 \\
\sin(\theta_{SPM} - \theta_{SC}) & 0 & 0 & 0
\end{bmatrix}. \qquad (2.20)
$$

That is, given the relative block motion rates m, the slip rates along the faults are computed by

$$s = Fm. \tag{2.21}$$

By ignoring small differences in strike among dislocations which are nearly parallel to the direction of relative block motions, we have assumed that the direction of relative motion is roughly parallel to the average of the traces of the faults in southern California and northern Baja.

We represent the block boundaries by rectangular dislocation surfaces allowing us to use Okada's expressions [*Okada,* 1985] to calculate the deformation rates at points on the surface of the blocks from the slip rate vector s. Symbolically, we have

$$A = GF, \tag{2.22}$$

where G represents the matrix of Green's functions used in the transformation from fault slip rates to surface deformation rates.

The last ingredient in the velocity calculation is a means by which we relate station location on the surface of the Earth to station location represented in the model. The calculated deformation rate on the surface of the blocks is related to the geodetic velocity field (representing motions at specific points on Earth's surface) through an approximative transformation from geodetic site coordinates to local Cartesian coordinates. In performing this transformation, we assume that the radii of curvature of the prime vertical and of the meridian are independent of the geodetic site coordinates. The errors incurred from this approximation grow with distance of the GPS stations from the block boundaries. However, since gradients in the Green's functions drop off rapidly with distance away from the block boundaries, errors in site location associated with this transformation result in negligible errors in the calculated velocities.

2.3.3 Results

Given the GPS velocity estimates v and their error variance-covariance matrix V, we obtained an estimate of the relative block motions $\tilde{m}$ with the inversion method described above. We achieved a minimum value for the misfit functional of $\Psi(\tilde{m}, \tilde{n}) = 129$ yielding a variance scale factor estimate of $\tilde{\sigma}^2 = 1.2$. The relative block motion estimates are listed in Table 2.8. The residual velocity field r is shown in Figure 2-6. Since we are only concerned with the components of the velocity field that cannot be explained by a systematic translation, errors included, we compare r to the projected variance-covariance matrix PVP^T. The resulting fault slip rates, $\tilde{s} = F\tilde{m}$, are listed in Tables 2.7. We compare our estimates with previous geological and geodetic results in Table 2.10.

We used horizontal velocity estimates for a total of 56 GPS stations to infer 4 model parameters yielding a total of 110 independent data and 106 degrees of freedom. Using the chi-square test criterion, we find that we can reject the null hypothesis ($\sigma^2 = 1$) in favor of the alternative hypothesis ($\sigma^2 > 1$) with only 94% confidence. However, we note that an increase of only 10% in the scale factor used to estimate the velocity errors ($2.3 \rightarrow 2.5$) would yield $\tilde{\sigma}^2 = 1$. A miscalibration of the velocity uncertainties of this level is likely given the general level of uncertainty associated with the assessment of the errors in GPS velocity estimates discussed above.

2.3.4 Sensitivity analyses

We investigated the sensitivity of our parameter estimates to the scaling and structure of the velocity error variance-covariance matrix using the ad hoc error model

$$V_{total} = \sigma^2(V + \alpha^2 I), \tag{2.23}$$

where α^2 is an arbitrary real number, and $\sigma^2 = \sigma^2(\alpha^2)$ is again an unknown variance scale factor to be estimated in the usual way. For example, from our solution above, we see that $\tilde{\sigma}^2(0) = 1.2$.

We ran several solutions using various values for α^2. The results, from which we make the following observations, are tabulated in Table 2.11. First, for α^2 equal to 1, the only appreciable difference to the parameter estimates is an increase in the uncertainty of the San Clemente slip rate estimate. Second, for values of α^2 of 10 or greater, the parameter estimates begin to fluctuate, though at a statistically insignificant level. Together, these results indicate that the estimates are relatively insensitive to the structure of the velocity error variance-covariance matrix. Finally, we notice that with $\alpha^2 = 1$ we achieve $\tilde{\sigma}^2 = 1$. That is, additive, uncorrelated noise at the level of $(1 \text{ mm/yr})^2$ significantly reduces the confidence level at which we could reject our null hypothesis regardig the error processes.

Next, we performed a series of inversions in which we held certain parameters fixed to zero in order to investigate the sensitivity of the chi-square fit to the model parameterization. First, we held the relative motions between the PB and PRB at zero to test the sensitivity of data to the existence of the San Clemente and Agua Blanca fault systems. We observe a small but appreciable change in the chi-square fit to the data (141 versus 129) yielding an F ratio of 1.1. From the cumulative F distribution, we cannot conclude that our preferred model provides a significantly better fit to the data. That is, the difference could be due to random fluctuations in the data. However, slip rate estimates for the San Andreas, San Jacinto, and Elsinore are 26 $\pm$ 2 mm/yr, 9 $\pm$ 2 mm/yr, and 8 $\pm$ 2 mm/yr; essentially the same as for the complete fault system solution; whereas, the total plate motion estimated across the block system drops to 42 $\pm$ 1 mm/yr, i.e. the slip rate along the Cerro Prieto fault. Furthermore, significant changes in the residual field occur only at sites BLUF and LLCO (Figure 2-7), near the San Clemente and Agua Blanca faults, and are parallel

to the directions of relative block motions. These residuals can easily be explained by motion along the San Clemente and Agua Blanca fault systems. We note finally that, if we are to account for the full plate rate, motion of greater than about 4 mm/yr must be accommodated outside the San Andreas, San Jacinto, and Elsinore fault systems. Based on these results, we maintain that this "missing" motion is accommodated along the San Clemente/Agua Blanca system.

For the second test, we held the relative motions between the PRB and RB at zero to test the sensitivity of the data to the existence of the Elsinore and Laguna Salada fault systems. Again, there is a small but appreciable change in the chi-square fit to the data (147 versus 129) giving an F ratio of 1.1. As before, the F value alone does not provide sufficient evidence to conclude that our prefered model provides a significantly better fit to the data. We notice that the slip rate estimated on the San Andreas fault drops to 25 $\pm$ 2 mm/yr as the estimated rate for the San Jacinto increases to 15 $\pm$ 1 mm/yr. The San Jacinto rate estimate increases to accommodate motion across the Elsinore fault zone while the San Andreas estimate decreases slightly to compensate for the increased deformation in the Coachella block implied by the San Jacinto estimate. The slip rate estimated for the San Clemente fault is 8 $\pm$ 3 mm/yr, nearly the same as for the preferred solution. The total plate motion estimated across the block system for this solution is 48 $\pm$ 3 mm/yr, comparable to the plate rate estimated using the preferred model. However, significant and systematic changes in the residual field occur about the Elsinore fault (Figure 2-8). While the results of this test corroborate our intuition that there exists a slight trade off between the rates of slip on the San Andreas, San Jacinto and Elsinore faults[13], the pattern of residuals is clearly indicative of unexplained motion along the Elsinore and Laguna Salada fault systems.

[13]Negative correlations among the San Andreas, San Jacinto, and Elsinore slip rate estimates are indeed indicative of a trade off, the sums of parameter estimates being better determined than the individual parameter estimates.

For the third test, we held the relative motions between the RB and CB at zero to test the sensitivity of the data to the existence of the the San Jacinto and Superstition Hills/Superstition Mountains fault systems. The change in the chi-square fit to the data is appreciable (159 versus 129), but the F ratio is still only 1.2. We cannot conclude from this value that our prefered model provides a significantly better fit to the data. The slip rate estimated on the San Andreas fault jumps to 30 $\pm$ 1 mm/yr and the Elsinore increases to 14 $\pm$ 1 mm/yr. The slip rate estimated on the San Clemente fault is 7 $\pm$ 3 mm/yr and the total plate motion estimated across the block system is 50 $\pm$ 3 mm/yr, a close match with the estimates from the preferred model. However, we observe significant and systematic changes in the residual field symmetric about the San Jacinto fault (Figure 2-9). While this result again reflects the slight trade off between between the rates of slip on the San Andreas, San Jacinto and Elsinore faults, the pattern of residuals is clearly indicative of missing motion along the San Jacinto fault.

For the fourth test, we held the relative motions between the CB and NAB at zero to test the sensitivity of the data to the existence of the the San Andreas and Imperial fault systems. The change in the chi-square fit to the data is large for this solution (550 versus 129). From the F ratio of 4.21, we may conclude with certainty that the increase in the misfit is too large to be accounted for by random fluctuations in the data. Furthermore, the slip rate estimated on the San Jacinto fault jumps to 29 $\pm$ 3 mm/yr while the Elsinore shrinks to an insignificant 2 $\pm$ 4 mm/yr. The parameter estimates attempt to account for the large velocity gradient associated with the San Andreas with an increased slip rate on the San Jacinto, while a corresponding decrease in the slip rate estimate for the Elsinore compensates for the increased motion of the Riverside block implied by the San Jacinto estimate. The slip rate estimated on the San Clemente fault is 5 $\pm$ 5 mm/yr. The total plate motion estimated across the block system for this solution is only 36 $\pm$ 5 mm/yr. Significant changes in the residual field are apparent at most stations in the network and are roughly symmetric

about the San Andreas fault (Figure 2-10). This result clearly demonstrates that the San Andreas plays a dominant role in accommodating Pacific-North America relative plate motion. That is, the details of the crustal deformation field observed from the southern California and northern Baja GPS network are compatible only with models for which a large portion of the total Pacific-North American relative plate motion is accommodated across the San Andreas fault system.

2.4 Discussion

During the period of our observations (1986-1995), southern California was jolted by its largest earthquake in forty years, the 1992 M_w 7.3 Landers earthquake. Most of the sites in the southern California GPS network appear to have been affected (Figure 2-3). While it is common practice to estimate secular velocities from GPS observations spanning durations of several years during the interseismic period, there is reason to suspect that temporal perturbations to the actual crustal deformation signal could result from accelerated slip rates on faults following an earthquake [e.g., *Yang and Toksöz,* 1981], or from post-seismic viscoelastic relaxation in an intra-crustal or sub-crustal asthenospheric layer [e.g., *Li and Rice,* 1987]. However, it is not clear whether we should expect our observations to contain post-seismic signals because, unfortunately, the parameters required by these more realistic models are not well constrained. Even less clear is the possibility of a pre-seismic signal. Therefore, we should carefully assess the applicability of the standard assumption of linear-in-time motions. Unfortunately, the frequency and total span of data for most sites in our network is too short to justify a rigorous mathematical treatment of this problem. Based on a qualitative investigation of the time series in Appendix C, and the results of *Savage et al.,* [1986], *Savage et al.,* [1987], *Savage et al.,* [1993], *Savage and Lisowski,,* [1995a], *Savage and Lisowski,,* [1995b], and *Savage,* [1995] who demonstrate that no

significant deviations from secular trends are found in nearly twenty years (1973-1991) of trilateration measurements in the vicinity of the San Andreas fault, we conjecture that the horizontal tectonic signal consists of a superposition of temporally uniform motions, episodic earthquake displacements, and normal noise processes. We show the velocity and earthquake displacement estimates that we have determined from the data together with the time series of coordinate determinations in Appendix C for comparison.

Another area of concern is that the ability to distinguish among competing types of geophysical models depends on knowledge of the errors in GPS velocity estimates. We have estimated the GPS site velocity errors using the standard assumption of Gaussian statistics, yet there is reason to suspect that this assumption is not true. By using an ad hoc error model, we find that our estimates for relative block motion rates are relatively insensitive to the structure of the GPS velocity error variance-covariance matrix. In addition, we find that additive white noise of variance $(1\ \mathrm{mm/yr})^2$, would be sufficient to yield $\tilde{\sigma}^2 = 1$. Taking the reverse approach to the problem, that is, assuming the model to be "correct", our estimate of $\tilde{\sigma}^2 = 1.2$ would imply that we have underestimated the GPS errors by only 10%, a reasonable possibility.

The residual velocity field shows outliers at the 95% confidence level for only two sites: BLAC and CPEI (Figure 2-6). Anomalous motion of monument BLAC, similar to that seen in the residual velocities has been observed from a combination of VLBI, GPS and EDM data [cf., *Dong,* 1993, Figure 8a]. While we share a common observation (TREX00, 1986) with this analysis, site BLAC is one of the most thoroughly observed sites in the STRC network (Table 2.2). We conclude that the apparent motion of site BLAC is real, but suspect that, based on the behavior of neighboring sites, it is not of tectonic origin. Investigation of the time series of site CPEI (Figure C-7) reveals that the large difference between the GPS rate estimates and the model prediction could likely be an artifact of the simultaneous estimation of site velocity

and earthquake displacements based on only three observations. But again, based on the behavior of neighboring sites, we do not believe that this residual reflects unmodeled or mismodeled crustal deformation such as an error in the locking depth used for the Cerro Prieto fault.

We identify no systematic components in the residual field (Figure 2-6). This implies that possible viscoelastic effects, which we have not accounted for in our simple model, are either less than about a few millimeters per year during this time period, or have effectively been averaged out by our having forced the pre- and post-earthquake velocities to be equal. That the slip rates we infer from the GPS velocity field are highly consistent with geolocally inferred rates, however, is highly consistent with the predictions of a simple elastic model.

Our data provide evidence for the partitioning of strain along a finite set of discrete faults in southern California and northern Baja. Sensitivity analyses indicate that each fault of our model explains a unique systematic component of the observed velocity field. In particular, the San Andreas appears to play an important role in the accommodation of Pacific-North American plate motion in southern California, picking up >50% of the total relative motion. Our slip rate estimate of 26 $\pm$ 2 mm/yr is indistinguishable from the geological estimate of 25 $\pm$ 4 mm/yr [*Weldon and Sieh,* 1985]. Paleoseismic evidence indicates that this segment of the fault has remained dormant throughout the historical period, not having ruptured since about 1680 [*Sieh,* 1986], while maintaining an average recurrence interval of about 300 years over the past 2,000 years [*Sieh,* 1986]. To the extent that the elastic Earth hypothesis is valid, we conclude that the San Andreas has accumulated about 8.2 m of slip deficit over the last 315 years or so, most of which is likely to be regained during a future earthquake.

We estimate a rate of 9 $\pm$ 2 mm/yr for the San Jacinto fault zone, in excellent

agreement with the geological estimates of 10 ± 2 mm/yr. There is evidence to suggest that the locking depth along the San Jacinto fault varies from south to north [e.g., *Johnson et al.,* 1994]. We assume the locking depth is constant along the entire fault, and we detect no statistically significant trends in the residual velocities. Also, our estimate for the ratio of slip rate to locking depth of (1.2 ± 0.3) $\times 10^{-6}$/yr is in excellent agreement with the estimate of *Savage and Prescott* [1976] of 1.2 $\times 10^{-6}$/yr for the northern part of the fault. Motion along the San Jacinto fault appears to explain a systematic component of the observed velocity field that cannot otherwise be explained by any combination of slip rates on the other faults of the model.

The sensitivity test in which the Elsinore fault was constrained to zero velocity results in estimates of 25 ± 2 mm/yr for the San Andreas and 15 ± 2 mm/yr for the San Jacinto. These values are quite geophysically reasonable. However, motion along the Elsinore fault explains systematic trends in the observed velocity field that are not explained by any combination of slip rates on the other faults of the model. Our estimate for the slip rate for the Elsinore fault zone of 7 ± 2 mm/yr is similar to, though slightly larger than, the average geological estimate of 4 mm/yr.

The Imperial and Cerro Prieto faults accommodate a large portion of the motion. For the Imperial Valley fault, there is little to compare with. Since the ruptures of the 1940 and 1979 Imperial Valley earthquakes were dissimilar, we cannot infer reliable slip rate estimates from them for comparison. Given the possibility of post-seismic motion following the 1940 event, it seems possible that aseismic creep might be relieving some strain accumulation along the fault. The seismic slip rate estimated for the Cerro Prieto fault by *Frez and Gonzalez* [1991] on the other hand (41 mm/yr neglecting the contribution to the slip rate from events of less than magnitude six), is indistinguishable from our estimate of 42 ± 1 mm/yr. This result appears to be fairly robust provided that the San Andreas system is included in the model.

Our results provide some evidence to suggest that the San Clemente and Agua Blanca fault zones accommodate 7 $\pm$ 2 mm/yr and 6 $\pm$ 2 mm/yr respectively. Our uncertainty estimates do not reflect the fact that we have neglected the San Miguel, Vallecitos, Rose Canyon, Newport Englewood, Coronado Bank, Bahia Soledad and similar fault systems in our model, which could each accommodate a small portion of the total motion. On the other hand, we detect no systematic trends in the residual field (Figure 2-6) indicative of significant motions along these features.

Our GPS based crustal deformation hypothesis provides us with an estimate of the total Pacific-North American relative plate motion of 49 $\pm$ 3 mm/yr, consistent with previous space geodetic results and NUVEL-1A (46 $\pm$ 1 mm/yr). The agreement is interesting in that the geologically inferred plate motion model's estimates represent motion averaged over millions of years (much longer than the $\sim$ 300 year recurrence interval for the San Andreas fault), whereas the geodetic estimates represent motions averaged over durations of only a fraction of a seismic cycle.

There are several other areas in which our model makes testable predications. We have assumed that the transition from crustal spreading in the Gulf of California to the right-lateral transforms of southern California involves bifurcations in the primary plate boundary transforms from south to north which result in great variability in tectonic environment along the plate boundary. Our model includes three generic types of tectonic environment: transcurrent, transpression, and transtension. Transcurrent environments are characterized by elastic strain above the deep crustal shear zones which serve as the primary vehicles for accommodation of Pacific-North American relative motion. The fault normal component of the displacement rate vectors associated with these features are zero. Transpressional environments are characterized by a combination of lateral translation and convergence orthogonal to the direction of translation. These environments are associated with compressional jogs in the dislocation surfaces of our block model and generally correlate with the occurrence of

mountainous terrain, and secondary left-lateral "cross faults." Transtensional environments are characterized by a combination of lateral translation and opening in a direction orthogonal to the direction of translation. These environments are associated with extensional jogs in the dislocation surfaces of our block model and generally correlate with the occurrence of pull-aparts, high heat flow, and/or normal faulting.

In our preferred model, we have placed a compressional dislocation jog in the vicinity of the Laguna Salada fault zone and the Sierra Cucapa mountains in northern Baja California, Mexico. We infer from our estimates of relative block motion rates that 7 ± 2 mm/yr of right-lateral strike-slip is transferred between the Cerro Prieto and Elsinore faults along this segment of our model and that a statistically insignificant 1 ± 1 mm/yr convergence is accommodated normal to the strike of the dislocation plane. However, the exact values are dependent on the difference in strike between the dislocations representing this feature and the Cerro Prieto fault which is not well defined by the geology. Indeed, this is a very complicated area, in which small scale pull-apart basins and associated secondary normal faults lie between right-stepping *en echelon* master fault strands, while uplifted slices of rock suggest a long term transpressional environment [*Sylvester and Smith,* 1976; *Mueller and Rockwell,* 1991]. Conventional geodetic measurements also provide variable results for this area. For example, trilateration measurements analyzed by *Johnson et al.* [1994] indicate compression along the southernmost Elsinore fault zone, while *Savage et al.* [1994] find that they can not explain observations of extension across the Laguna Salada fault using a model for normal dip-slip at depth on the Laguna Salada fault without adopting unusual values for the dip of their model fault, because, as they note, normal dip slip implies compression above the fault under usual circumstances. Therefore, we conjecture that reverse dip-slip along the Laguna Salada could accommodate convergence.

We have placed a compressional dislocation jog in the vicinity of Superstition

Mountain. We infer rates of 8 ± 2 mm/yr and 4 ± 1 mm/yr of right-lateral slip and normal compression respectively along this feature. This range is bordered on either side by the Superstition Hills and Superstition Mountain faults. Left-lateral cross faults such as the recently ruptured Elmore Ranch fault are common to the area and are intimately linked to the right-lateral fault systems. *Larsen et al.* [1992], for example, provide evidence for a triggering relationship between the conjugate Superstition Hills and Elmore Ranch events. The geometry and sense of motion of these cross faults are consistent with conventional geodetic measurements which, when combined with space geodetic observations, indicate significant clockwise rotation just to the east of this area [*Dong,* 1993].

Along the southern face of the San Bernadino mountains, we place a pair of compressional dislocation jogs to represent the "Big Bend" segment of the San Andreas fault. This range, containing the highest mountain peak in California south of Mt. Whitney, has undergone rapid uplift in the last 5 Ma. [e.g., *Meisling and Weldon,* 1989]. Faulting here is extremely complicated and spread over a broad area [e.g., *Seeber and Armbruster,* 1995]. The rates of convergence that we estimate across these features (12 ± 1 and 13 ± 1 for the SA1 and SA3 segments respectively), are not well constrained, however, due primarily to uncertainties regarding the location and nature of the Eastern California Shear Zone [e.g., *Dokka and Travis,* 1990a]. As a result, the San Bernadino mountains could be moving with respect to North America as fast as 7 mm/yr. The occurrence of the 1992 M_w 6.5 Big Bear earthquake (a.k.a. Landers aftershock) is suggestive of a relationship between left- and right-lateral conjugate structures similar to that found in the vicinity of Superstition Mountain. In fact, this event may have involved both right- and left-lateral rupture along conjugate planes [*Jones et al.,* 1993]. Of related interest, is that trilateration analyses indicate extension east of the San Bernadino mountains in the vicinity of the 1992 Joshua Tree and Landers earthquake epicenters [*Lisowski et al.,* 1991; *Savage et al,* 1993, *Johnson et al.,* 1994]. It is interesting to note the similarity between this area and

the transpressional/transtensional environment pairs in our model to the south (the Mexicali Seismic Zone and Sierra Cucapa range, and the Brawley Seismic Zone and Superstition Mountain).

We also represent the trans-Baja Agua Blanca fault zone by a compressional dislocation jog. That is, the geometry of the model in this region requires some degree of convergence to occur along the model fault. However, we are not aware of clear evidence to support convergence in this area. Our assumption that the Agua Blanca fault somehow transfers motion to the San Clemente fault zone is based on the following controversial argument. First, *Goff et al.* [1987] demonstrate that fault kinematics in the northern Gulf of California can be understood in terms of a fault-fault-fault triple junction in which the Agua Blanca or similar fault transfers a portion of the plate motion to faults west of the Elsinore. Second, *Farina et al.,* [1994] provide evidence suggesting that the Agua Blanca fault slips at a rate of at least 6 mm/yr. Third, seismic evidence suggests that the Agua Blanca fault zone extends beyond the coast under the ocean [*Gonzalez and Suarez,* 1984]. Fourth, *Legg et al.* [1989] and *Legg* [1991b] find that the San Clemente fault appears to be the dominant off shore fault zone exhibiting clear and significant Quaternary offsets. On the other hand, *Legg et al.* [1989] and *Legg et al.* [1991a] provide compelling evidence to suggest that the Agua Blanca system connects with the Coronado Bank fault rather than the San Clemente fault. They conclude that the San Clemente fault is continuous with the San Isidro fault located offshore from Baja California. Weak agreement between Pacific-North American relative plate motion estimates from GPS (e.g., 47 ± 7 mm/yr, [*Dixon et al.,* 1990]; 48 ± 5 mm/yr, Figure 2-2) and NUVEL-1A (46 ± 1) cannot rule out the possibility of plate motion accommodated off the Baja California coast. Nevertheless, we speculate that the Agua Blanca fault somehow transfers plate motion to the San Clemente fault. We have included a transverse dislocation to represent this transfer and under this assumption, we estimate a slip rate of 6 ± 2 mm/yr and an insignificant rate of convergence of 1 ± 1 mm/yr. Figure

2-7 effectively demonstrates the change in the residual velocity at site LLCO which results from neglecting the Agua Blanca fault.

In the Imperial Valley, the Salton Trough is characterized by high rates of seismicity and high heat flow. It is the location of the Brawley Seismic Zone; a manifestation of the transfer of motion from the Imperial to the San Andreas fault. Seismic velocities [*Fuis et al.,* 1984] and gravity modeling [*Biehler,* 1964] indicate that the crust beneath the valley is composed of a thick layer of low density sediment above a basement of greenschist facies metasedimentary rock which is in turn underlain by a subbasement of gabroic material. This is in contrast to the neighboring southern California batholith of granitic igneous and metamorphic rocks. The Salton Trough appears to represent a pull-apart structure which has evolved over the last 5 Ma. Geodetic and geophysical evidence suggest, however, that active spreading in the trough near the Brawley Seismic Zone is quite young (3,000-100,000 years) and appears to be migrating to the north [*Larsen and Reilinger,* 1991]. *Lachenbruch et al.* [1985] estimate an extension rate of 25-50%/Ma for the trough throughout its history because slower rates are inconsistent with the crustal composition, and higher rates would result in massive melting of the crust. We estimate a contemporary rate of opening of 12 $\pm$ 1 mm/yr across the Brawley Seismic Zone. Assuming that this rate is representative of spreading over the trough's history, we conclude that the average width of the spreading center is in the range of 25-50 km, consistent with the current width of the Brawley Seismic Zone but much smaller than the length of the Salton Trough. This result suggests that spreading centers in the trough are transient or perhaps migratory as suggested by *Larsen and Reilinger* [1991].

Our model also assumes components of opening across the San Pedro Martir detachment fault across the Mexicali Seismic Zone. We estimate rates of opening of 31 $\pm$ 1 across the Mexicali Seismic Zone and 5 $\pm$ 2 across the San Pedro Martir fault. These rates are highly dependent on the geometry of the model which is poorly

constrained in these areas. Assuming that the Mexicali Seismic Zone represents a process of oblique rifting similar to the Brawley Seismic Zone, we predict, based on extension rate constraints appropriate for the Imperial Valley to the north, either a larger ratio of strike-slip to opening for the oblique Mexicali spreading center than that predicted for the Brawley Seismic Zone, that the spreading center is wider than that predicted for the Brawley Seismic Zone, or that melting of the crust is occurring.

2.5 Conclusions

Our GPS observations are consistent both with the notion that Pacific-North American relative plate motion in southern California and northern Baja, Mexico is accommodated across a finite set of discrete, relatively narrow shear zones which lie below fault zones having undergone significant Quaternary offset, and with the notion that strain accumulation about these features is largely elastic. Across southern California, deformation appears to be partitioned among the San Andreas, San Jacinto, Elsinore, and San Clemente faults. By fitting a simple elastic block model to our data, we infer slip rates of 26 $\pm$ 2 mm/yr, 9 $\pm$ 2 mm/yr, 7 $\pm$ 2 mm/yr, and 7 $\pm$ 2 mm/yr for these faults respectively. We also infer rates of 35 $\pm$ 2 mm/yr, and 42 $\pm$ 1 mm/yr for the the Imperial and Cerro Prieto faults respectively. The San Andreas fault appears to be the primary vehicle for accommodating this motion in southern California. We estimate that the southernmost San Andreas has accumulated about 8.2 m of slip deficit over the last few hundred years. Our results are consistent with seismic, geological, and geomorphological estimates for long-term slip rate on these faults, and we observe no systematic trends in the residual velocity field. We also infer a total rate of Pacific-North American relative plate motion of 49 $\pm$ 3 mm/yr., consistent with the NUVEL-1A estimate of 46 $\pm$ 1 mm/yr. About 85% of the total relative plate motion is accommodated across the San Andreas, San Jacinto, and Elsi-

nore fault systems. In addition to transcurrent motions, we hypothesize that either convergence or divergence occurs along block boundaries transverse to the direction of plate motion. Convergent boundaries correlate well with mountainous terrain, reverse faulting, and/or cross-faults. Divergent boundaries correlate well with crustal spreading, high heat flow, and/or normal faulting.

Table 2.1: List of Experiments

Name	Date	Rxrs	Ant.	Survey Area	Sites
STRC 88	Feb 88	TI4100	TI4100	Imperial Valley	13
GEOMEX	May 89	TI4100	TI4100	Mexicali Valley	6
STRC 90	Feb 90	TI4100 TRM SLD TRM SST	TI4100 TRM SLD TRM SST	Salton Trough– Riverside County	98
STRC 91	Mar 91	TRM SST	TRM SST	Salton Trough– Riverside County	51
JTRE 92	Apr 92	Ashtech	Ashtech	Joshua Tree	9
STRC 93	Feb 93	TRM SST, TRM SSE, Ashtech	TRM SST Ashtech	SaltonTrough – Riverside County	54
STRC 95	Feb 95	TRM SST TRM SSE	TRM SST	Salton Trough – Riverside County	58

Table 2.2: STRC Station History: Observation Sessions Per Experiment†

Site Id	Marker	88	89	90	91	92a	92b	93a	93b	95
1109	HPGN-CALIF STA 11-09				2			3		2
ACUT	Acute 1934 (reset)			3						
AGUA	Aguana			2					2	
AHRR	AHRR			1						
ALAM	Alamo 1934 (USGS)			3						2
ANZA	Anza			5	2				2	
ASA1	Mexicali Airport				1			3		
BACH	Bachelor			1						
BEEC	Beecroft			1						
BERD*	Berdoo Canyon			2	3			3		3
BLAC	Black Butte NCMN	2		10	10	2	4	12	12	3
BLOR	Bloree			1						
BLUF♭	BLUFF 1933									
BOTR	Palm Canyon Wash			3	3			2		3
BOUC	Boucher 2			2						
BRSH♮	BRUSH 1876									
CABA	Cabazon			3	2			3	3	2
CAHU	Lake Cahuilla			3	3			2		3
CALI	Calipatria 2 (Reset)			2						3
CHER	Cherry Valley			2	4				1	1
CHKO	Chuckwalla Springs			2						
COAC	Coach 2	2		2						3
COCH	Coach MWD				2		3	2	2	
COLL	College 1967 (Reset)	2		3				3		3
COXO	Cadiz Valley			2	2			3		3
CP03	Cerro Prieto 03			1						
CP13	Cerro Prieto 13			1	1			3		3
CPEI	CPEI				1			2		2
DAIT	Dammit			1						

† 92a = Pre-Joshua Tree earthquake observations, 92b = Post-Joshua Tree earthquake observations, 93a = STRC93, 93b = IC93.

* We had trouble obtaining a reasonable velocity for site BERD, therefore, since station density is not lacking in the vicinity of this site we have neglected it.

♭ BLUF observations from *Feigl et al,* [1993] experiment numbers 0 (1986), 10 (1988), 13 (1989), 18 (1990), 20 (1991).

♮ BRSH observations from *Feigl et al,* [1993] experiment numbers 10 (1988), 13 (1989), 18 (1990), 20 (1991).

Site Id	Marker	88	89	90	91	92a	92b	93a	93b	95
DESO	Desert Center			2	2			2		3
DSHO	Desert Shores			3	1					1
DUNP	Duneport			3	1			2		3
E122	E1223			3				3		2
EDOM	EDOM 2 1974 (USGS)			3	4			3		
ENDA*	CICESE (Ensenada)		5					12		
ENDD	End (USGS)			2	1			3		3
EXTR	Extra			3				2		3
F726	BM F726			3	2			2	2	2
FORD	Ford Dry Lake			3	2			3		3
FRIN	Frink 1934 (USGS)	2		3				3		2
GARN‡	Garnet Hill			3	5	3	3	3	3	
GLOC	G. L. O. Corner 1934	3		2						3
HAMA	Hamar 2 1967 (Reset)			3						3
HOLT	Holt 1924 (Reset)			2						
IMP1	IMP 1934			2						
IMP2	Imperial Valley 2			2						
IMP5	Imperial Valley 5			1						
IMP8	Imperial Valley 8			1						
INA4	Indian Ave. 4				3					
INA6	Indian Ave. 6				2					
INDI	Indio				3					
INDO	Indian Vista			2	3				3	
IPE0	Imperial Valley Prof.							2		3
JTRE	BM B1254			3	3			3		3
JUNC	Junction			2						3
KANE	Kane 1939 (USGS)	2		3						
L589	L589 1967	4		3						3
LACH	La Hechicera							3		
LAKE	Lake Elsinore			1	2			3		3
LLCO•	Llano Colorado		5	1				3		3
LN11	Leveling N11							2		
LPUR	La Puerta							6		3

⋆ Site ENDA appears to have been disturbed sometime after 1993 [*Rob Reilinger, Pers. Comm.*, 1995]. The extent of the disturbance has yet to be investigated, however.

‡ Site destroyed sometime after 1993 [*Rob Reilinger, Pers. Comm.*, 1995].

• GEOMEX 1989 observations from site LLCO appear to have been made from mark 7883 RM1. We have applied the tie -55.9931 40.5165 8.0171 NEU (meters).

Site Id	Marker	88	89	90	91	92a	92b	93a	93b	95
MACK	Mack 2 1967 reset			2						
MAYO	El Mayo Seis. Station			1	1			2		3
MCFN	McFarren			1						
MESA	Blythe Airport			1						
METZ	Perris-Metz Basin			2	3				3	3
MONT	CICESE N29							3		2
MONU$^{\diamond}$	Monument Peak NCMN		2	2	1			12		
N125	BM N1254			2	2			3		3
NIGU$^{\bowtie}$	Niguel A 1884 1981									
O216	Offset 216 1934			1						
O217	Offset 217 1934	2		2						
O225	Offset 225			2						3
O227	Offset 227			2						
OAKD	Oak Street Dam			2	3				3	3
OCOT	Ocotillo	2		8	1			5		3
OCTI	Ocotillo 1935	2		3						3
ORIE	Orient 1939 (Reset)	1		3				2		3
PAIN	Painted Canyon			4	3			3		3
PEGL	Peg Leg Smith (77AAR)				2					
PENA	Puerto Penasco		5					6		6
PIN1$^{\triangle}$	Pinyon Flat 1		2	11		3	4	10	10	12
PSAR	Palm Springs East			2	4			3		
PVER$^{\heartsuit}$	Palos Verdes ARIES									

$\diamond$ GEOMEX 1989 observations from site MONU appear to have been made from the old ARIES mark, monument number 7220. We have applied the tie 3.7666 2.1790 -0.0812 NEU (meters). MONU observations from *Feigl et al,* [1993] experiment number 0 (1986).

$\triangle$ PIN1 observations from *Feigl et al,* [1993] experiment numbers 0 (1986), 18 (1990), SB1 (1991), VB2 (1992). *Feigl et al* experiment 0 and GEOMEX 1989 observations were made from monument PINY (tie 125.588 117.655 279.910 XYZ meters). STRC91 and *Feigl et al.,* experiment 18 observations were made from monument PIN2 (tie -44.038 24.468 -0.438 XYZ meters).

$\bowtie$ NIGU observations from *Feigl et al,* [1993] experiment numbers 0 (1986), 10 (1988), 13 (1989), 20 (1991).

$\heartsuit$ PVER observations from *Feigl et al,* [1993] experiment numbers 0 (1986), 10 (1988), 13 (1989), 14 (1989), 16 (1989), 18 (1990), 20 (1991), SB1 (1991) VB2 (1992).

Site Id	Marker	88	89	90	91	92a	92b	93a	93b	95
RAMO	East Thousand Palms			2	3		2			
RIAL	Rialport			1	2					
RICE	Rice			1						
ROBO	Fig Tree (Reset)			3	3			3		5
ROSA	Rosa (CDH)			2	2				2	
RYAN	AHMI Ryan			2					2	
SAN1	Sandy Beach (Tide)	2		3	2					
SAND	Sand Hill(Deadman Lake)				5				5	
SANO	Sansev				1					
SFBC	San Felipe AP		5	1	1			3		3
SIO1♯	Scripps 1			12			2	8	12	12
SIPH	Siphon 20 (GPS 60061)			4	2			3		
SM01	San Miguel							3		2
T122	BM T1226			2						3
TAMA	Tamarisk 3 1967	2		2						
THOU	Thousand Palms			1			2			3
TRAN	Bob1 (Reset) (Tide)			3	3			2		
U587	BM U587			3				3		
UBUN	Ubrun			1						
VA01	Vallecitos							3		3
VARN	St. Park Tide Reset			3	3			3		3
VIEW‡	View 2 1986 (USGS)			3	3		2	3		
VORO	Thermal Airp. Reset			3	3					
WIDE	Wideview			5	4		4	3	3	3
YUMA□	Yuma NCMN							12		
YUNG	Rainbow Rancho			1				3	3	3

♯ SIO1 observations from *Feigl et al,* [1993] experiment numbers 18 (1990), SB1 (1991) VB2 (1992). STRC90, *Feigl et al,* experiment 18, and STRC93 observations from monument SIO2 (tie 17.538 10.674 26.055 XYZ). IC93 and STRC95 observations from monument SIO3 (tie -65.299 267.391 271.357 XYZ meters).

‡ Site destroyed sometime after 1993 [*Rob Reilinger, Pers. Comm.,* 1995].

□ Site YUMA unusable after 1993. New site LORW (with tie) has been established by Ruben Hernandez, Yuma Proving Grounds (US ARMY) [*Karl Feaux, UNAVCO, Pers. Comm.,* 1995]. YUMA observations from *Feigl et al,* [1993] experiment number 0 (1986).

Table 2.3: Parameter Constraints

Parameter	A priori	Stochastic
Coordinate time series solution		
local coordinates	10 m	10 m^2/yr
deterministic coordinates	10 m	
deterministic horizontal velocities	1 m/yr	
forced vertical velocities	5 mm/yr	
tracker coordinates	10 mm	
tracker velocities	0.5 mm/yr	
Velocity solution		
local horizontal coordinates	10 m	
local vertical coordinates	10 m	1 m^2/yr
local horizontal velocities	1 m/yr	
tracker coordinates	50 mm	
tracker velocities	1 mm/yr	

Table 2.4: Cartesian Coordinates and Velocities for Tracking sites in (m) and (m/yr)

Station	Coordinates			Velocities		
	X	Y	Z	U	V	W
Algonquin	918129.2910	-4346071.1708	4561977.8500	0.0014	-0.0035	0.0006
Fairbanks	-2281621.3797	-1453595.4442	5756962.0183	0.0004	-0.0039	0.0008
Ft. Davis	-1324192.2386	-5332059.7997	3232043.5187	0.0007	0.0004	-0.0005
Kokee	-5543838.2131	-2054586.9316	2387809.6890	-0.0008	0.0603	0.0563
Mojave	-2356216.2769	-4646736.3740	3668456.4180	-0.0011	0.0084	0.0035
Penticton	-2059164.8417	-3621108.0877	4814432.4849	0.0020	-0.0022	0.0017
Pietown	-1640917.0849	-5014780.9260	3575447.2304	0.0005	0.0030	-0.0031
Richmond	961309.0431	-5674075.7942	2740539.0972	0.0011	-0.0021	0.0018
St. John's	2612631.1088	-3426807.0866	4686757.7636	0.0002	-0.0001	0.0002
Yarragadee	-2389024.9679	5043317.1157	-3078530.9240	-0.0616	0.0099	0.0539
Yellowknife	-1224399.6033	-2689272.9605	5633620.2845	-0.0008	-0.0086	0.0111

Table 2.5: Velocity Estimates Relative to ENDD (mm/yr)

Station	Estimate		Uncertainty		Corr.
	East	North	East	North	
1109	-25.81	25.68	3.24	3.08	0.0698
ANZA	-16.84	26.32	6.64	5.04	-0.0233
BLAC	-7.91	0.33	2.89	2.65	0.0732
BLUF	-30.82	37.39	3.57	3.02	0.0374
BOTR	-18.02	20.38	3.12	2.94	0.0605
BRSH	-31.03	34.42	3.83	3.20	0.0447
CABA	-15.83	21.30	3.16	2.97	0.0678
CAHU	-15.82	13.61	3.09	2.89	0.0725
CHER	-12.56	20.32	3.85	3.51	0.0129
COAC	-1.15	1.86	4.70	3.90	-0.0409
COLL	-12.20	20.69	3.14	2.89	0.0760
COXO	-2.62	0.81	3.19	2.88	0.1125
CP13	-10.63	8.32	3.15	3.01	0.0549
CPEI	-9.62	11.48	3.34	3.07	0.0813
DESO	-2.25	3.26	3.17	2.93	0.0893
DUNP	-13.84	13.31	3.19	3.06	0.0671
E122	-20.57	22.38	3.07	3.01	0.0517
EDOM	-15.00	13.29	6.52	5.59	-0.2057
ENDA	-32.19	31.83	5.97	5.50	-0.0049
F726	-3.46	1.70	3.23	3.01	0.0683
FORD	-3.25	-1.40	3.44	3.06	0.1125
FRIN	-4.96	2.52	2.90	2.80	0.0559
GARN	-10.42	16.09	4.60	3.96	0.0168
IPE0	-6.12	2.53	3.96	4.21	0.0310
JTRE	-4.27	3.11	3.08	2.86	0.0764
L589	-24.04	25.63	4.02	3.60	-0.0267
LAKE	-30.74	26.84	3.44	3.33	0.0841
LLCO	-37.42	31.45	3.53	3.10	0.0690

Station	Estimate		Uncertainty		Corr.
	East	North	East	North	
LPUR	-21.93	31.26	3.16	3.03	0.0545
MAYO	-28.22	30.08	3.36	3.10	0.0643
METZ	-21.97	26.80	3.54	3.30	0.0458
MONU	-29.37	29.78	3.47	2.98	0.0684
N125	-8.48	5.83	3.10	2.89	0.0751
NIGU	-30.61	32.07	3.37	2.90	0.0630
OAKD	-22.83	25.61	3.77	3.47	0.0433
OCOT	-27.60	25.64	3.15	2.87	0.0704
OCTI	-26.63	26.92	5.63	4.84	-0.0612
ORIE	-4.43	6.11	3.13	2.86	0.0638
PAIN	-12.29	7.81	3.11	2.90	0.0736
PENA	-0.90	0.60	3.49	3.02	0.0911
PIN1	-18.53	18.30	2.88	2.58	0.0804
PSAR	-17.01	16.00	5.89	4.87	-0.0773
PVER	-30.34	31.83	3.11	2.78	0.0653
ROBO	-13.96	15.40	2.98	2.83	0.0532
ROSA	-29.83	33.48	7.77	5.79	-0.2393
SFBC	-31.42	28.16	3.46	3.06	0.0788
SIO1	-31.54	29.26	3.02	2.71	0.0753
SIPH	-10.39	9.29	6.47	5.85	-0.2099
SM01	-30.55	34.78	3.58	3.40	0.0775
TRAN	-13.86	11.72	6.00	4.76	-0.1747
VA01	-28.99	31.19	3.49	3.41	0.0697
VIEW	-3.55	12.94	6.65	5.39	-0.1796
WIDE	-12.81	11.98	3.08	2.89	0.0746
YUMA	-1.45	1.82	4.25	3.95	0.0339
YUNG	-27.10	25.88	3.54	3.33	0.0786

Table 2.6: 1992 Landers Earthquake Displacement Estimates (mm)

Station	Estimate		Uncertainty		Corr.
	East	North	East	North	
1109	11.0	16.0	11.97	11.13	0.015
ANZA	13.6	49.2	23.31	19.53	0.009
BLAC	59.8	-17.1	8.61	7.14	-0.002
BOTR	53.8	99.5	49.98	49.98	0.001
CABA	80.3	178.1	24.15	23.94	0.005
CAHU	36.4	30.3	34.23	34.02	0.003
CHER	64.3	129.6	17.43	16.38	-0.016
COAC	-1.4	-4.8	24.15	18.90	-0.150
COLL	4.7	-8.5	11.76	10.71	-0.039
COXO	41.0	-17.0	10.71	9.45	0.102
CP13	23.2	1.3	12.60	11.55	-0.020
CPEI	3.3	-13.9	10.50	9.66	0.033
DESO	30.5	-27.3	11.97	11.34	0.043
DS10	-7.5	1.7	155.40	155.40	0.000
DUNP	41.1	28.4	71.82	71.61	0.000
E122	19.3	-5.5	12.18	11.76	-0.032
EDOM	58.4	114.6	140.07	140.07	-0.001
ENDD	12.3	-4.7	11.97	10.92	0.008
F726	114.4	-61.3	43.05	42.84	0.005
FORD	24.1	2.0	11.76	10.50	0.094
FRIN	8.1	-10.7	12.81	12.39	-0.025
GARN	77.9	169.2	16.80	9.24	-0.108
JPLM	-47.3	10.2	45.99	28.35	-0.049
JTRE	61.9	-35.9	17.64	17.22	0.012
L589	19.1	-6.0	18.06	16.17	-0.134
LAKE	42.3	32.1	11.34	10.71	0.053
LLCO	6.9	6.7	13.02	11.97	-0.027

Station	Estimate		Uncertainty		Corr.
	East	North	East	North	
MAYO	15.1	-15.1	10.92	10.29	0.010
METZ	19.1	41.4	13.23	11.97	-0.001
MONU	4.1	1.7	10.71	8.40	0.033
N125	42.4	-23.8	17.01	16.59	0.014
NIGU	48.9	0.8	10.92	8.19	0.015
OAKD	0.2	23.1	12.81	11.13	0.017
OCOT	22.9	13.2	10.92	10.08	-0.014
OCTI	3.4	6.4	29.19	24.57	-0.176
ORIE	24.4	-18.2	11.97	10.92	-0.055
PAIN	44.5	-11.8	21.00	20.58	0.007
PENA	-0.8	2.7	10.92	10.50	-0.013
PIN1	33.7	49.9	7.77	6.30	0.009
PSAR	55.4	124.6	85.26	85.05	-0.001
ROBO	20.1	1.1	14.70	14.49	0.007
ROSA	33.6	16.7	20.16	15.33	-0.178
SFBC	3.5	-9.8	9.45	8.82	0.015
SIO1	20.9	14.9	8.19	6.72	0.004
SIPH	37.9	-20.7	15.54	14.49	-0.117
TRAN	30.5	-10.7	15.54	13.65	-0.073
VIEW	139.5	-69.6	24.15	13.65	0.440
WIDE	67.2	132.8	9.03	7.56	0.011
YUNG	26.2	38.6	14.91	13.86	-0.007

Table 2.7: Model Faults and Displacement Rate vector estimates

No.	Segment†	Name	Az (deg)	D (km)‡	Rate (mm/yr) Parallel	Normal
1	SA1	San Andreas	294	12	33 ± 2	12 ± 1
2	SA2	San Andreas	313	12	35 ± 2	
3	SA3	San Andreas	284	12	22 ± 2	13 ± 1
4	SA4	San Andreas	314	12	26 ± 2	
5	B	Brawley	341	7.5	23 ± 2	-12 ± 1
6	I	Imperial	324	7.5	35 ± 2	
7	M	Mexicali	207	6	16 ± 1	-31 ± 1
8	CP	Cerro Prieto	216	6	42 ± 1	
9	SJ	San Jacinto	213	7.5	9 ± 2	
10	S	Superstition	104	7.5	8 ± 2	4 ± 1
11	E	Elsinore	211	7.5	7 ± 2	
12	LS	Laguna Salada	121	7.5	7 ± 2	1 ± 1
13	SC	San Clemente	215	12	7 ± 2	
14	AB	Agua Blanca	108	12	6 ± 2	1 ± 1
15	SPM	San Pedro Martir	170	12	5 ± 2	-5 ± 2

† Faults segments which intersect the boundary of Figure 2-4 extend to ∞.

‡ See Section 2.3, pg. 35, for references which provide evidence (e.g., seismicity cutoff, geodetic strain measurements, etc) for locking depth.

Table 2.8: Inversion Results(mm/yr)

Block Pair	Relative Motion Rate
PB – PRB	26 ± 2
PRB – RB	9 ± 2
RB – CB	7 ± 2
CB – NAB	7 ± 2
NAB – CB	35 ± 2
NAB – RB	42 ± 1
NAB – PB	49 ± 3

Table 2.9: Residual Velocities (mm/yr)

Station	Estimate		Uncertainty		Corr.
	East	North	East	North	
1109	-1.82	2.79	2.15	2.19	-0.0153
ANZA	4.55	4.72	6.12	4.50	-0.0553
BLAC	-3.95	-3.06	1.61	1.53	-0.0315
BLUF	3.41	3.90	2.26	1.87	-0.0756
BOTR	-1.51	2.89	1.90	2.00	-0.0473
BRSH	0.06	4.13	2.65	2.13	-0.0316
CABA	-0.91	2.49	1.94	2.01	-0.0289
CAHU	0.14	-2.28	1.89	1.94	-0.0227
CHER	1.11	1.60	2.89	2.71	-0.0770
COAC	2.00	-1.57	4.04	3.23	-0.1114
COLL	4.90	2.42	2.02	1.89	-0.0196
COXO	-0.36	-1.09	2.01	1.88	0.1043
CP13	1.32	-3.22	2.44	2.16	0.0051
CPEI	-3.87	6.36	2.37	2.18	0.0149
DESO	0.52	1.09	2.10	2.03	0.0442
DUNP	-1.01	0.33	1.98	2.12	-0.0173
E122	0.64	-0.79	2.21	2.17	-0.0145
EDOM	-2.96	0.43	6.02	5.13	-0.2629
ENDA	-1.09	1.02	5.43	4.95	-0.0360
ENDD	2.29	-1.62	2.46	2.08	0.1362
F726	-0.31	-1.73	2.07	2.05	0.0013
FORD	-0.69	-3.08	2.47	2.19	0.1170
FRIN	-0.18	-3.74	1.89	1.84	-0.0308
GARN	2.58	-0.04	3.86	3.29	-0.0280
IPE0	-1.54	-0.10	3.46	3.69	0.0088
JTRE	-1.12	0.12	1.88	1.85	0.0106
L589	-1.62	3.19	3.26	2.88	-0.1131
LAKE	-2.44	-1.58	2.40	2.52	0.0230
LLCO	-3.05	-3.80	2.70	2.23	-0.0164

Station	Estimate		Uncertainty		Corr.
	East	North	East	North	
LPUR	4.63	3.18	2.40	2.22	-0.0001
MAYO	0.95	0.50	2.42	2.25	-0.0230
METZ	2.10	1.62	2.47	2.43	-0.0445
MONU	-0.06	1.33	2.14	1.80	-0.0114
N125	-2.86	0.55	1.87	1.89	-0.0107
NIGU	-0.33	2.14	1.99	1.69	-0.0298
OAKD	4.20	-1.97	2.77	2.65	-0.0401
OCOT	-3.38	0.90	2.08	1.92	-0.0273
OCTI	0.39	-0.91	5.09	4.31	-0.1063
ORIE	2.76	0.22	2.02	1.86	-0.0455
PAIN	-2.29	-1.98	1.92	1.91	-0.0097
PENA	2.15	-2.28	2.64	2.09	0.0347
PIN1	-0.27	-0.07	1.23	1.17	-0.0958
PSAR	-2.53	0.37	5.32	4.34	-0.1247
PVER	0.38	2.00	1.41	1.44	-0.0842
ROBO	2.99	-0.91	1.95	1.92	-0.0370
ROSA	-1.51	5.23	7.33	5.32	-0.2962
SFBC	-1.05	-2.88	2.62	2.18	-0.0069
SIO1	-0.87	-0.83	1.57	1.50	-0.0995
SIPH	-3.98	4.46	6.04	5.46	-0.2587
SM01	0.24	4.12	2.90	2.72	0.0239
TRAN	-2.14	1.02	5.52	4.27	-0.2379
VA01	1.28	0.83	2.58	2.69	-0.0046
VIEW	1.08	7.77	6.17	4.93	-0.2327
WIDE	-4.75	2.78	1.82	1.87	-0.0111
YUMA	1.54	0.21	3.33	3.14	-0.0136
YUNG	1.89	-2.84	2.50	2.55	0.0057

Table 2.10: Summary of Fault Slip and Plate Rate Estimates (mm/yr)

Parameter	Rate	Δ	Reference
Pacific-North America			
NUVEL-1A	46 ± 1	-3 ± 3	*DeMets et al.*, 1994
VLBI Calif. + model	~ 48	-1 ± 3	*Kroger et al.*, 1987
GPS Calif.	53 ± 3	4 ± 3	*Argus and Heflin*, 1990
GPS Gulf of Calif.	47 ± 7	-2 ± 3	*Dixon et al*, 1990
Southern San Andreas			
Geology	25 ± 4	-1 ± 2	*Weldon and Sieh*, 1985
EDM + model	11–23	26 ± 2	*Johnson*, 1993
San Jacinto			
Geology	10 ± 2	1 ± 2	*Wesnouski*, 1986
EDM + model	7–25	9 ± 2	*Johnson*, 1993
Elsinore			
Geology	4	-3 ± 2	*Wesnouski*, 1986
EDM + model	0–17	7 ± 2	*Johnson*, 1993
Imperial Valley			
EDM traverse	37 ± 1	2 ± 2	*Lisowski et al.*, 1990
Cerro Prieto			
Scaled Seismic	53	12 ± 1	*Frez and Gonzalez*, 1991
Unscaled Seismic	41	-1 ± 1	*Frez and Gonzalez*, 1991
San Clemente			
Geology	4 ± 4	-3 ± 2	*Humphreys and Weldon*, 1986
GPS	6 ± 2	-1 ± 2	*Larson*, 1993
Agua Blanca			
Geology	4 ± 2	-2 ± 2	*Hatch and Rockwell*, 1986
GPS	> 6	6 ± 2	*Farina et al.*, 1994
Laguna Salada			
Geology	> 1	7 ± 2	*Mueller and Rockwell*, 1991
GPS site PIN1 Relative to GPS site BLAC			
1986-1989	14 ± 8	-7 ± 3	*Larsen and Reilinger*, 1992
1986-1991	23 ± 2	2 ± 3	*Feigl et al.*, 1993

Δ = difference between rate quoted by reference and rate inferred from our GPS. Uncertainties are for our estimates, not the differences themselves. Where the rates quoted are of the form of inequalities or ranges, we list our rate estimates.

Table 2.11: Parameter Estimate Sensitivity to Velocity Variance-Covariance

α^2	Estimates (mm/yr)				Uncertainties (mm/yr)†				$\tilde{\sigma}^2$
	m_1	m_2	m_3	m_4	m_1	m_2	m_3	m_4	
0	26	9	7	7	2	2	2	2	1.2
1	26	9	7	7	2	2	2	3	1.0
10	27	8	7	7	2	2	2	3	0.4
100	27	8	8	7	2	2	2	3	0.1
1000	27	8	7	6	2	2	2	3	0.01

† The values listed have been scaled by $\sqrt{\tilde{\sigma}^2}$.

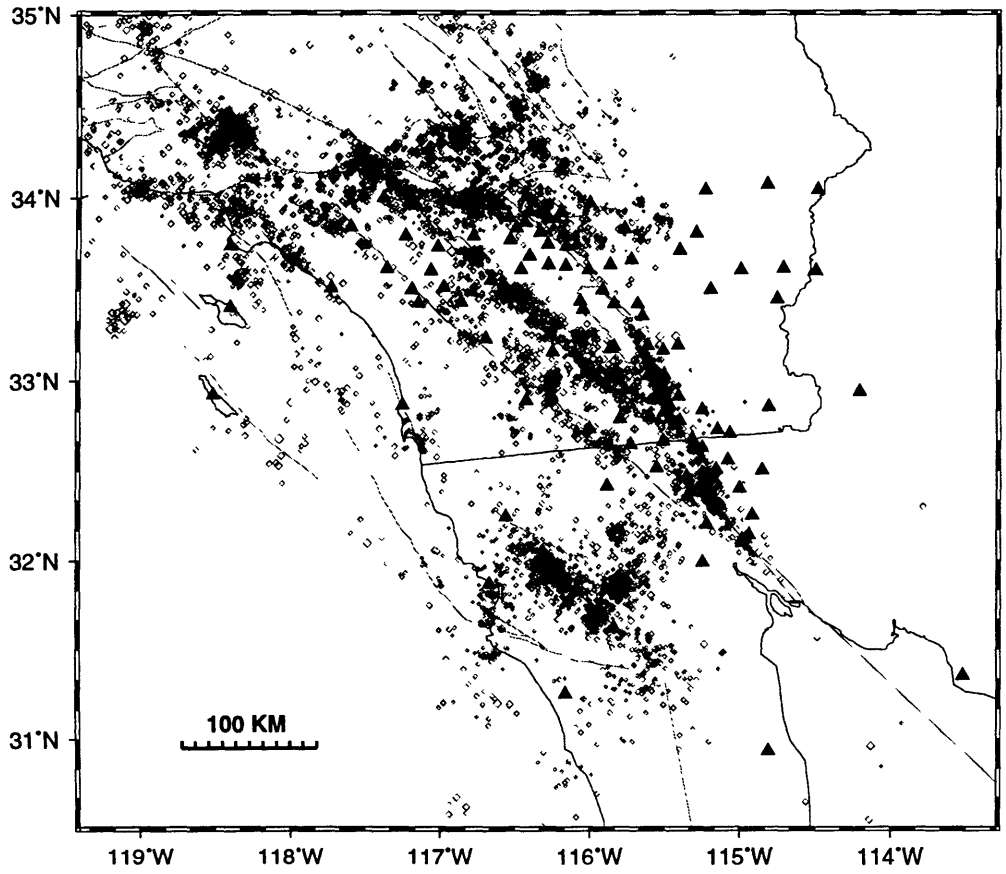

Figure 2-1: Simplified fault map showing the southern California and northern Baja, Mexico GPS network (triangles) established during the period 1986 - 1995. Diamonds show seismicity from Caltech and CICESE catalogs for the period of 1960-1990.

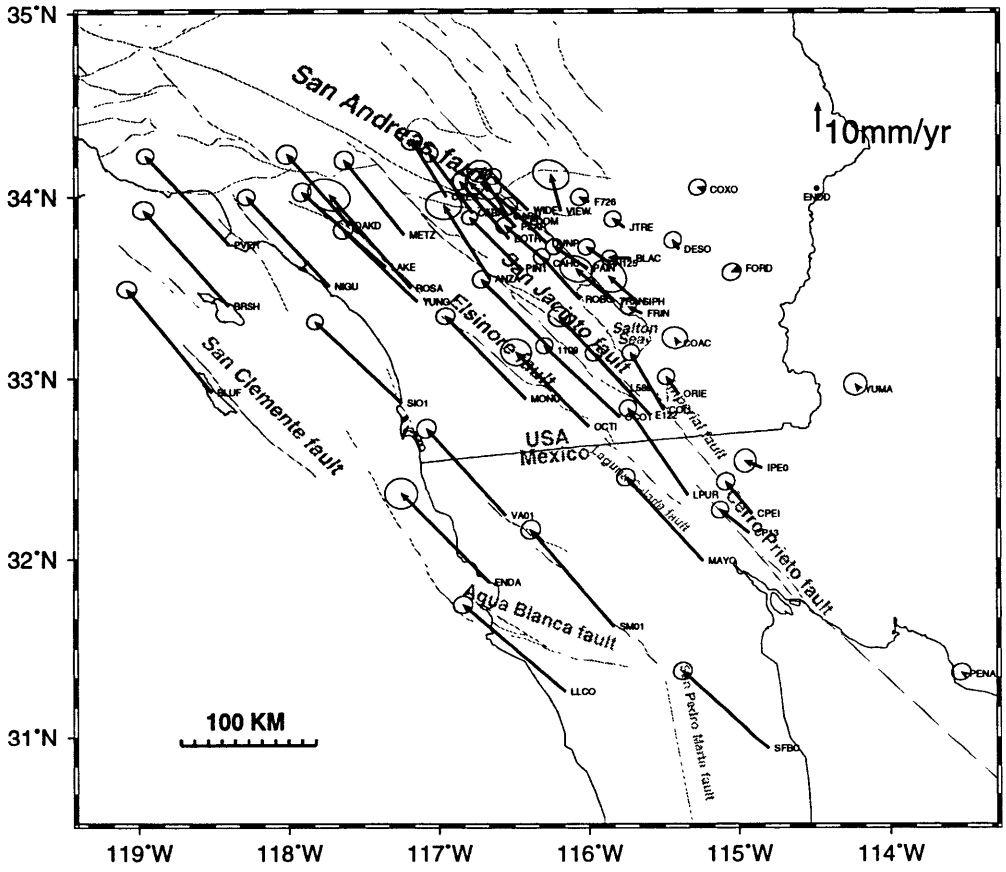

Figure 2-2: The southern California and northern Baja, Mexico 1986 to 1995 GPS velocity field in an approximate North America fixed reference frame. Error ellipses represent the 39% confidence level after scaling the formal uncertainties by a factor of 2.3.

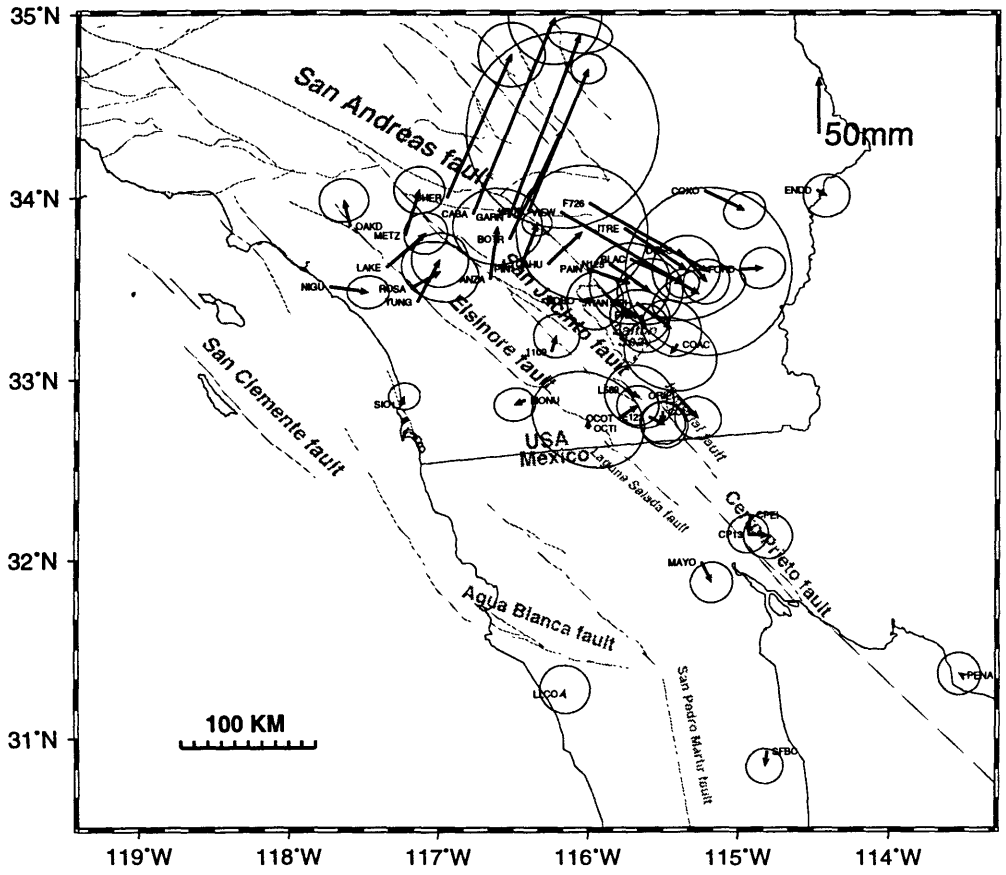

Figure 2-3: The 1992 Landers earthquake displacement estimates. Error ellipses represent the 95% confidence level after scaling the formal uncertainties by a factor of 2.3.

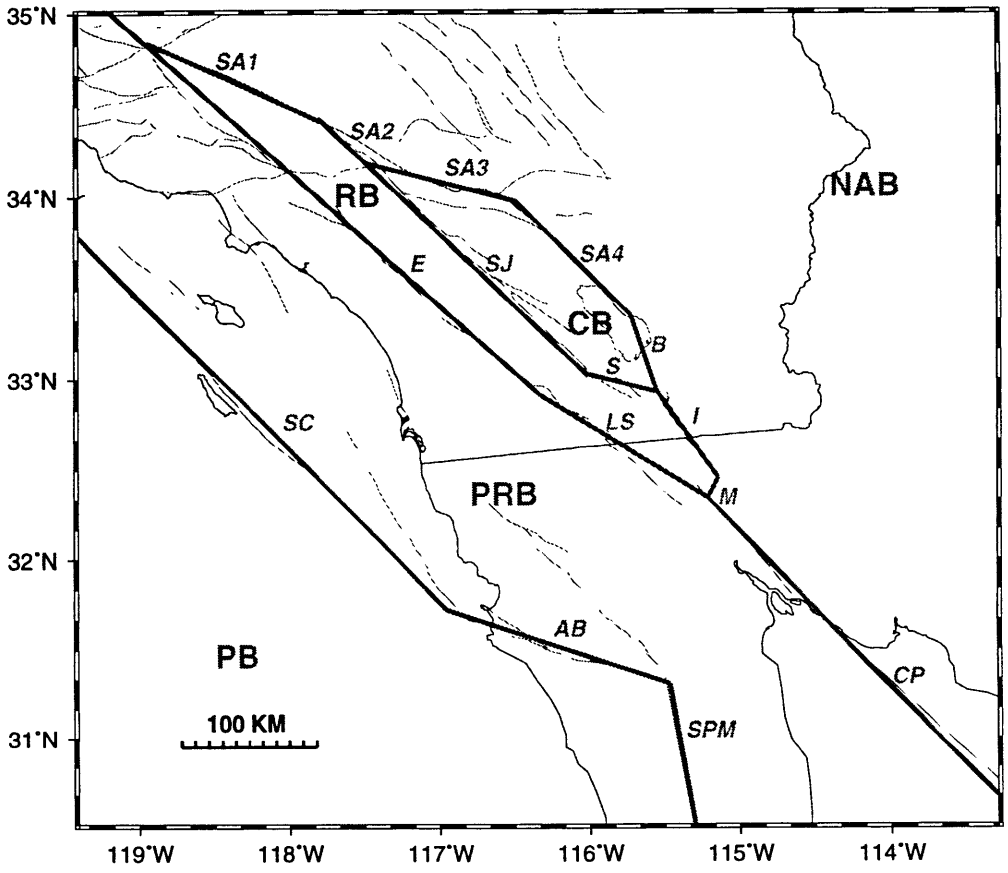

Figure 2-4: An elastic block model representing the primary faults of the Pacific-North American plate boundary in southern California and northern Baja, Mexico. Faults represented by the model include the San Clemente (SC), Agua Blanca (AB), San Pedro Martir (SPM), Elsinore (E), Laguna Salada (LS), Cerro Prieto (CP), segments of the San Andreas (SA1, SA2, SA3, SA4), San Jacinto (SJ), Superstition (S), Brawley (B), Mexicali (M), and Imperial (I) faults. Model blocks represent the region west of the San Clemente (PB), between the San Clemente and Elsinore faults (PRB), between the Elsinore and San Jacinto faults (RB), between the San Jacinto and San Andreas faults (CB), and east of the San Andreas fault (NAB).

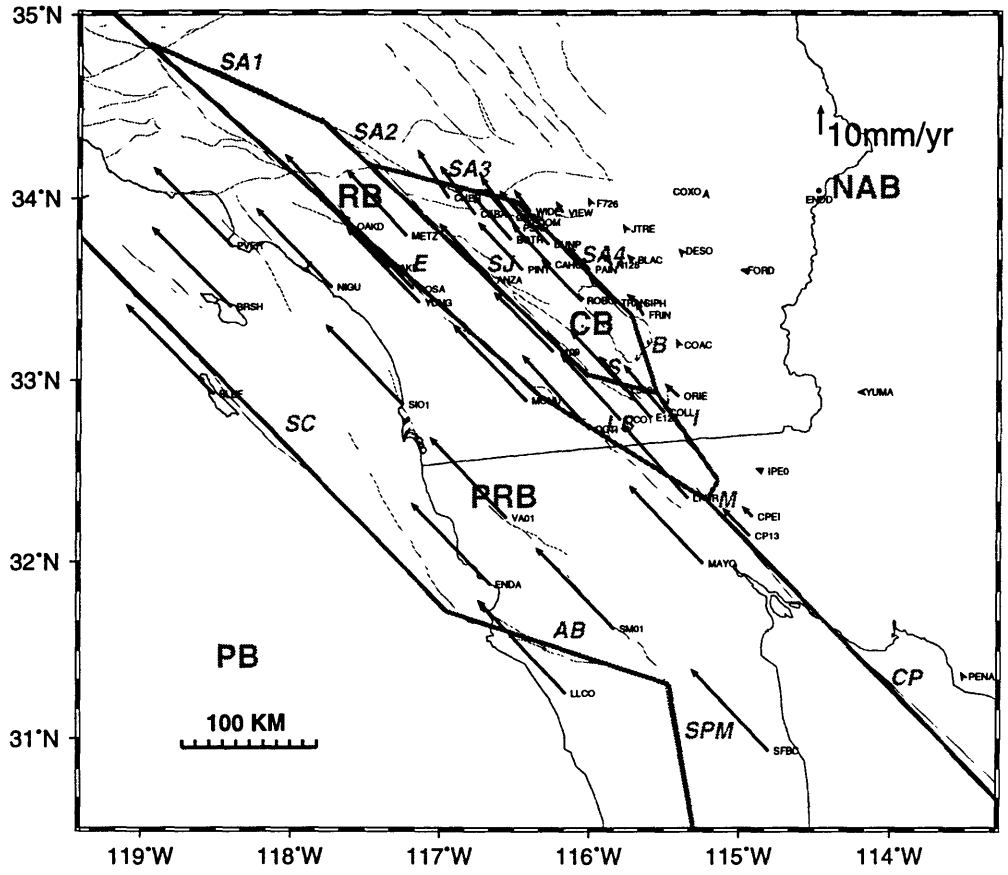

Figure 2-5: Model velocities for southern California and northern Mexico in the same approximate North America fixed reference frame as for Figure 2-2.

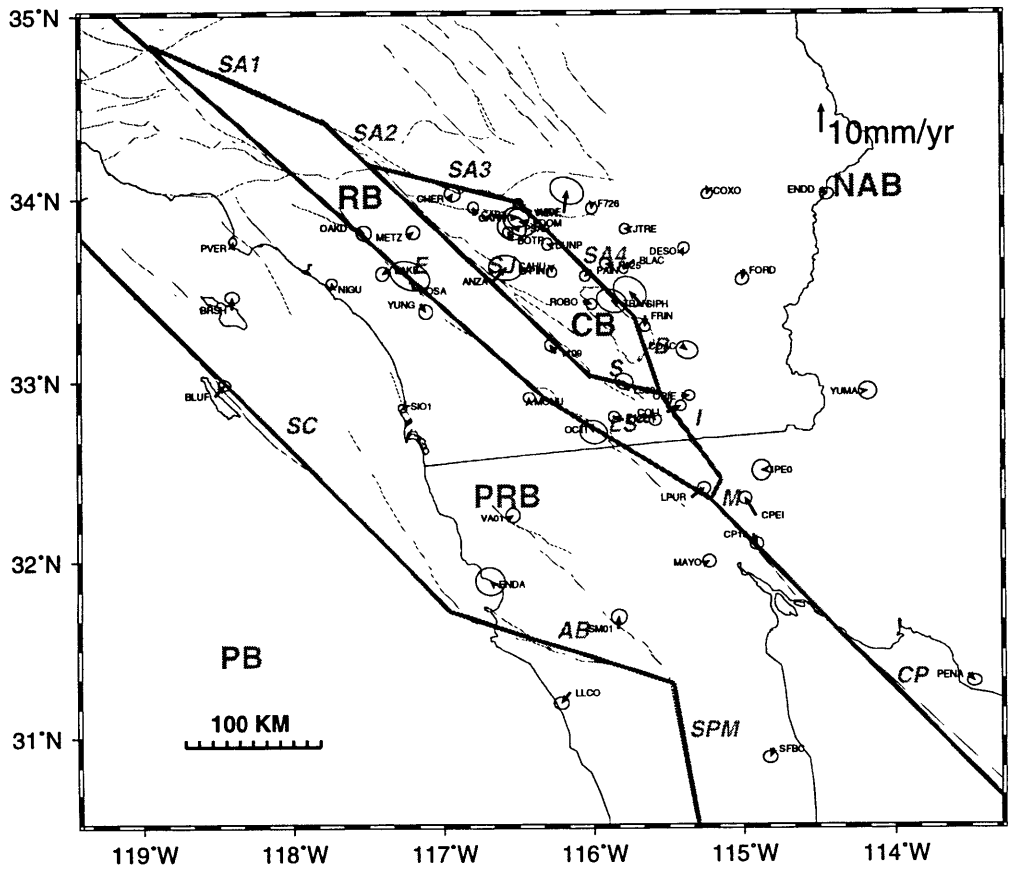

Figure 2-6: Residual velocities after removing the effects of a block model for southern California and northern Mexico. The relative block motions were inferred by a least squares fit to the GPS velocity field. Error ellipses represent the formal uncertainties at the 39% confidence level in the projected reference frame.

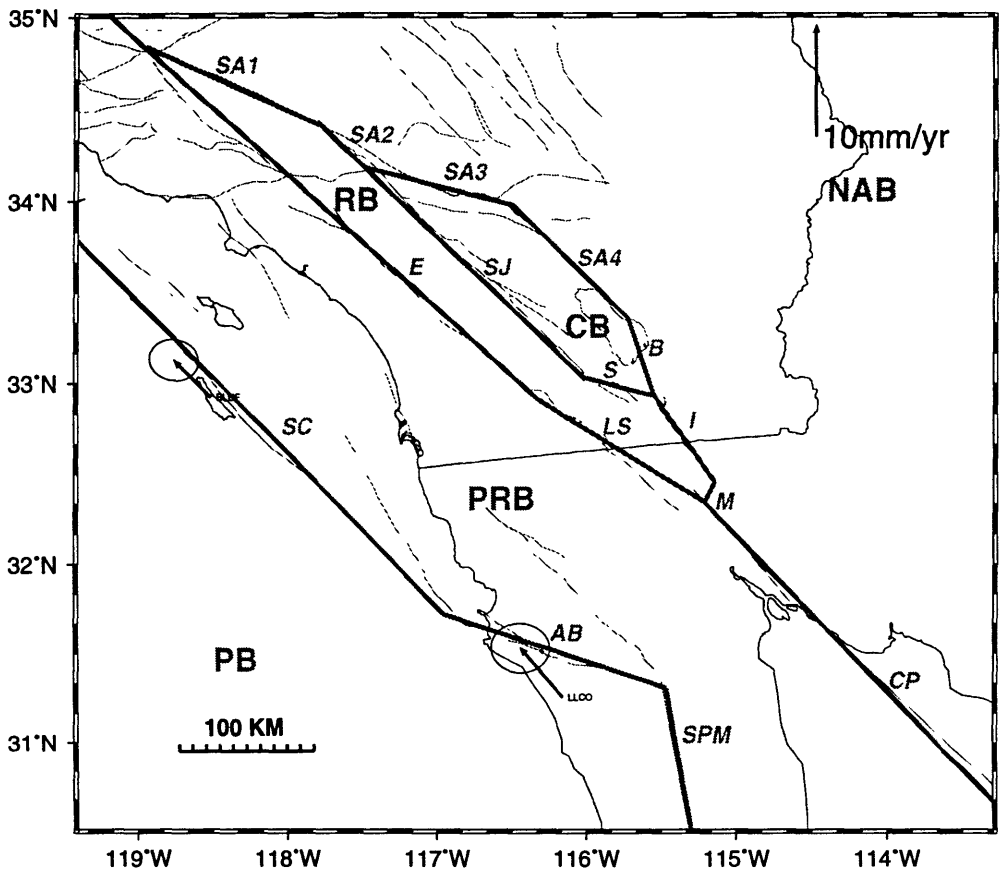

Figure 2-7: Difference between residual velocities resulting from a model in which the relative motions between the PB and PRB is fixed to zero and the residuals shown in Figure 2-6. Error ellipses represent the formal data uncertainties at the 39% confidence level after scaling by 2.3 in the projected reference frame.

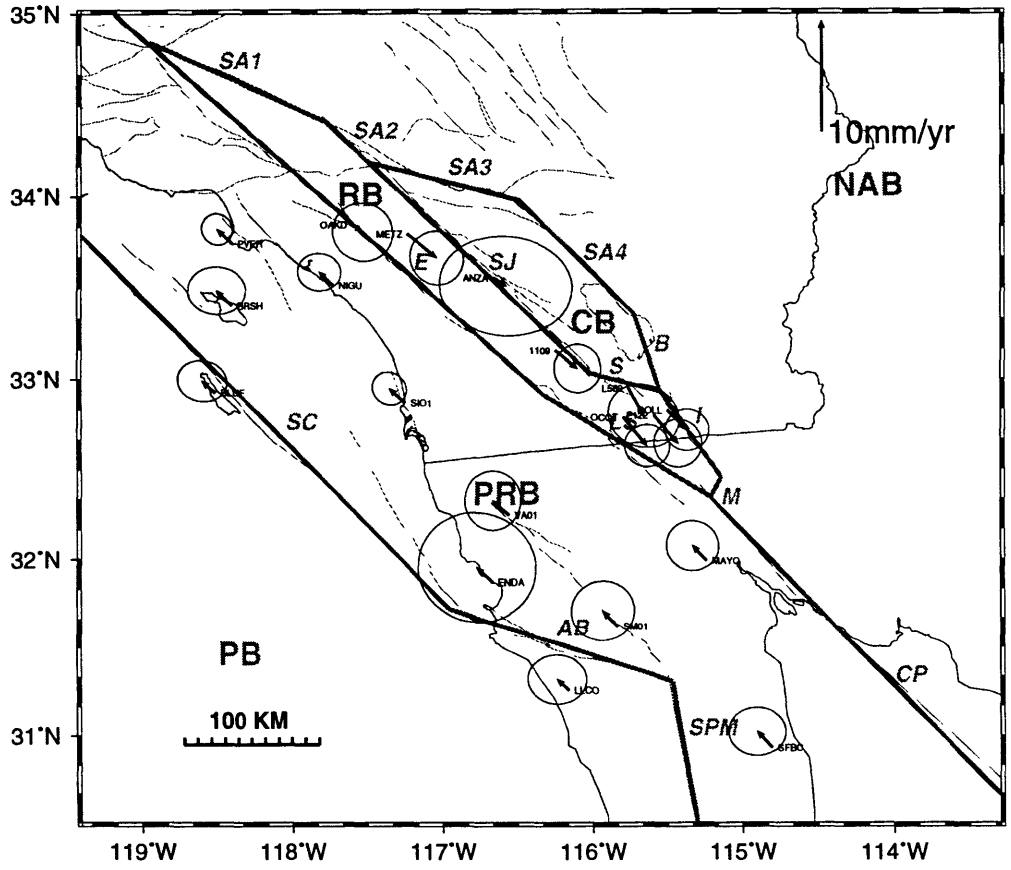

Figure 2-8: Difference between residual velocities resulting from a model in which the relative motions between the PRB and RB is fixed to zero and the residuals shown in Figure 2-6. Error ellipses represent the formal data uncertainties at the 39% confidence level after scaling by 2.3 in the projected reference frame.

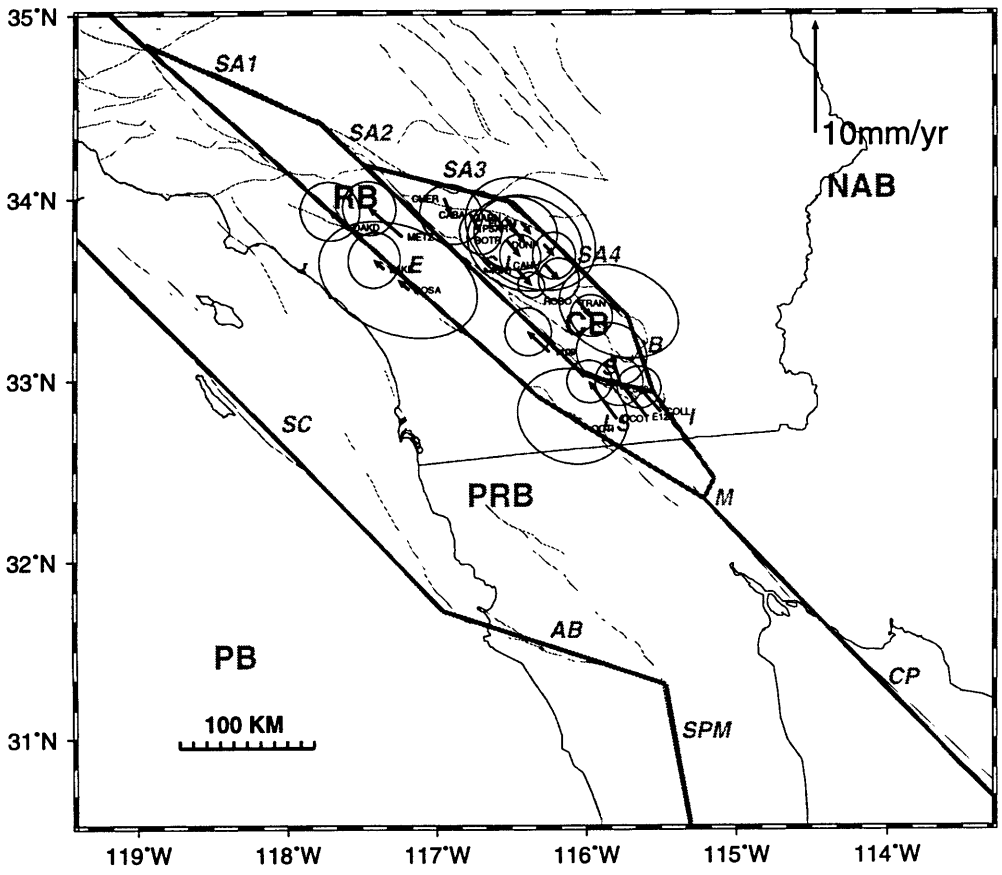

Figure 2-9: Difference between residual velocities resulting from a model in which the relative motions between the RB and CB is fixed to zero and the residuals shown in Figure 2-6. Error ellipses represent the formal data uncertainties at the 39% confidence level after scaling by 2.3 in the projected reference frame.

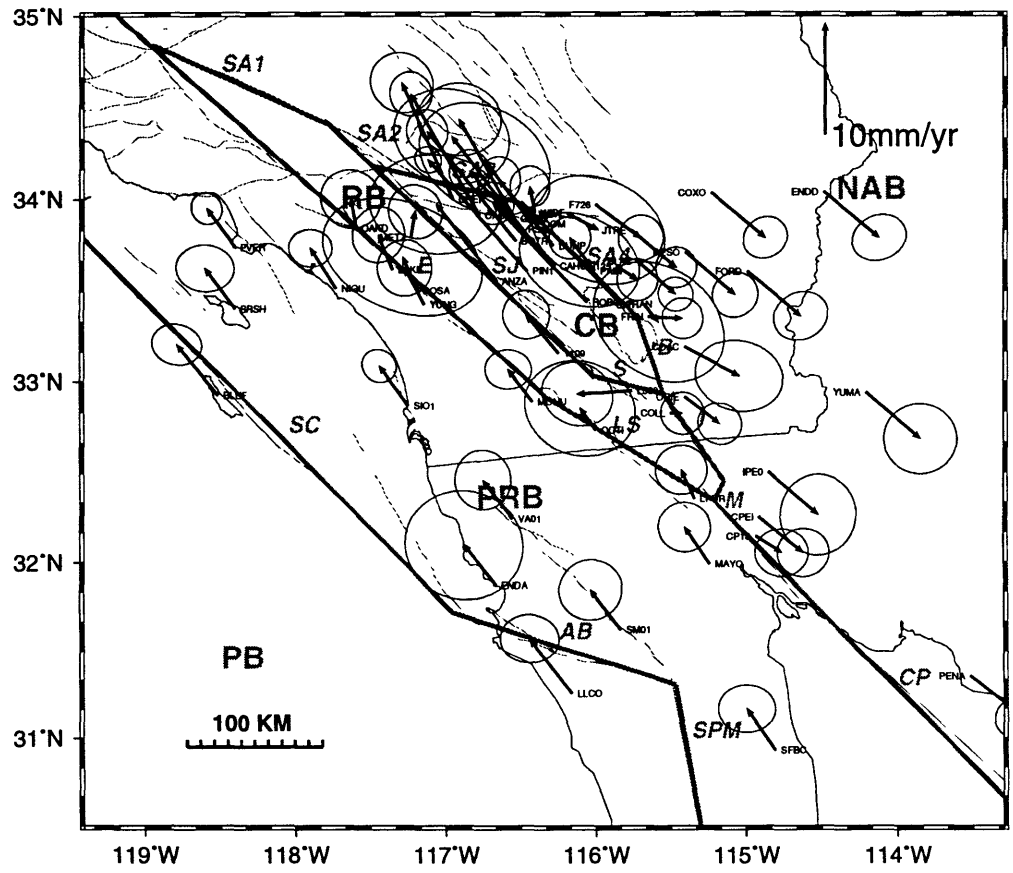

Figure 2-10: Difference between residual velocities resulting from a model in which the relative motions between the CB and NAB is fixed to zero and the residuals shown in Figure 2-6. Error ellipses represent the formal data uncertainties at the 39% confidence level after scaling by 2.3 in the projected reference frame.

Chapter 3

Tikhonov regularization of coseismic crustal deformation for earthquake slip

A veritable witness have you hitherto been, Ishmael; but have a care how you seize the privilege of Jonah alone; the privilege of discoursing upon the joists and beams; the rafters, ridge-pole, sleepers, and underpinnings, making up the framework of the leviathan; and belike the tallow-vats, dairy-rooms, butteries, and cheeseries in his bowels.

Herman Melville, Moby Dick

3.1 Introduction

Myths, models, metaphors, and theories.

While it seems likely that human beings have always known about earthquakes from direct, potentially horrifying experience, it is not known when in the long history of human thought that man scratched earthquakes from the list of things that go "bump in the night." Embedded in the most ancient cultural myths are vestiges of the first earthquake models. These early explanations testify that human speculation about the causes of earthquakes predates written history. But while it appears that all cultures rooted in or around seismically active regions began understanding earthquake phenomena with myths (these in reference to more general metaphors, or theories), understanding is the cumulation of thought. Inspired by new observations, theories are distilled, sometimes abandoned.

The first rational, or scientific, account of the earthquake source, for example, is attributed to Thales of Miletus [640-550 BC]. Consistent with his belief that the underlying substance of all things was water, he supposed the Earth to be superimposed upon the sea, a flat floating disc. In accordance with this general theory, Thales *reduced* earthquakes to the effect of the motion of underground water. We may only speculate at the reasoning behind Thales' conclusions as none of his writings remain in existence. But surely he was familiar with Poseidon, Greek god of the sea, "Earthshaker", and "lord of quakes and tremors," who stormed "with giant, lightning strides" such that "the looming peaks and tall timber quaked beneath his immortal feet" [Homer, 1000 BC]. Similarly, it is likely that he was aware of the discovery (reported by Xenophanes [570-480 BC]) of fossil sea shells near the tops of mountains. Contemporary tides of thought carry us to the shores. New observations, in waves, rework our beliefs.

Scientific inference.

Science is the enterprise of inferring hypotheses[1] from observations. Yet, there are perhaps as many techniques for doing science as there are scientists. Nevertheless, models and theories are the usual tools of the trade. In this chapter, we adopt somewhat abstract definitions of these tools. For example, we will use the term *model* simply to indicate some symbolic construct, either mathematical or purely conceptual. A model, by itself then, can be neither true nor false. By *theory*, we literally mean a metaphor between a model and the real world; the relationship of a model to observable phenomena[2]. The elasticity theory of dislocations, for example, asks us to consider observations of coseismic deformation as the effect of a displacement discontinuity located within a homogeneous, isotropic, linearly elastic medium (a conceptual model), for which we have an adequate mathematical understanding [*Steketee,* 1958a,b]. A theory, in our view, encourages one to compare the outcome of an experiment with proposed states of a model, i.e. *hypotheses.* Of particular interest is the converse of this statement, namely that, in accordance with a theory, a model is a source of plausible hypotheses. Using the process of abduction, we may infer which hypothesis is most consistent with our observations and we refer to it as the *solution* to the problem.

This chapter presents a procedure for testing geophysical hypotheses using geodetic measurements of coseismic crustal deformation. We apply the method of Tikhonov regularization [*Tikhonov and Arsenin,* 1977] to the elasticity theory of dislocations [*Steketee,* 1958a,b] with the aim of making inferences on earthquake slip distributions.

[1] We understand *hypothesis* to mean some statement about the real world to which we may assign some measure of belief regarding its truth.

[2] *model* is commonly used in the geophysics literature as a verb in reference to the application of a theory to a specific construct.

3.2 The dislocation metaphor

Since its introduction in 1958, the elasticity theory of dislocations [*Steketee,* 1958a,b] has been one of the most commonly used formalisms for studies of the earthquake source. In conformity to the theory, a dislocation model relates a distributed displacement discontinuity $\Delta u = (\Delta u_1, \Delta u_2, \Delta u_3)$ across a surface Σ to the resultant static displacement $u = (u_1, u_2, u_3)$ at a point $r = (x_1, x_2, x_3)$ in an elastic medium $\mathcal{E}$. This is the Volterra integral [e.g., *Aki and Richards,* 1980]

$$u_p(r) = \frac{1}{8\pi\mu} \int\int_{\Sigma} \Delta u_j(\xi) w_{jk}^p(r,\xi) \nu_k(\xi) d\Sigma(\xi),$$
$$p = 1,2,3 \tag{3.1}$$

where μ is the rigidity in the source region, ν is the normal vector to the dislocation surface Σ, and w_{jk}^p is an appropriate Green's tensor. Analytic solutions for this integral have been obtained for the case when Δu is constant and $\mathcal{E}$ is a homogeneous, isotropic, linearly elastic half-space given a number of dislocation geometries [e.g., *Chinnery,* 1961; *Savage and Hastie,* 1966; *Mansinha and Smylie,* 1971; *Okada,* 1985]. For the case of a layered half-space, complete expressions for the w_{jk}^p together with efficient numerical computation techniques have been developed [*Ben-Menahem and Singh,* 1968; *Ben-Menahem and Gillon,* 1970; *Singh,* 1970; *Jovanovich et al.,* 1974a].

As is usually the case in geophysics, the model is applied with the dislocation representing the two-dimensional surface of the ruptured fault plane within Earth. The effects of Earth's curvature are negligible over distances of less than about 2000 km [*Ben-Menahem et al.,* 1970], therefore, a half-space model is sufficiently accurate for all but perhaps the very largest events. Theoretical studies [e.g., *Jovanovich et al.,* 1974b; *Savage,* 1987] suggest that the effects of layering in rigidity within Earth over distance scales of up to a couple of fault lengths under nominal crustal conditions are small relative to homogeneous half-space models. In fact, for the case of a Poisson solid, (3.1) is independent of the rigidity [e.g., *Okada,* 1985].

In general, we will require a knowledge of the orientation and location of the rupture plane. This may be determined from seismic estimates for focal mechanism or from precisely located aftershocks. The extent of the rupture does not need to be specified because it will be determined by the data. This is insured by extending the edges of the dislocation surface laterally and in depth so as to render the effects of the boundary conditions on the side and bottom edges of the dislocation negligible. We define a fault plane coordinate system such that Σ is in the x_1-x_3 plane, where x_3 is distance along the direction of maximally increasing depth, and x_1 is distance along the strike direction (x_2 is normal to Σ).

Finally, we may exploit knowledge of the direction of slip in the plane of rupture. This information may come from direct observations of surface rupture, general knowledge of past fault behavior, the general tectonic environment, or from focal mechanism estimates. The restriction to purely strike-slip or purely dip-slip motion reduces the three-vector Δu to a scalar slip function s. By convention, right-lateral strike-slip and normal dip-slip motions are defined positive. For events involving left-lateral or thrusting motions, the negative sign can be absorbed into the Green's functions.

Geodetic observations provide estimates of the components of coseismic surface displacement u at various locations. The ith datum, denoted y_i, is thus $y_i = u_{p_i}(r_i)$, where r_i is the location of one of the geodetic monuments and $p_i = 1$, 2, or 3 depending on the component of motion represented by y_i. Given these specifications, equation (3.1) can be used to relate N such data to the slip function s as

$$y_i = \int\int_\Sigma g_i(\xi) s(\xi) d\Sigma(\xi) + \eta_i, \quad i = 1, 2, \ldots, N \tag{3.2}$$

where, from (3.1), the functions g_i are given by

$$g_i(\xi) = \frac{1}{8\pi\mu} w_{k2}^{p_i}(r_i, \xi), \tag{3.3}$$

where $k = 1$ for strike-slip and $k = 3$ for dip-slip, and the η_i are the *a posteriori* errors in the estimates y_i obtained during the geodetic data reductions. By defining N linear functionals G_i as

$$G_i(s) = \int\int_\Sigma g_i(\xi) s(\xi) d\Sigma(\xi), \quad i = 1, 2, \ldots, N, \tag{3.4}$$

equation (3.2) can be written more concisely as

$$y_i = G_i(s) + \eta_i. \tag{3.5}$$

Knowledge of slip at particular points on the fault plane may be incorporated by assuming M discrete measurements, b_i. This information is included in the analysis via the equations

$$b_i = \delta_{\xi_i} s + \epsilon_i, \quad i = 1, 2, \ldots, M \tag{3.6}$$

where the ϵ_i are assumed errors in these observations and δ_{ξ_i} are the point evaluation functionals, $\delta_{\xi_i} s = s(\xi_i)$ for the set of M points ξ_i in the dislocation plane at which the slip is believed known *a priori*. The variance of these pseudo-data must be specified.

By letting

$$d = (y_1, \ldots, y_N, b_1, \ldots, b_M). \tag{3.7}$$

$$e = (\eta_1, \ldots, \eta_N, \epsilon_1, \ldots, \epsilon_M), \tag{3.8}$$

and

$$A = (G_1, \ldots, G_N, \delta_{\xi_1}, \ldots, \delta_{\xi_M}), \tag{3.9}$$

equations (3.5) and (3.6) can be written together concisely as

$$d = As + e. \tag{3.10}$$

3.3 The model as a source of plausible hypotheses

The use of geophysical data to infer distributed earthquake slip has been studied and demonstrated by several investigators using a variety of approaches [e.g., *Hartzell and Heaton,* 1983; *Ward and Barrientos,* 1986; *Segall and Harris,* 1987; *Mendoza and Hartzell,* 1988; *Matthews,* 1991; *Larsen et al.,* 1992; *Du et al.,* 1992; *Wald and Heaton,* 1994]. We here adopt ideas discussed by *Matthews* [1991] and *Du et al.* [1992].

We would like to use (3.10) to infer the slip function s. However, it is clear that even exact measurements of the surface displacements resulting from the earthquake are not sufficient to determine the slip function uniquely using (3.10) alone since the continuous slip function is infinite dimensional. An approximate representation of s that is unique and stable under small perturbations to the data must suffice. A family of such approximations can be constructed by exploiting prior knowledge about the slip function and by minimization of a physically motivated, sufficiently stabilizing functional. The procedure is most conveniently carried out in a Hilbert space setting.

We assume that the data errors e_i are zero mean random variables and let V denote their known variance-covariance matrix (i.e., $V_{ij} = \mathrm{E}e_i e_j$, where E is the expectation operator). We then let $\mathcal{D}$ be the Hilbert space of data vectors defined by the linear space $\Re^{N+M}$ under the norm

$$\|d\|_{\mathcal{D}}^2 = \sum_{i,j=1}^{N+M} V_{ij}^{-1} d_i d_j \tag{3.11}$$

where V^{-1} is the inverse of V.

Our objective is to find a slip function s subject to the following three constraints:

1. The geodetic misfit, or weighted residual sum of squares $\chi^2 \equiv \sum_{i,j=1}^{N} V_{ij}^{-1} \Delta y_i \Delta y_j$ (where the $\Delta y_i = y_i - G_i(s)$ are the residuals) should be consistent with the given variance-covariance matrix of the errors η_i in the geodetic data.

2. Among competing models satisfying constraint 1, the solution should, in some sense, have minimal structure. For our problem, a suitable measure is given by the functional $\int\int_\Sigma \left[\nabla^2 s(\xi)\right]^2 d\Sigma(\xi)$. This choice is particularly satisfying since, as shown by *Matthews* [1991], it is a good approximation to a measure of fault surface traction variability and therefore provides a physical basis for our minimization criterion. Matthews coined the term "stress variability" norm for this functional.

3. The model must allow only unidirectional slip. This translates into the positivity constraint $s(\xi) \geq 0$ for each $\xi \in \Sigma$.

We employ the method of Tikhonov regularization [*Tikhonov and Arsenin,* 1977] to achieve this objective.

We define a real valued functional Ψ_α for each real number $\alpha > 0$ as

$$\Psi_\alpha(s; d) = \|d - As\|_{\mathcal{D}}^2 + \alpha^2 \Omega(s) \tag{3.12}$$

where the stabilizing functional $\Omega(s)$ represents the "stress variability" functional together with homogeneous boundary conditions for s on the edges of the dislocation, $\partial\Sigma$:

$$\Omega(s) = \int\int_\Sigma \left[\nabla^2 s(\xi)\right]^2 d\Sigma(\xi) + \int_{\partial\Sigma} s(\xi)^2 d\sigma(\xi). \tag{3.13}$$

Constraints 1 and 2 are satisfied by minimization of Ψ_α over a suitable space of slip functions $\mathcal{S}_+$ and careful selection of the regularization parameter α. In other words, we define the solution s_α by

$$\Psi_\alpha(s_\alpha; d) = \inf_{s \in \mathcal{S}_+} \Psi_\alpha(s; d), \tag{3.14}$$

such that constraint 1 is true. For $\mathcal{S}_+$, we use the space of positive functions on Σ with square integrable second order derivatives, that is, the Sobolev space $W^2(\Sigma)$ restricted to the positive orthant. This choice insures constraint 3.

Owing to the positivity constraint and the properties of the point evaluation

functionals, we must appeal to a rather general formulation of regularization due to *Morozov* [1993]. In Appendix D, we demonstrate that Morozov's conditions for the existence and uniqueness of the solution s_α are satisfied for our problem for arbitrary d and $\alpha > 0$. We can thus write

$$s_\alpha = R(d, \alpha), \tag{3.15}$$

where R is known as the regularization operator.

3.4 Computation of the regularization operator

To numerically compute a solution the model is discretized on a 1 km square grid. The slip function s is assumed to be constant on each of the resulting 1 km square fault elements. The forward problem then reduces to a matrix equation with well known analytic expressions for the elements of the discretized g_i [e.g., *Chinnery,* 1961; *Okada,* 1985]. The number of assumed observations of slip, M, can be chosen such that each datum b_i represents a single fault element. Discretization of the stabilizing functional Ω yields a functional of the form $(Ls)^T Ls$, where the matrix L is a difference operator.

Program NNLS of *Lawson and Hanson* [1974] can then be used to obtain solutions to the discrete problem. This algorithm is very convenient and efficient and has been successfully applied to problems of slip determination by numerous investigators: *Hartzell and Heaton* [1983] using strong motion waveforms, *Mendoza and Hartzell* [1988] using teleseismic waveforms, and *Du et al.* [1992] using static ground displacements.

3.5 Defining the solution: The discrepancy method

The regularization procedure outlined above provides a means of computing a family of hypotheses. Increasing the regularization parameter α leads to simpler hypotheses (i.e., more uniform slip over the dislocation), while decreasing α allows more structure into the distribution (Figure 3-1). As mentioned above, we look for the least complicated explanation of the observations such that the geodetic misfit is consistent with our *a priori* knowledge of the geodetic data errors. This corresponds to the "discrepancy" method for selecting α [*Tikhonov and Arsenin,* 1977].

In standard statistical least squares it is common practice to obtain an *a posteriori* estimate of the data variance. However, such estimates are difficult to obtain from regularized inversions due to the fact that s_α is a biased estimator when $\alpha > 0$. While approximative methods exist for obtaining the number of degrees of freedom and *a posteriori* variance [*Wahba,* 1990], we know of no such method which accounts for nonlinearity. Rather than naively applying an existing methodology, we advocate simple verification of the consistency of the misfits and *a priori* uncertainties by performing numerical experiments.

One recipe is a follows. Begin by assuming a test value of the regularization parameter. Then, apply the regularization operator to the geodetic data to obtain a solution for slip. Generate reference displacements using this solution at each of the geodetic stations and simulate observations by adding noise to these reference displacements. The noise processes used should have a variance-covariance matrix of the form of the given error variance-covariance matrix times a scale factor σ^2. By performing several inversions using several realizations for various values of σ^2, all the while using the same test value of the regularization parameter we obtain the probability distribution of misfit as a function of σ^2. Finally, comparing the reference model misfit to the means of the simulated distributions yields an *a posteriori*

estimate of σ^2. This method is analogous to the usual *a posteriori* variance estimate in linear least squares, where the probability distribution is known to be chi-square with number of degrees of freedom equal to the number of data minus the rank of the system matrix.

For large values of the regularization parameter, the variance scale factor thus inferred will be greater than one, indicating that the resulting residuals have a scatter more consistent with a larger variance than that used in the inversion. For smaller values of the regularization parameter, the variance scale factor is less than one, indicating that we are fitting the data better than the assumed variance of the data requires. The discrepancy method is, then, to select the value of the regularization parameter α that yields $\sigma^2 = 1$. Figure (3-2) shows a simulation using a "good" choice of the value of regularization parameter given our *a priori* uncertainty estimates meaning that, for this value of α, the solution weighted residual sum of squares indeed implies that $\sigma^2 = 1$.

3.6 Conclusions

In this chapter, we have presented a procedure for making inferences on earthquake slip distributions which is appropriate for use with geodetic estimates of coseismic displacement associated with earthquakes. The procedure utilizes a Tikhonov regularization operator which is based on the elasticity theory of dislocations which is appropriate for use with geodetic measurements of coseismic displacements associated with earthquakes. The operator minimizes a linear combination of data misfit and an approximate measure of variability in fault surface traction while allowing for unidirectional slip and point evaluation constraints.

By restricting the acceptable values of the regularization parameter such that

the solution (abduced hypothesis) is consistent with the *a priori* uncertainties in the observations, we obtain, in effect, a solution with no more structure than is required by the data. This is not to say that the true distribution of slip could not be more complicated than that derived from the geodetic measurements in this way, only that the data do not warrant and cannot resolve further detail given their uncertainties.

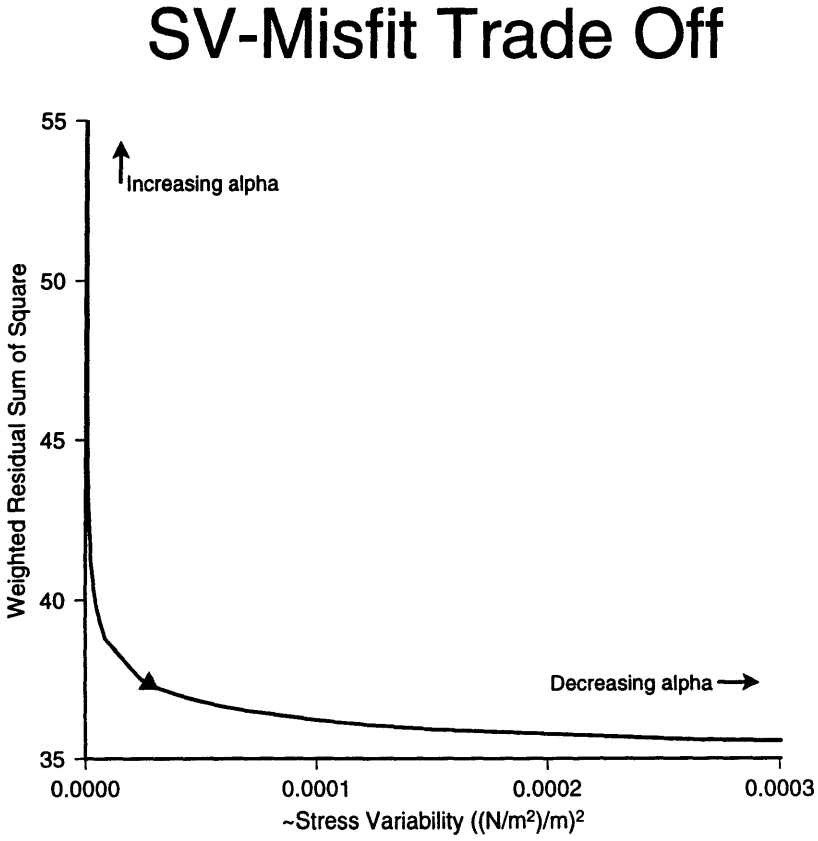

Figure 3-1: Trade-off between Stress Variability and the residual sum of squares as a functions of the regularization parameter α.

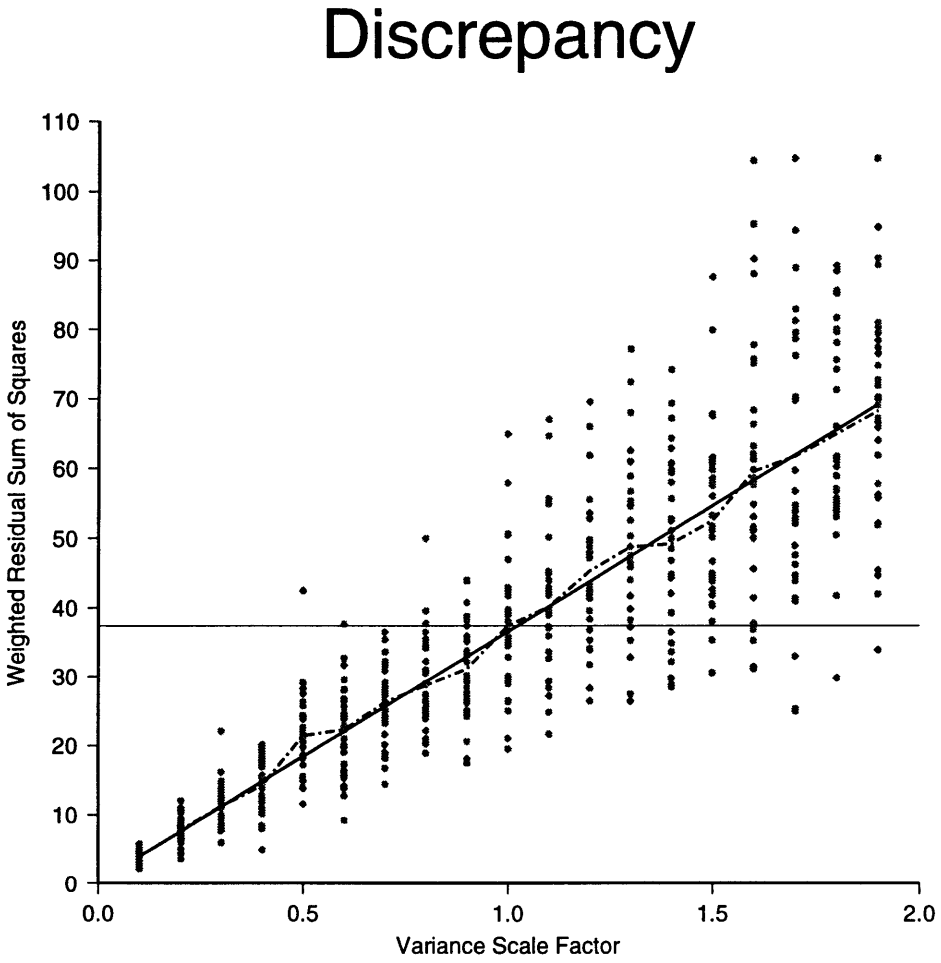

Figure 3-2: Probability distribution of data misfit as a function of the variance scale factor σ^2 illustrating the consistency of the geodetic misfit for a particular α and the *a priori* knowledge of the geodetic data errors.

Chapter 4

Coseismic fault slip associated with the 1992 M_w 6.1 Joshua Tree, California, earthquake: Implications for the Joshua Tree-Landers earthquake sequence

> Every motion is incomplete.
>
> *Aristotle, Metaphysics*

4.1 Introduction

The M_w 6.1, April 23, 1992, Joshua Tree, California, earthquake resulted from right-lateral rupture along a previously unmapped north trending late Quaternary fault

located about 20 km south of the Pinto Mountain fault and about 10 km northeast of the Mission Creek branch of the San Andreas fault system (Figures 4-1 and 4-2). This and other subparallel late Quaternary faults, identified following the earthquake, offset an older northwest trending system [*Rymer,* 1992]. Seismicity here is characterized by frequent earthquake swarms suggesting that faults in the area are immature [*Hauksson et al.,* 1993]. It is also the location of a sequence of moderate earthquakes occurring between 1940 and 1948 [*Richter et al.,* 1958; *Sykes and Seeber,* 1985] which included the 1940 M_L 5.3 Covington Flat, 1947 M_L 5.4 Morongo Valley, and 1948 M_L 6.5 Desert Hot Springs earthquakes. The Covington Flat earthquake likely involved rupture along one of these north trending faults, possibly the same fault ruptured during the Joshua Tree earthquake.

These north trending faults lie in what is known as the Eastern California Shear Zone (ECSZ) [*Dokka and Travis,* 1990a], a zone of intracontinental right-lateral shear bordering the southern San Andreas fault system to the east and extending northwestward through the Mojave Desert and on into Death Valley. Geologic and geodetic evidence [*Sauber et al.,* 1986; *Dokka and Travis,* 1990b; *Savage et al.,* 1990] suggests that 9 to 23% of the total Pacific-North American relative plate motion is accommodated within this zone. However, *Savage et al.* [1990] found that the strain rate is too large to be regionally distributed and inferred the existence of a localized zone of shear controlled by "some flaw in the lithosphere," noting further that local northwest trending faults do not serve this purpose because their traces are not easily reconciled with observed principal strain axes. One intriguing idea, proposed by *Nur et al.* [1992], is that the Joshua Tree and Landers earthquakes belong to a series of events all occurring along a new fault trending N10°W and extending roughly 100 km across the Mojave desert.

The Joshua Tree earthquake preceded by nearly two months the M_w 7.3 Landers earthquake, southern California's largest earthquake in 40 years. The distance be-

tween hypocenters for these earthquakes is near 30 km, and both events involved rupture along roughly the same north trending plane within the ECSZ. However, while the Landers earthquake resulted in spectacular surface ruptures extending about 85 km in length, no surface rupture was observed for the Joshua Tree event [*Rymer,* 1992]. This is unfortunate in that detailed knowledge of the two-dimensional distribution of slip is prerequisite to accurate calculation of coseismic stress transfer and investigation of its implications for the temporal development of the Joshua Tree-Landers earthquake sequence.

Fortunately, coseismic deformation associated with this event is well represented by estimates of geodetic monument displacements at 20 locations (Figure 4-2) derived from geodetic observations consisting of a subset of the GPS measurements described in Chapter 2 (STRC90, STRC91, JTRE), and trilateration measurements collected since 1973 [e.g., *Savage et al.,* 1993]. In this chapter, we analyze geodetic estimates for displacements associated with the Joshua Tree event using the techniques developed in Chapter 3. The result is a hypothesis on the distribution of slip associated with the Joshua Tree earthquake. We compare the size, shape, and location of the inferred distribution with main shock and aftershock locations and seismic moment and source time function estimates. These independent observations serve not only to constrain many of the important features of the slip distribution but also provide complimentary information facilitating a more complete seismotectonic analysis. By integrating seismic and geodetic information, we attempt to resolve possible complexities of the Joshua Tree rupture process and to assess the significance of coseismic stress transfer in the spatio-temporal evolution of earthquake activity following this event.

4.2 Geodetically derived distribution of fault slip

4.2.1 Coseismic surface deformation

The U.S. Geological Survey has been monitoring deformation in the vicinity of the Joshua Tree earthquake by trilateration since 1973 (Figure 4-2). Measurements include pre- and post-Joshua Tree earthquake observations and provide estimates of the coseismic displacements associated with the event. *Savage et al.* [1993] investigated deformation of this network associated with the earthquake and found that it is compatible with slip on a buried 7×12 km^2 rectangular fault with strike of 353°, dip of 90°, and moment of 1.8×10^{18} N m. Geodetic estimates for coseismic deformation were not reported in this study, but estimates for coseismic displacement at 14 sites (Figure 4-2) from these same trilateration data are provided by *Dong* [1993]. Dong's displacement estimates are incorporated in the present study.

GPS estimates of coseismic deformation associated with the Joshua Tree earthquake is shown in Figure (4-3). These estimates have a root-mean-square (rms) signal of 15 mm and error of 5 mm giving an rms signal-to-noise ratio of about 3.0, and together with the trilateration estimates of *Dong* [1993], shown in Figure (4-3), form the basis of this study. The combined GPS and trilateration set consists of 40 displacements (two components of horizontal displacement for each of the 20 geodetic stations) with rms signal of 20 mm and error of 11 mm giving an rms signal-to-noise ratio of about 1.8.

4.2.2 The Joshua Tree earthquake

To apply the regularization operator of Chapter 3 to the Joshua Tree earthquake data described above, we must specify the the orientation of the plane of rupture and the direction of slip in this plane. Focal mechanism estimates indicate right-lateral, almost purely strike-slip motion along a steeply dipping rupture plane striking at about 352° [*Incorporated Research Institutions for Seismology* (IRIS), 1992]. Accordingly, we restrict the model to pure right-lateral, strike-slip motion. We also assume a vertical dislocation plane based on the results of *Hauksson et al.* [1993] and *Savage et al.* [1993]. We define our coordinate system such that Σ is in the x_1-x_3 plane, where x_3 is depth and x_1 is distance along the strike direction (x_2 is normal to Σ). The restriction to purely strike-slip motion reduces the three-vector Δu to the form $\Delta u = (s, 0, 0)$, where s is a scalar slip function. The assumption of right-lateral motion implies that s is of one sign and by convention is defined positive giving $s(\xi) \geq 0$ for all $\xi \in \Sigma$.

No surface rupture has been observed [*Rymer,* 1992] but the conjugate distribution of aftershock epicenters occurring between April and June 1992 [*Hauksson et al.,* 1993] forms a cross marking the event's general location (Figure 4-2). We assumed the horizontal location of the dislocation centroid to be roughly the center of the aftershock pattern as determined by eye. The lateral and depth extent of the rupture in the plane of the dislocation need not be specified as it is to be determined by the data. This is insured by extending the edges of the dislocation surface laterally and in depth so as to render the effects of the boundary conditions on these edges negligible.

The geodetic observations described above provide estimates of the horizontal components of coseismic surface displacement u at various locations. The ith datum, denoted y_i, is thus $y_i = u_{p_i}(r_i)$, where r_i is the location of one of the geodetic monuments and $p_i = 1$ or 2. Using the notation of Chapter 3, we relate our N data to the

scalar slip function s as

$$y_i = G_i(s) + \eta_i. \tag{4.1}$$

where the η_i are the a posteriori errors in the estimates y_i obtained during the geodetic data reductions.

Observations of zero surface slip [*Rymer,* 1992] are incorporated by assuming M discrete measurements, b_i, of zero slip at several locations along the intersection of the dislocation plane with the surface of the half-space. This information is included in the analysis via the equations

$$b_i = \delta_{\xi_i} s + \epsilon_i, \quad i = 1, 2, \ldots, M \tag{4.2}$$

where the ϵ_i are assumed errors in the observations of the surface slip and δ_{ξ_i} are the point evaluation functionals, $\delta_{\xi_i} s = s(\xi_i)$ for a set of M points ξ_i on the edge of the dislocation plane along the half-space surface. A rather large variance of $E\epsilon_i\epsilon_i = (30 \text{ mm})^2$ is assigned to these pseudo-data.

As in Chapter 3, equations (4.1) and (4.2) can be written together concisely as

$$d = As + e. \tag{4.3}$$

Two sets of bias parameters representing rigid body translations of the GPS and trilateration observations were also added to resolve indeterminacy and align the displacement estimate sets within the dislocation reference frame. This is equivalent to the "denuissancing" procedure described in Chapter 2 of this thesis (with two nuissance parameters).

4.2.3 Goodness of fit and selection of the regularization parameter

With the regularization operator thus parameterized, we search for the value of the regularization parameter which produces the smoothest distribution of slip consistent with the uncertainties in the geodetic observations. This was achieved following the recipe provided in Chapter 3. All solutions presented below were obtained using the value of the regularization parameter which yields $\sigma^2 = 1$.

Figure (4-3) shows the fit of the model displacement implied by this solution to the observed site displacements. Table (4.1) lists the displacements and postfit residuals. Since our data and their uncertainties were derived from two independent analyses (GPS displacements from this study; trilateration displacements from *Dong* [1993]) and we used both sets of uncertainties in verifying the appropriateness of the selected value of the regularization parameter, we were able to check that both sets of uncertainties are mutually consistent. Figure (4-4) shows the residuals versus distance from the slip centroid. We observe no significant indication of systematics with distance from the event. This again supports the use of an elastic half-space model.

4.2.4 The inferred slip distribution

Figure (4-5) shows the inferred distribution of slip. The distribution is characterized by three main features. A large central patch of slip with a maximum value of near 0.8 m dominates the inferred model. Nearly all of the mass of the total distribution is centered on this main feature. A secondary, near-surface feature appears to the northwest with maximum slip of about 0.2 m. Finally, a small patch of slip appears to the southeast with a maximum slip of about 0.3 m. The geodetic moment derived

from this distribution (computed as $\mu \sum_i s_i$, where s_i is the value of slip estimated for the ith, unit area fault element) is 1.7×10^{18} N m.

4.2.5 Resolution analysis

Uncertainty analysis for the inferred slip distribution is complicated owing to the nonlinearity of the regularization operator (due to the positivity constraint). Similarly, Backus-Gilbert resolution analysis [*Backus and Gilbert,* 1968] strictly applies only to linear inverse problems. With this in mind, we investigate the response of our regularization operator numerically by running forward models and then applying the operator to the resulting synthetic data. Each forward model assumed a slip distribution in which slip is concentrated at a single point, i.e., a slip impulse. We can then easily interpret three effects of imperfect resolution: location bias, amplitude bias, and smearing.

Figures (4-6) to (4-9) shows images obtained by operating on synthetic data generated from slip impulses at different locations: the centroid of our derived slip distribution, above this centroid, below this centroid, and at the center of the small patch of slip to the southeast of the Blue Cut fault (compare Figure 4-5 and Figure 4-9). Each of the test models has a moment of 1.7×10^{18} N m. The images have been normalized by the root sum square of the image signal. The ratio of the slip image to true slip function moments is indicated for each case.

The image centroids generally coincide with the locations of the slip impulses indicating no appreciable location bias. Even near the edges of the fault, where we expect the zero slip boundary conditions to strongly influence the solution, location bias is small. As expected, shallow slip impulses are resolved better than deeper slip impulses, as indicated by the degree of smearing. Horizontal resolution is better

than depth resolution, particularly for shallow slip. This effect appears to be less pronounced for slip impulses located near the base of the dislocation plane since the boundary conditions along the bottom of the dislocation surface affect the images of test models involving deeper slip. The ratio of slip image to actual slip function moments is greater than one (up to 1.23) near the surface and decreases to less than one (down to 0.80) at depth. We interpret this to result from the fact that the data do not contribute as much information at depth relative to the smoothness constraints as they do near the surface. Hence the distribution is damped more at depth than it is near the surface. The fact that the moment ratio is greater than one near the surface is a result of the data "seeing" the fault at a scale smaller than that preferred given our choice of regularization parameter. (Recall that the regularization parameter was chosen based on the overall fit to the data.)

We conclude that features of the inferred distribution are better resolved near the surface and that the small patch of slip near the surface to the southeast is well resolved relative to slip on other areas of the fault. The true slip is not likely to be more spatially distributed than the inferred distribution, although it could very well be more localized. The location does not appear to be biased. The moment, on the other hand, may be biased by as much as 20%.

4.2.6 Comparison of trilateration and GPS data sets

To assess the relative importance of the GPS and trilateration data sets in determining the slip distribution, we performed independent solutions using the trilateration and GPS data sets separately.

The trilateration solution shown in Figure (4-10) is qualitatively consistent with the 7×12 km^2 rectangular dislocation model of *Savage et al.* [1993]. However, the

moment obtained from this study is near 1.4×10^{18} N m, about 20% smaller than the Savage et al. model after correcting for differences in the assumed values of Earth's rigidity (we have here assumed $\mu = 28$ GPa). The maximum slip of our distribution reaches 0.76 m, comparable to the average value of 0.73 m used by *Savage et al.* [1993]. The lack of slip at depth is expected given the observed displacements at distant sites (palm, quee, stub, valm; Figure 4-2) which are largely incompatible with right lateral slip on the assumed fault plane.

The GPS solution is shown in Figure (4-11). This solution yields a moment of 2.2×10^{18} N m. There is little control of the depth extent of the slip given the GPS observations due to the sparse GPS station coverage along profiles perpendicular to the dislocation strike (Figure 4-2). Slip appears at depth as a result of the minimization of stress variability. The distribution is generally similar to the combined GPS and trilateration solution. The small patch of near surface slip to the southeast is clearly determined from the GPS data alone.

4.2.7 Independent evidence for the geodetically derived slip model

Three primary sources of independent evidence are used to assess the significance of the inferred slip distribution. The main shock and aftershock hypocenters provide information about both the location and size of the rupture. In addition, seismic moment estimates provide an independent measure of the integral of slip over the dislocation surface. Last, an empirical Green's functions analysis provides estimates of the source time function of the event. The source time function provides an important estimate of rupture duration and hence of rupture size. Thus we have independent estimates of the location, magnitude, and extent of the fractured area to compare with our solution for slip.

Location.

In this analysis slip has been allowed to lie below 1 km depth along the specified fault plane with the lateral and depth extent of the slip completely free in the dislocation plane. The 352° striking dislocation was located so as to best coincide with the epicentral distribution of aftershocks. The centroid of the dislocation surface was placed at the intersection of the conjugate planes determined by the aftershock epicenters which roughly defines the centroid of the aftershocks (Figure 4-2).

The slip distribution together with the aftershock locations of *Hauksson et al.* [1993] is shown in Figure (4-5). The relative location of the main mass of the slip distribution and hypocenter is consistent with unilateral rupture propagation to the northwest with rupture initiating near the bottom of the fractured area. That the aftershocks tend to occur along the edges of the inferred rupture is consistent with the expected occurrence of large stress increases along these edges. This correlation is most notable for aftershocks of magnitude greater than four (Figure 4-5 solid diamonds).

Geodetic versus seismic moment.

The geodetic moment can be obtained by integrating the slip function (Figure 4-5) over Σ. In the absence of positivity constraints, the moment would be expected to fluctuate with roughness. However, this is not the case for strictly positive s. While excessive damping (large regularization parameter) decreases the moment linearly with the regularization parameter (due to the homogeneous boundary conditions), the moment remains relatively constant over several orders of magnitude increase in stress variability (compare Figures 4-12 and 3-1).

A moment of 1.7×10^{18} N m is estimated. This result is quite similar to that of *Savage et al.* [1993]. However, it has been pointed out that our distribution for slip obtained from the trilateration data alone yields a moment of only 1.4×10^{18} N m. Our estimate is slightly smaller than seismically determined moment estimates [*IRIS,* 1992] in the range of $1.9 - 2.4 \times 10^{18}$ N m, but these differences are not unexpected given the above mentioned moment biasing effect.

Rupture dimensions.

The slip distribution presented in Figure (4-5) does not provide an accurate estimate of the details of the actual fractured fault. Only slip averages are resolved. In order to investigate the rupture process and static stress drop, an independent estimate of source dimensions is required.

Both the Joshua Tree event and its largest aftershock (M 4.8) were well recorded by several regional seismic stations (Figure 4-1). Using this aftershock as a source of empirical Green's functions (eGf), the relative source time function for the Joshua Tree event was estimated (Figure 4-13). The source time function is impulsive and indicates a relatively simple rupture history with total rupture duration of about 5 s. Assuming a liberal range of average rupture velocities of 2.4 to 3.2 km/s, and a circular rupture area, we infer a radius in the range of 6 to 8 km. This agrees qualitatively with the distribution of slip shown in Figure (4-5).

Given the computed moment for the event and assuming a circular rupture with radius in the range of 6 to 8 km based on the eGf source time function, we calculate a stress drop in the range of 2 to 4 MPa. This is significantly smaller than the estimate of 20 MPa from *Lindley* [1993]. However, it is well known that stress drop estimates determined by different methods can be expected to vary by up to a factor of 5

[*Scholz,* 1990]. The difference possibly results from complexities of the earthquake source below the resolution of our analyses, which might contribute significantly to Lindley's result. We note that to match Lindley's result given our estimated moment would require a rupture radius of about 4 km.

The source time function shown in Figure (4-13) provides some indication of temporal complexity in the rupture process with a small but distinct burst of energy release occurring within about 2 seconds of rupture initiation followed by the majority of the energy release. Such temporal disbursement of energy release might be indicative of spatial complexities, such as those seen in Figure (4-5). The variation in amplitudes of the source time functions obtained between stations GSC and PFO (Figure 4-13) marginally suggests rupture propagation to the northwest, although the azimuthal distribution of stations is limited (Figure 4-1). This is in agreement with the hypocenter slip relationship noted above.

4.3 Earthquake-induced stress changes

Coseismic stress transfer has been the subject of numerous studies [e.g., *Stein and Lisowski,* 1983; *Stein et al.,* 1992; *Du and Aydin,* 1993; *King et al.* 1994]. Coseismic stress and strain changes within the half-space can be computed by differentiation of the displacement field. We assume a Poisson solid with, $\lambda = \mu = 28$ GPa. The Coulomb failure stress τ_c is then

$$\tau_c = \tau_s + \frac{3}{4}\sigma_n, \tag{4.4}$$

where the τ_s and σ_n are the shear and normal stress, respectively, acting on planes parallel to the dislocation surface. We have assumed an apparent coefficient of internal friction of 3/4.

Comparison of predicted Joshua Tree-induced Coulomb stress changes with the aftershock locations of *Hauksson et al.* [1993] is shown in Figures (4-14) and (4-15). Figure (4-14) shows a horizontal cross section of stress resolved onto planes parallel to the main shock rupture plane. Figure (4-15) shows the same stress field on a vertical section along the main shock rupture plane. We acknowledge that the focal mechanisms of the aftershocks are not expected to coincide with that of the main shock, and we expect the effectiveness of Coulomb stress increases in bringing the brittle crust to failure to be maximal on planes optimally aligned for failure. Nevertheless, aftershocks do occur predominantly in areas for which the mainshock rupture resulted in Coulomb stress increases of greater than 0.1 MPa as computed. While the pattern of Coulomb stress changes can be modified by consideration of the direction of regional stress [e.g., *King et al.,* 1994], improvement to the correlation of aftershock occurrence with stress increases is marginal (compare with *King et al.* [1994, Figure 6]). These results support the notion that the crust must have been near failure under a relatively uniform preearthquake stress field with regional stress direction consistent with optimal right-lateral failure planes parallel to the Joshua Tree rupture plane. It is interesting to note that the largest of the Landers aftershocks to occur in the vicinity of the Joshua Tree event appear to fill in gaps in the seismicity where Joshua Tree-induced stress increased to the southeast (Figure 4-15) and where stress perturbations due to the Landers earthquake would have increased the potential for failure to the northwest of the Joshua Tree rupture.

Du and Aydin [1993], in studying stress transfer along the central Calaveras fault, found that levels of earthquake-induced stress increase at the hypocenters of subsequent earthquakes along the fault are less than 5% of the static stress drop. Figure (4-15) shows an even smaller Joshua Tree-induced stress increase at the hypocenter of the Landers earthquake. However, about 70% of the area fractured during the Landers earthquake is thought to have sustained significant increases in Coulomb stress (0.07–0.1 MPa) prior to the event as a result of the cumulative effect of the 1975

Galaway Lake, 1979 Homestead Valley, 1986 North Palm Springs, and 1992 Joshua Tree earthquakes [*Stein et al.,* 1992; *King et al.,* 1994].

4.4 Discussion

A temporally and spatially heterogeneous process of slip along a north trending, late Quaternary fault located predominantly between the Pinto Mountain and Blue Cut faults began with the Joshua Tree earthquake (Figure 4-2). The generally impulsive source time function and the primary features of the slip distribution are indicative of the rupture of a single large asperity. This aspect of our slip distribution is in agreement with the dislocation model of *Savage et al.* [1993]. Though resolution of finer details is limited by the nature of the Tikhonov regularization procedure, Figure (4-5) does suggest that smaller near surface features, one to the northwest and another to the southeast, may represent ruptures of additional asperities. The small patch of slip to the southeast lies south of the Blue Cut fault in the vicinity of mapped north trending late Quaternary faults [*Clark,* 1984]. Resolution at this location is good.

Aftershocks of both the Joshua Tree and Landers earthquake appear to fill in regions along the fault plane that were not previously fractured during the sequence. Many of the largest of the Joshua Tree aftershocks occur along the southern edge of the primary patch of slip (Figure 4-5). The $M = 5.7$ Landers aftershock which occurred just south of the Pinto Mountain fault appears to fill in slip to the north of the Joshua Tree rupture. We conclude from these observations that the Joshua Tree earthquake and its aftershocks, as well as some large Landers aftershocks, ruptured much of the fault between the Blue Cut and Pinto Mountain faults.

The absence of significant slip and the occurrence of several aftershocks of magnitude greater than four in the vicinity of the intersection of the Blue Cut fault with

the Joshua Tree main shock rupture plane (Plate 2) suggest to us that the Blue Cut fault may have largely impeded rupture propagation to the south. *Hough et al.* [1993], based on careful relocation of a $M = 5.7$ Landers aftershock, conclude that rupture associated with the Landers earthquake need not be continuous at depth across the Pinto Mountain fault. *Hauksson et al.* [1993] observe that there appear to be no aftershocks associated with either of these two east trending left-lateral structures.

Figure (4-5) indicates that little slip occurred below the seismogenic cut off defined by the aftershocks with rupture initiating near the base of the slipped area. Both of these observations are in agreement with rheological models for shearing in the lithosphere [e.g., *Scholz,* 1988] which consider the geology of exhumed fault zones, fault rock mechanisms, rate and state dependent friction models, seismicity, and rock behavior at increased pressure and temperature. *Sibson* [1982] found that large earthquakes tend to nucleate near the base of the seismogenic zone, a region of high shear resistance and strain energy concentration. A relevant exception, however, is the Landers earthquake which initiated at very shallow depth.

The coseismic stress increase predicted at the hypocenter of the June 28, 1992, Landers event due to the Joshua Tree earthquake is near zero (Figure 4-15). We conclude, then, that the Landers event was not directly triggered by coseismic stress increase associated with the Joshua Tree rupture. However, migration of aftershocks to the northwest in the months following the Joshua Tree event is illustrated by the occurrence of a small cluster about 20 km beyond the northern edge of Joshua Tree slip (Figure 4-15 arrow). This cluster began with a $M = 4.3$ aftershock on June 11 near 7 km depth within about 10 km of the June 28 Landers hypocenter. Predicted Joshua Tree-induced Coulomb stress increase at the hypocenter of this $M = 4.3$ aftershock is near 0.06 MPa (Figure 4-15).

Clearly, the spatial correlation of aftershocks and Coulomb stress changes indicates

a causal relationship. Less clear, however, is the time dependent mechanism through which these changes produce the aftershocks and the level at which the stress increase becomes significant. We may only speculate as to the exact process or combination of processes which lead to the Landers earthquake. Nevertheless, the close proximity in space and time of the Joshua Tree and Landers earthquakes, their occurrence on virtually the same fault, and migration of Joshua Tree earthquake aftershocks to the northwest suggest to us that the Joshua Tree and Landers earthquakes are part of a single northwest propagating rupture process.

4.5 Conclusion

We have used geodetically derived estimates of coseismic displacement at 20 sites to infer the slip distribution and static stress transfer associated with the April 23, 1992, Joshua Tree, California, earthquake. Source parameter estimates obtained by application of a Tikhonov regularization operator agree well with independent estimates from seismic studies. The estimated geodetic moment is 1.7×10^{18} N m. The source time function inferred from empirical Green's function analyses indicates a rupture duration of about 5 s. Assuming a circular rupture yields a fracture radius in the range of 6 to 8 km. The stress drop is in the range of 2 to 4 MPa. The Joshua Tree event involved rupture of at least one asperity with the possibility of minor amounts of slip occurring near the surface to the north of the main slip patch, and also to the south of the Blue Cut fault. The fit between observed and predicted ground motions, location of the rupture relative to the hypocenter, a strong correlation of the aftershock locations and predicted stress change patterns, and qualitative agreement of source time function and static coseismic slip provide strong support for the geodetically derived slip distribution.

For the Joshua Tree event, aftershock activity is highly correlated with Coulomb stress increases of greater than about 0.1 MPa. This supports the notion that the brittle crust in this area was near failure under a relatively uniform preearthquake stress field. Stress increase predicted at the hypocenter of the Landers earthquake is near zero implying that the Landers event was not directly triggered by coseismic stress changes. We speculate that redistribution of Joshua Tree-induced stress perturbations during the two months following the Joshua Tree event could explain the temporal development of the earthquake sequence culminating in the M_w 7.3, June 28, 1992, Landers event. In particular, we suggest that the Joshua Tree and Landers earthquakes are part of a single northwest propagating rupture process.

Table 4.1: Displacement Estimates and Postfit Residuals

	Observed		Calculated		Sigma		Residuals	
Site	East	North	East	North	East	North	East	North
BLAC	−5.4	−3.7	2.3	−1.6	5.0	3.5	−7.7	−2.1
GARN	11.6	12.3	6.7	8.0	6.8	3.7	4.8	4.2
VIEW	21.6	−9.7	22.9	−15.9	9.1	5.2	−1.2	6.2
RAMO	19.6	19.3	14.2	18.7	5.0	3.8	5.4	0.5
COCH	0.6	−11.7	6.9	−6.7	7.0	3.8	−6.3	−4.9
WIDE	22.6	23.3	19.3	25.4	4.8	3.5	3.3	−2.1
stub	−11.7	−6.8	−1.2	1.8	4.8	5.0	−10.5	−8.6
insp	44.3	−19.8	23.2	−15.9	15.0	10.1	21.1	−3.9
berd	17.3	−21.8	12.6	−8.5	15.6	26.6	4.7	−13.3
edom	33.3	28.1	16.2	22.7	11.1	17.8	17.0	5.0
warr	−42.7	22.2	−31.1	26.1	13.2	9.4	−11.6	−3.9
keys	−15.7	−22.8	−16.6	−18.7	10.8	10.8	0.8	−4.1
quee	11.3	6.2	−6.1	−7.2	12.6	13.2	13.4	13.4
dome	5.3	6.2	−2.6	12.0	14.7	16.6	7.8	−5.8
paxn	−5.7	11.2	−7.4	6.3	8.3	6.2	1.7	4.9
mesq	−5.7	−0.2	−7.0	−9.0	11.8	6.2	1.3	9.2
palm	19.3	14.2	−1.5	−2.8	14.8	13.9	20.8	17.0
valm	4.3	11.2	−3.9	−4.3	8.7	10.9	8.2	15.5
beac	−7.7	−2.8	0.9	3.9	8.2	19.4	−8.6	−6.7
laqu	19.3	−3.8	3.2	3.3	15.4	12.2	16.1	−7.1

In millimeters.

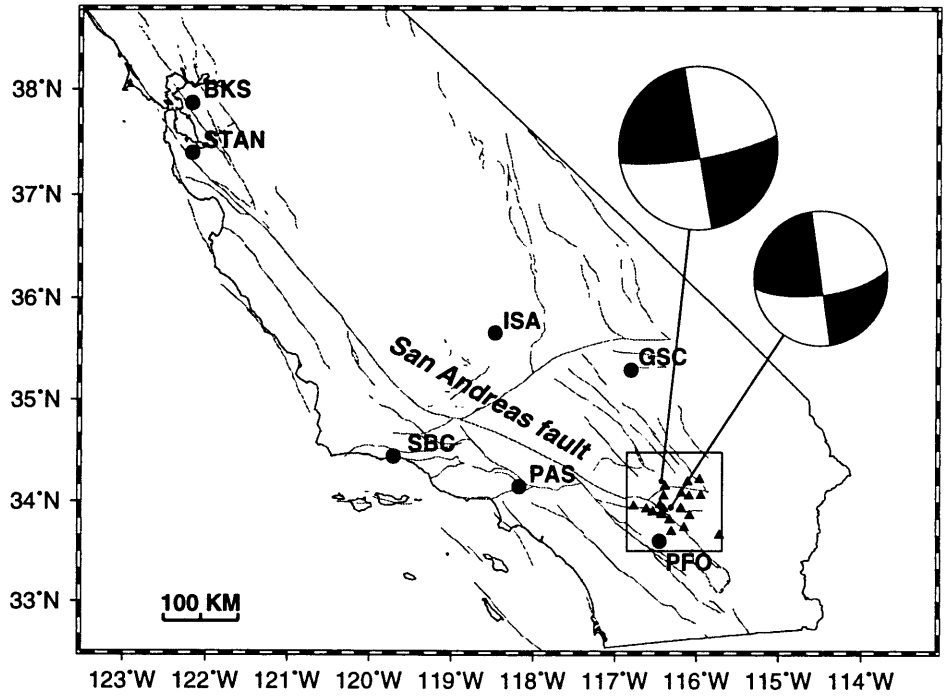

Figure 4-1: Simplified fault map showing the location of the GPS and trilateration monuments (triangles) in the vicinity of the 1992 Joshua Tree earthquake in southern California. Also shown (dots) are the locations of the seismic stations used for the empirical Green's functions analysis. Focal mechanisms from *Hauksson et al.* [1993] are shown for the Joshua Tree (southern event) and Landers (northern event) earthquakes. The square around the geodetic monuments shows the location of Figure 4-2.

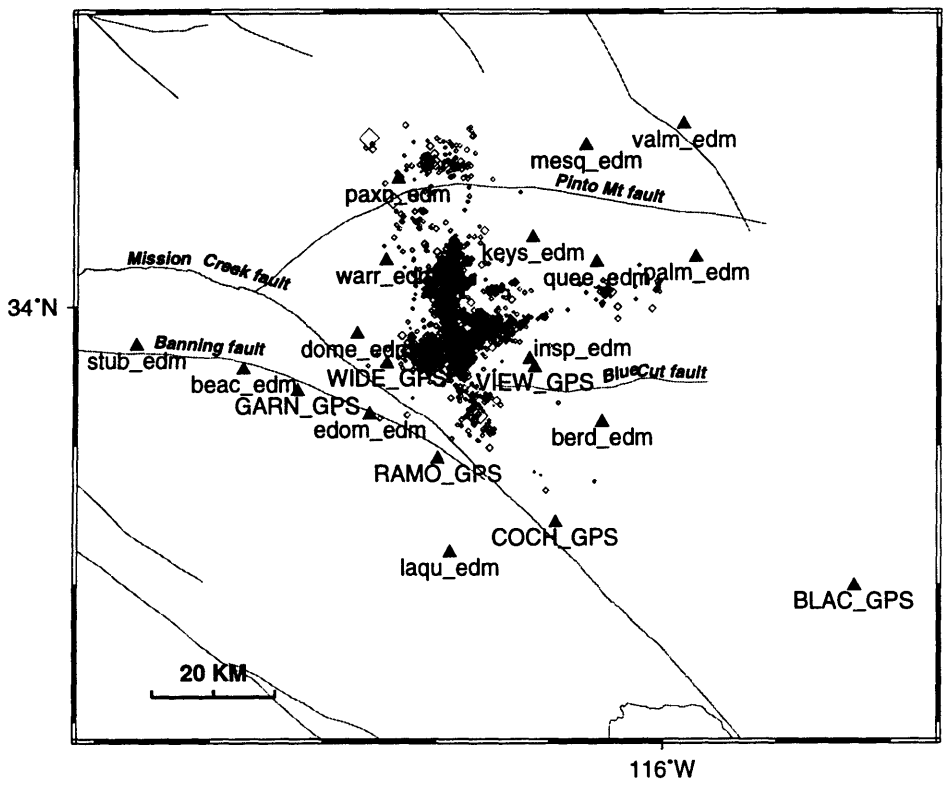

Joshua Tree GPS and trilateration geodetic network

Figure 4-2: Map showing location of the geodetic stations (triangles) in relation to the 1992 Joshua Tree earthquake. Aftershocks from *Hauksson et al.* [1993] are shown as diamonds. The large diamond northwest of site paxn shows the location of the Landers epicenter.

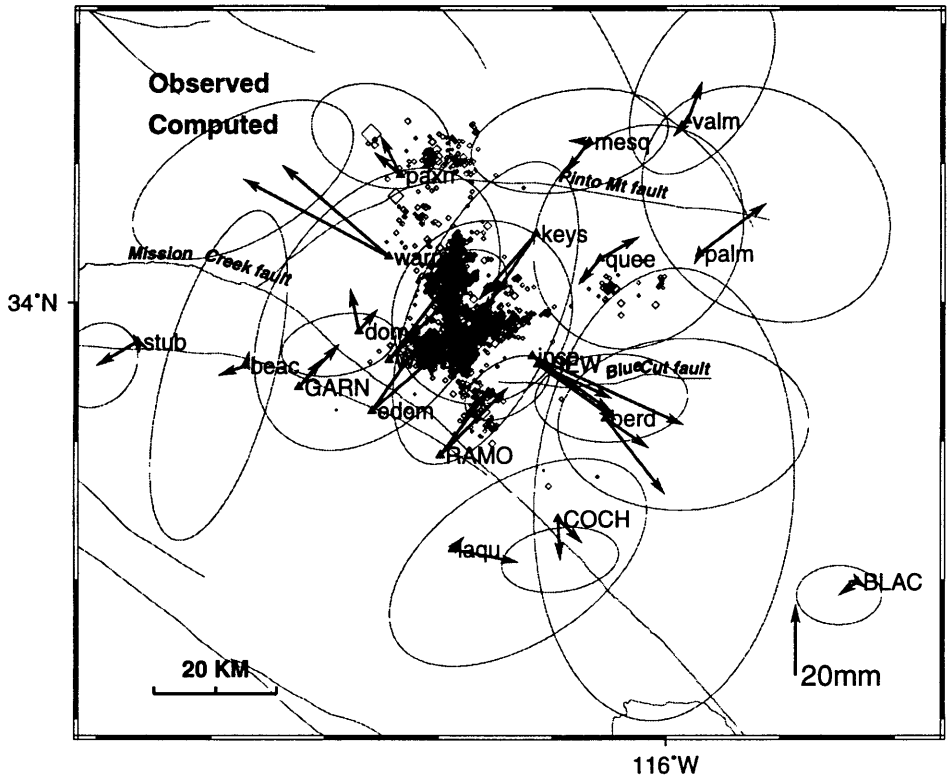

23 April 1992 Joshua Tree Earthquake
Input file : isdwp_disp.out
95% confidence level ellipses

Figure 4-3: Geodetically observed and model predicted horizontal displacements. GPS sites are indicated by all capital site names. Trilateration sites are indicated by all lowercase site names. Ninety-five percent confidence level error ellipses are shown for observed displacements.

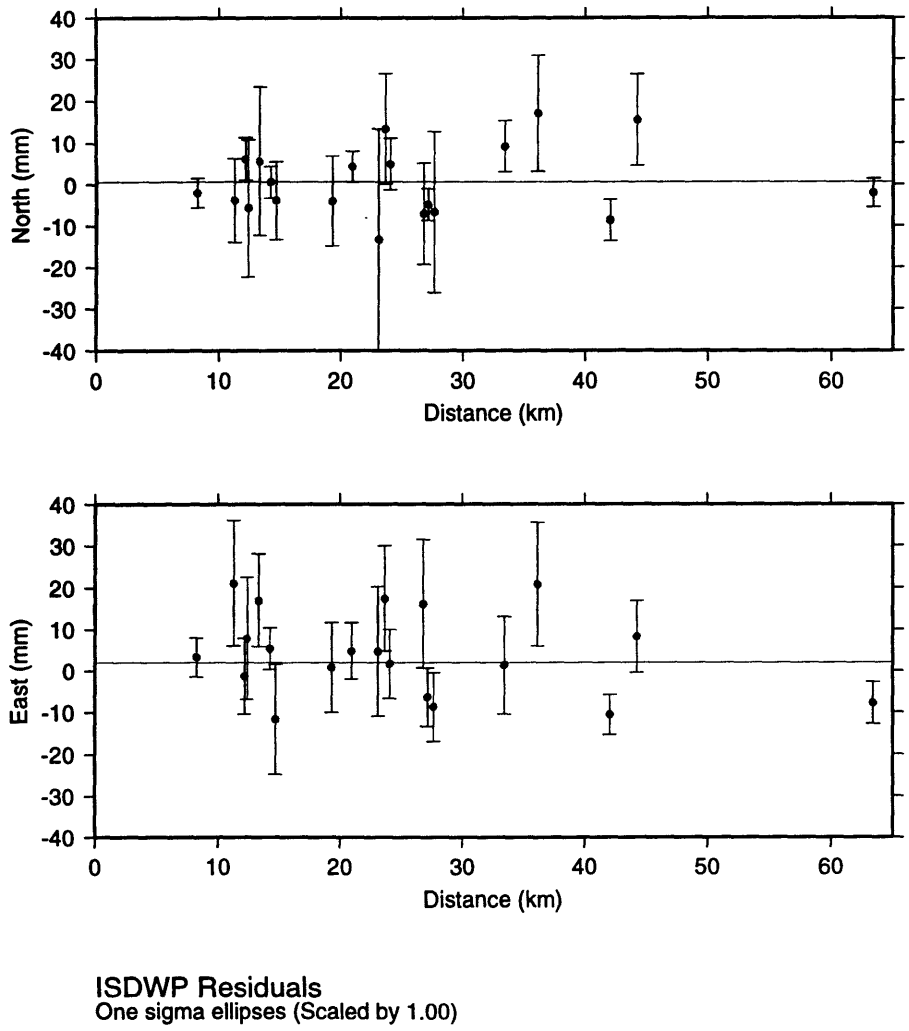

Figure 4-4: East and north coseismic displacement residuals versus distance of the geodetic site from the slip centroid. The means (zero slope lines) are not significantly different from zero.

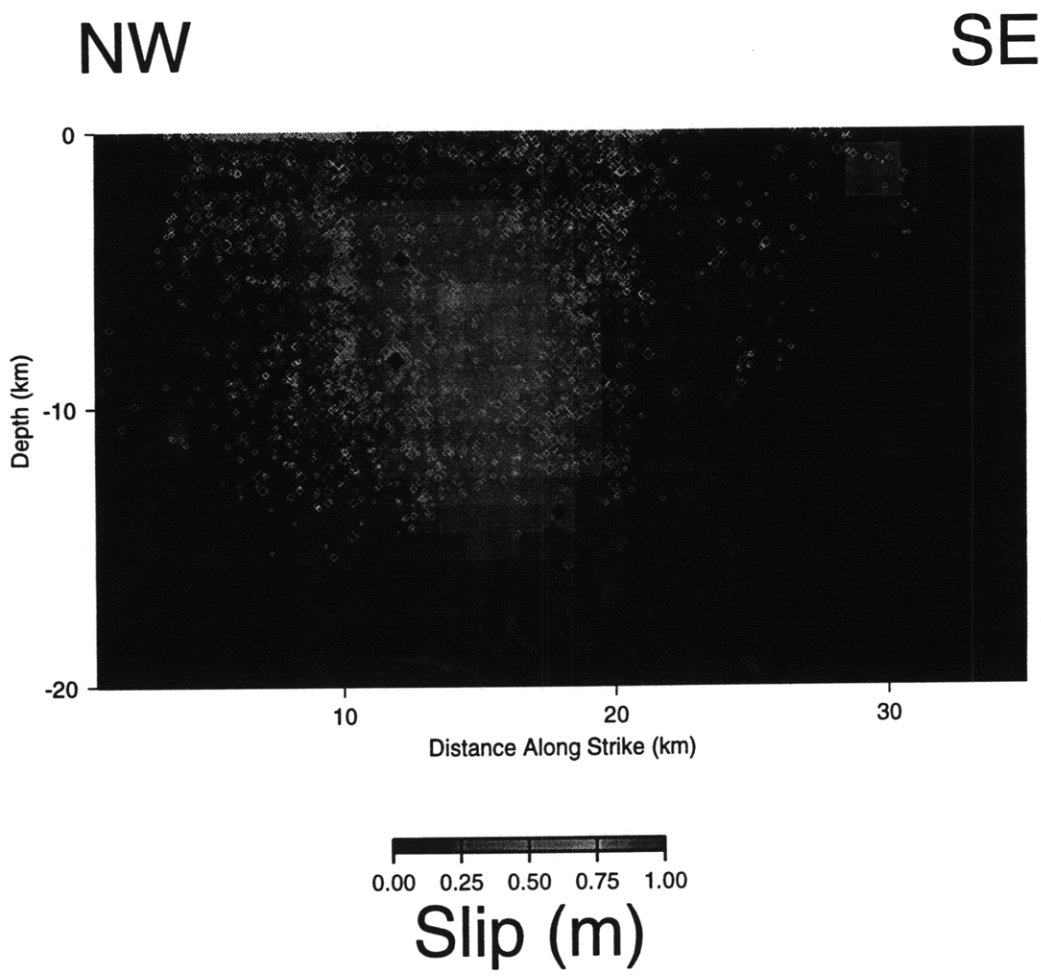

Figure 4-5: Slip distribution inferred from GPS and trilateration estimates of horizontal surface deformation together with aftershocks (diamonds) within 1.5 km of the fault projected onto the fault plane. The solid black diamonds indicate the location of the Joshua Tree hypocenter and foreshock. Solid grey diamonds indicate the locations of magnitude greater than four aftershocks or large Landers earthquake aftershocks.

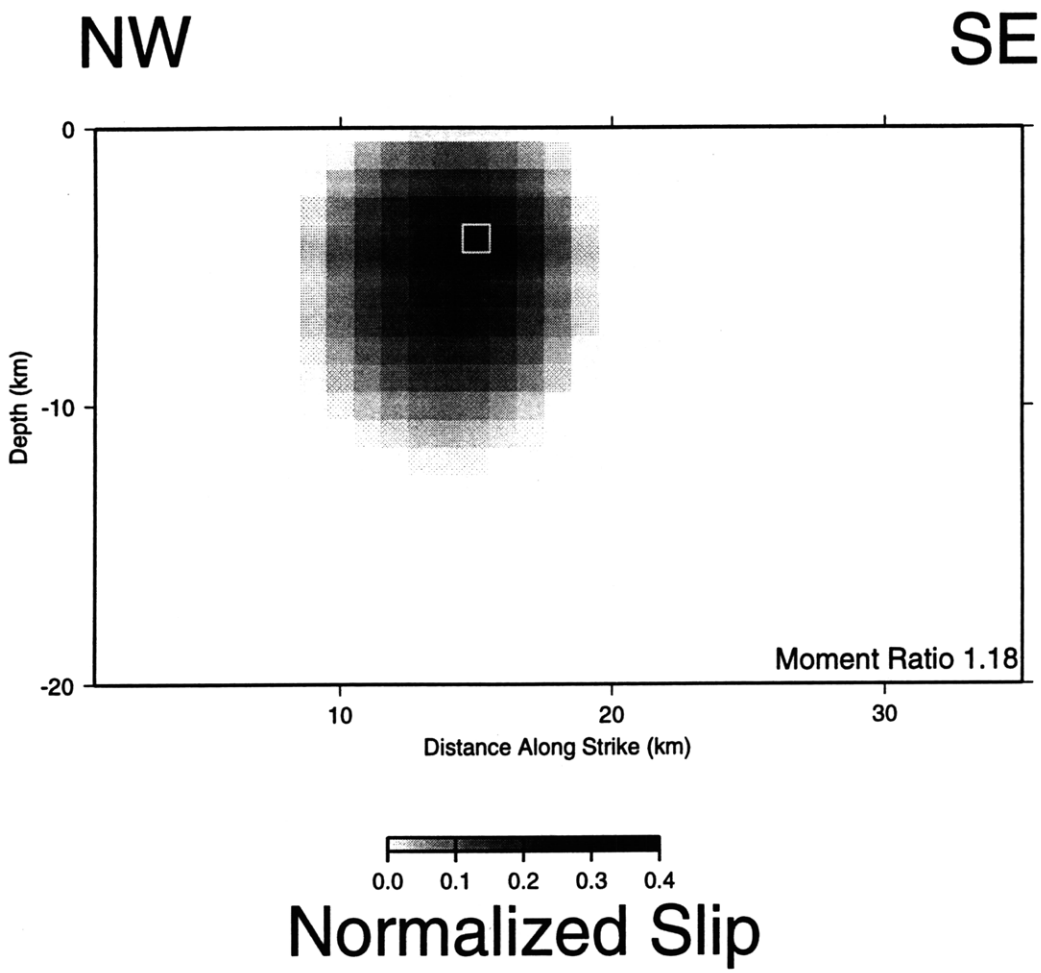

Figure 4-6: Normalized slip image from synthetic observations derived from slip on individual near surface fault element. The ratio of the image to model moments is indicated.

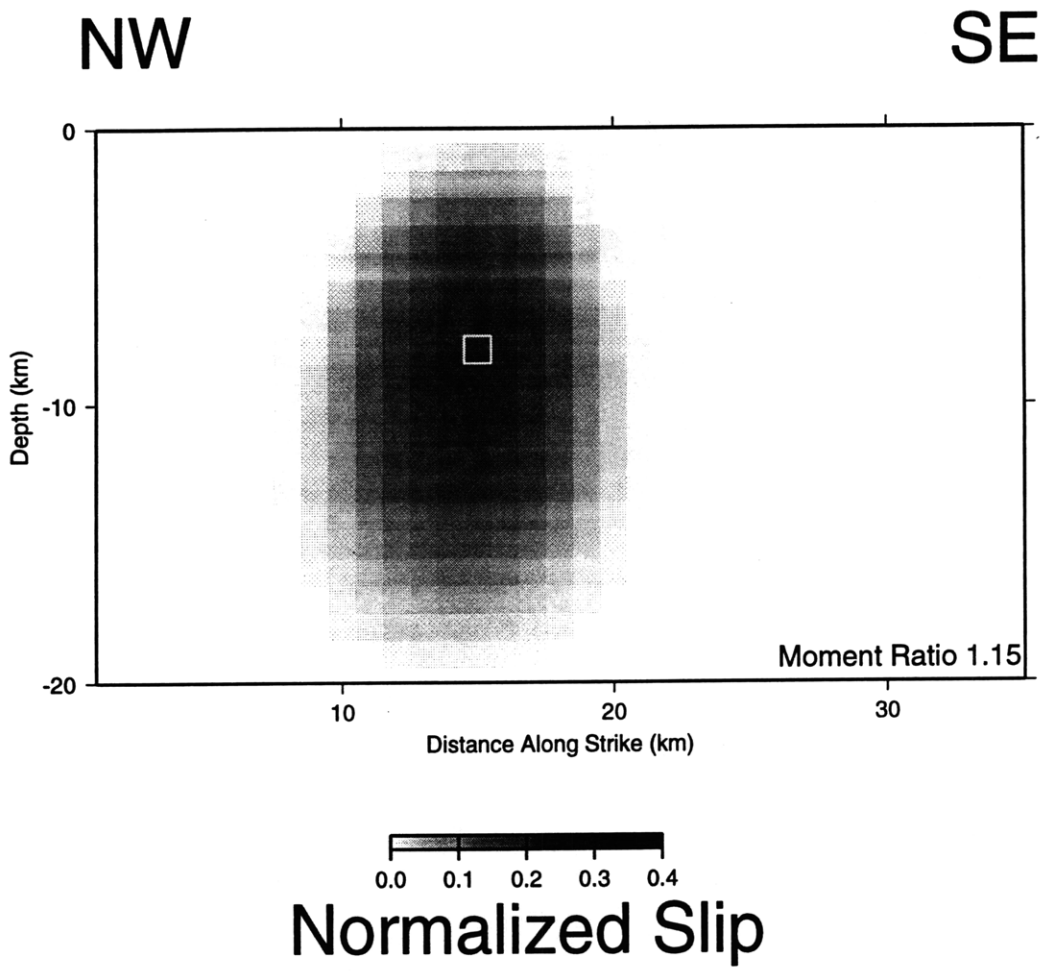

Figure 4-7: Normalized slip image from synthetic observations derived from slip on individual near center fault element. The ratio of the image to model moments is indicated.

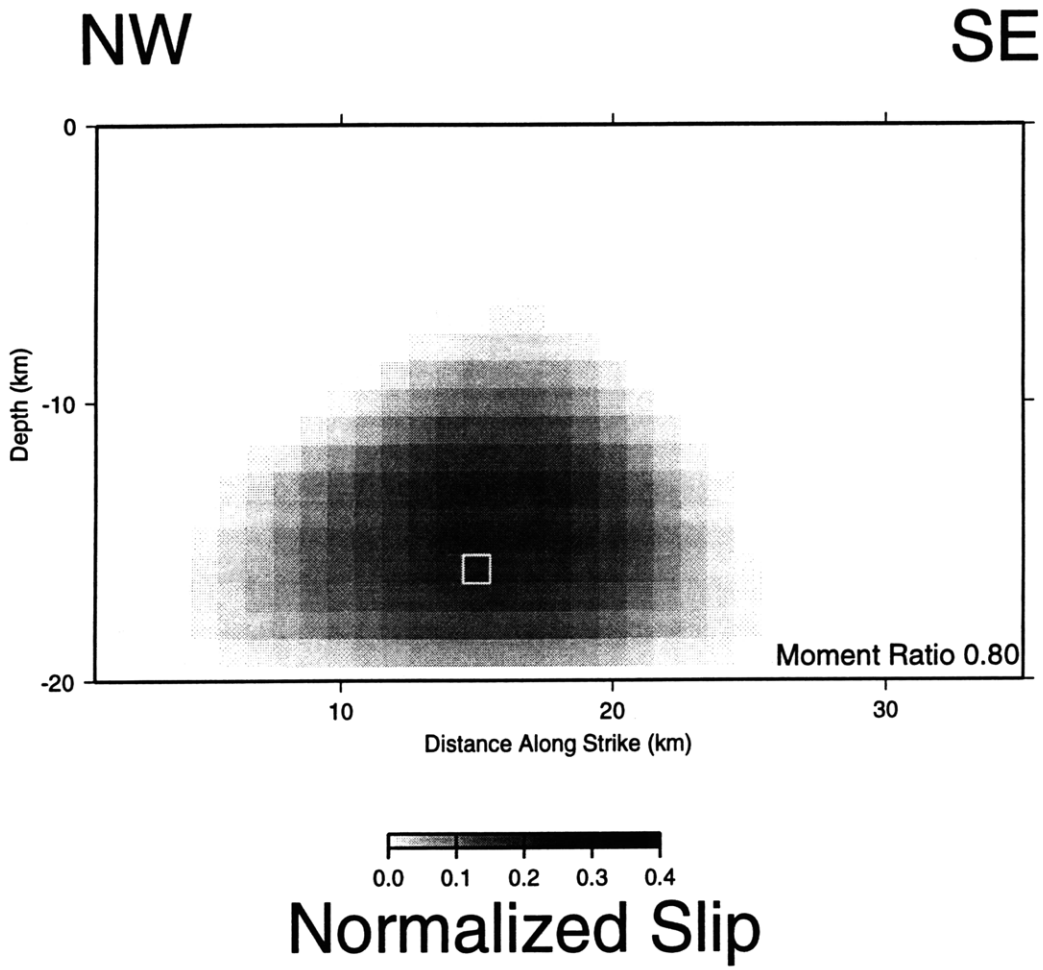

Figure 4-8: Normalized slip image from synthetic observations derived from slip on individual near bottom fault element. The ratio of the image to model moments is indicated.

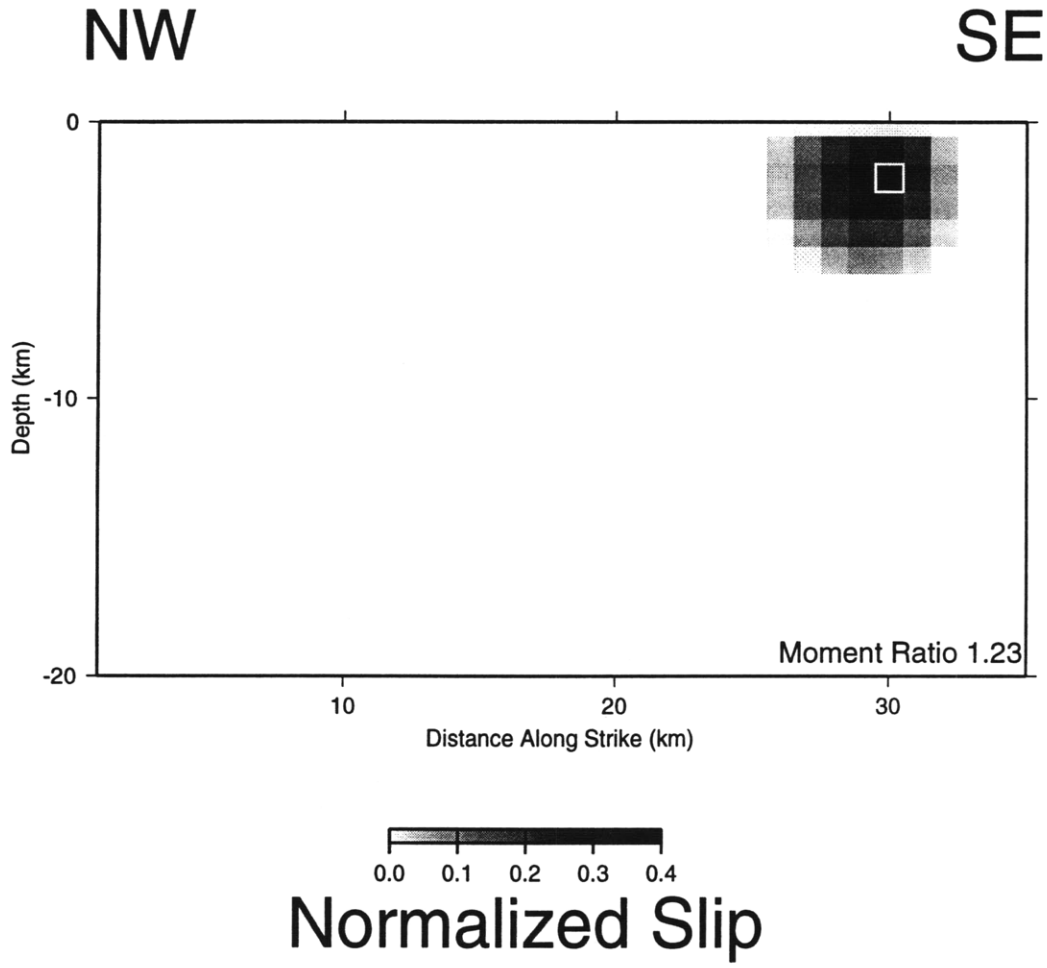

Figure 4-9: Normalized slip image from synthetic observations derived from slip on individual near surface fault element near inferred small patch of slip. The ratio of the image to model moments is indicated.

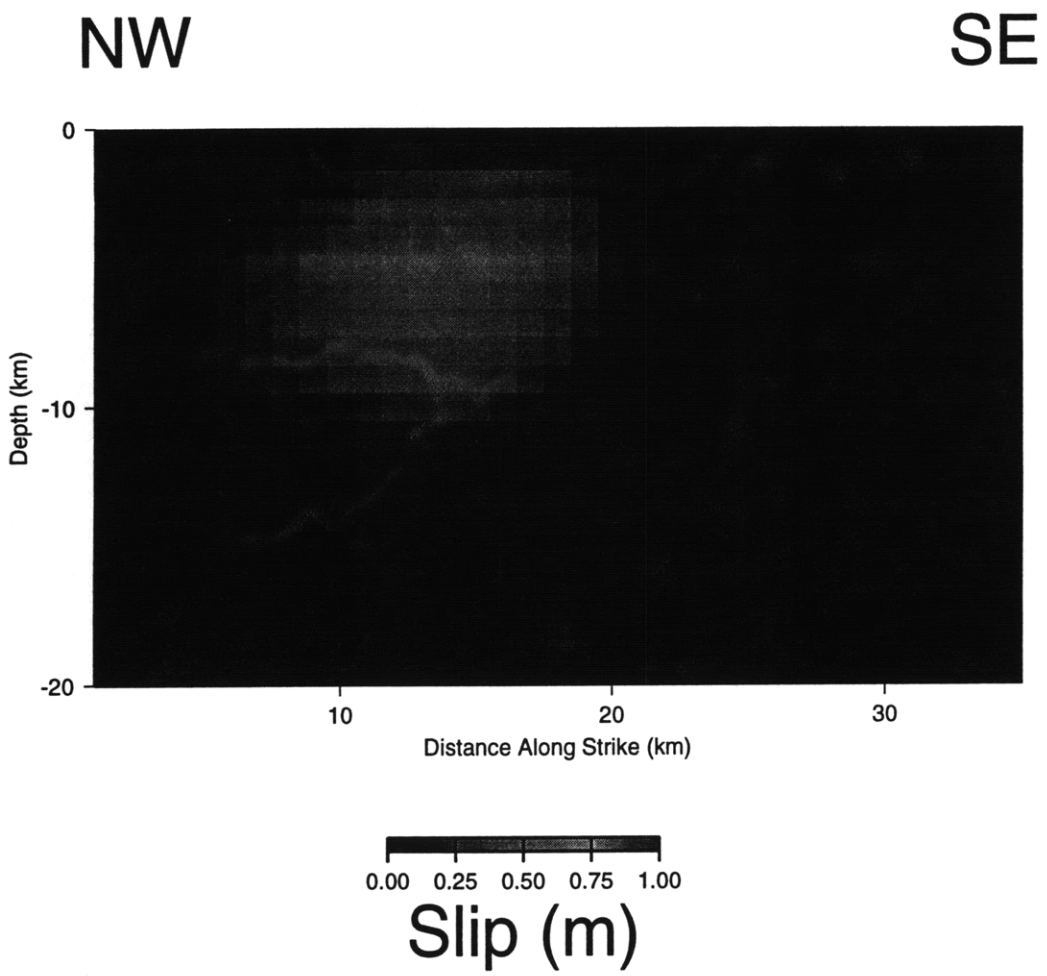

Figure 4-10: Slip distribution derived from trilateration data only. The solid diamonds indicate the locations of the Joshua Tree hypocenter and foreshock.

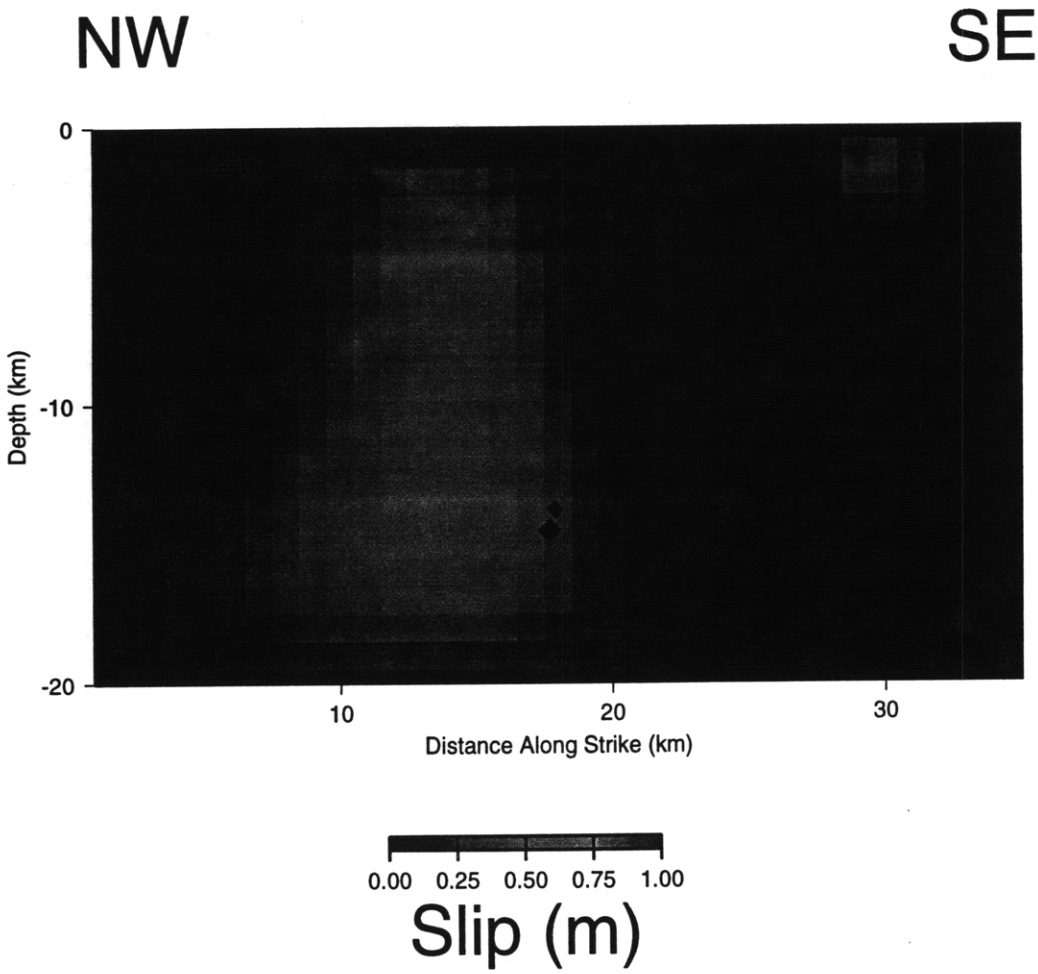

Figure 4-11: Slip distribution derived from GPS data only. The solid diamonds indicate the locations of the Joshua Tree hypocenter and foreshock.

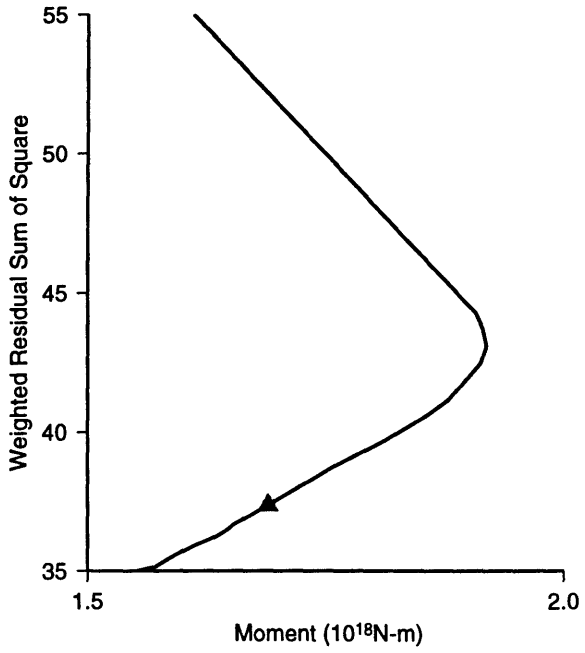

Figure 4-12: Geodetically derived moment versus data misfit. Triangle shows the location on the curve corresponding to the inferred model.

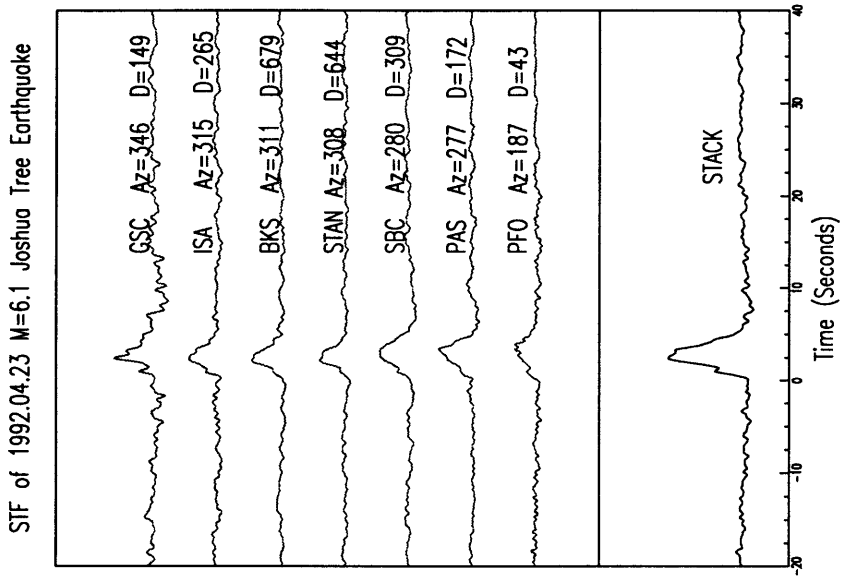

Figure 4-13: Source time functions for the 1992 Joshua Tree earthquake determined for each of the seismic stations shown in Figure 1 with stacked average at bottom.

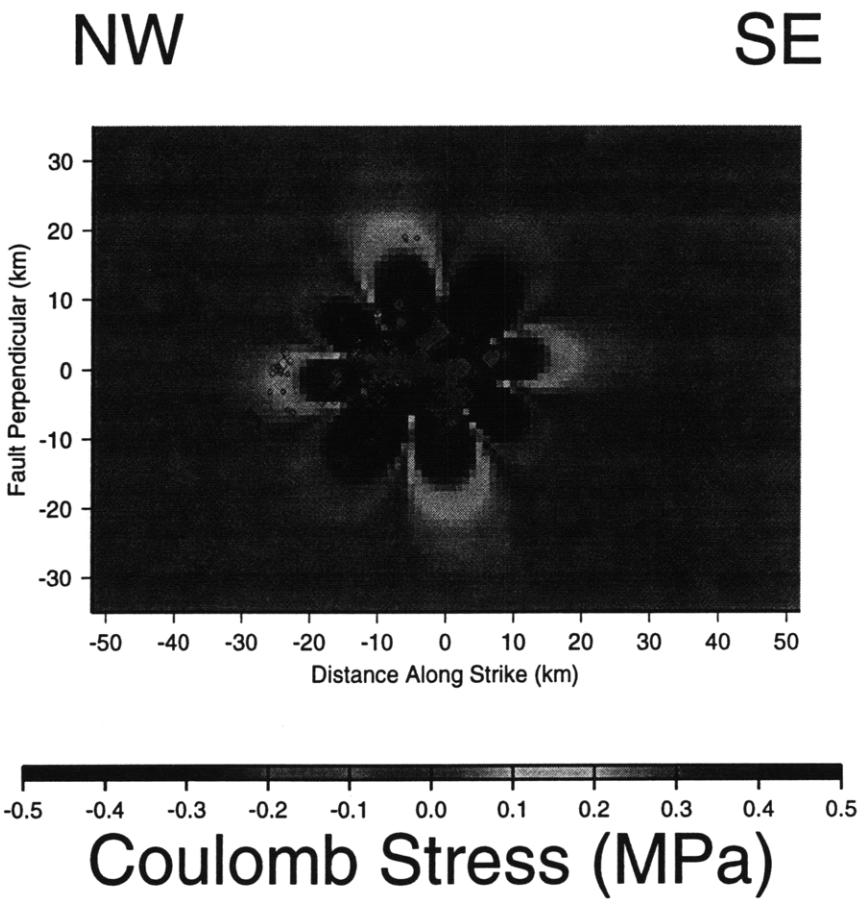

Figure 4-14: Predicted Coulomb failure stress changes and aftershocks (diamonds) in the depth range of 6 to 14 km projected onto a horizontal plane centered on the dislocation at 10 km depth. Solid black indicates Coulomb failure stress changes of 0.5 MPa or greater. Diamonds indicate locations Joshua Tree aftershocks and the Landers hypocenter (largest) and a large of Landers aftershock.

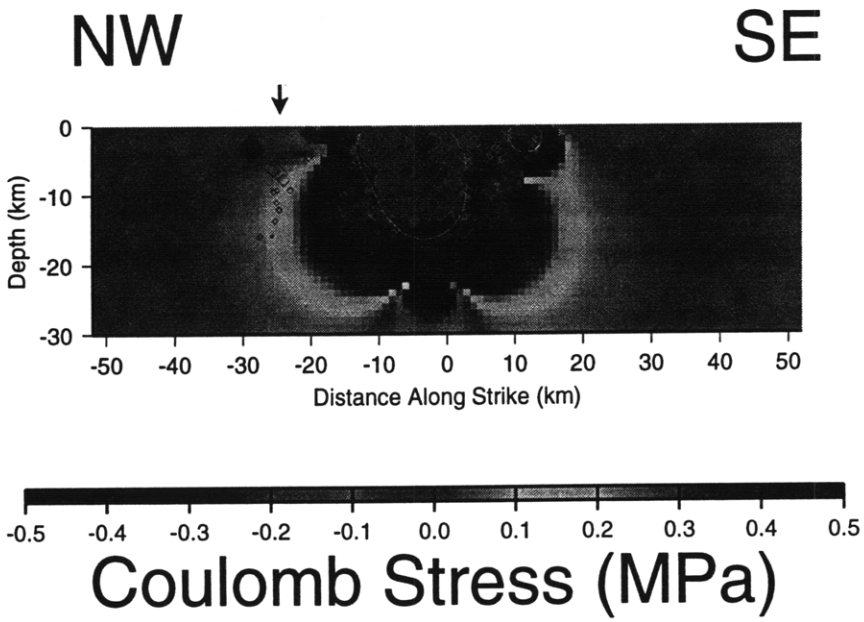

Figure 4-15: Predicted Coulomb failure stress changes resolved in the plane of the dislocation and aftershocks (diamonds) within 1 km of the fault projected onto the fault plane. Diamonds indicate locations Joshua Tree aftershocks, and the Landers hypocenter (largest) and large Landers aftershocks. Solid black indicates Coulomb failure stress changes of greater than 0.5 MPa. Arrow indicates the location of the aftershock cluster which began with the June 11 M 4.3 event. Two contour lines outline the regions of main shock slip greater than 0.01 m.

References

Aki, K. and P. Richards, *Quantitative Seismology, Theory and Methods,* vol. 1, W. H. Freeman and Co., New York, 1980.

Allen, C. R. , L. T. Silver, and F. G. Stehli, Agua Blanca fault – a major transverse structure of northern Baja California, Mexico, *Bull. Seis. Soc. Am., 71,* 457–482, 1960.

Allen, C. R. , P. St. Amand, C. F. Richter, and J. M. Nordquist, Relationship between seismicity and geologic structure in the southern California region, *Bull. Seis. Soc. Am., 55,* 753–797, 1965.

Argus, D. and R. G. Gordon, Pacific-North American plate motion from Very Long Baseline Interferometery compared with motion inferred from magnetic anomaliesm transform faults, and earthquake slip vectors, *J. Geophys. Res., 95,* 17,315–17,324, 1990.

Argus, D. F. and M. B. Heflin, Plate motion and crustal deformation estimated with geodetic data from the Global Positioning System, *Geophys. Res. Let., 22,* 1973–1976, 1995.

Ash, M. E. , Determination of Earth satellite orbits, tech. note 1972-5, Technical report, Massachusetts Institute of Technology, Lincoln Laboratory, Lexington, 1972.

Atwater, T. , Implications of plate tectonics for the Cenozoic tectonic evolution of western North America, *Geol. Soc. Am. Bull., 81,* 3513–3536, 1970.

Backus, G. and F. Gilbert, The resolving power of gross Earth data, *Geophys. J. R. Astr. Soc., 16,* 169–205, 1968.

Ben-Menahem, A. and A. Gillon, Crustal deformation by earthquakes and explotions, *Bull. Seis. Soc. Am., 60,* 193–215, 1970.

Ben-Menahem, A. and S. J. Singh, Multipolar elastic fields in a layered half space, *Bull. Seis. Soc. Am., 58,* 1519–1572, 1968.

Ben-Menahem, A. , S. J. Singh, and S. Solomon, Deformation of a homogeneous earth model by finite dislocations, *Rev. Geophys. Space Phys., 8,* 591–632, 1970.

Bennett, R. A. , R. E. Reilinger, and J. Gonzalez, GPS measurements in southernmost California/northern Baja-Mexicali Valley: Continental deformation in a transcurrent/extensional environment, *EOS, Trans. AGU, 75,* 164, 1992.

Bennett, R. A. , R. E. Reilinger, W. Rodi, Y. Li, M. N. Toksöz, and K. Hudnut, Coseismic fault slip associated with the 1992 M_w 6.1 Joshua Tree, California earthquake: Implications for the Joshua Tree-Landers earthquake sequence, *J. Geophys. Res., 100,* 6443–6462, 1992.

Biehler, S. , *Geophysical study of the Salton Trough of southern California,* PhD thesis, California Institute of Technology, 1964.

Bierman, G. J. , *Factorization methods in discrete sequential estimation, Mathematics in Engeneering, Vol. 128,* Academic Press, Inc., San Diego, CA., 1977.

Chinnery, M. , The deformation of the ground around surface faults, *Bull. Seis. Soc. Am., 51,* 335–372, 1961.

Clark, M. M. , Map showing recently active breaks along the San Andreas fault and associated faults between Salton Sea and Whitewater River - Mission Creek, California, in *Miscelaneous Investigations Series Map I-1483, 2 sheets, scale1:24000,* U.S. Geological Survey, 1984.

Couch, R. W. , G. E. Ness, O. Sanchez-Zamora, G. Calderon-Riveroll, P. Douguin, T. Plawman, S. Coperude, B. Huehn, and W. Gumma, Gravity anomalies and crustal structure of the gulf and peninsular province of the Californias, in *The Gulf and Peninsular Province of the Californias,* edited by Dauphin, J. P. and B. R. T. Simoneit, pp. 25–46, AAPG Memoir 47, 1991.

Darby, D. , J. J. Gonzalez, and P. Lesage, Geodetic studies in Baja California, Mexico, and the evaluation of short-range data from 1974 to 1982, *J. Geophys. Res., 89,* 2478–2490, 1984.

DeMets, C. , R. G. Gordon, D. F. Argus, and S. Stein, Current plate motions, *Geophys. J. Int., 101,* 425–478, 1990.

DeMets, C. , R. G. Gordon, D. F. Argus, and S. Stein, Effects of recent revisions to the geomagnetic reversal time scale on estimates of current plate motions, *Geophys. Res. Let., 21,* 2191–2194, 1994.

Dickson, W. R. and W. S. Snyder, Geometry of subducted slabs related to San Andreas transform, *Journ. Geol., 87,* 609–627, 1979.

Dixon, T. H. , G. Gonzalez, S. M. Lisowksi, and D. M. Tralli, Preliminary determination of Pacific-North American relative motion in the southern Gulf of California using the Global Positioning System, *Geophys. Res. Let., 18,* 861–864, 1991.

Dokka, R. K. and C. J. Travis, Late Cenozoic strike-slip faulting in the Mojave desert, California, *Tectonics, 9,* 311–340, 1990a.

Dokka, R. K. and C. J. Travis, Role of the Eastern California Shear Zone in accomodating Pacific-North American plate motion, *Geophys. Res. Let., 17,* 1323–1326, 1990b.

Dong, D. , *The horizontal velocity field in southern California from a combination of terrestrial and space geodetic data,* PhD thesis, Massachusetts Institue of Technology, 1993.

Doser, D. and H. Kanamori, Depth of seismicity in the Imperial Valley region (1977-1983) and its relationship to heat flow, crustal structure, and the October 15, 1979, earthquake, *J. Geophys. Res., 91,* 675–688, 1986.

Du, Y. and A. Aydin, Stress transfer during three sequential moderate earthquakes along the central Calaveras fault California, *J. Geophys. Res., 98,* 9947–9962, 1993.

Du, Y. , A. Aydin, and P. Segall, Comparison of various inversion techniques as applied to the determination of a geophysical deformation model for the Borah Peak earthquake, *Bull. Seis. Soc. Am., 82,* 1840–1866, 1992.

Farina, F. , T. Dixon, F. Suarez, E. Humphreys, and M. Miller, Preliminary GPS results bearing on the motion of the Agua Blanca fault zone, Baja California, Mexico, *EOS, Trans. AGU, 75,* 182, 1994.

Feigl, K. L. , D. C. Agnew, Y. Bock, D. Dong, A. Donnellan, B. H. Hager, T. A. Herring, D. D. Jackson, T. H. Jordan, R. W. King, S. Larsen, K. M. Larson, M. H. Murray, S. Z., and F. H. Webb, Space geodetic measurement of crustal deformation in central and southern California, 1984-1992, *J. Geophys. Res., 98,* 21,677–21,712, 1993.

Fliegel, H. F. and T. E. Gallini, Global Positioning System radiation force model for geodetic applications, *J. Geophys. Res., 97,* 559–568, 1992.

Frez, J. and J. J. Gonzalez, Crustal structure and seismotectonics of northern Baja California, in *The Gulf and Peninsular Province of the Californias,* edited by Dauphin, J. P. and B. R. T. Simoneit, pp. 261–284, AAPG Memoir 47, 1991.

Fuis, G. S. , W. D. Mooney, J. H. Healy, G. A. McMechan, and W. J. Lutter, A seismic refraction survey of the Imperial Valley region, California, *J. Geophys. Res., 89,* 1165–1189, 1984.

Gelb, A. , *Applied optimal estimation,* MIT Press, Cambridge, MA, 1974.

Gilbert, L. E. , C. H. Scholz, and J. Beavan, Strain localization along the San Andreas fault: consequences for loading mechanisms, *J. Geophys. Res., 99,* 23,975–23,984, 1994.

Gonzalez, J. J. and F. Suarez, Geological and seismic evidence of a new branch of the Agua Blanca fault, *Geophys. Res. Let., 11,* 42–45, 1984.

Hartzell, S. H. and T. H. Heaton, Inversion of strong ground motion and teleseismic waveform data for the fault rupture histroy of the 1979 Imperial Valley, California, earthquake, *Bull. Seis. Soc. Am., 73,* 1553–1583, 1983.

Hatch, M. E. and J. K. Rockwell, Neotectonics of the Agua Blanca fault, Agua Blanca Valley, northen Baja California, Mexico, *Geol. Soc. Am. Abs. Prog., 78,* 114, 1986.

Hauksson, E. , L. M. Jones, K. Hutton, and D. Eberhart-Phillips, The Landers earthquake sequence: seismological observations, *J. Geophys. Res., 98,* 19,835–19,858, 1993.

Herring, T. A. , J. L. Davis, and I. I. Shapiro, Geodesy by radio interferometry: the application of Kalman filtering to the analysis of Very Long Baseline Interferometry data, *J. Geophys. Res., 95,* 12,561–12,581, 1990.

Herring, T. A. , GLOBK: Global Kalman filter VLBI and GPS analysis program, Technical report, Massachusetts Institute of Technology, Cambridge, MA, 1993.

Hough, S. E. , J. Mori, E. Sembera, G. Glassmoyer, C. Mueller, and S. Lydeen, Southern surface rupture associated with the 1992 M 7.4 Landers earthquake: Did it all happen during the mainshock?, *Geophys. Res. Let., 20,* 2615–2618, 1993.

Humphreys, E. D. and R. J. Weldon, Deformation across the western United States: A local estimate of Pacific-North America transform deformation, *J. Geophys. Res., 99,* 19,975–20,010, 1994.

Incorporated Research Institutions for Seismology Data Management Center, U. o. W. , 1992.

Jackson, D. and Y. Kagan, Implications of characteristic earthquakes, *EOS, Trans. AGU, 76,* 199, 1995.

Johnson, H. O. , D. C. Agnew, and F. K. Wyatt, Present-day crustal deformation in southern California, *J. Geophys. Res., 99,* 23,951–23,974, 1994.

Johnson, H. O. , *Techniques and studies in crustal deformation,* PhD thesis, University of California, San Diego, 1993.

Jones, L. E. , S. E. Hough, and D. V. Helmberger, Rupture process of the June 28, 1992 Big Bear earthquake, *Geophys. Res. Let., 20,* 1907–1910, 1993.

Jovanovich, D. B. , M. I. Husseini, and M. A. Chinnery, Elastic dislocations in a layered half-space: I. basic theory and numerical methods, *Geophys. J. R. Astr. Soc., 39,* 205–217, 1974a.

Jovanovich, D. B. , M. I. Husseini, and M. A. Chinnery, Elastic dislocations in a layered half-space: II. the point source, *Geophys. J. R. Astr. Soc., 39,* 219–239, 1974b.

Kagan, Y. Y. and D. D. Jackson, Seismic gap hypothesis: ten years after, *J. Geophys. Res., 96,* 21,419–21,431, 1991.

Kalman, R. E. , A new approach to linear filtering and prediction problems, *J. Basic Eng., 82,* 35–46, 1960.

Kasser, M. , J. C. Ruegg, P. Lesage, L. Ortlieb, J. Pagarete, N. Duch, J. Guerrero, and J. Roldan, Geodetic measurements of plate motions across the central Gulf of California, 1982-1986, *Geophys. Res. Let., 14,* 5–8, 1987.

Keller, E. A. , R. J. Bonkowski, R. J. Korsch, and R. J. Shiemon, Tectonic geomorphology of the San Andreas fault zone in the southern Indio Hills, Coachella Valley, California, *Geol. Soc. Am. Bull., 93,* 46–56, 1982.

King, R. W. and Y. Bock, Documentation for the MIT GPS analysis software: GAMIT, Technical report, Massachusetts Institute of Technology, Cambridge, MA, 1995.

King, R. W. , J. Collins, E. M. Masters, C. Rizos, and A. Stolz, *Surveying with Global Positioning System, Monograph No. 9,* School of Surveying, University of New South Wales, Sydney, 1985.

King, G. , R. Stein, and J. Lin, Static stress changes and the triggering of earthquakes, *Bull. Seis. Soc. Am., 84,* 935–953, 1994.

Kroger, P. M. , G. A. Lyzenga, K. Wallace, and J. M. Davidson, Tectonic motion in the western United States inferred from Very Long Baseline Interferometry measurements, *J. Geophys. Res., 92,* 14,151–14,163, 1987.

Lachenbruch, A. H. , J. H. Sass, and S. P. Galanis Jr., Heat flow in southernmost California and the origin of the Salton Trough, *J. Geophys. Res., 90,* 6709–6736, 1985.

Larsen, S. and R. E. Reilinger, Age constraints for the present fault configuration in the Imperial Valley, California: Evidence for the northwestward propagation of the Gulf of California rift system, *J. Geophys. Res., 96,* 10,339–10,346, 1991.

Larsen, S. and R. Reilinger, Global Positioning System measurements of strain accumulation across the Imperial Valley, California: 1986-1989, *J. Geophys. Res., 97,* 8865–8876, 1992.

Larsen, S. , R. Reilinger, H. Neugebauer, and W. Strange, Global Positioning System measurements of deformations associated with the 1987 Superstition Hills earthquake: evidence for conjugate faulting, *J. Geophys. Res., 97,* 4885–4902, 1992.

Larson, K. M. , Application of the Global Positioning System to crustal deformation measurements, 3, result from the southern California borderlands, *J. Geophys. Res., 98,* 21,713–21,726, 1993.

Lawson, C. L. and R. J. Hanson, *Solving least squares problems,* Prentice Hall, Inc., Englewood Cliffs, New Jersey, 1974.

Legg, M. R. , B. P. Luyendyk, J. Mammerickx, C. de Moustier, and R. Tyce, Sea beam survey of an active strike-slip fault: The San Clemente fault in the California continental borderland, *J. Geophys. Res., 94,* 1727–1744, 1989.

Legg, M. R. , V. Wong, and F. Suarez, Geologic structure and tectonics of the inner continental borderland of northern Baja California, in *The Gulf and Peninsular Province of the Californias,* edited by Dauphin, J. P. and B. R. T. Simoneit, pp. 145–178, AAPG Memoir 47, 1991.

Legg, M. R. , Sea beam evidence of recent tectonic activity in the California continental borderland, in *The Gulf and Peninsular Province of the Californias,* edited by Dauphin, J. P. and B. R. T. Simoneit, pp. 179–196, AAPG Memoir 47, 1991.

Li, V. C. and J. R. Rice, Crustal deformation in great Californian earthquake cycles, *J. Geophys. Res., 92,* 11,533–11,551, 1987.

Lichten, S. M. and W. J. Bertiger, Demonstration of sub-millimeter GPS orbit determination and 1.5 parts in 10^8 three-dimensional baseline accuracy, *Bull. Geod., 63,* 167–189, 1989.

Lichten, S. M. and J. Border, Strategies for high-precision Global Positioning System orbit determination, *J. Geophys. Res., 92,* 12,751–12,762, 1987.

Lindley, G. T. , Source parameters of the 23 April 1992 Joshua Tree, California, earthquake, its largest forshock, and aftershocks, *EOS, Trans. AGU, 74,* 397, 1993.

Lisowski, M. , J. C. Savage, and W. H. Prescott, The velocity field along the San Andreas fault in central and southern California, *J. Geophys. Res., 96,* 8369–8389, 1991.

Mansinha, L. and D. E. Smylie, Displacement fields of inclined faults, *Bull. Seis. Soc. Am., 61,* 1433–1440, 1971.

Matthews, M. , *On the estimation of fault slip in space and time,* PhD thesis, Stanford, 1991.

Meisling, K. E. and R. J. Weldon, Late-Cenozoic tectonics of the northwestern San Bernadino mountains, southern California, *Geol. Soc. Am. Bull., 101,* 106–128, 1989.

Mendoza, C. and S. H. Hartzell, Inversion for slip distribution using teleseismic P waveforms: North Palm Springs, Borah Peak, and Michoacan earthquakes, *Bull. Seis. Soc. Am., 78,* 1092–1111, 1988a.

Morozov, V. A. , *Regularization methods for ill-posed problems,* CRC Press, Boca Raton, Florida, 1993, 257 pages.

Mueller, K. J. and T. K. Rockwell, Late Quaternary structural evolution of the western margin of the Sierra Cucapa, northern Baja California, in *The Gulf and Peninsular Province of the Californias,* edited by Dauphin, J. P. and B. R. T. Simoneit, pp. 249–260, AAPG Memoir 47, 1991.

Nishenko, S. P. and L. R. Sykes, Comment on "Seismic gap hypothesis: ten year after" by Y. Y. Kagan, and D. D. Jackson, *J. Geophys. Res., 98,* 9909–9916, 1993.

Nur, A. , H. Ron, G. Beroza, and L. Alfonsi, A fault is born: the mechanical origin of the Mojave seismic line, *EOS, Trans. AGU, 73,* 362, 1992.

Okada, Y. , Surface deformation due to shear and tensile faults in a half space, *Bull. Seis. Soc. Am., 75,* 1135–1154, 1985.

Oral, M. B. , *GPS measurements of Crustal Deformation in Turkey (1988-1992): Kinematics of the Arabia-Africa-Eurasia Plate Collision Zone,* PhD thesis, Massachusetts Institue of Technology, 1994.

Reilinger, R. and S. C. Larsen, Vertical crustal deformation associated with the 1979 M6.6 Imperial Valley, California, earthquake: Implications for fault behavior, *J. Geophys. Res., 91,* 14,044–14,056, 1986.

Reilinger, R. , Coseismic and postseismic vertical movements associated with the 1940 M7.1 Imperial Valley, California, earthquake, *J. Geophys. Res., 89,* 4531–4537, 1984.

Rodi, W. L. , *Regularization and Backus-Gilbert estimation in non-linear inverse problems: application to magnetotellurics and surface waves,* PhD thesis, Pennsylvania State University, 1989.

Rymer, M. J. , The 1992 Joshua Tree, California, earthquake: Tectonic setting and triggered slip, *EOS, Trans. AGU, 73,* 363, 1992.

Sanders, C. O. and H. Kanamori, A seismotectonic analysis of the Anza seismic gap, San Jacinto fault zone, southern California, *J. Geophys. Res., 89,* 5873–5890, 1984.

Sauber, J. , W. Thatcher, and S. C. Solomon, Geodetic measurement of deformation in the central Mojave desert, California, *J. Geophys. Res., 91,* 12,683–12,693, 1986.

Savage, J. C. and L. M. Hastie, Surface deformation associated with dip-slip faulting, *J. Geophys. Res., 71,* 4897–4904, 1966.

Savage, J. C. and W. H. Prescott, Strain accumulation on the San Jacinto fault near Riverside, California, *Bull. Seis. Soc. Am., 66,* 1749–1754, 1976.

Savage, J. C. , W. H. Prescott, and G. Gu, Strain acummulation in southern California, 1973-1984, *J. Geophys. Res., 91,* 7455–7473, 1986.

Savage, J. C. , W. H. Prescott, and M. Lisowski, Deformation along the San Andreas fault, 1982-1986, as indicated by frequent geodetic measurements, *J. Geophys. Res., 92,* 4785–4797, 1987.

Savage, J. C. , M. Lisowski, and W. Prescott, An apparent shear zone trending north-northwest across the Mojave desert into Owens Valley, eastern California, *Geophys. Res. Let., 17,* 2113–2116, 1990.

Savage, J. C. , M. Lisowski, and M. Murray, Deformation from 1973 through 1991 in the epicentral area of the 1992 Landers, California, earthquake (Ms = 7.5), *J. Geophys. Res., 98,* 19,951–19,958, 1993.

Savage, J. C. , M. Lisowski, N. E. King, and W. K. Gross, Strain accumulation along the Laguna Salada fault, Baja California, Mexico, *J. Geophys. Res., 99,* 18,109–18,116, 1994.

Savage, J. C. , Effect of crustal layering upon dislocation modeling, *J. Geophys. Res., 92,* 10,595–10,600, 1987.

Savage, J. C. , Principle component analysis of interseismic deformation in southern California, *J. Geophys. Res., 100,* 12691–12701, 1995.

Savage, J. C.and Lisowski, M. , Geodetic monitoring of the southern San Andreas fault, California, 1980–1991, *J. Geophys. Res., 100,* 8185–8192, 1995a.

Savage, J. C.and Lisowski, M. , Interseismic deformation along the San Andreas fault in southern california, *J. Geophys. Res., 100,* 12703–12717, 1995b.

Scholz, C. , The brittle-plastic transition and the depth of seismic faulting, *Geo. Runds., 77,* 317–328, 1988.

Scholz, C. , *The mechanics of earthquakes and faulting,* Cambridge University Press, Cambridge, 1990.

Sedlock, R. L. and D. H. Hamilton, Late Cenozoic evolution of southwestern California, *J. Geophys. Res., 96,* 2325–2351, 1991.

Seeber, L. and J. G. Armbruster, The San Andreas fault system through the Transverse Ranges as illuminated by earthquakes, *J. Geophys. Res., 100,* 8285–8310, 1995.

Segall, P. and R. Harris, Earthquake deformation cycle on the San Andreas fault near Parkfield, California, *J. Geophys. Res., 92,* 10,511–10,525, 1987.

Sibson, R. , Fault zone models, heat flow, and depth distribution of earthquakes in the continental crust of the United States, *Bull. Seis. Soc. Am., 72,* 151–163, 1982.

Sieh, K. E. , Slip rate across the San Andreas fatuls and prehistoric earthquakes at Indio, California, *EOS, Trans. AGU, 67,* 1200, 1986.

Singh, S. J. , Static deformation of a multilayered half-space by internal sources, *J. Geophys. Res., 75,* 3257–3263, 1970.

Snay, R. A. and A. R. Drew, Supplementing geodetic data with prior information for crustal deformation in the Imperial Valley, California, Technical report, University of Stuttgart, 1988.

Snay, R. A. , M. W. Cline, and E. L. Timmerman, Horizontal deformation in the Imperial Valley, California between 1934 and 1980, *J. Geophys. Res., 87,* 3959–3968, 1982.

Sobolev, S. L. , *Applications of Functional Analysis in Mathematical Physics,* American Mathematical Society, Providence, RI, 1963.

Stein, R. S. , G. C. P. King, and J. Lin, Changes in failure stress on the southern San Andreas fault system caused by the 1992 magnitude = 7.4 Landers earthquake, *Science, 258,* 1328–1332, 1992.

Steketee, J. A. , On volterra's dislocations in a semi-infinite elastic medium, *Can. J. Phys., 36,* 192–205, 1958a.

Steketee, J. A. , Some geophysical applications of the elasticity theory of dislocations, *Can. J. Phys., 36,* 1168–1198, 1958b.

Swift, E. R. , Mathematical description of the GPS multisatellite filter/smoother, NSWC tr-87-187, Technical report, Naval Surface Warfare Center, Dahlgren, VA., 1987.

Sykes, L. R. and L. Seeber, Great earthquakes and great asperities, San Andreas fault, southern California, *Geology, 13,* 835–838, 1985.

Sylvester, A. G. and R. R. Smith, Tectonic transpression and basement-controlled deformation in the San Andreas fault zone, Salton Trough, California, *Am. Assoc. Pet. Geol. Bull., 60,* 2081–2102, 1976.

Tennyson, M. E. , Pre-transform Early Miocene extension in western California, *Geology, 17,* 792–796, 1989.

Thatcher, W. , Horizontal crustal deformation from historic geodetic measurements in southern California, *J. Geophys. Res., 84,* 2351–2370, 1979.

Thatcher, W. , Microplate versus continuum descriptions of active tectonic deformation, *J. Geophys. Res., 100,* 3885–3894, 1995.

Tikhonov, A. N. and V. Y. Arsenin, *Solutions to ill-posed problems,* V. H. Winston and Sons, Washington D. C., 1977.

Wahba, G. , Spline models for observational data, in *CBMS-NSF Regional Conference series in applied mathemmatics, 59,* Philadelphia, Pennsylvania, 1990, Society for Industrial and Applied Mathematics.

Wald, D. J. and T. H. Heaton, Spatial and temporal distribution of slip for the 1992 Landers, California earthquake, *Bull. Seis. Soc. Am., 84,* 668–691, 1994.

Ward, S. N. and S. E. Barrientos, An inversion for slip distribution and fault shape from geodetic observations of the 1983, Borah Peak, Idaho, earthquake, *J. Geophys. Res., 91,* 4909–4919, 1986.

Ward, S. N. , Pacific-North American plate motion: new results from Very Long Baseline Interferometry, *J. Geophys. Res., 95,* 21,965–21,981, 1990.

Ward, S. N. , A multidisciplinary approach to seismic hazard in southern california, *Bull. Seis. Soc. Am., 84,* 1293–1309, 1994.

Weldon, R. J. and K. E. Sieh, Holocene rate of slip and tentative recurrence interval for large earthquakes on the San Andreas fault Cajon Pass, southern California, *Geol. Soc. Am. Bull., 96,* 793–812, 1985.

Wesnouski, S. G. , Earthquakes, Quaternary faults, and seismic hazard in California, *J. Geophys. Res., 91,* 12,587–12,631, 1986.

Yang, M. and M. Toksöz, Time-dependent deformation and stress relaxation after strike-slip earthquakes, *J. Geophys. Res., 86,* 2889–2901, 1981.

Appendix A

Multiday GPS orbit determination with the GLOBK Kalman filter

A.1 Introduction

It is a well know that the relative error of interstation distance determinations is proportional to the relative error of the satellite ephemerides. Therefore, a prerequisite for precisions of better than 10 part per billion using the GPS is a knowledge of the satellite orbital position at the decimeter level over the duration of the experiment. Since the error in the broadcast ephemeris can reach the ten meter level [e.g., *King et al,* 1985], it is necessary to estimate orbital parameters along with the other parameters of interest.

Determination of orbital parameters is complicated by unpredictable fluctuations in the satellite accelerations. To date, several strategies have been employed for parameter estimation in the presence of such accelerations. The use of "short-arcs" provides a convenient means of dealing with the effects of random fluctuations by

absorbing long-period orbital perturbations into the estimates of the initial state [e.g., *King et al,* 1985]. This is the approach commonly employed for single session GAMIT analyses. However, *Lichten and Border* [1987] have demonstrated significant benefits of multiday arc solutions. By allowing for constant corrections to nominal orbital parameters, the estimation of single arcs of up to one week in duration resulted in improvements in the precision and accuracy of baseline estimates. This improvement is attributed to a more accurate determination of the orbital period and position of the orbital nodes with observations over multiple revolutions. Multiday arcs are particularly useful when global tracking data are scarce. The GLOBK Kalman filter allows us to exploit this added strength by "globalizing" the orbits used in single session GAMIT analyses.

Lichten and Bertiger [1989], using the pseudo-epoch state formalism of *Bierman* [1977], have demonstrated the utility of stochastic models for the satellite force parameters in generating arcs longer than a week. One difficulty here is in obtaining expressions which correctly account for correlations among the satellite states over large batch times. In this appendix, we derive expressions for the state transitions for satellite pseudo-states appropriate for large batch times and discuss their relationship to those equations implemented in the GLOBK Kalman filter.

Typical GPS data analyses using the GAMIT/GLOBK software proceed as follows. First one generates reference orbits in the form of tabular ephemerides by integrating the equations of motion using nominal initial conditions and force parameters. These ephemerides contain for each satellite the inertial positions and velocities of the satellites as well as the partial derivatives of these states with respect to the initial conditions and force parameters. GAMIT is then used to obtain a sequence of parameter estimates, each estimate based on a weighted least-squares analysis of independently batched, doubly differenced GPS carrier phase observations. For the next stage of processing, this sequence of parameter estimates is input to GLOBK for

a final simultaneous adjustment of all experiment specific and session specific parameters. Within GLOBK, a random walk stochastic model can be used to kinematically constrain the successive constant correction orbital parameter estimates from the first stage of processing with the independent short arc and constant correction multiday arc solutions forming the end members of the range of possible solution types.

We base the following analysis on the hypothesis that observed variations in the estimates for initial orbital state parameters can be accounted for by long-term variations in the force parameters.

A.2 The pseudo-state transition equations

Recursive least squares for discrete-time, deterministic models can be traced to Gauss (circa 1800) who invented the method to help astronomers locate the asteroid Ceres [*Gelb,* 1974]. But it was not until *Kalman* [1960] that recursive least squares was combined with the idea of state-space model representation to solve stochastic problems.

Kalman's work assumes that a linear dynamic system can be described by the vector differential equation

$$\dot{m}(t) = F(t)\, m(t) + G(t)\, w(t), \qquad w(t) \sim N(0, Q(t)) \tag{A.1}$$

and the observation equation

$$d(t) = A(t)\, m(t) + v(t), \qquad v(t) \sim N(0, R(t)). \tag{A.2}$$

$m(t)$ is the n-vector model state, and $d(t)$ is a p-vector denoting observable data output from the system. $v(t)$ are the normally distributed, random observation errors of known covariance $R(t)$ and zero mean. $w(t)$ is an m-vector ($\mathrm{m} \leq \mathrm{n}$) of independent, normally distributed, zero mean forcing functions of known covariance $Q(t)$. It is the

dynamic system, equations (A.1) and (A.2), between these primary random sources and the observer that is used to explain any statistical correlation among realizations of a random process. Finally, A, F, and G are p $\times$ n, n $\times$ n, and n $\times$ m matrices respectively.

We treat initial orbital position and velocity as *pseudo-state* parameters. That is, they are the initial conditions that we would have inferred by assuming zero process noise had we been given the true position of the satellite over some interval of time [*Bierman,* 1977]. There are two main advantages of pseudo-state variables. The first is that the partial derivatives required are just those generated during the integration of the nominal orbit and are thus readily available. The second is that the GAMIT analysis software uses these same variables and as a result can be used to generate a sequence of satellite state estimates to be filtered. To arrive at the final form of the equations it is convenient to start with the general satellite orbit determination problem and then transform the system to pseudo-state form.

A.2.1 Modeling the physical system

The first step toward estimating high-accuracy GPS orbits is the generation of reference ephemerides. These tabular orbits are computed by numerically integrating a set of nominal initial satellite states along with force models representing the Earth's gravitational potential, the point-mass effects of the sun and moon, and nominal values for non-gravitational accelerations [*Ash,* 1972]. The time varying partial derivatives of the satellite state with respect to the initial conditions and non-gravitational force parameters are also computed. The nature of the non-gravitational accelerations are generally not well understood. However major contributions to these accelerations are believed to be a result of solar and thermal radiation pressure, the effects of which are difficult to model owing to fluctuations in the solar flux, solar panel misalignment,

and the shape and optical properties of the GPS satellites [*Fliegel and Gallini,* 1992]. Other effects such as gas emission, Earth and ocean tide effects, and albedo pressure may also be important when generating longer arcs. Consequently, scaling parameters representing departures from nominal acceleration values in the satellite-sun, and Y and Z satellite body axis directions are conveniently modeled as stochastic processes. Note that the satellite-sun and Z-axis directions are not mutually orthogonal.

Expressing the equations of motion as a system of coupled first-order differential equations and linearizing we arrive at the form of equation (A.1). It is convenient to partition the model state $m(t)$ as follows. Random fluctuations in unmodeled satellite accelerations in the satellite-sun, and Y and Z satellite body axis directions will be represented by stochastic processes $p(t)$. Non-stochastic time varying parameters $x(t)$ will represent observable deviations from the nominal satellite position and velocity. Often terms representing constant biases are introduced in order that the stochastic models remain zero mean. Since GLOBK adopts a random walk model to describe the evolution of the orbital parameters it does not require such a bias type parameter.

The random walk process is a relative of the more general first-order Gauss-Markov (FOGM) process model. The FOGM model is representative of a wide variety of random phenomena. Mathematically, the FOGM can be expressed as

$$\dot{p} = -\left(\frac{1}{\tau}\right) p + w \tag{A.3}$$

and

$$f\left[p(t_j) \mid p(t_{j-1}), \ldots, p(t_1)\right] = f\left[p(t_j) \mid p(t_{j-1})\right] \tag{A.4}$$

where f is the probability distribution of the process p, τ is the *correlation time* (i.e. the time required for the process to decay to 1/e its original value), and w is the white noise which drives the process. The process approaches white noise in the limit as τ approaches zero and a random walk in the limit as τ approaches infinity. Experience has demonstrated that for many applications the filter is quite insensitive

to the specific value chosen for τ. The use of a random walk model for the p states to represent the evolution of weighted averages of the orbital parameters is an attempt to capture long term variations in the force and hence the initial conditions estimates.

Partitioning and expanding the linearized system dynamics equation (A.1), we obtain

$$\begin{bmatrix} \dot{x}(t) \\ \dot{p}(t) \end{bmatrix} = \begin{bmatrix} F_x & F_p \\ 0 & 0 \end{bmatrix} \begin{bmatrix} x(t) \\ p(t) \end{bmatrix} + \begin{bmatrix} 0 \\ w(t) \end{bmatrix} \tag{A.5}$$

where

$$F_x = \frac{\partial \dot{x}}{\partial x}, \quad F_p = \frac{\partial \dot{x}}{\partial p}, \tag{A.6}$$

$$w \sim N(0, Q). \tag{A.7}$$

It is easy to show that any general linear system of the form of equation (A.1) has a solution of the form

$$m(t) = \phi(t, t_0)\, m(t_0) + \int_{t_0}^{t} \phi(t, \tau)\, G(\tau)\, w(\tau)\, d\tau, \tag{A.8}$$

where the state transition matrix ϕ is given by

$$\phi(t, \tau) = e^{F(t-\tau)} = \sum_{n=0}^{\infty} \frac{F^n (t-\tau)^n}{n!}, \quad F^0 \equiv I. \tag{A.9}$$

A.2.2 Transformation to discrete-time

From equations (A.5) and (A.8) we see that the subset of equations involving only the x states are

$$x(t) = \phi_x(t, t_0)\, x(t_0) + \phi_p(t, t_0)\, p(t_0) + w_x. \tag{A.10}$$

where

$$\phi_x(t, t_0) = \frac{\partial x}{\partial x_0}$$

$$\phi_p(t,t_0) = \frac{\partial x}{\partial p_0} \tag{A.11}$$

(A.12)

and

$$w_x = \int_{t_0}^{t} \phi_p(t,\tau)\, w(\tau)\, d\tau. \tag{A.13}$$

Since acceleration parameters can be inferred reliably only for the interval over which the satellites are observed, short arc strategies using constant corrections simultaneously estimate the initial satellite state and force parameters as if the "observed" force had been acting without change since the epoch of the initial conditions. The partial derivatives which are generated with the reference orbit are appropriately based on such a constant force model. Therefore, we must rewrite equation (A.10) as

$$x(t) = \phi_x(t,t_0)\, x_0(t) + \phi_p(t,t_0)\, p(t). \tag{A.14}$$

Equation (A.14) serves as our mathematical definition of the $x_0(t)$ pseudo-states. From equation (A.14) we may compute the total expected change in the pseudo-state correction estimates given a change in the stochastic process states. The result is

$$\left.\frac{dx_0}{dp}\right|_{x(t)} = -\phi_x^{-1}(t,t_0)\, \phi_p(t,t_0). \tag{A.15}$$

Figure (A-1) shows the evolution of the elements of the first row of $\left.\frac{dx_0}{dp}\right|_{x(t)}$ for an eight day reference orbit (21-29 Jan 1991).

Integrating (A.15) over time and imposing the random walk model we arrive at a discrete difference equation for the pseudo-states

$$x_{0|j+1} = x_{0|j} - \int_{t_j}^{t_{j+1}} \phi_x^{-1}(\tau,t_0)\, \phi_p(\tau,t_0)\, w(\tau)\, d\tau \tag{A.16}$$

where we have introduced the abbreviated notation $x_{0|j} = x_0|_{x(t_j)}$. The pseudo-state transition equation is thus

$$\begin{bmatrix} x_0 \\ p \end{bmatrix}_{j+1} = \begin{bmatrix} x_0 \\ p \end{bmatrix}_j + \begin{bmatrix} w_{x_0} \\ w_p \end{bmatrix}_j \tag{A.17}$$

where

$$w_{x_0,j} = -\int_{t_j}^{t_{j+1}} \phi_x^{-1}(\tau, t_0)\, \phi_p(\tau, t_0)\, w(\tau)\, d\tau, \tag{A.18}$$

and

$$w_{p,j} = \int_{t_j}^{t_{j+1}} w(\tau)\, d\tau. \tag{A.19}$$

A.2.3 Piece-wise constant parameterization

To impose the restriction that the evolution of the p states be piecewise constant, we need only replace the continuous white noise process $w(t)$ with the discrete random sequence

$$w_T(t) = w(t)\, \delta(t - T_i), \qquad i = 1, ..., N \tag{A.20}$$

where δ is the Dirac delta function and the T_i are chosen to specify the discretization.

To incorporate the batched, weighted least-squares estimates as input to the filter, we need equation (A.2) in discrete-time form. For the jth batch of GPS data, the least-squares pseudo-state estimates d_j are related to the model parameters m_j by

$$d_j = A_j m_j + v_j, \qquad v_j \sim N(0, R_j), \tag{A.21}$$

where R_j is the error covariance of the estimates for the jth batch. The Kalman filter algorithm allows us to solve equations (A.21), and (A.17) recursively. A complete description of the filter algorithm and its implementation for geodetic data analysis is given by *Herring* [1990].

A.3 Conclusions

In filtering batched least-squares estimates, we are making the assumption that the process noise contribution to the state uncertainty can be ignored over time inter-

vals much shorter than the time constants of the linear system model [e.g., *Swift,* 1987]. Variations within the chosen interval are effectively averaged out. As is often exploited for geophysical inverse problems, the degree to which a parameter estimate is contaminated by noise is inversely proportional to the extent of this averaging. Hence, there exists a trade-off between the ability to reproduce the observed data and the variance of the estimates of the model averages [e.g., *Rodi,* 1989]. The constant correction orbit model is an example. The optimal batch interval has yet to be explored.

This state-transition model is significantly different from that of *Bierman* [1977]. Using the *Bierman* formalism, other authors have reported that the noise contribution due to the discretization in forming the discrete difference equation is negligible for sufficiently small batch times [e.g., *Swift,* 1987]. We too have neglected this noise contribution with the assumption that the parameters evolve as piecewise constant. We believe that our model, though not fully tested, allows us much freedom in the choice of batch interval. However, due to the growth of the derivative of initial state with respect to the force parameters, the total duration of the orbits is limited.

The covariance matrix is the principal mechanism for propagation of information within the filter. By building some of the orbital dynamics into the covariance matrix during the state transition, we force the the individual estimates of the orbital states to be more dynamically consistent. However the relative importance of information between successive pseudo-state estimates decays with distance from the pseudo-state epoch. Furthermore, we must beware numerical round off. Also, as the pseudo-states begin to deviate from the epoch of the reference orbits, it becomes less and less clear that the partial derivatives used continue to approximate the true partial derivative and we run the risk of biasing the estimates. We conclude then, that there is effectively a maximum duration of useful stochastic multiday orbits derived in this fashion.

In GLOBK one is allowed to specify the noise processes driving each element of the pseudo-state independently; the correlations among the processes driving the states are assumed negligible. While we lose some of the kinematic information in neglecting these correlations, we gain computational efficiency. Since the effects of pseudo-state noise processes are magnified away from the pseudo-state epoch, when using GLOBK to estimate stochastic multiday orbits we must balance the strength we could obtain from the estimates representing sessions near the pseudo-state epoch against the danger of underestimating the noise contribution to the error covariance in the transition between sessions distant from the pseudo-state epoch. Independent short-arcs can be handled by specifying large process noise on all states but are best handled if each orbit arc is allowed its own pseudo-state epoch centered on its respective batch interval. One of the most important features of the GLOBK software, however, is the relative ease with which constant correction multiday arcs are achieved by simply setting the level of process noise to zero.

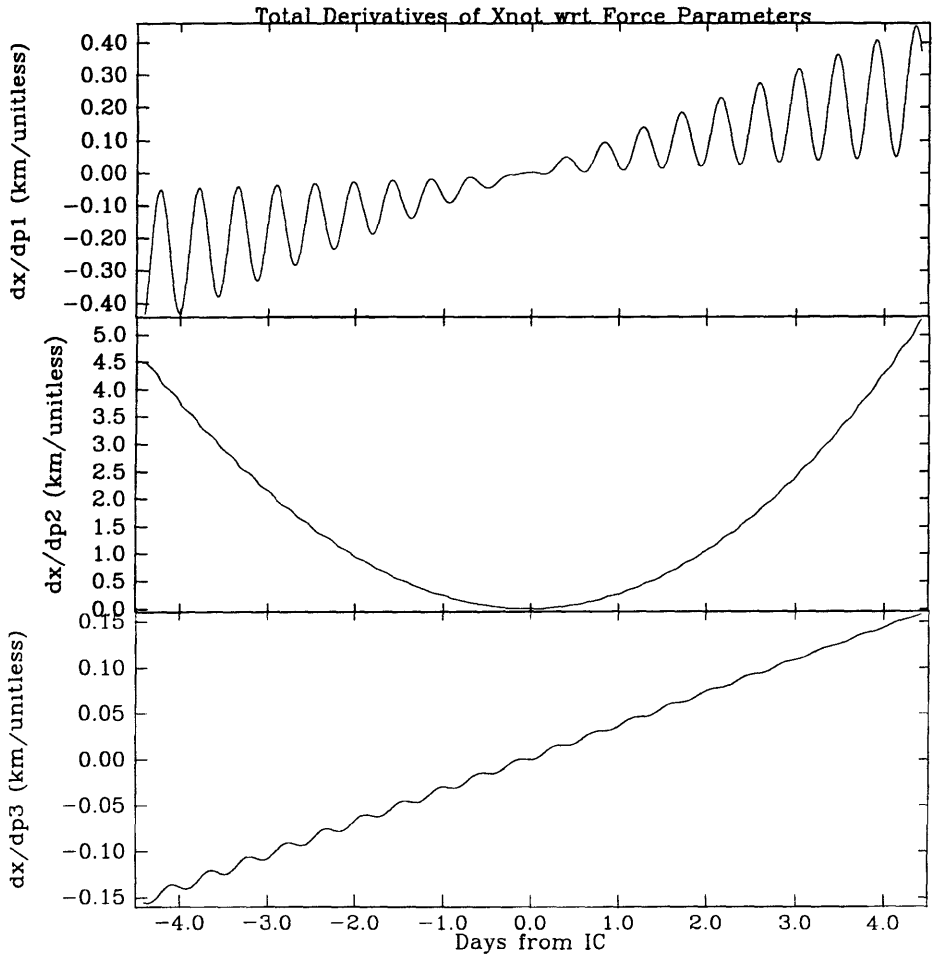

Figure A-1: First row of dx_0/dp generated using partials in reference ephemerides for PRN 2. p1 = direct solar radiation pressure, p2 = y-bias, p3 = z-bias.

Appendix B

STRC data analyses

In this appendix, we outline our treatment of the individual STRC GPS experiments. We follow the two-step processing procedure outlined by *Feigl et al.,* [1993]. We here detail step one, the outcome of which is a set of experiment solutions each consisting of site coordinate and corresponding variance-covariance estimates representative of each particular experiment. Before forming the experiment solutions, we assess the precision of each experiment from the scatter of the session-to-session baseline components estimates.

The 1988 Imperial Valley experiment.

During February and March of 1988, the STRC consortium conducted an experiment involving 13 stations in the Imperial Valley (Table 2.1 and Table 2.2). The experiment included nine sessions each lasting seven hours. TI4100 receivers and antennae were deployed. Only seven satellites were available throughout the observation sessions. Because high quality global tracking data are scarce for this time, we opted simply to use broadcast ephemerides. That is, we integrated sets of initial conditions which were

derived from the broadcast ephemeris to produce tabular ephemerides for each session of observation. These orbits were then constrained at the level of 0.5 ppm. Because of the size of the network, we believe the relative error in the baseline estimates that we incur due to satellite errors ($\sim$ 8 mm) is inappreciable relative to the total level of uncertainty given the limited availability of satellites.

We combined and edited all carrier phase data collected in each session using the GAMIT software. In our first analysis, real valued parameters representing integer phase biases were estimated with no attempt to resolve their integer values. The resulting single session bias-free solutions were then combined in a multi-session analysis using the GLOBK Kalman filter. Using GLOBK, we estimated a single set of site coordinates representative of the experiment as a whole while constraining adjustments to satellite parameters (representing the broadcast ephemeris) at the level of 0.5 parts per million in single session short arc mode (see Appendix A).

We then used GLOBK to investigate the precision of the experiment. Figure B-1 shows the root-weighted-mean-square session-to-session scatter of this experiment as a function of baseline length. The significance of statistical inferences drawn from the scatter is limited due the fact that only six of the observed baselines were actually repeated. Nevertheless, we observe the means of the scatters in the the baseline components of less than 10 mm. Baseline dependence is small but poorly resolved given the small number of samples and limited length range. The mean normalized rms (Figure B-2) suggests that short-term precision is actually better than predicted by the formal error estimates. It is interesting that the length nrms is higher than that for east or north. This is a consequence of using the orbits to define the reference frame and the fact that length is better determined than orientation.

The data were combined using 0.5 ppm orbit constraints into an STRC88 campaign solution. In this combination, a single set of site coordinates was estimated

under weak *a priori* constraints.

The 1989 GEOMEX experiment.

The 1989 experiment dubbed "GEOMEX89" was conducted by the Jet Propulsion Laboratory using TI4100 receivers and antennae. The portion of the experiment that we are concerned with consists of five nine-hour sessions during which six sites were simultaneously observed (Table 2.1 and Table 2.2). Four of these sites are located in northern Mexico. The remaining two are in southern California. We also combined data from a small set of tracking stations (RICM, MOJF, KOK0) directly with the regional data.

For this experiment, we integrated one set of orbital initial conditions to produce tabular ephemerides representative of the entire five day experiment. This reduces the number of independent parameters to be estimated from the experiment by 36 (4 sessions, 9 elements per session). Using the GAMIT software, the data were edited and single session solutions were formed with no attempt to resolve integer phase biases. Then, with the coordinates of the global trackers constrained, we employed a constant correction multiday arc strategy (Appendix A) using GLOBK to analyze the session-to-session scatter.

Session-to-session repeatability statistics as functions of baseline length are shown in Figures B-3 and B-4. While the north baseline component estimates have scatter of about 6.0 mm with virtually no baseline dependence, scatter in the east reflects our failure to resolve integer phase biases. While there are a couple of baselines with large root-weighted-mean-square in the vertical, the normalized root-mean-square deviation indicates that the level of uncertainty associated with these parameters is large.

1990 Salton Trough–Riverside County.

In the winter of 1990, the largest of the STRC experiments was performed. A total of 98 stations were established; most occupied during one to three sessions (Tables 2.1 and 2.2). Up to 23 dual-frequency receivers (Trimble SLD, and SST, and TI4100) were fielded during each of the 18 six hour sessions of data collection. Four stations (BLAC, OCOT, PIN1, and SIO1) were each occupied at least 12 times during the experiments.

Unfortunately, for a large number of sites, the log sheets recorded during this experiment do not clearly indicate the whether Trimble SST or SLD equipment was used. Furthermore, it is often not clear which type of antenna height measurement was made. Therefore, for many of the stations, we had to take our best guess as to which type of equipment and measurement scheme were used.

Good quality global tracking data during this period are severely limited. Encouraged by the results of *Lichten and Border* [1987], we attempt to compensate for this loss by using long (5-7 day) constant correction multiday orbital arcs (see Appendix A).

For this experiment, we integrated three sets of orbital initial conditions to produce three non-overlapping tabular ephemerides covering the entire 18 day experiment, significantly reducing the number of independent parameters to be estimated from the total data set. We used the GAMIT software, to edited the data and form single session bias-fixed solutions. We then used GLOBK to analyze the session-to-session scatter with the coordinates of sites PIN1 and SIO1 constrained to their well known "fiducial" values.

The root-weighted-mean-square session-to-session scatter is shown in Figure B-5. Despite the use of a multiday satellite arc strategy, our results clearly suffer from orbit

related baseline dependent errors. However, in Figure B-6 we see from the normalized root-mean-square deviation in the baseline components that the formal uncertainties in the estimates sufficiently reflect the weakness of the determined satellite orbits. The extremely poor repeatability in the vertical component of the baseline estimates could be a result of our lack of knowledge of the antenna types and measurement schemes used, however, the formal uncertainties appear to be large enough to mask these potential blunders for most baselines.

1991 Salton Trough–Riverside County.

During March and April of 1991, much of the Salton Trough–Riverside County network was re-occupied. Up to 23 Trimble SST receivers and antennae were fielded during each of the 12 six hour sessions. A total of 51 stations were observed (Tables 2.1 and 2.2). Adequate amounts of good global tracking data (HOBA, KOKT, MOJM, RICM, TOWN, TSUK, WELL, WETM, WSFM, YKN1) were available during this time and were combined directly with the local measurements.

The data were processed using a set of non-overlapping three-day constant correction arcs (see Appendix A). Using the GAMIT software, the data were edited and single session bias-fixed solutions were formed. Then, with the coordinates of the global trackers constrained, we used GLOBK to analyze the session-to-session scatter in the baseline component estimates.

Figure B-7 shows the root-weighted-mean-square session-to-session scatter for this experiment. Precision in both north and east baseline components is good with little baseline length dependence. The noticeable increase in the normalized root-mean-square deviation in the baseline components estimates (Figure B-8) relative to that from earlier experiments reflects a drop in formal uncertainties from the increased

number of satellites and global tracking stations used in the analysis. The large values for the root-weighted-mean-square scatter (> 30 mm) and in the normalized root-mean-square deviation (> 2) in the vertical component all involve site OAKD.

1992 Joshua Tree.

In the days preceding the 23 April 1992 Joshua Tree earthquake, three STRC sites were observed as part of the Inter County surveys [*K. Hudnut, personal communication,* 1992]. Then, in the week following the earthquake, these two sites and an additional seven STRC sites were re-observed (Tables 2.1 and 2.2). Unlike the other campaigns, these measurements were recorded only once every two minutes. Ashtech equipment was used. There is an abundance of of high quality global tracking data for this time period. These data were combined directly with that from the local sites.

Because available tracking data (ARON, GOLD, FAIR, KOKB, KOSG, MADR, MATE, MCMU, NALL, ONS0, PENT, USUD, WETR, YAR1, YKN1) are well distributed and of high quality we adopted a single session short arc strategy (Appendix A). Using the GAMIT software, the data were edited and single session bias-fixed solutions were formed. GLOBK was then used to assess the session-to-session scatter in the pre- and post-earthquake observations separately. During both of these GLOBK runs, the coordinates of the global trackers were tightly constrained.

Figure B-9 shows the root-weighted-mean-square session-to-session scatter for the pre-earthquake sessions. Precision in both north and east baseline components appears to be good with little baseline length dependence though the limited span of baseline lengths precludes any degree of confidence. The normalized root-mean-square deviation of the baseline component estimates (Figure B-10) is quite small consider-

ing the strength of the GPS constellation and global tracking network at this time. Figure B-11 shows the weighted root-mean-square session-to-session scatter for the post-earthquake sessions. Again precision in both north and east baseline components is good with little baseline length dependence. The normalized root-mean-square deviation of the baseline component estimates (Figure B-12) reflects that the precision of the measurements is adequately represented by the formal uncertainties.

Separate pre- and post-earthquake data combinations were formed for use in the multi-experiment analysis for site velocities. For each of these solutions, a single set of site coordinates were estimated under weak constraints on all *a priori* site and satellite parameters.

1993 Salton Trough–Riverside County.

During March of 1993, the STRC consortium re-occupied 54 of the sites in the network. Up to 23 Trimble SST and SSE receivers with Trimble SST antennae were deployed during each of the 12 eight hour observation sessions (Tables 2.1 and 2.2). An overabundance of high quality, well distributed global tracking data is available for this time. Rather than combine the data directly with our local observations, these two sets of data were processed separately with GAMIT and then combined using GLOBK. We used solutions from the tracking data provided by the Scripps Orbit and Permanent Array Center (SOPAC).

Two problematic events occured during this experiment worth mentioning. First, the Department of Defense was testing Anti-Spoofing. This resulted in receivers switching from code correlating mode to codeless mode during some of the observation sessions. This switch appears to have been problematic for Rogue receivers with the effect being degraded estimates of vertical coordinates. This problem was mitigated

by processing the global tracking and regional data separately. Second, we observed ionospheric fluctuations at the level of half a cycle which affected our ability to resolve integer biases. To circumvent this problem, we applied ionospheric constraints at the level of 100 ppm. We succeeded in resolving most integer phase biases. We processed our local data using SOPAC orbits constrained to 50 parts per billion under a single session short arc strategy (Appendix A).

Figure B-13 shows the weighted root-mean-square session-to-session scatter for this experiment. Despite the above mentioned problems, precision in both north and east baseline components is good with little baseline length dependence. The normalized root-mean-square deviation in the baseline components estimates (Figure B-14) indicates that the formal uncertainties are consistent with the observed scatter. Particularly large normalized root-mean-square values reflect very small (< 2 mm) baseline estimate uncertainties.

1995 Salton Trough–Riverside County.

During February of 1995, the STRC consortium again fielded up to 23 Trimble SSE and SST receivers in southern California and northern Mexico, occupying 58 stations of the STRC network over a 12 day period (Tables 2.1 and 2.2). By this time, both the the GPS satellite constellation and the IGS tracking network were fully operational. Consequently, there is an abundance of good global tracking data for this time.

We processed our local data using SOPAC orbits constrained to 50 parts per billion under a single session short arc strategy (Appendix A). We combined data from two regional tracking stations (PIE1 and DS10) directly with that from the local survey. We did not otherwise include SOPAC solutions for IGS trackers in our analyses of STRC95.

Figure B-15 shows the weighted root-mean-square session-to-session scatter for this experiment. Precision in both north and east baseline components is very good. However, the normalized root-mean-square deviation in the baseline components estimates (Figure B-16), indicate that the formal uncertainties slightly underestimate the observed scatter.

Reflections.

In retrospect, there are several aspects of these analyses that one might want to test and/or change during re-processing of the data. For example, the baseline dependence apparent in the repeatability plots for STRC90 reflects the absence of good fiducial data. We have attempted to combine tracking data directly with the local data, and we have attempted to process it separately. Unfortunately, both strategies have failed to produce useful results. However, we have not attempted to process the tracking data in batches according to receiver/antenna type. This approach has led to success in processing data collected in 1990 during different campaigns [*R. W. King, Pers. Comm.,* 1995]. Similarly, a large part of the scatter that we observe for this experiment may be a result of our having mixed data from several different antenna types, for some of which we do not have accurate phase center variation models. In general, we had the best results (least problems) with those experiments in which we did not attempt to mix equipment types (STRC88, STRC91, JTRE92, STRC95, GEOMEX 1989 being an exception).

Our failure to resolve integer ambiguities for the GEOMEX observations may be related to ionospheric activity. We did not experiment with ionospheric constraints and/or site and satellite constraints in an attempt to resolve these biases.

There is also an abundance of additional geodetic data relevant to our studies

that have not yet been included in our analyses. These include additional GPS observations collected during 1991 and 1993 in the Imperial Valley by the National Geodetic Survey, VLBI observations [e.g., *Feigl et al.,* 1993], and EDM observations [e.g., *Dong,* 1993], as well as observations from the PGGA, and specific sites at various times such as the observations to the new site LORW (including the tie to YUMA). A tie between PGGA site MONP and STRC site MONU would be useful. An analysis of the possible displacements at site ENDA could also be important. We did not add SOPAC solutions for IGS trackers to our analyses of STRC95. While we have achieved "satisfactory" results without including this data, we could very well could have achieved even better results had it been added. This could be important as new measurements of comparable strength are collected.

Given the large variety of circumstances associated with these sets of data, they might prove useful for studying the utilities of the various processing strategies. For example, one might want to re-process each of the experiments using a set of "standard" strategies in an attempt to identify the strengths and weaknesses of the approaches under different circumstances.

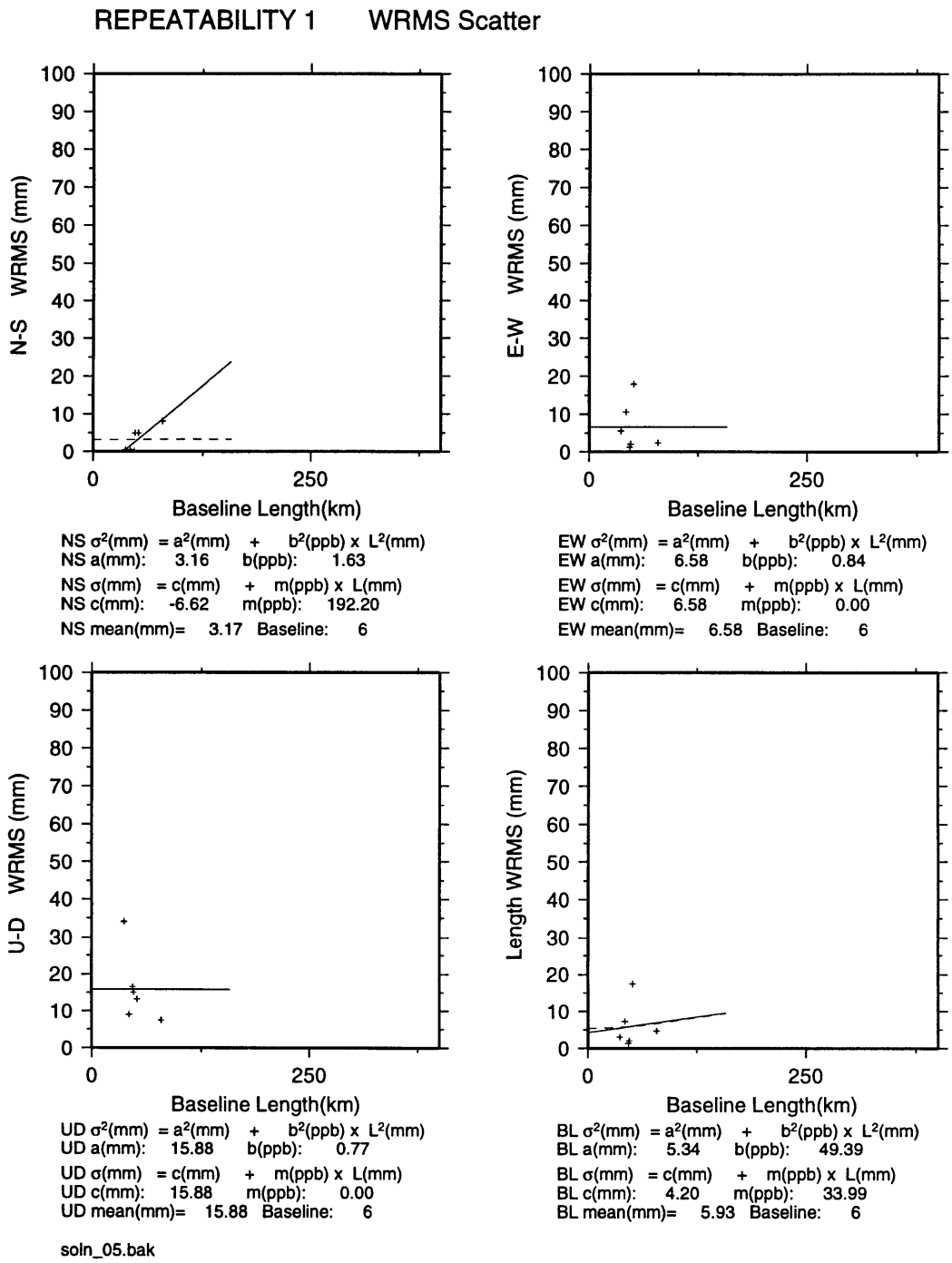

Figure B-1: STRC88 weighted root-mean-square scatter and error models for the session-to-session baseline component (North, East, Up) and baseline length estimates.

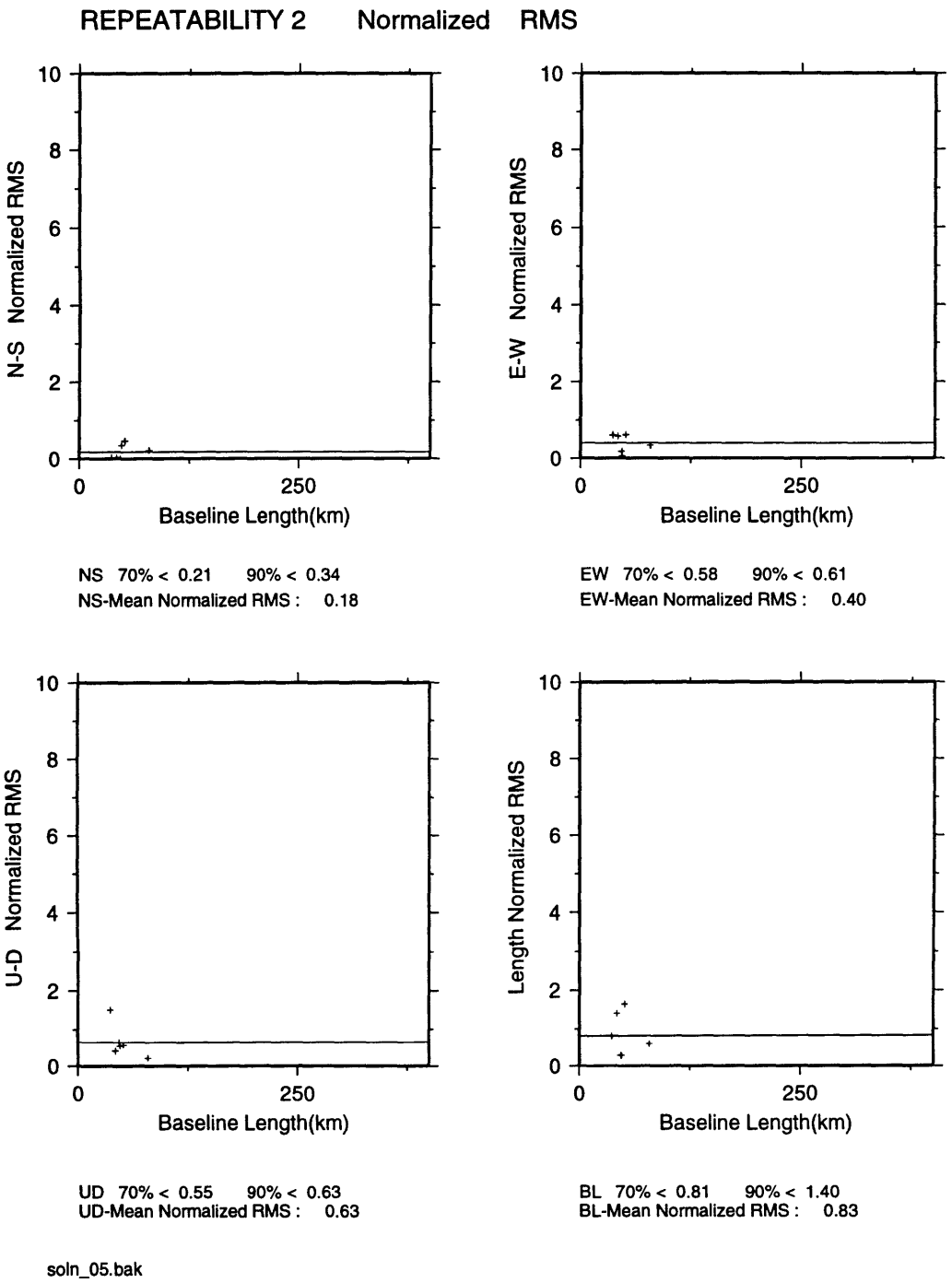

Figure B-2: STRC88 normalized root-mean-square scatter for the session-to-session baseline component (North, East, Up) estimates. Horizontal line represents the mean.

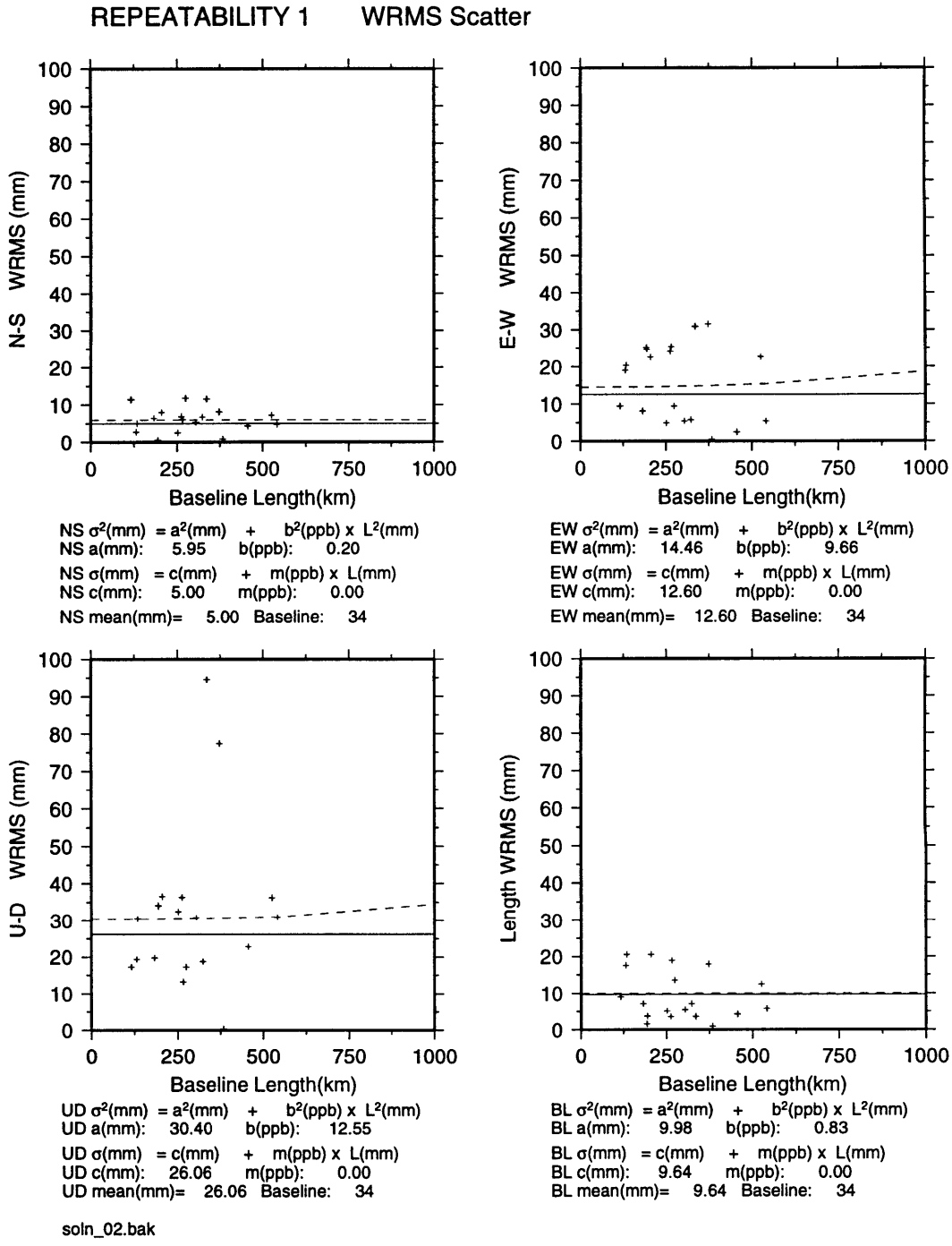

Figure B-3: GEOMEX89 weighted root-mean-square scatter and error models for the session-to-session baseline component (North, East, Up) and baseline length estimates.

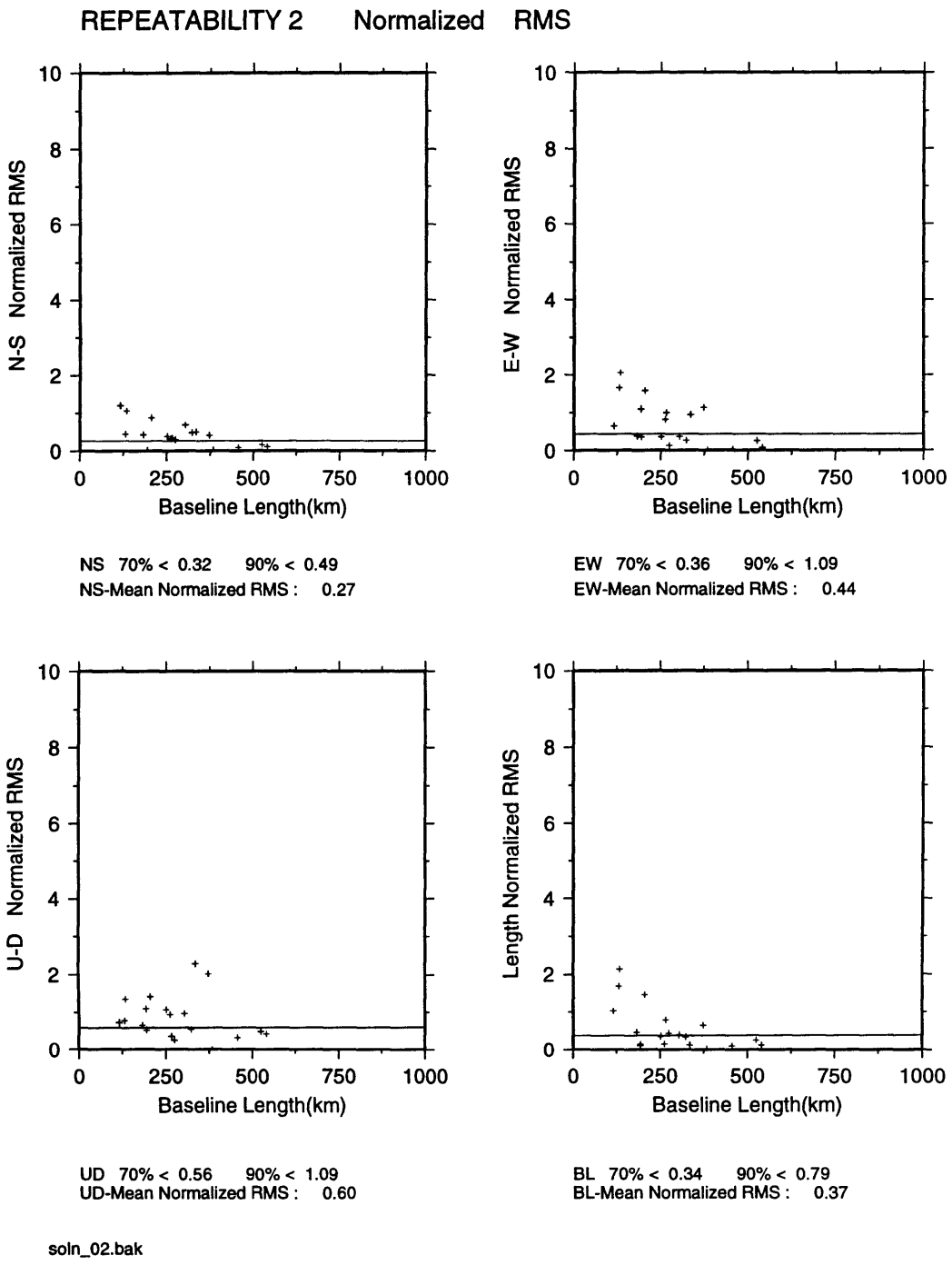

Figure B-4: GEOMEX89 normalized root-mean-square scatter for the session-to-session baseline component (North, East, Up) estimates. Horizontal line represents the mean.

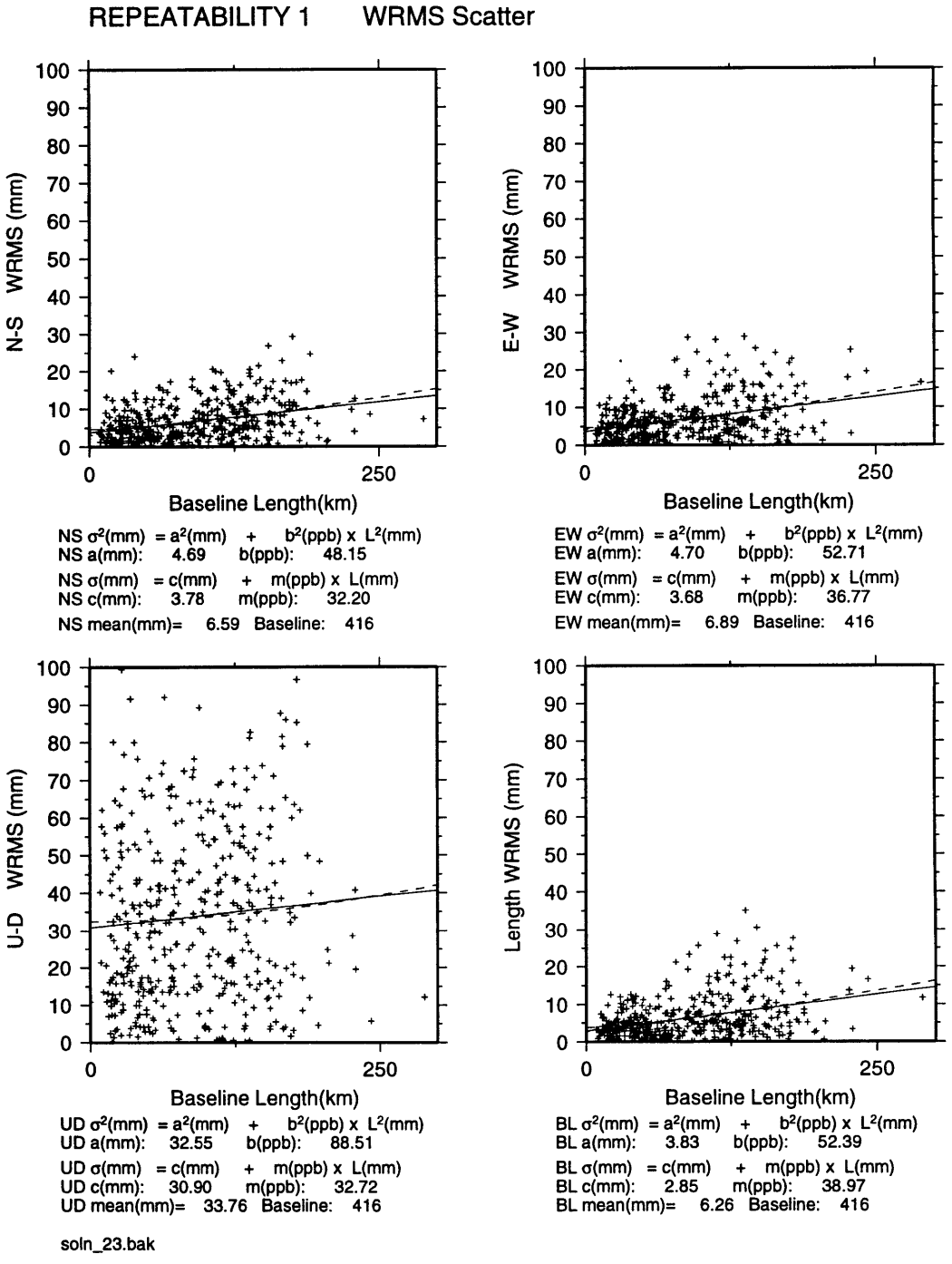

Figure B-5: STRC90 weighted root-mean-square scatter and error models for the session-to-session baseline component (North, East, Up) and baseline length estimates.

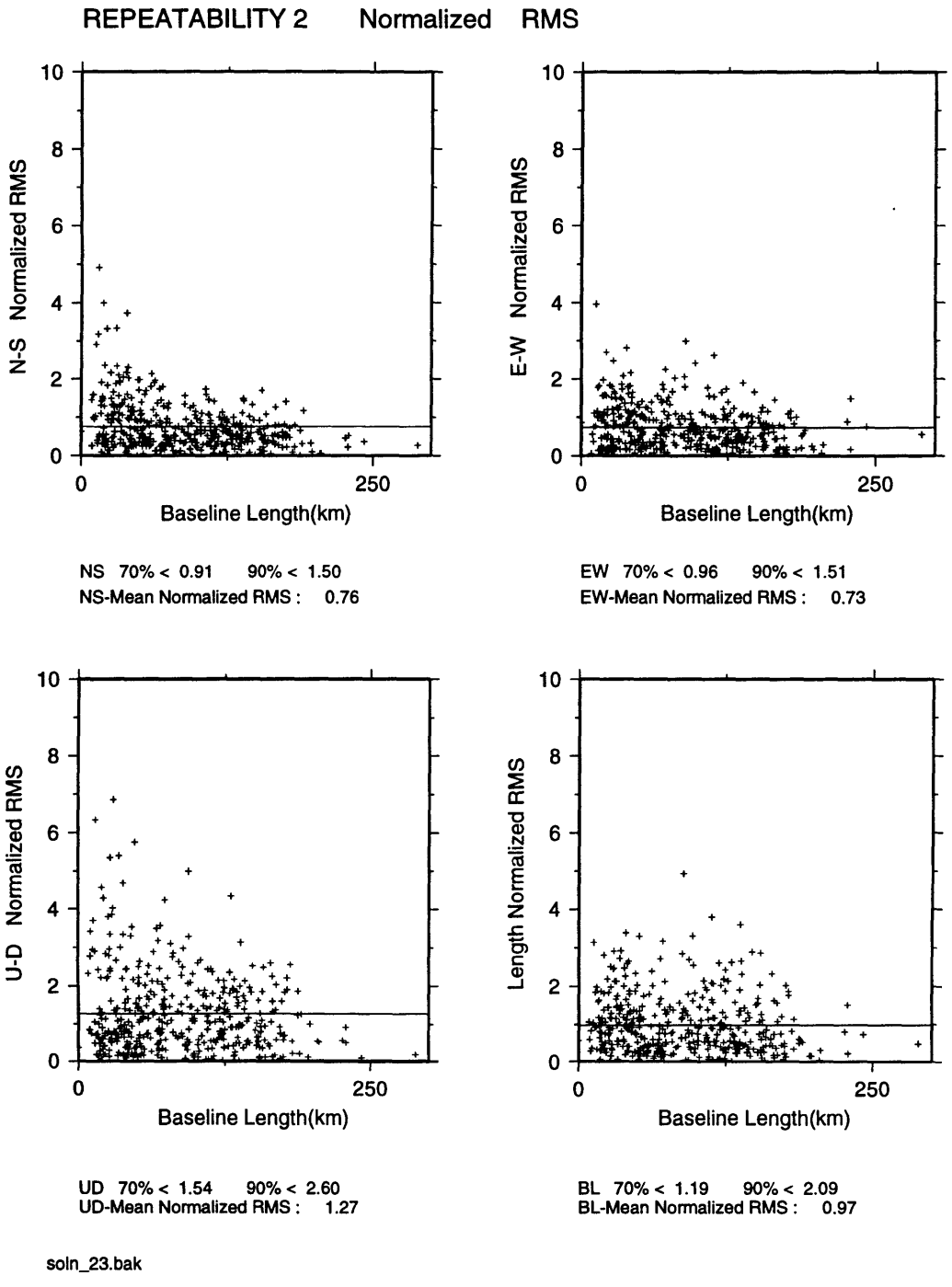

Figure B-6: STRC90 normalized root-mean-square scatter for the session-to-session baseline component (North, East, Up) estimates. Horizontal line represents the mean.

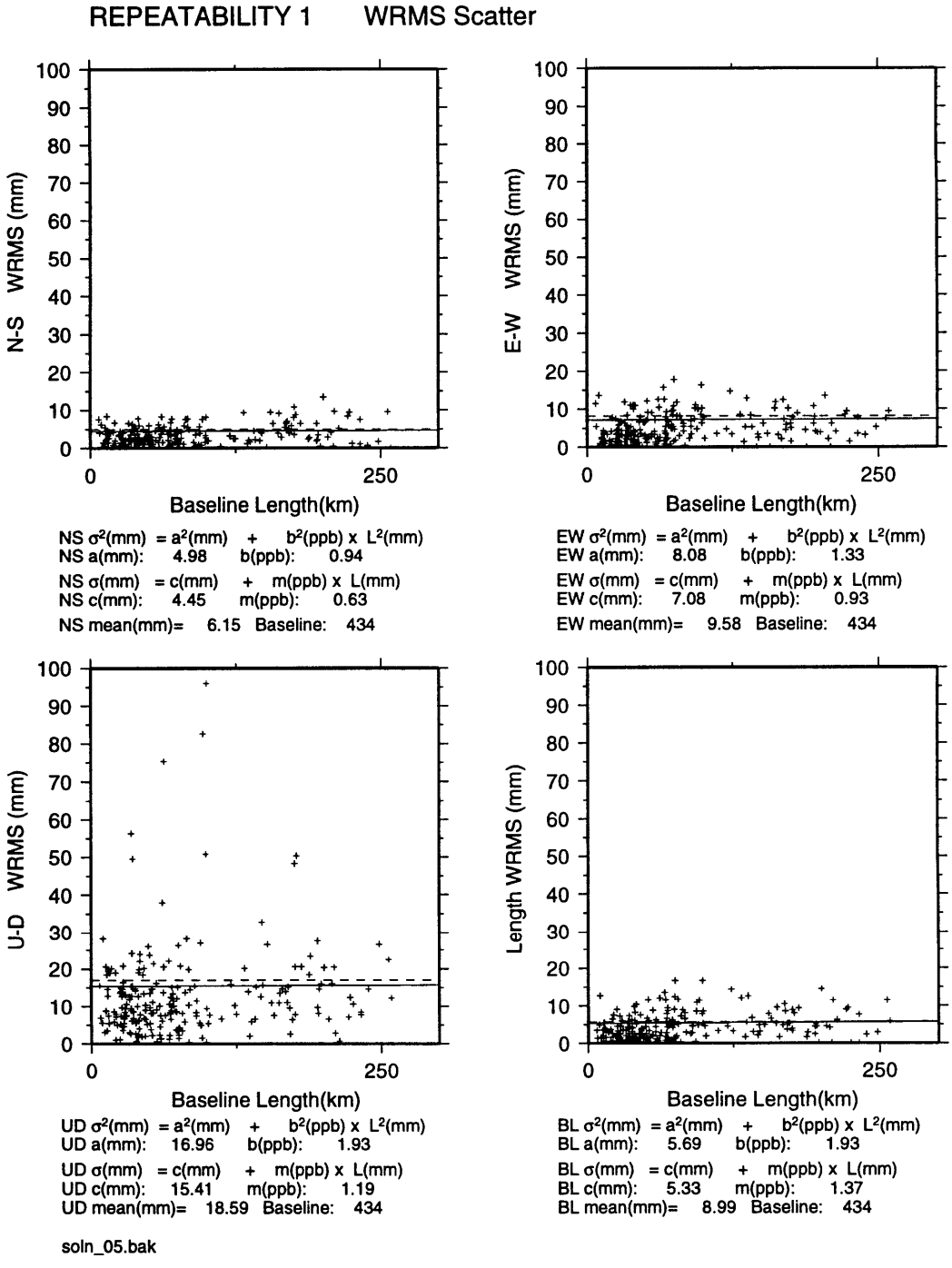

Figure B-7: STRC91 weighted root-mean-square scatter and error models for the session-to-session baseline component (North, East, Up) and baseline length estimates.

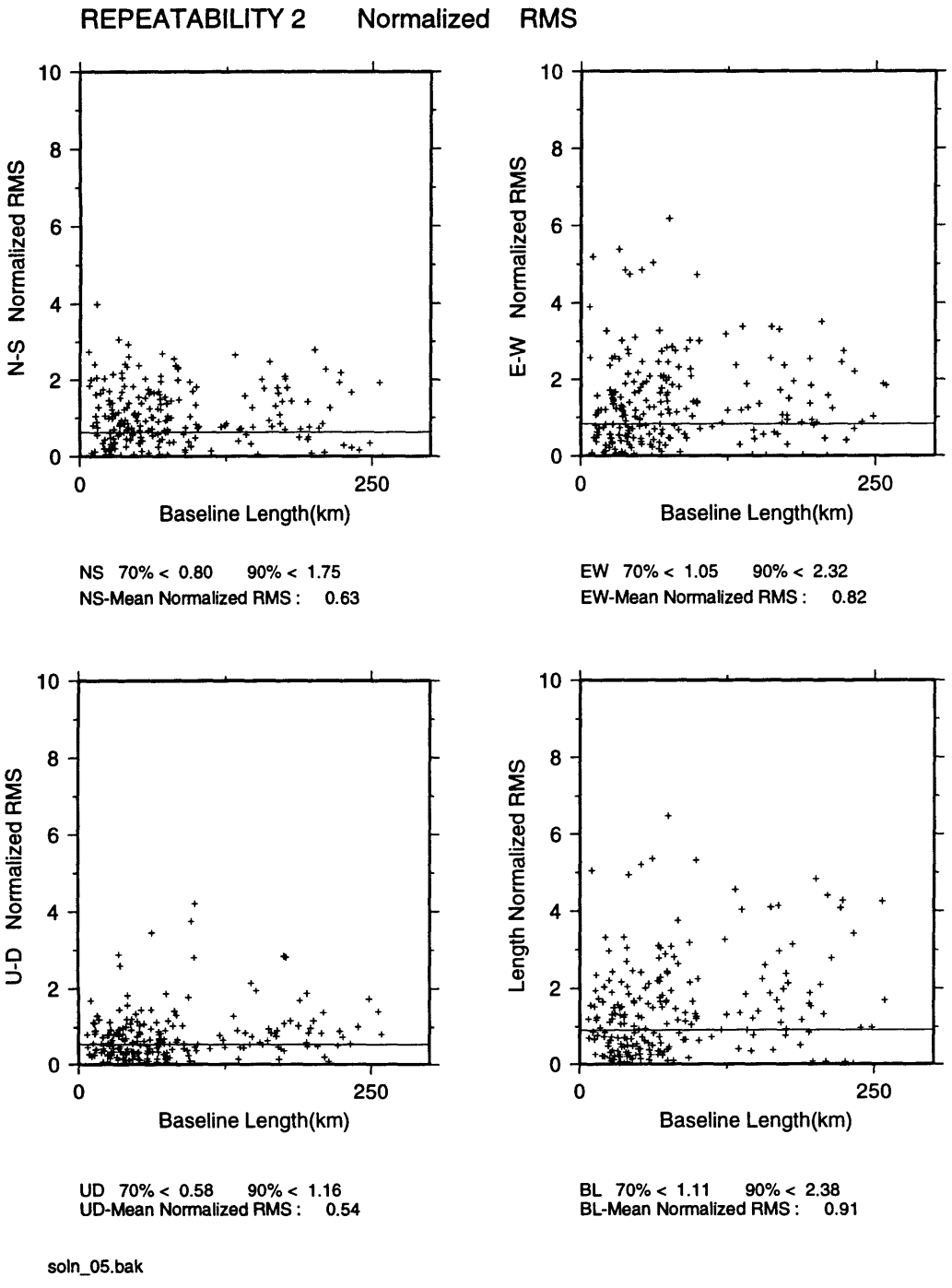

Figure B-8: STRC91 normalized root-mean-square scatter for the session-to-session baseline component (North, East, Up) estimates. Horizontal line represents the mean.

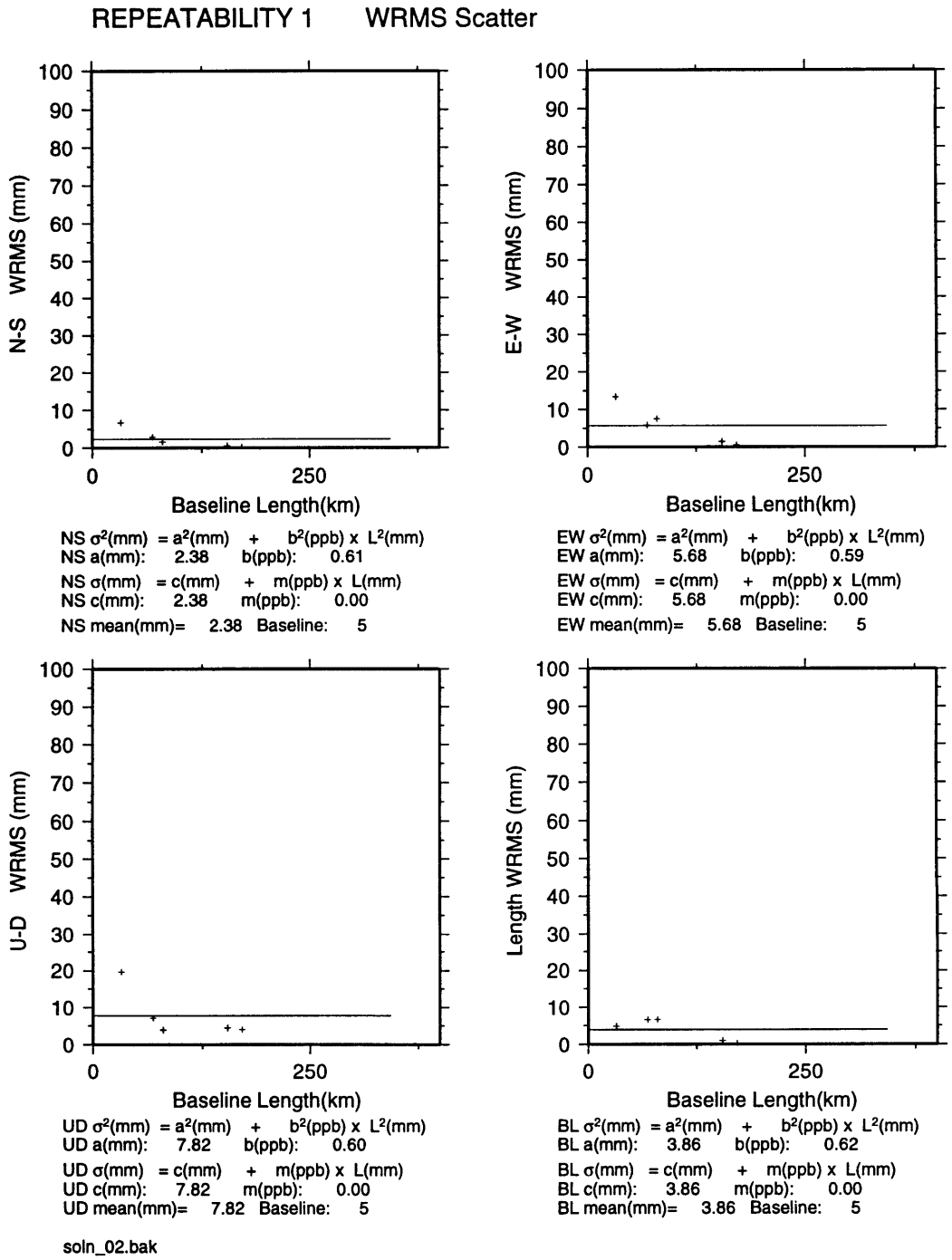

Figure B-9: JTRE92 Pre-earthquake weighted root-mean-square scatter and error models for the session-to-session baseline component (North, East, Up) and baseline length estimates.

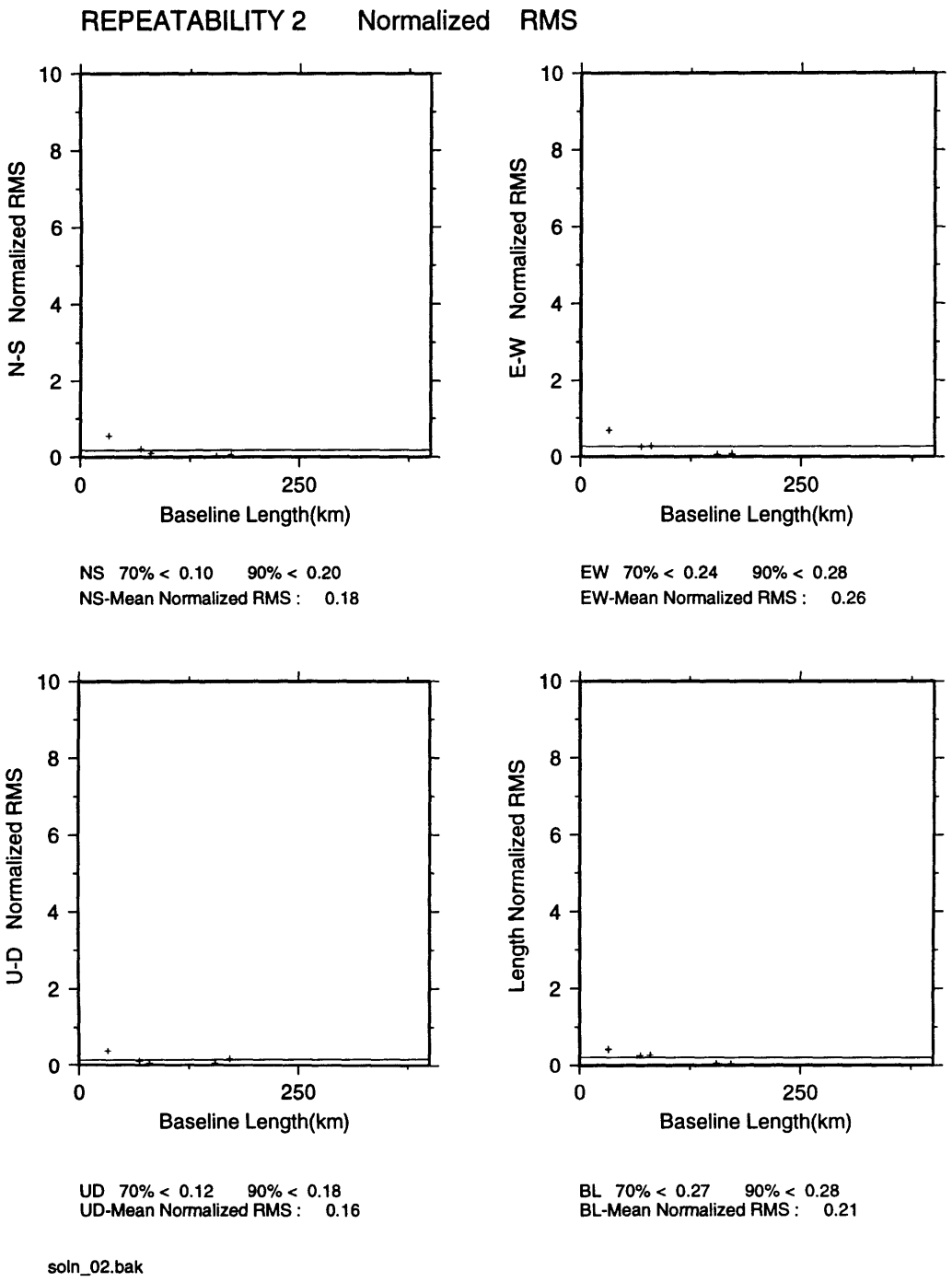

Figure B-10: JTRE92 Pre-earthquake normalized root-mean-square scatter for the session-to-session baseline component (North, East, Up) estimates. Horizontal line represents the mean.

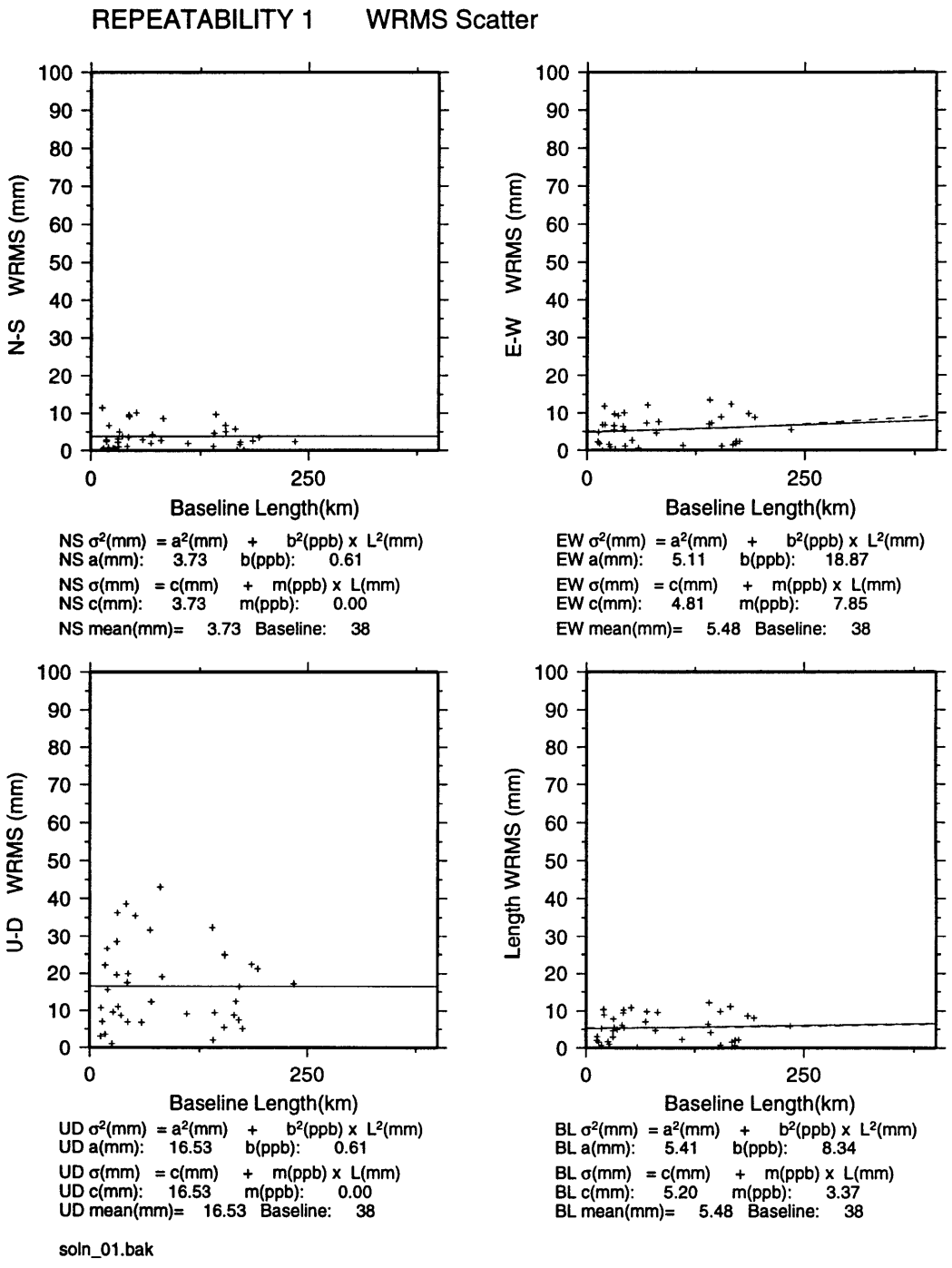

Figure B-11: JTRE92 Post-earthquake weighted root-mean-square scatter and error models for the session-to-session baseline component (North, East, Up) and baseline length estimates.

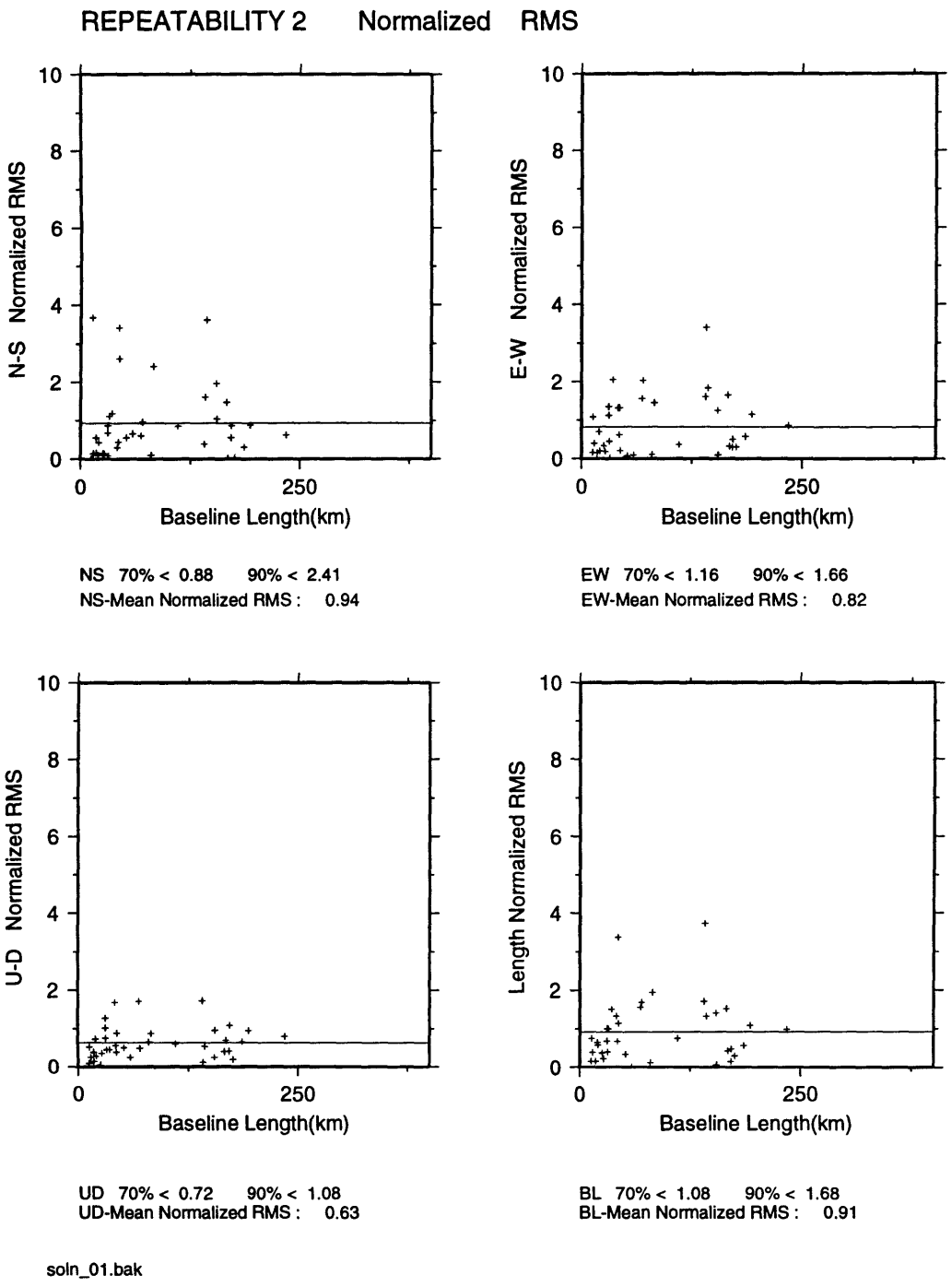

Figure B-12: JTRE92 Post-earthquake normalized root-mean-square scatter for the session-to-session baseline component (North, East, Up) estimates. Horizontal line represents the mean.

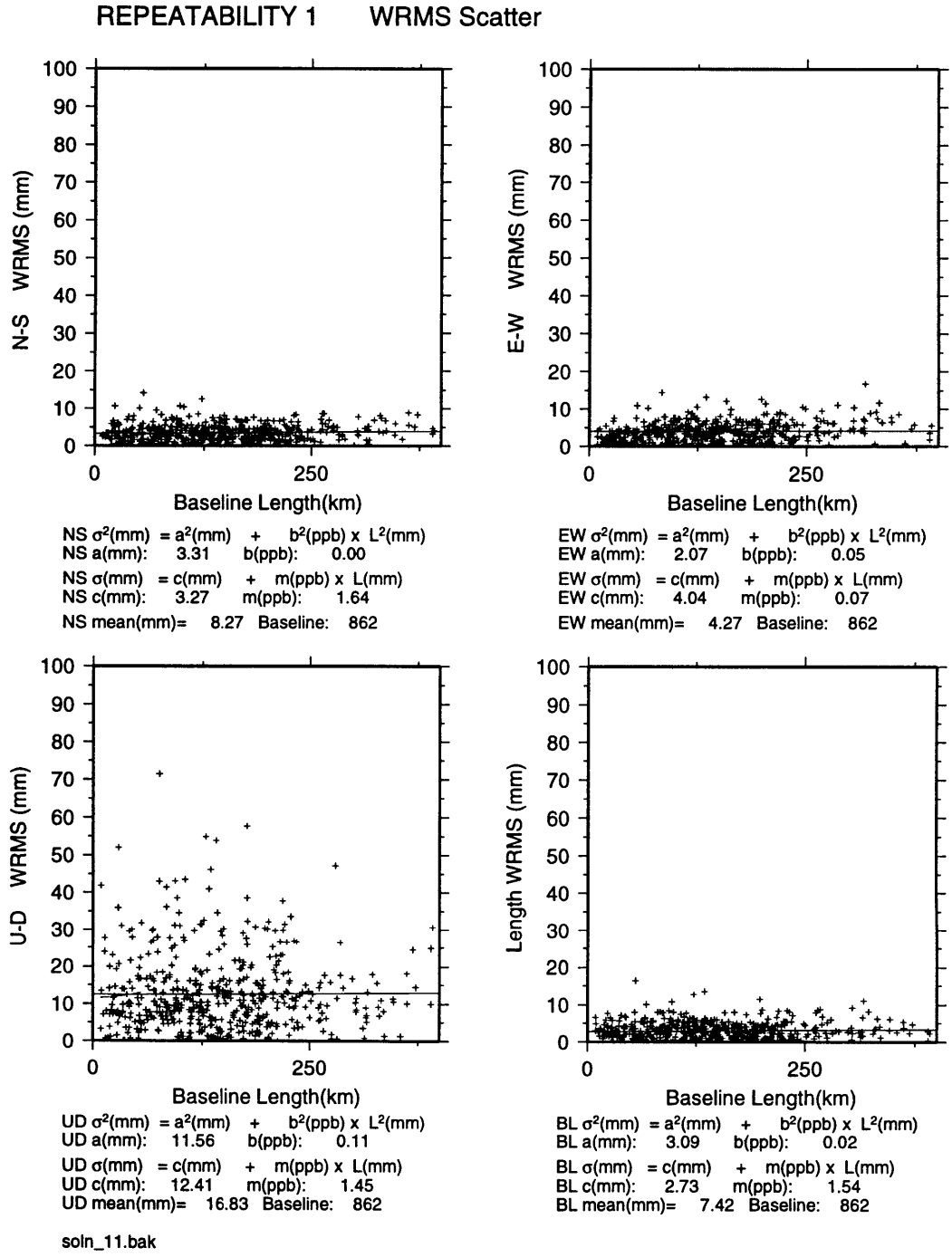

Figure B-13: STRC93 weighted root-mean-square scatter and error models for the session-to-session baseline component (North, East, Up) and baseline length estimates.

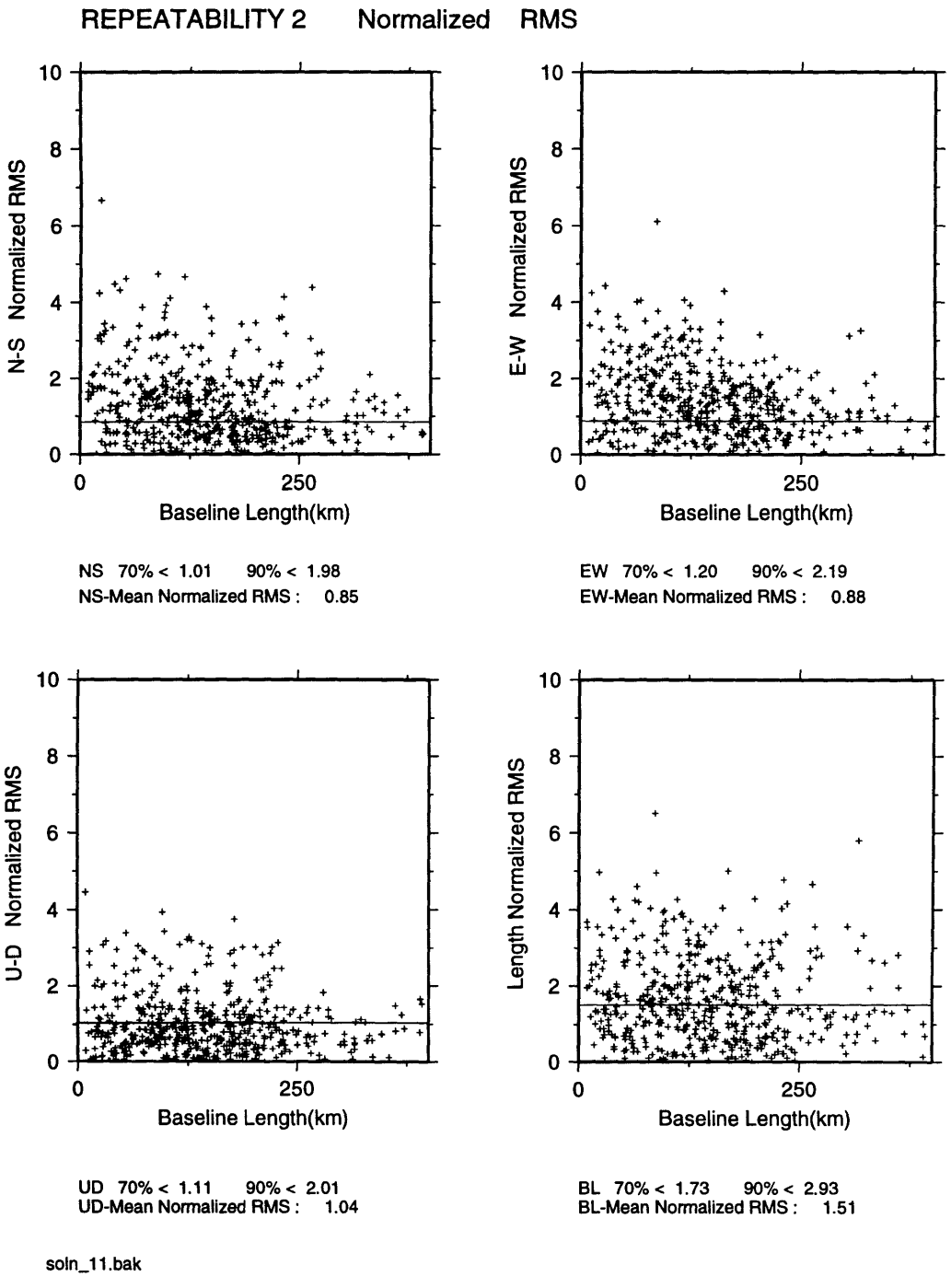

Figure B-14: STRC93 normalized root-mean-square scatter for the session-to-session baseline component (North, East, Up) estimates. Horizontal line represents the mean.

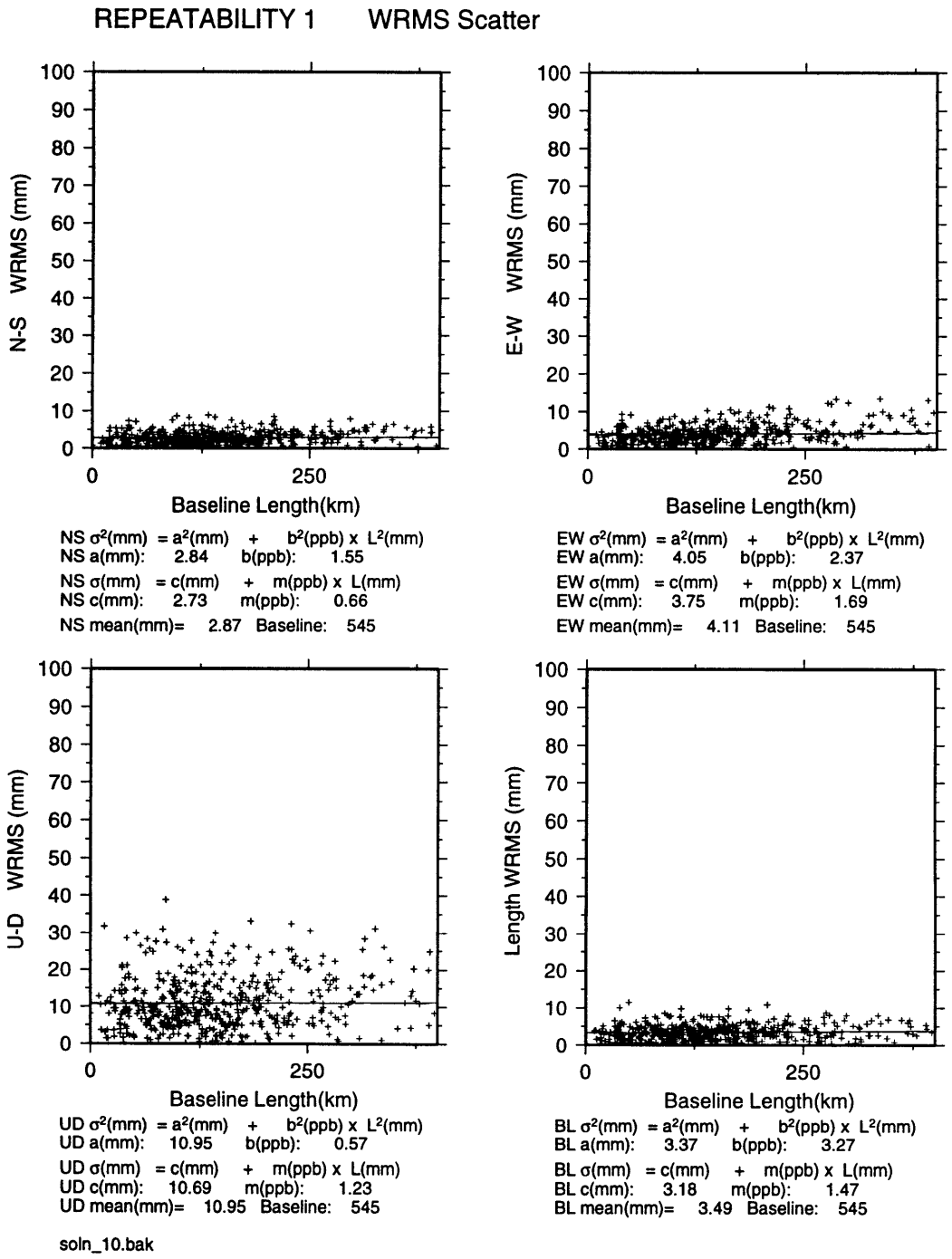

Figure B-15: STRC95 weighted root-mean-square scatter and error models for the session-to-session baseline component (North, East, Up) and baseline length estimates.

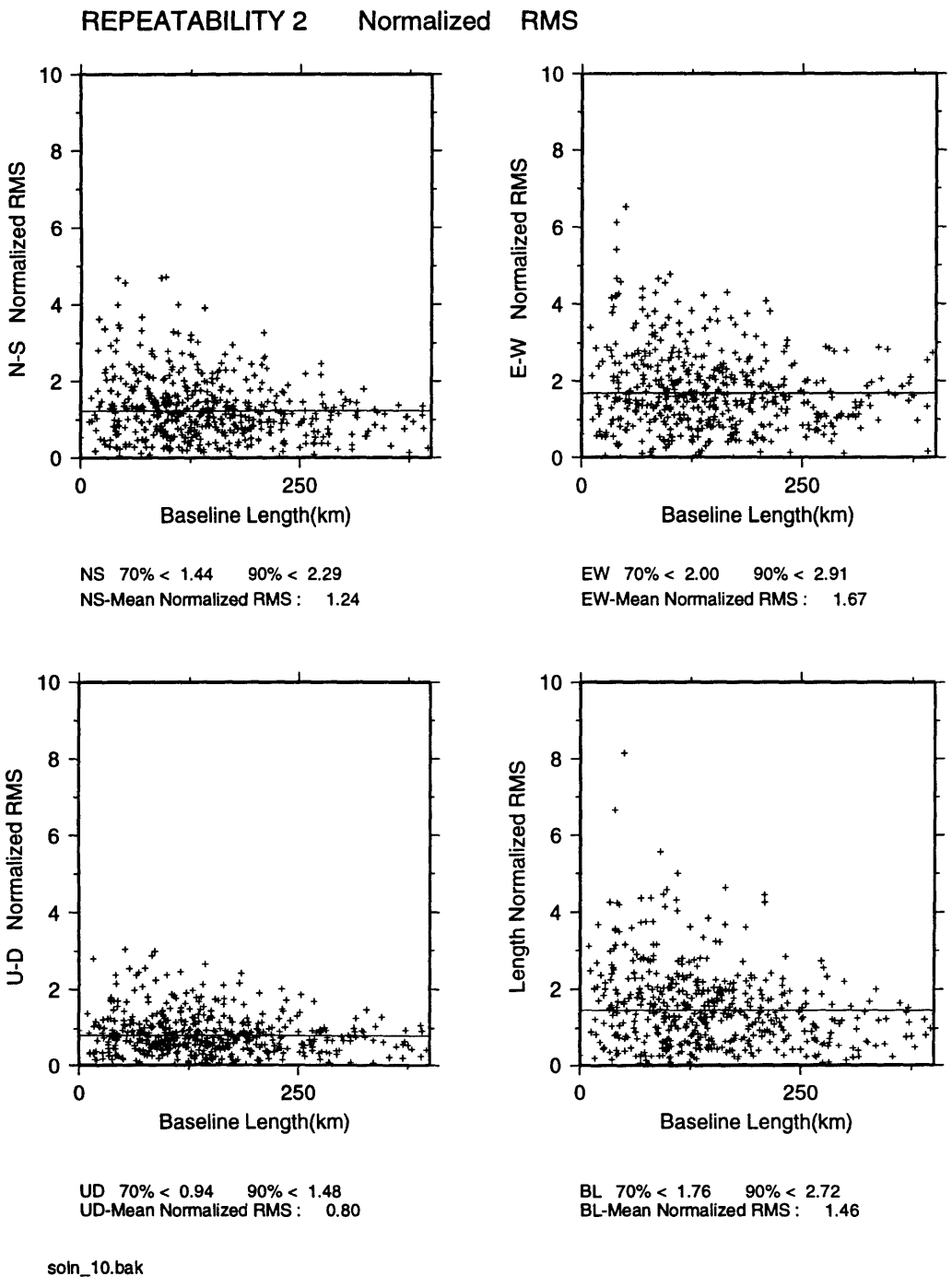

Figure B-16: STRC95 normalized root-mean-square scatter for the session-to-session baseline component (North, East, Up) estimates. Horizontal line represents the mean.

Appendix C

Time series of STRC coordinate estimates

In this appendix we present the temporal evolution of the southern California and northern Baja, Mexico GPS site coordinate estimates (North, East, and Up) obtained with the GLOBK Kalman filter. For all figures, the error bars represent the formal uncertainties at the 68% confidence level (prior to rescaling by 2.3). We explain each horizontal time series by a superposition of secular-in-time motion, a step-function at the epochs Joshua Tree and Landers earthquakes ($\sim$ 1992.3 and 1992.5), and normal noise processes. As mentioned in Chapter 2, we did not attempt to interpret the vertical components. Instead, they are allowed to evolve freely from experiment to experiment so as to decouple the horizontal and vertical motions and hence avoid possibly projecting vertical errors into the estimates for horizontal velocity. The scatters in the vertical appears to be most pronounced in the earlier campaigns. The horizontal components of the velocities and earthquake displacements estimated are shown with the time series for comparison. Both the velocities and coordinate time series refer to a North America fixed reference frame. For reference, the east and

north velocities at sites ENDD, PENA, and YUMA in this reference frame are 3.1 ± 1.3 mm/yr, -2.7 ± 1.1 mm/yr, 2.2 ± 1.4 mm/yr, -2.1 ± 1.1 mm/yr , and 1.6 ± 1.7 mm/yr, -0.9 ± 1.5 mm/yr respectively.

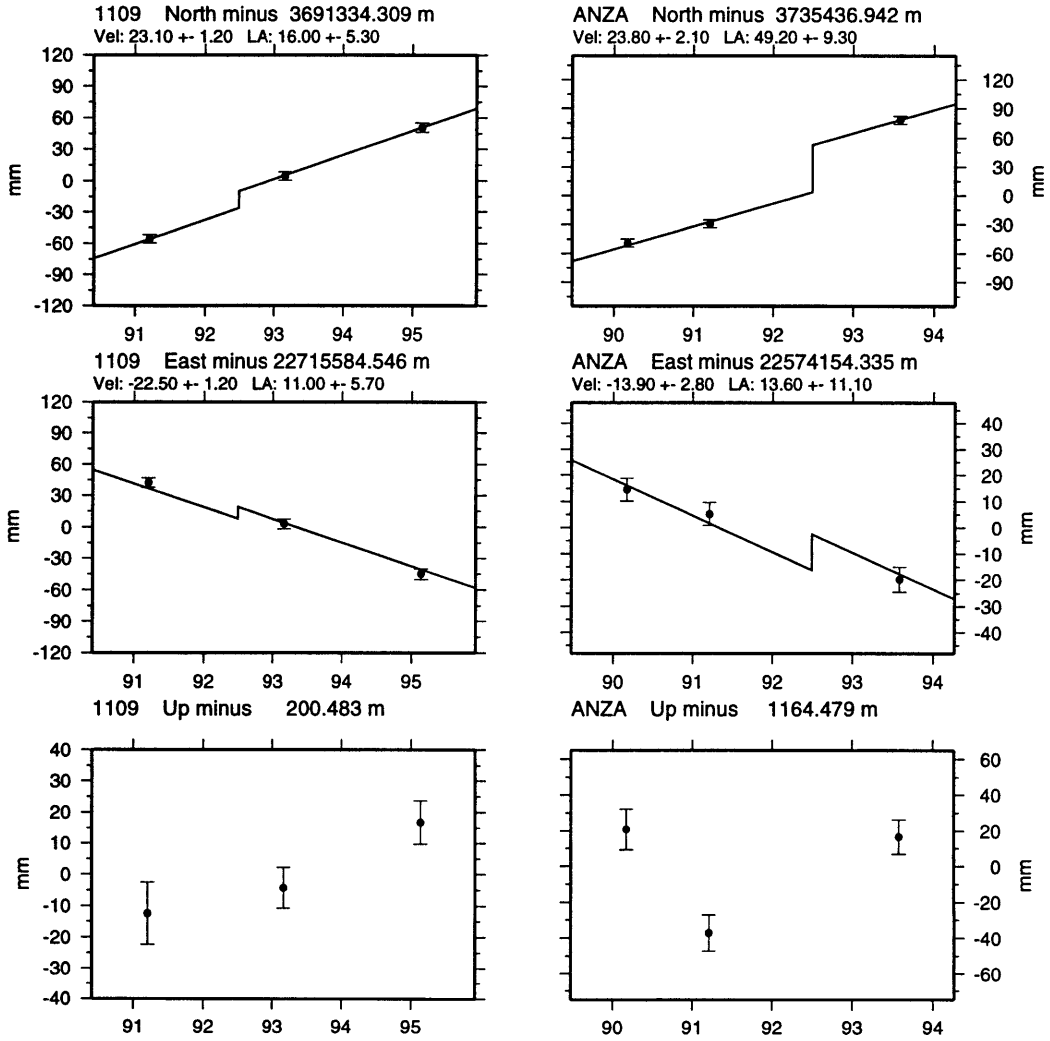

Figure C-1: Time series of GPS coordinate estimates for sites 1109 and ANZA. With only three observations, it is difficult to ascertain possible earthquake signals. Neither of the series for north and east components of site 1109's position presents a strong argument for coseismic displacements. The north component of site ANZA is slightly more convincing.

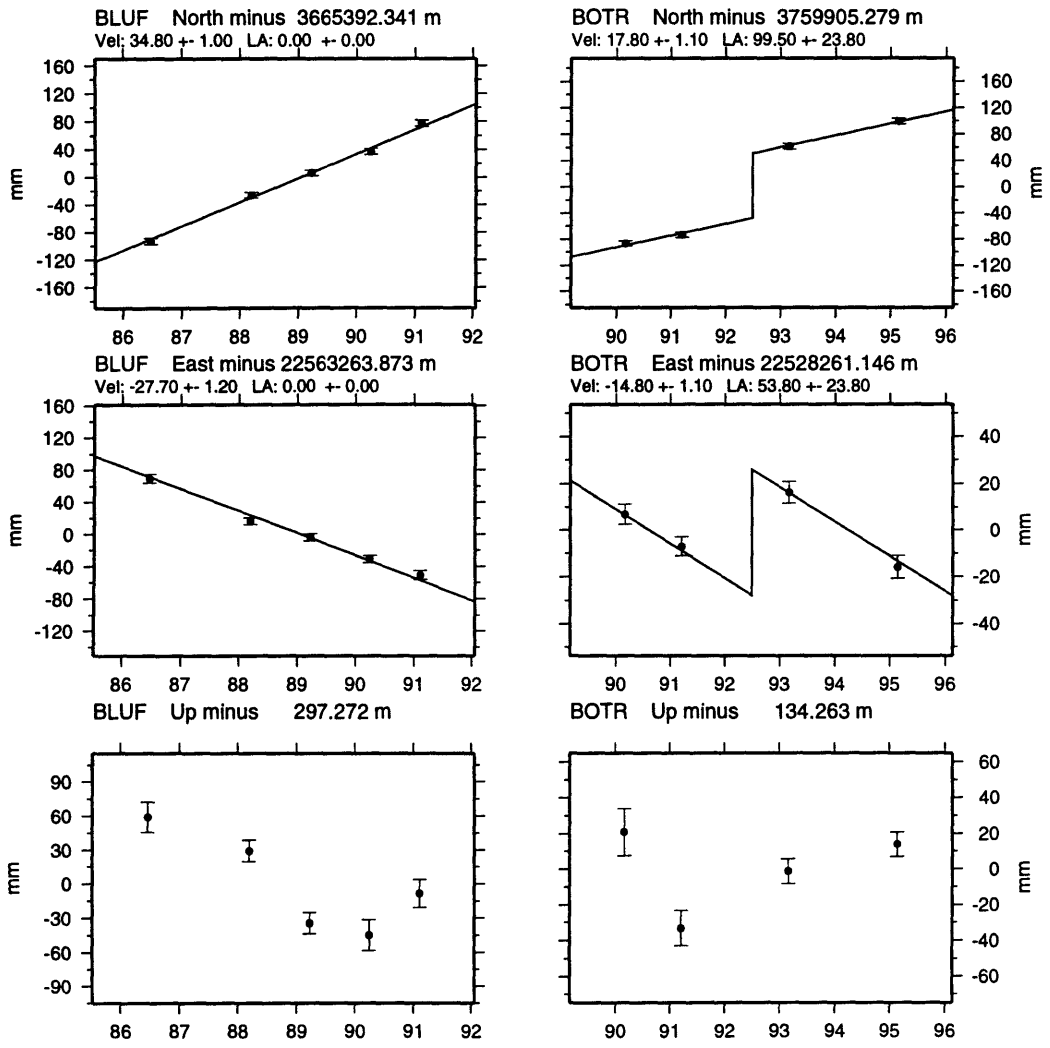

Figure C-2: Time series of GPS coordinate estimates for sites BLUF and BOTR. BLUF provides a good example of the level of scatter about a secular trend for the time period before the earthquakes. The north component of the coordinate estimates for site BOTR clearly shows the superposition of a linear-in-time trend and an episodic earthquake related discontinuity.

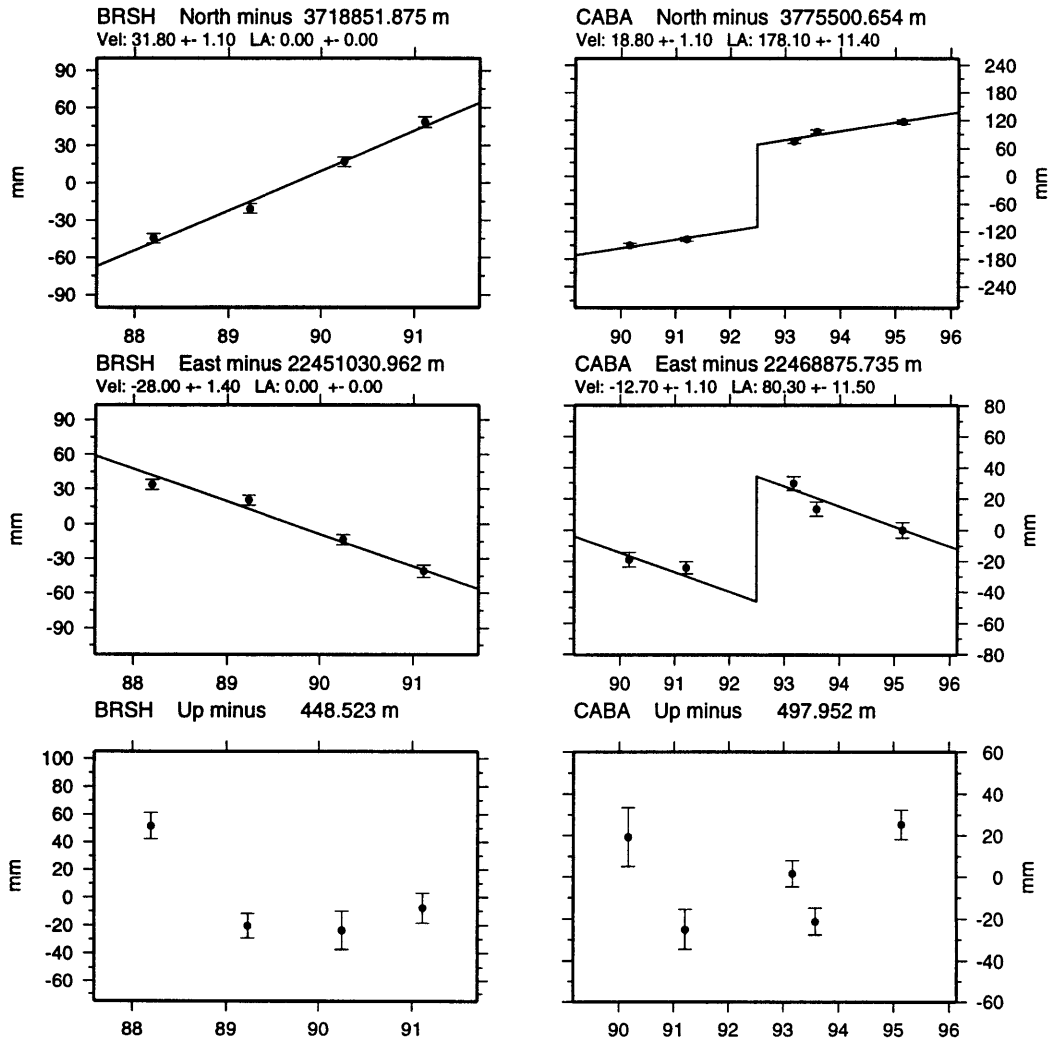

Figure C-3: Time series of GPS coordinate estimates for sites BRSH and CABA. BRSH provides a good example of the level of scatter about a secular trend for the time period before the earthquakes.The evolution of the horizontal coordinate estimates for site CABA clearly exhibit both linear-in-time and episodic earthquake related motions.

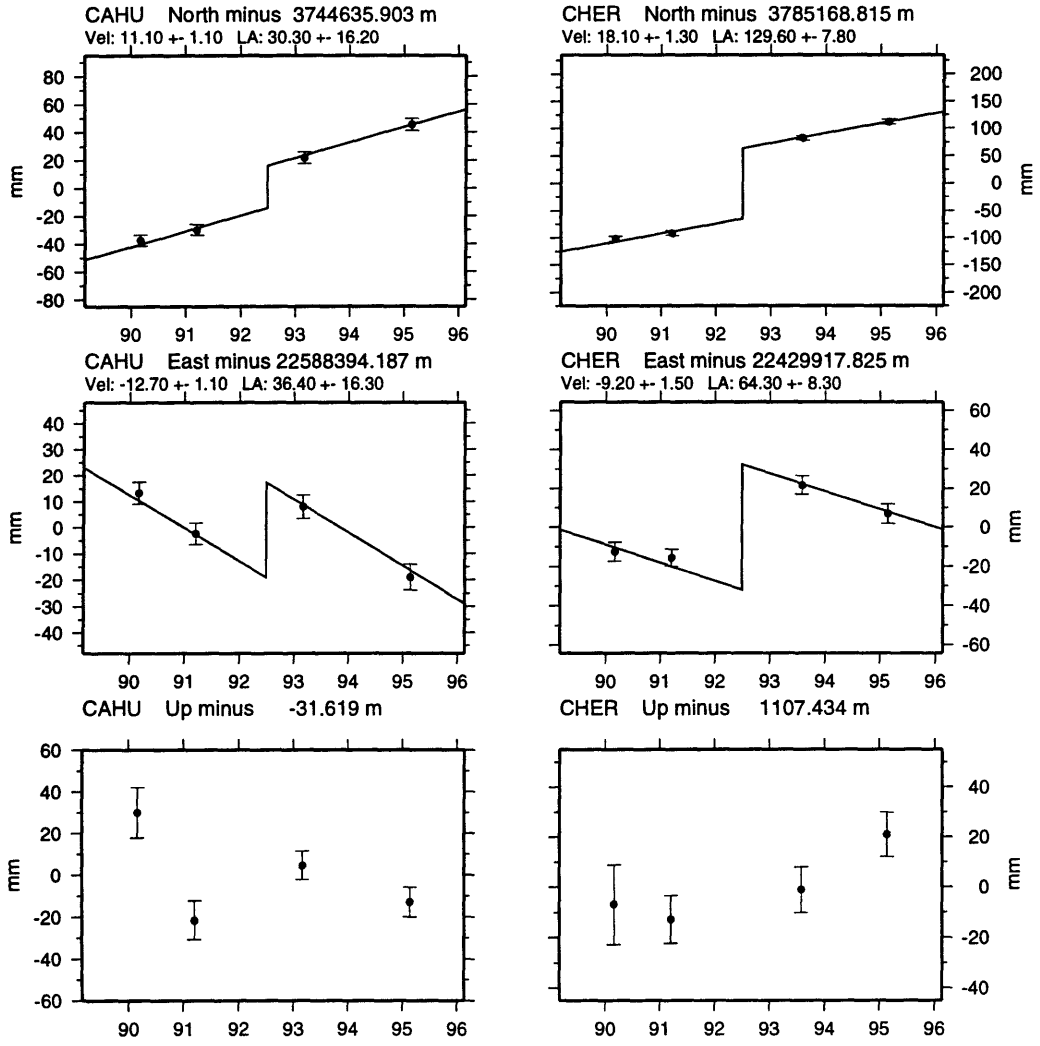

Figure C-4: Time series of GPS coordinate estimates for sites CAHU and CHER. Coordinate estimates for both sites, except perhaps the east component of CAHU, support the notion of a superposition of a linear-in-time trend and an episodic earthquake related discontinuity.

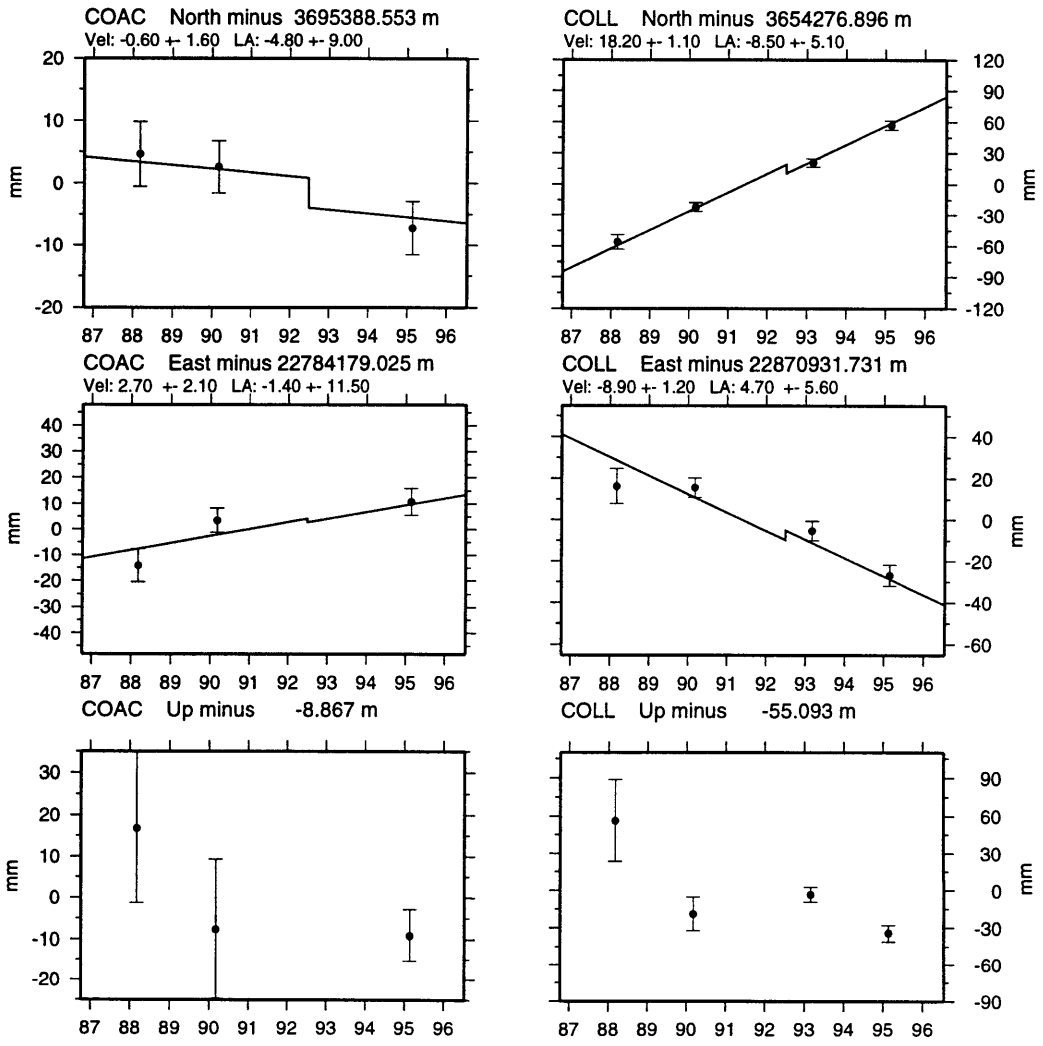

Figure C-5: Time series of GPS coordinate estimates for sites COAC and COLL. It is difficult to discern horizontal earthquake displacements from the three observations at either site.

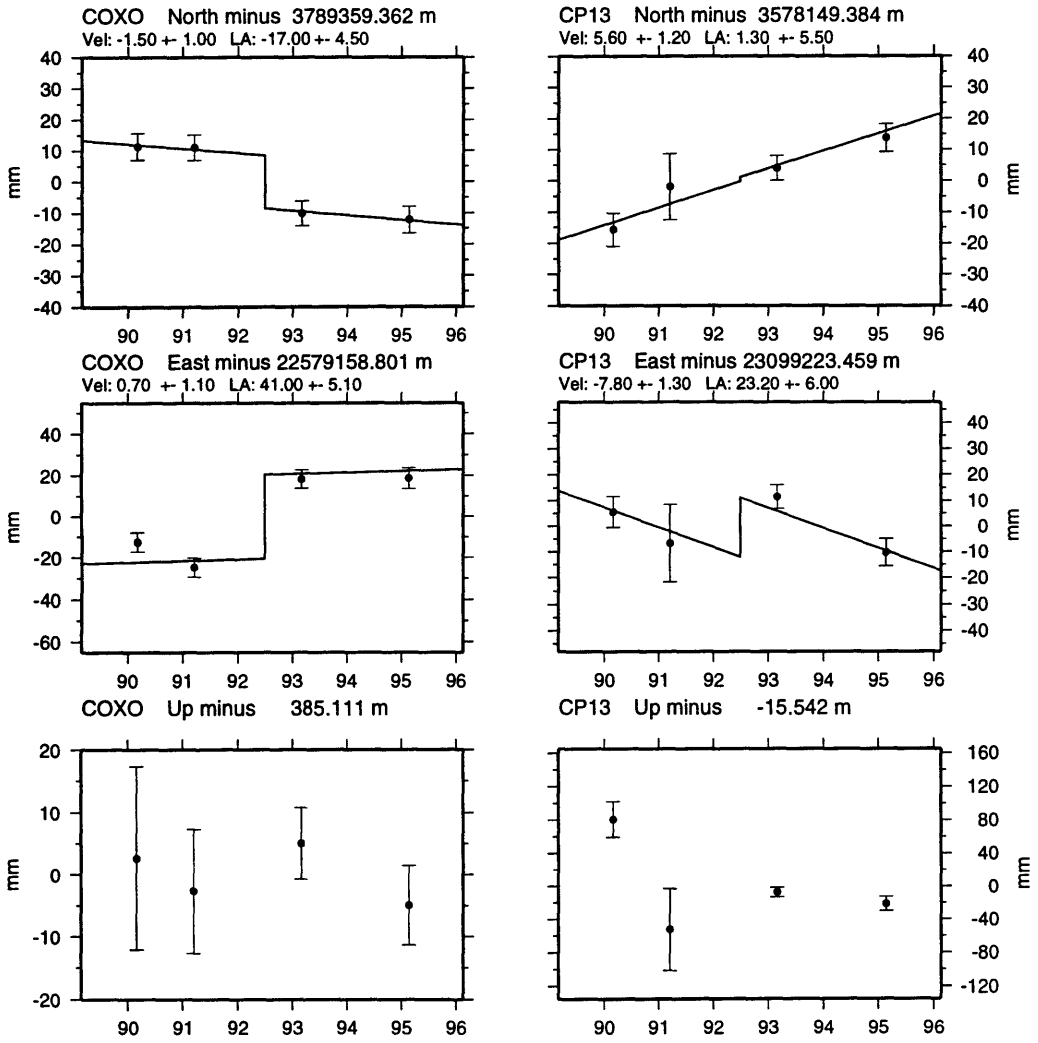

Figure C-6: Time series of GPS coordinate estimates for sites COXO and CP13. While horizontal coordinate estimates for site COXO provide evidence for earthquake related effects, earthquake related displacements for site CP13 (located in northern Mexico), are more difficult to accept.

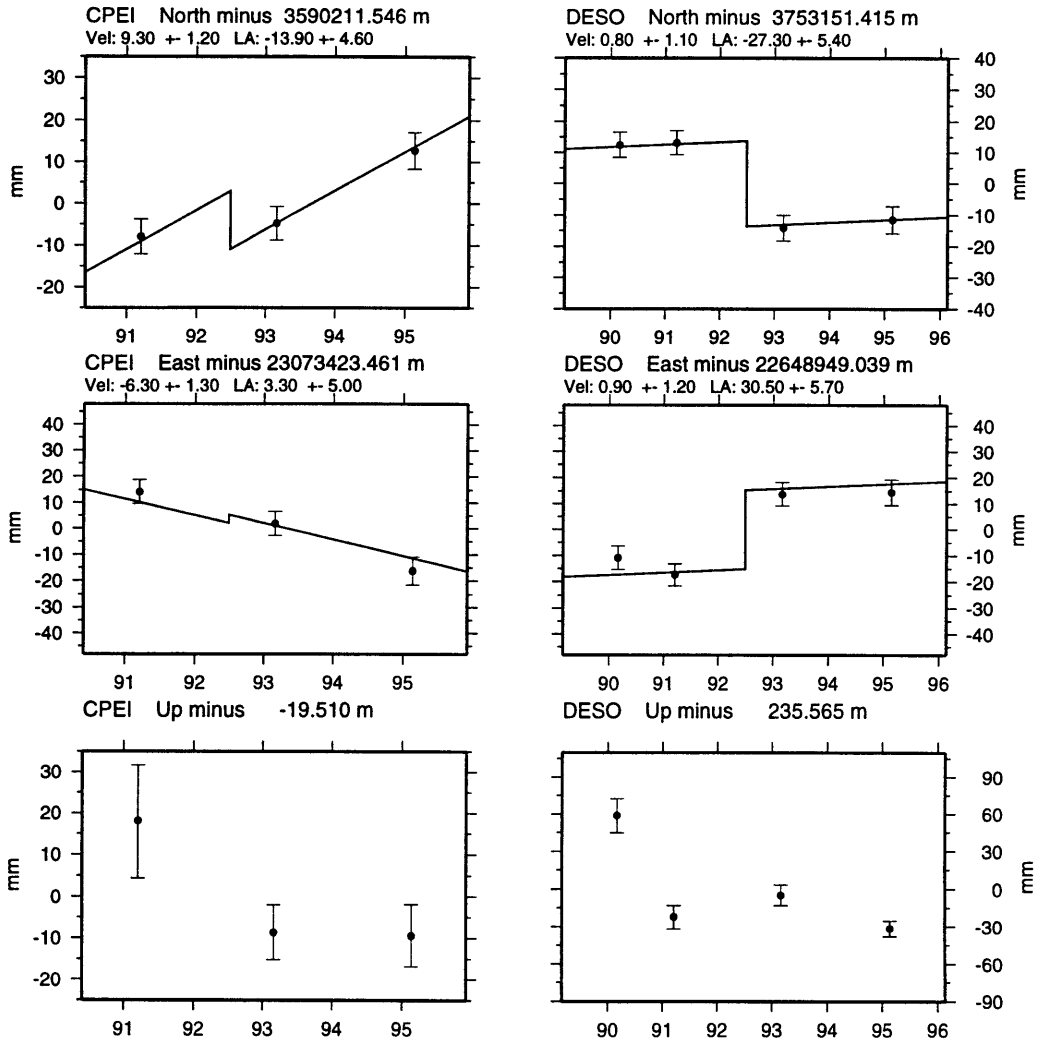

Figure C-7: Time series of GPS coordinate estimates for sites CPEI and DESO. It is difficult to accept the large earthquake displacement estimates for site CPEI (located in northern Mexico) given the three observations in the time series. In fact, the north component of velocity as computed by our model is much smaller than the GPS estimate. We suspect that the discrepancy, clear in the residual velocity field (Figure 2-6) is a result of this velocity versus earthquake displacement ambiguity. Horizontal coordinate estimates for site DESO, on the other hand, provide a more convincing argument for earthquake related effects, particularly in the north component.

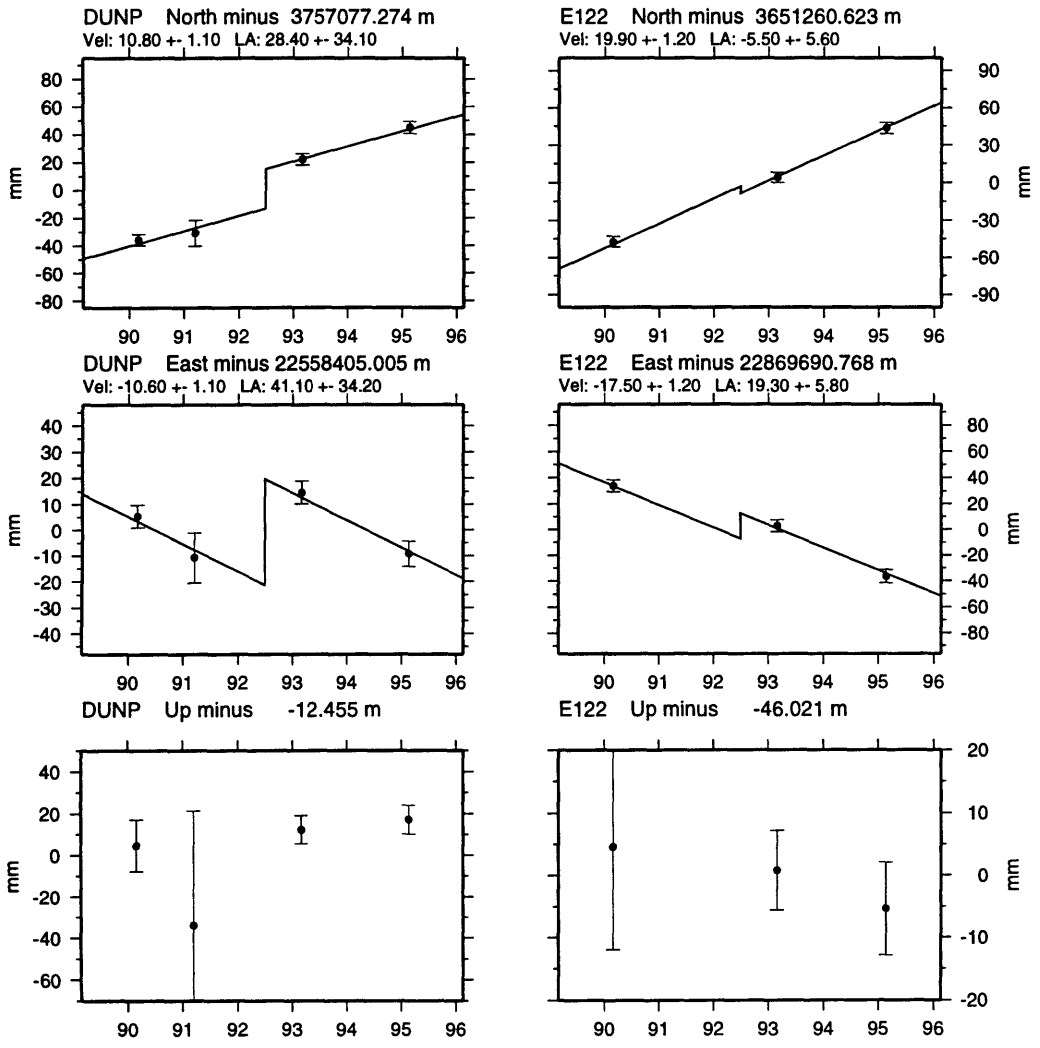

Figure C-8: Time series of GPS coordinate estimates for sites DUNP and E122. Horizontal coordinate estimates for site DUNP demonstrate small but believable earthquake displacements. The three observations for site E122 are not sufficient to discern possible earthquake signals.

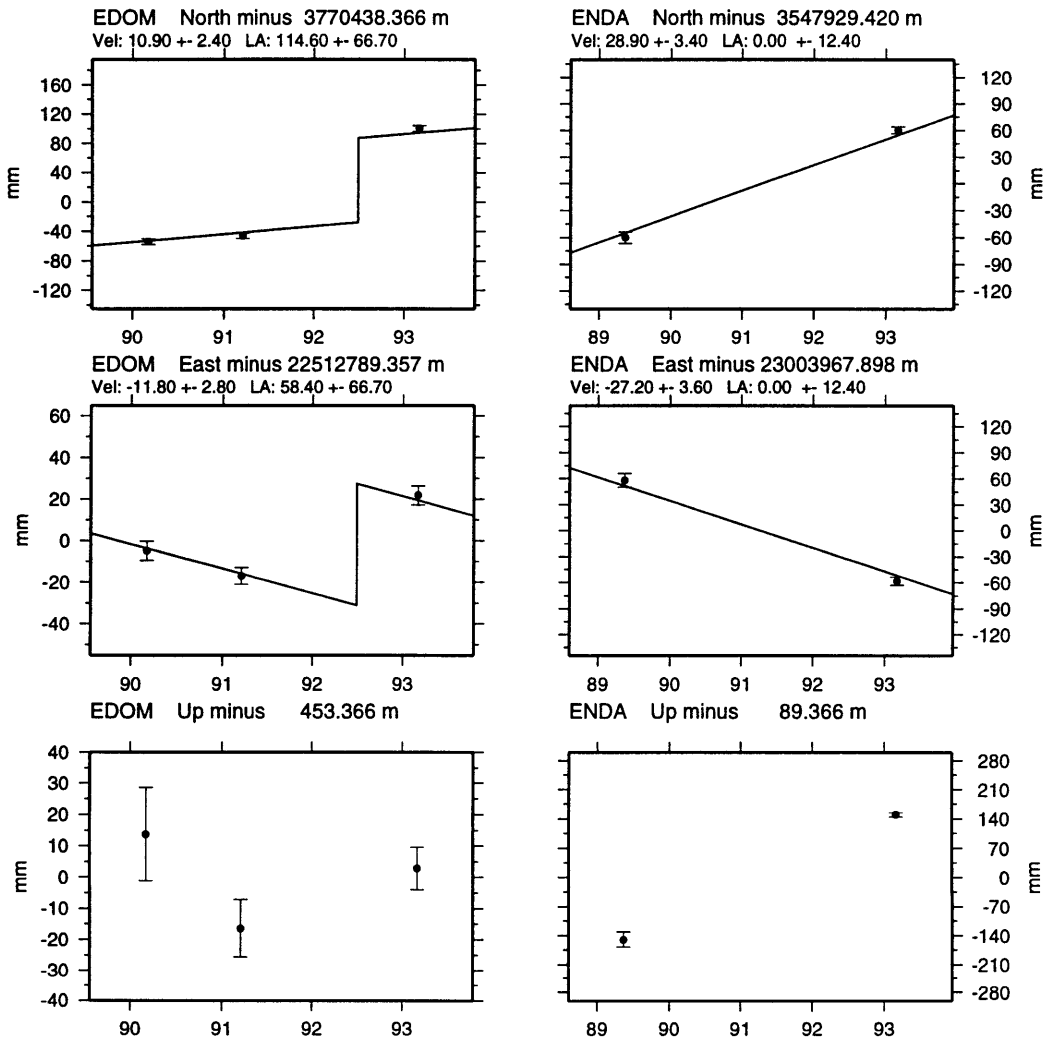

Figure C-9: Time series of GPS coordinate estimates for sites EDOM and ENDA. With only three epoch of measurement at site EDOM it is difficult to assess the significance of the seemingly large earthquake displacements. Earthquake displacements are not estimable for site ENDA from only two epochs of measurement. We have been unable to isolate the source of the large deviation in the height estimates at ENDA.

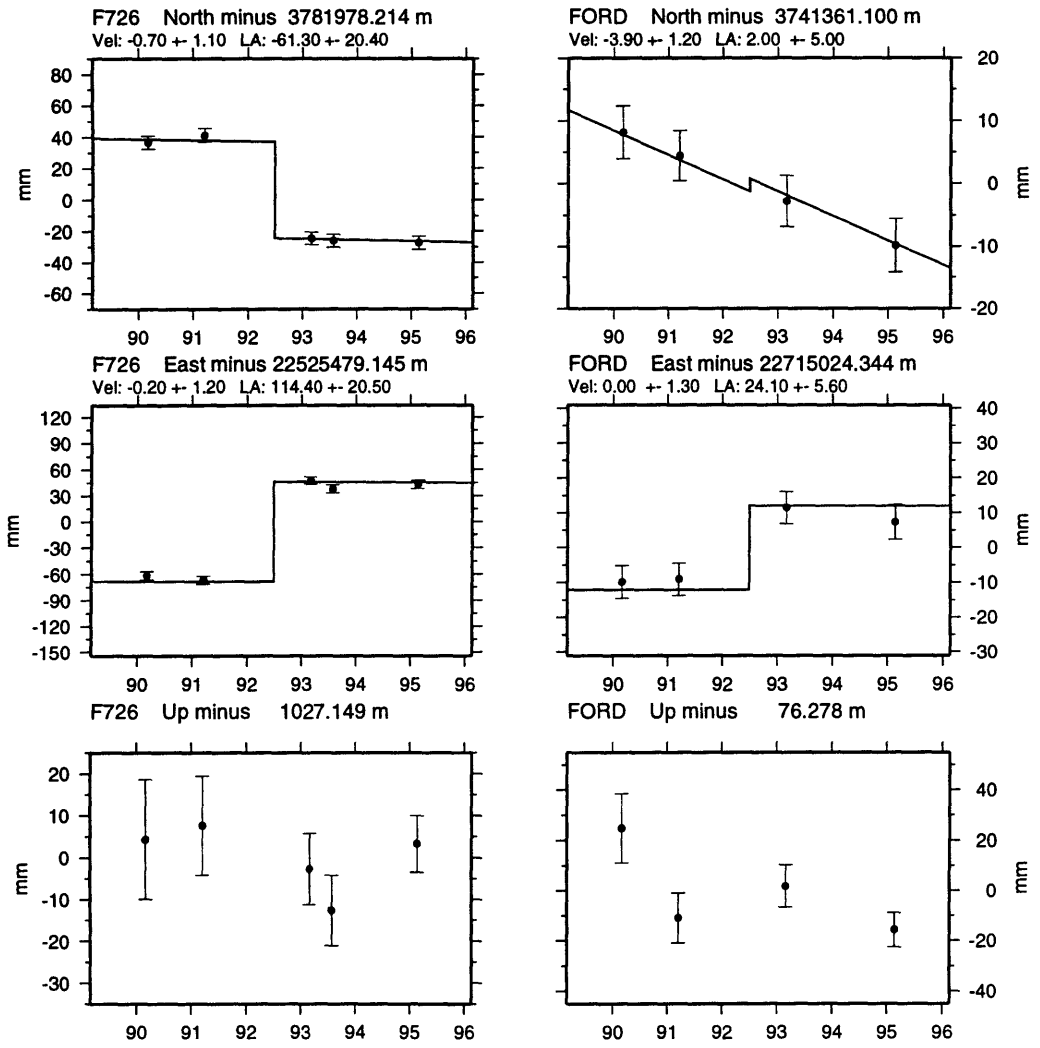

Figure C-10: Time series of GPS coordinate estimates for sites F726 and FORD. Horizontal coordinate estimates for site F726 supports the secular velocity plus episodic displacement hypothesis.

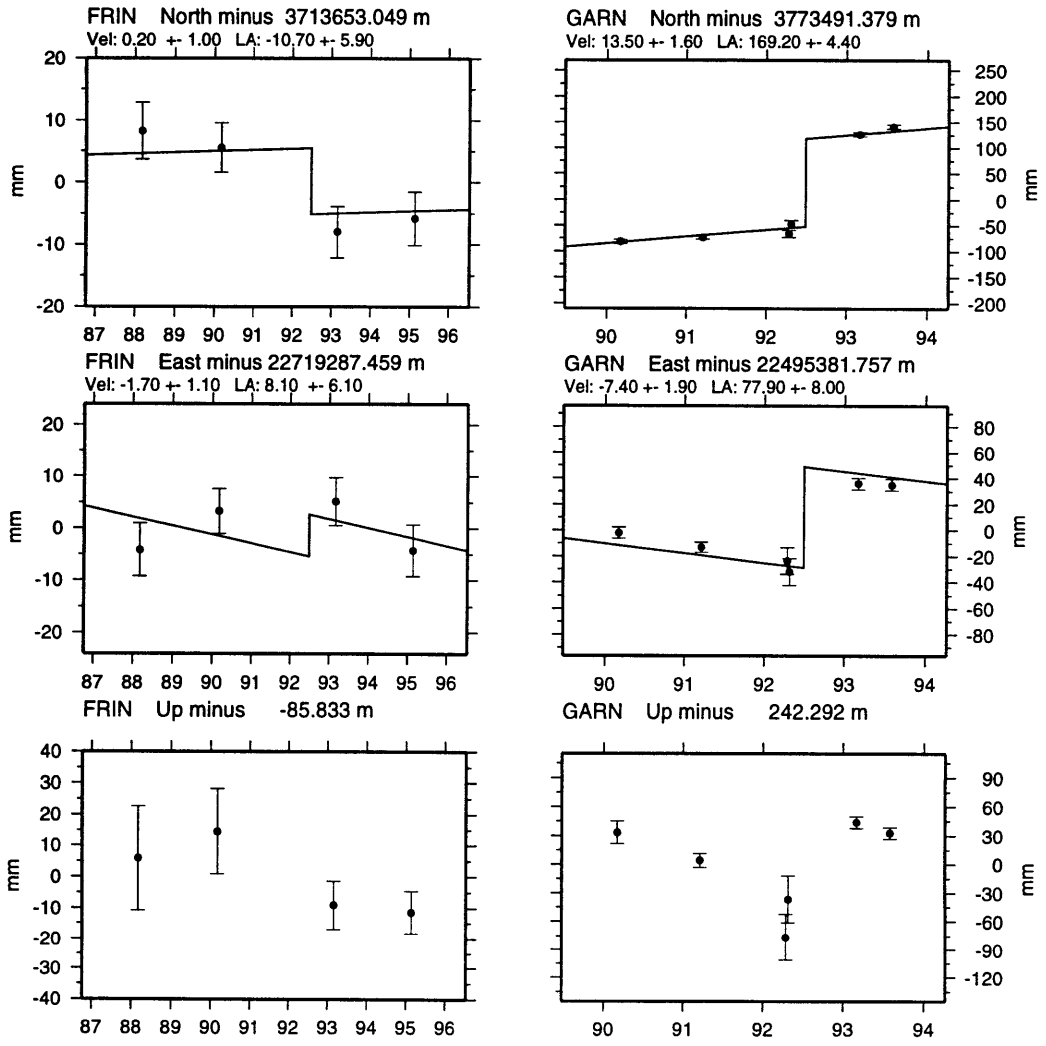

Figure C-11: Time series of GPS coordinate estimates for sites FRIN and GARN. Horizontal coordinate estimates for site GARN provide one of the best examples of secular and episodic displacement signals.

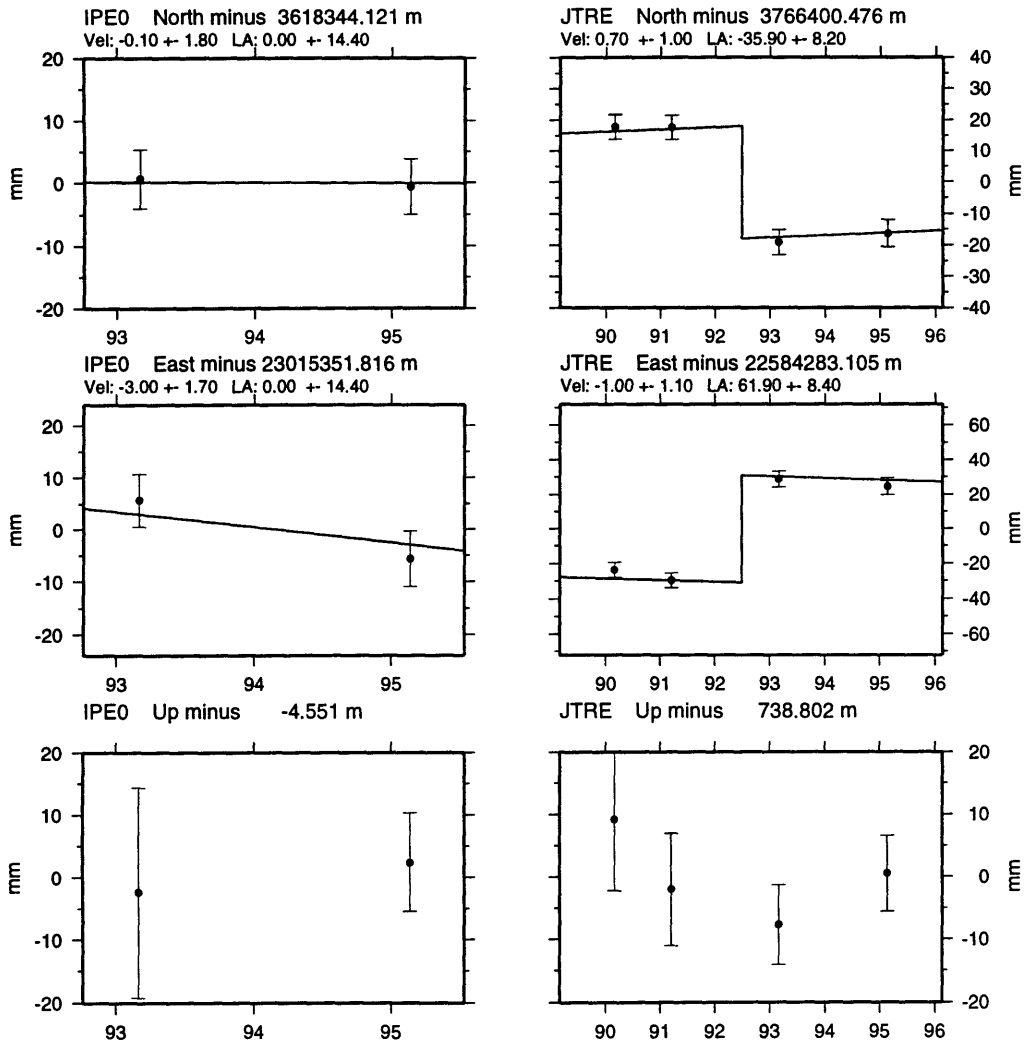

Figure C-12: Time series of GPS coordinate estimates for sites IPE0 and JTRE. While we cannot estimate possible earthquake displacements for site IPE0 from with only two epochs of measurement, site JTRE provides convincing evidence for secular velocities and episodic earthquake displacements¿

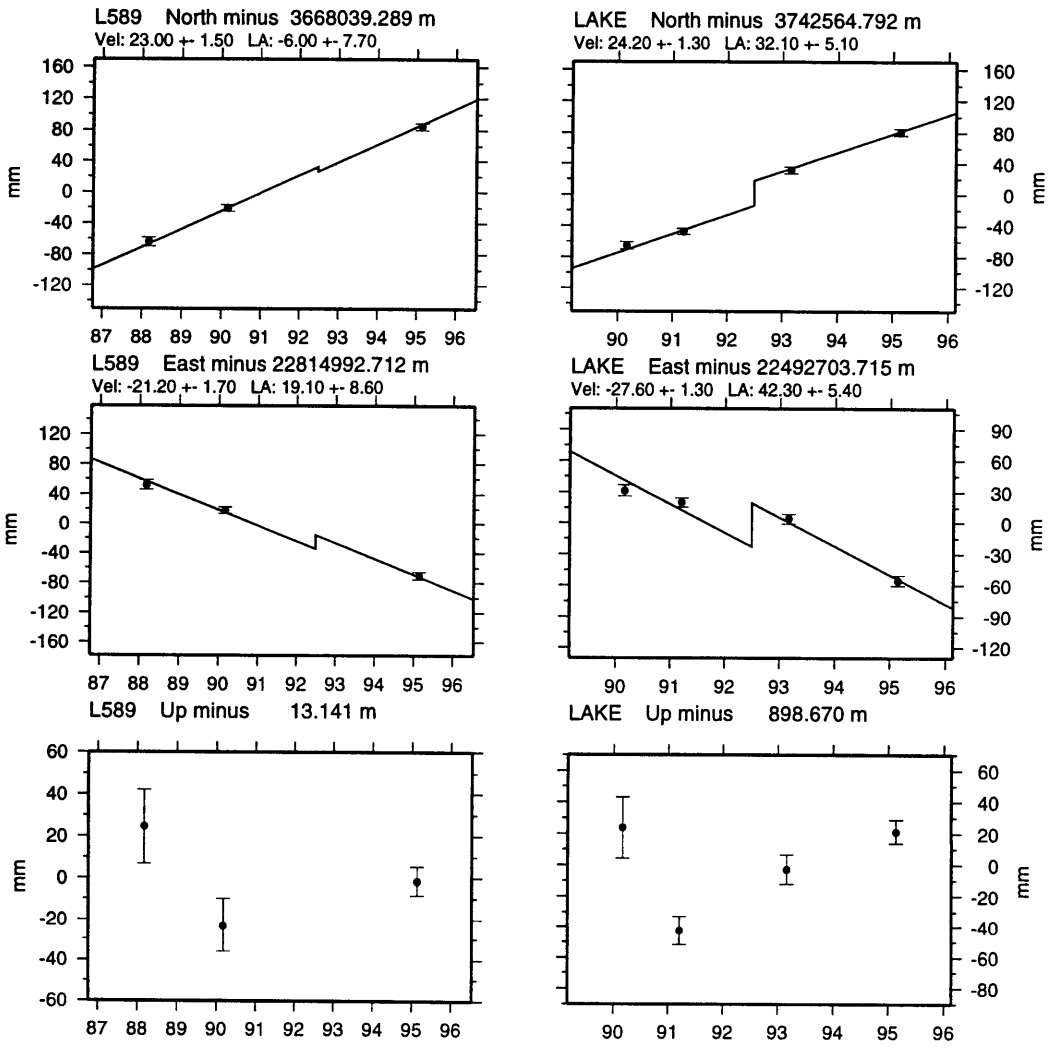

Figure C-13: Time series of GPS coordinate estimates for sites L589 and LAKE. Neither station provides a strong argument for earthquake displacements.

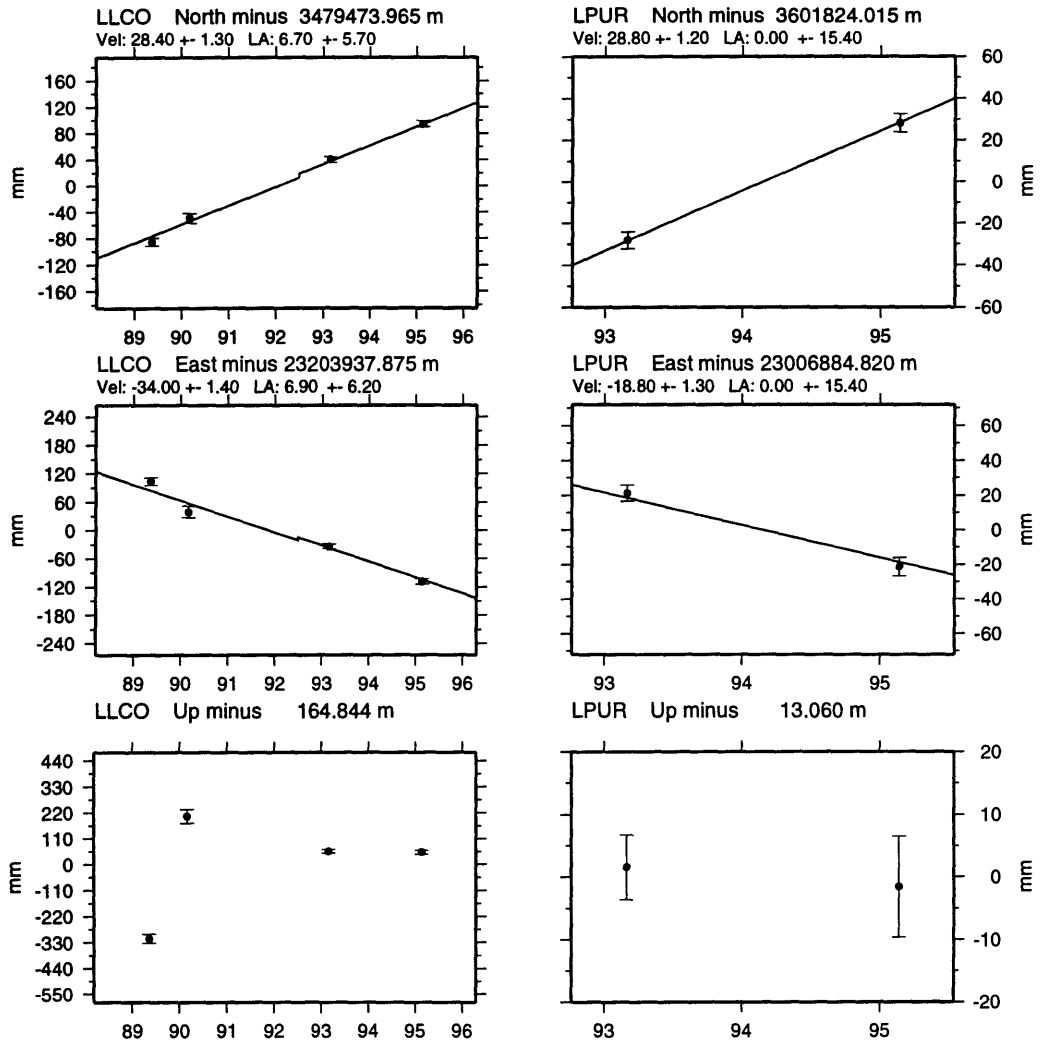

Figure C-14: Time series of GPS coordinate estimates for sites LLCO and LPUR. Horizontal coordinate estimates for these sites, both located in northern Mexico, suggest that they were relatively undisturbed by the Landers earthquake. The 1989 estimate for height at site LLCO appears to an outlier. We have been unable to conclusively isolate the source of this anomaly. We suspect that it may be related to an error in our knowledge of the recorded antenna height measurement.

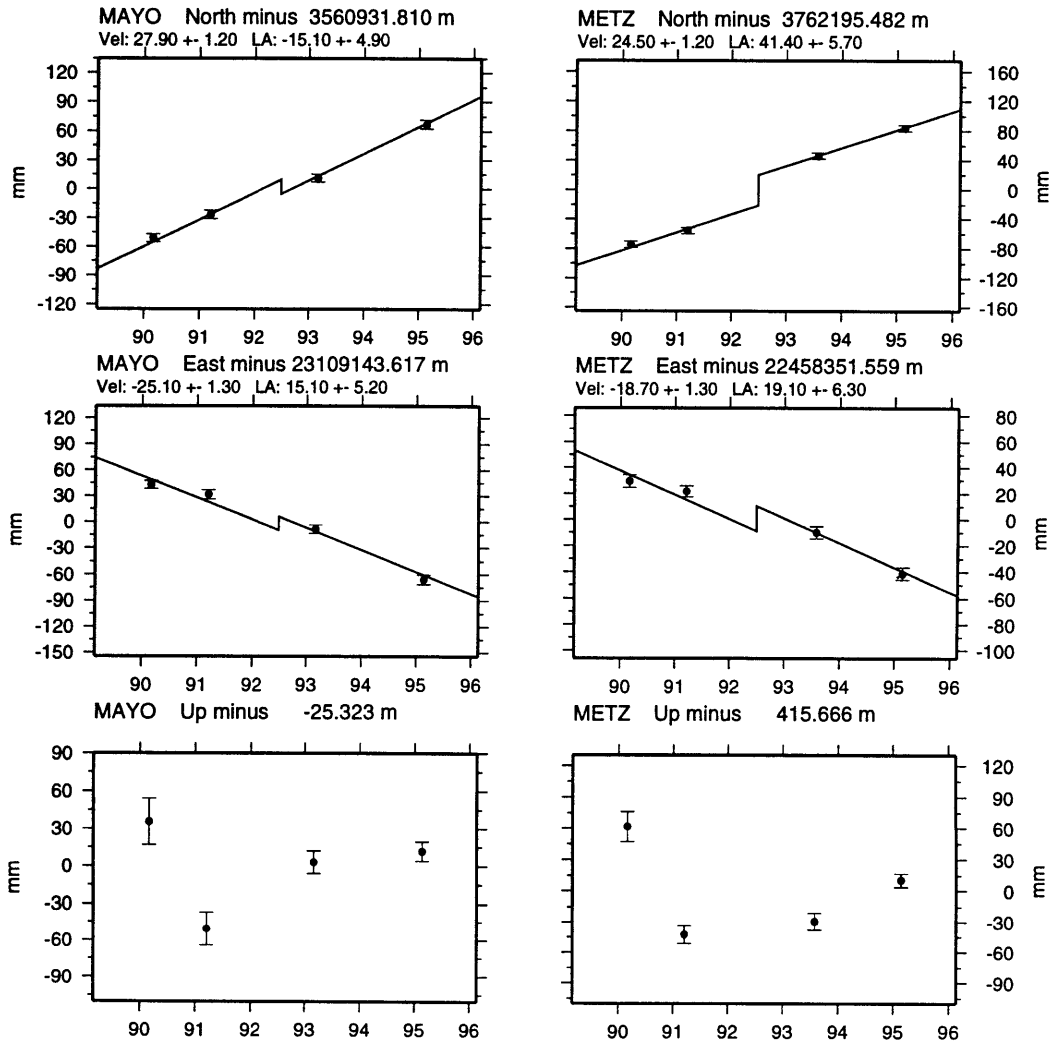

Figure C-15: Time series of GPS coordinate estimates for sites MAYO and METZ. Neither station provides a strong argument for earthquake displacements.

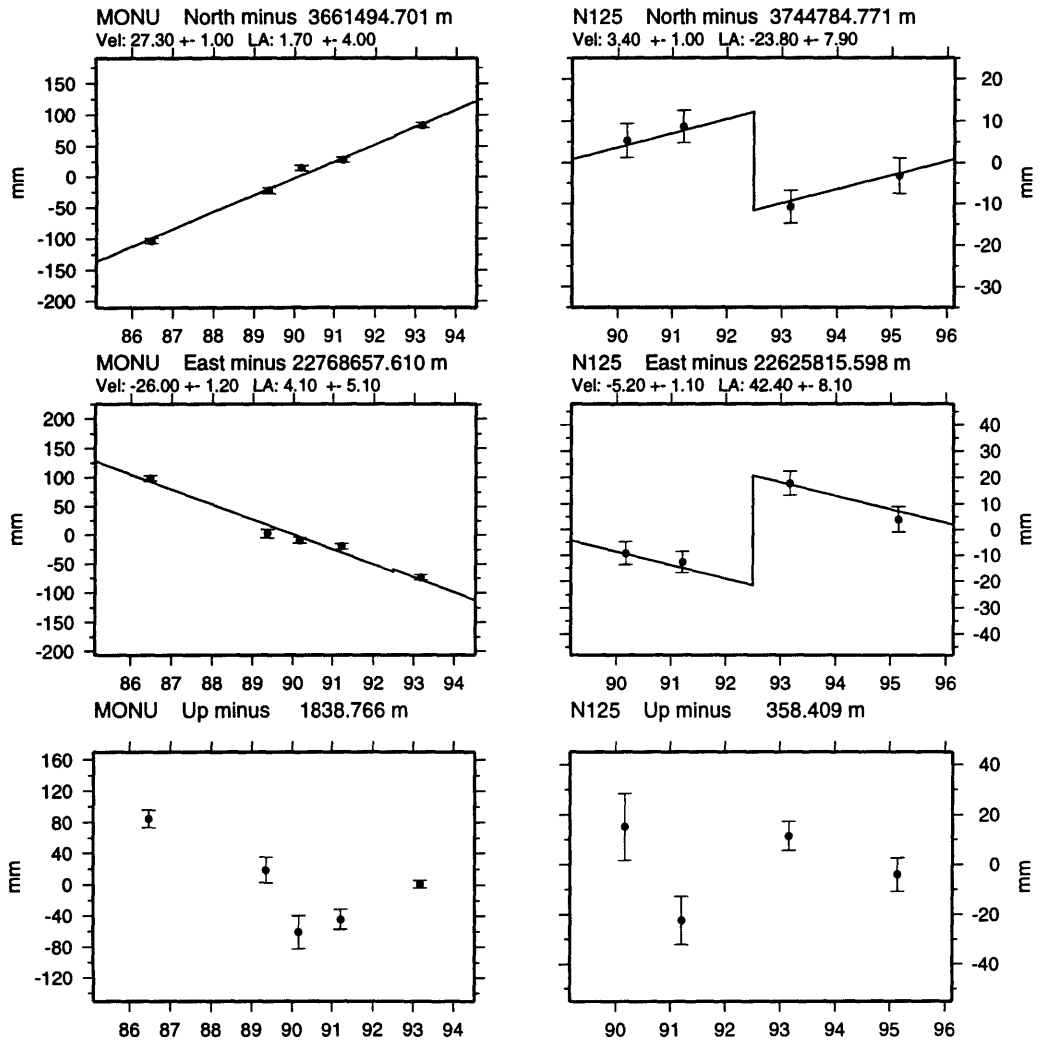

Figure C-16: Time series of GPS coordinate estimates for sites MONU and N125. Horizontal coordinate estimates for site MONU provide useful constraints on the extent of the Landers deformation. Estimates for site N125 are consistent with secular motions and episodic displacements.

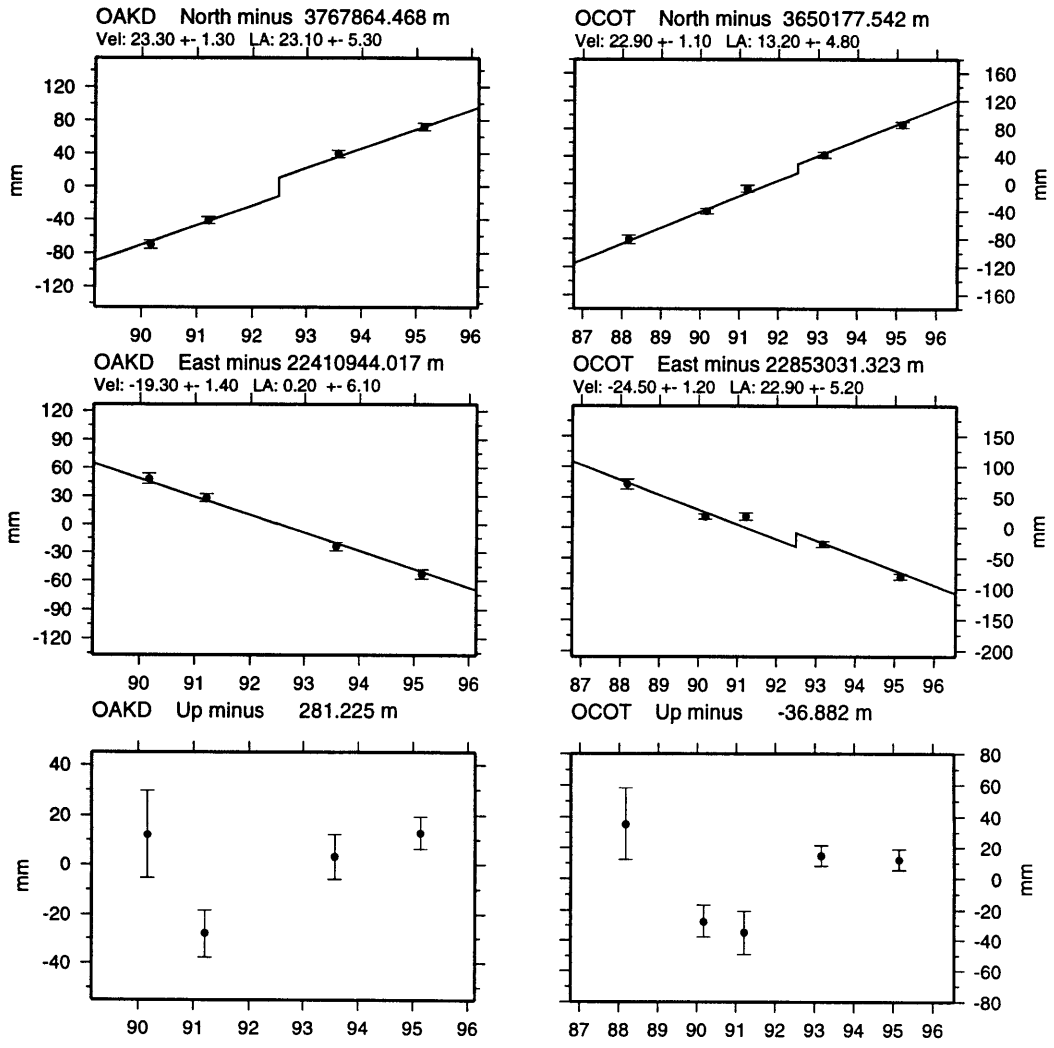

Figure C-17: Time series of GPS coordinate estimates for sites OAKD and OCOT. Neither station provides a strong argument for earthquake displacements.

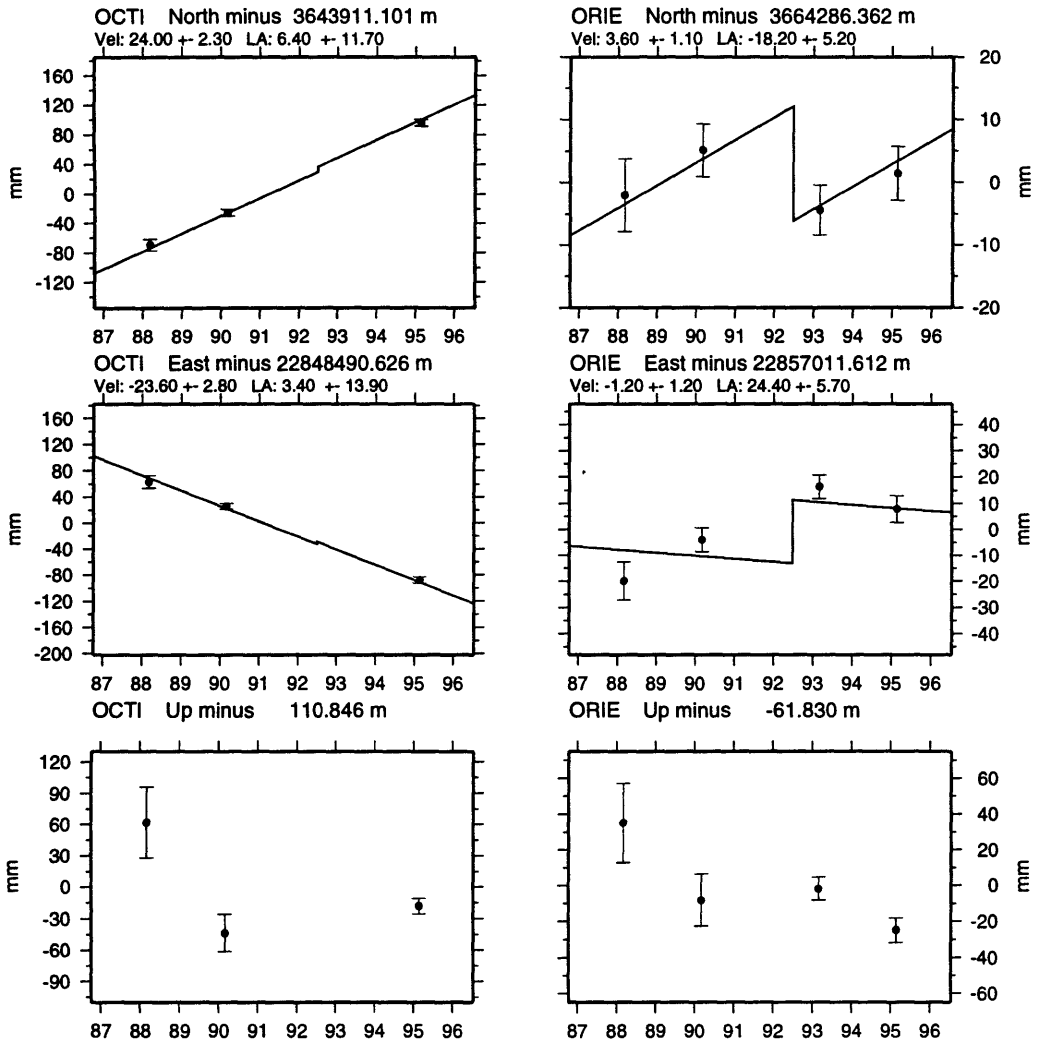

Figure C-18: Time series of GPS coordinate estimates for sites OCTI and ORIE. With only three epoch of measurement at site OCTI it is difficult discern possible earthquake effects. The east component of the coordinate estimates for site ORIE does not provide convincing support for liner-in-time motions independent of the possibility of earthquake displacements.

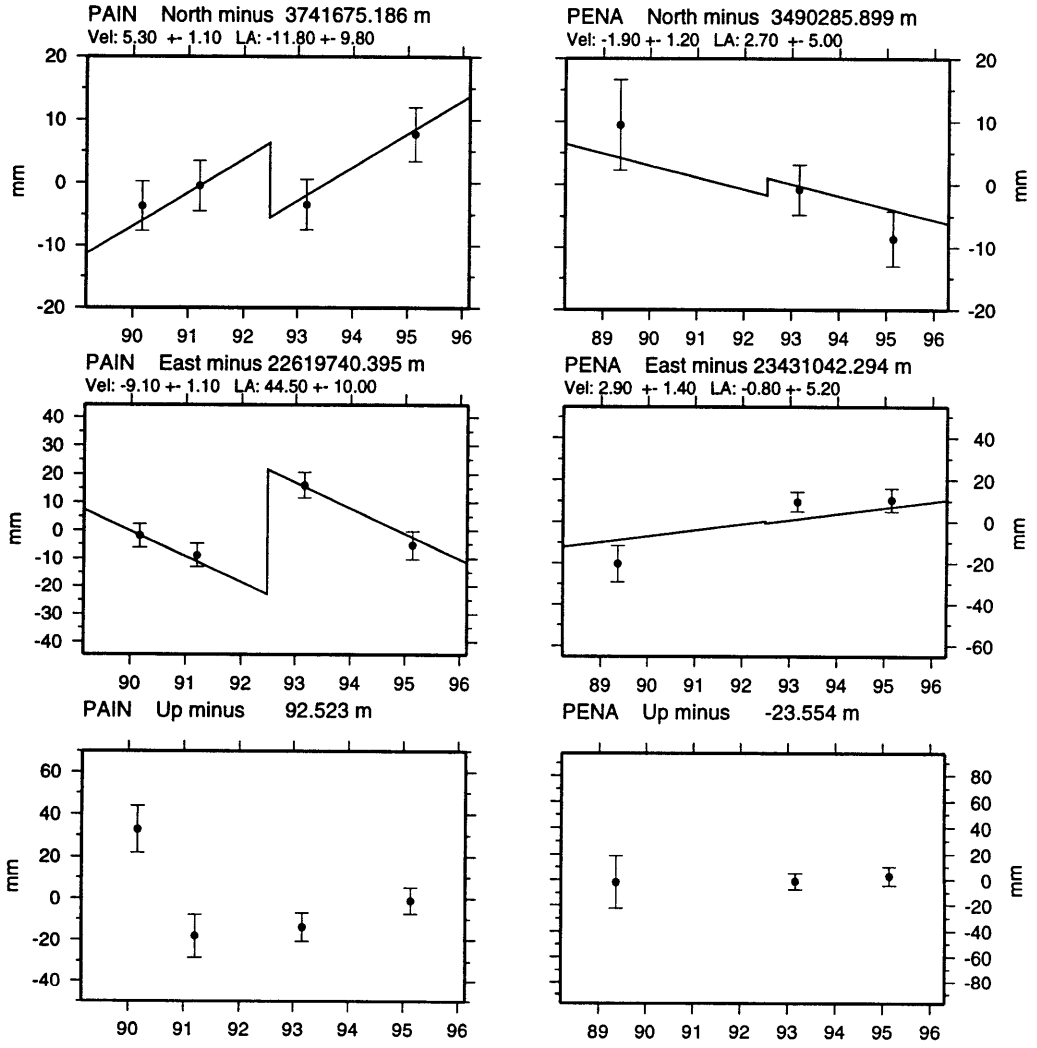

Figure C-19: Time series of GPS coordinate estimates for sites PAIN and PENA. Horizontal coordinate estimates for site PAIN provide a good example of both secular and episodic motions in the east direction. It is difficult to discern possible earthquake related displacements at PENA from only three epochs of observation.

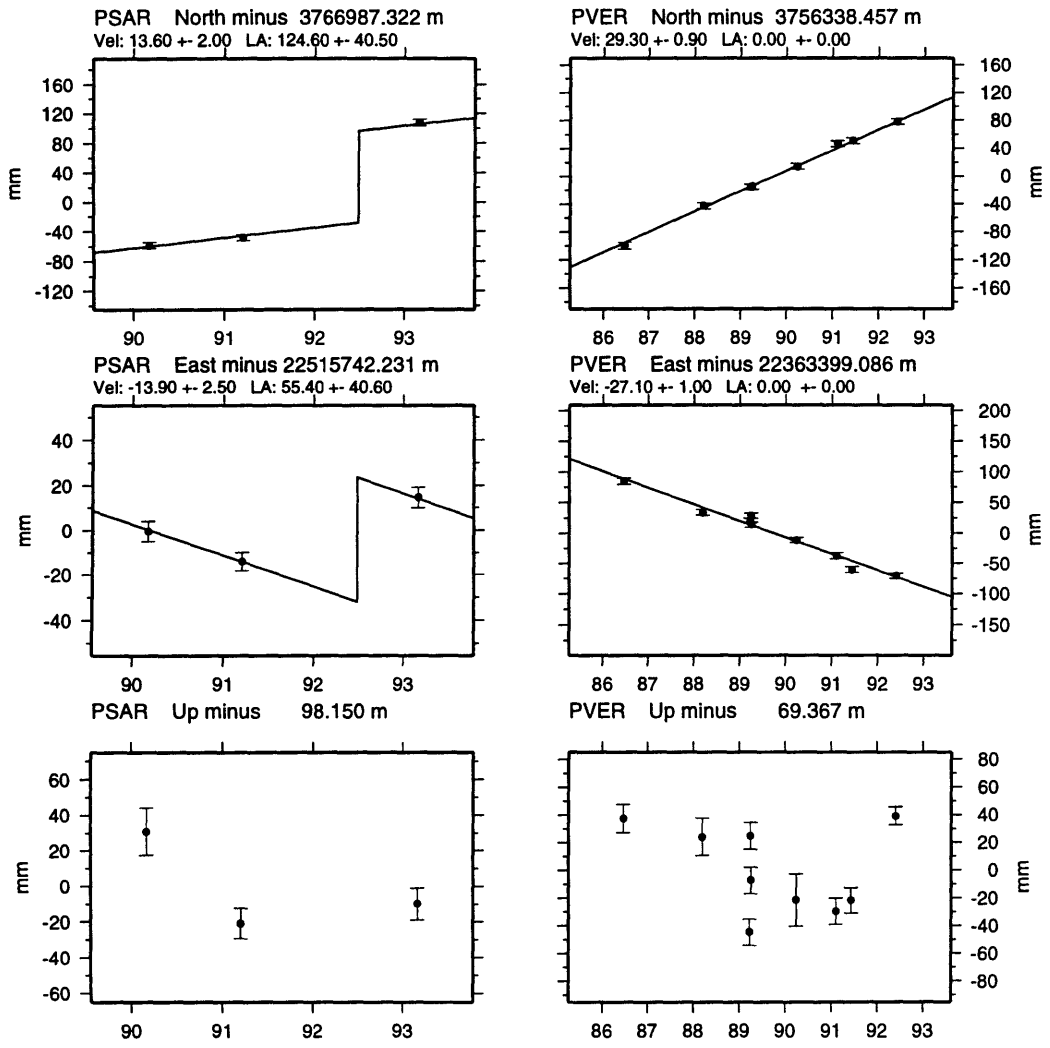

Figure C-20: Time series of GPS coordinate estimates for sites PSAR and PVER. It is difficult to assess the seemingly large earthquake displacements at site PSAR from only three observations. PVER provides a good example of the level of scatter about a secular trend for the time period before the earthquakes.

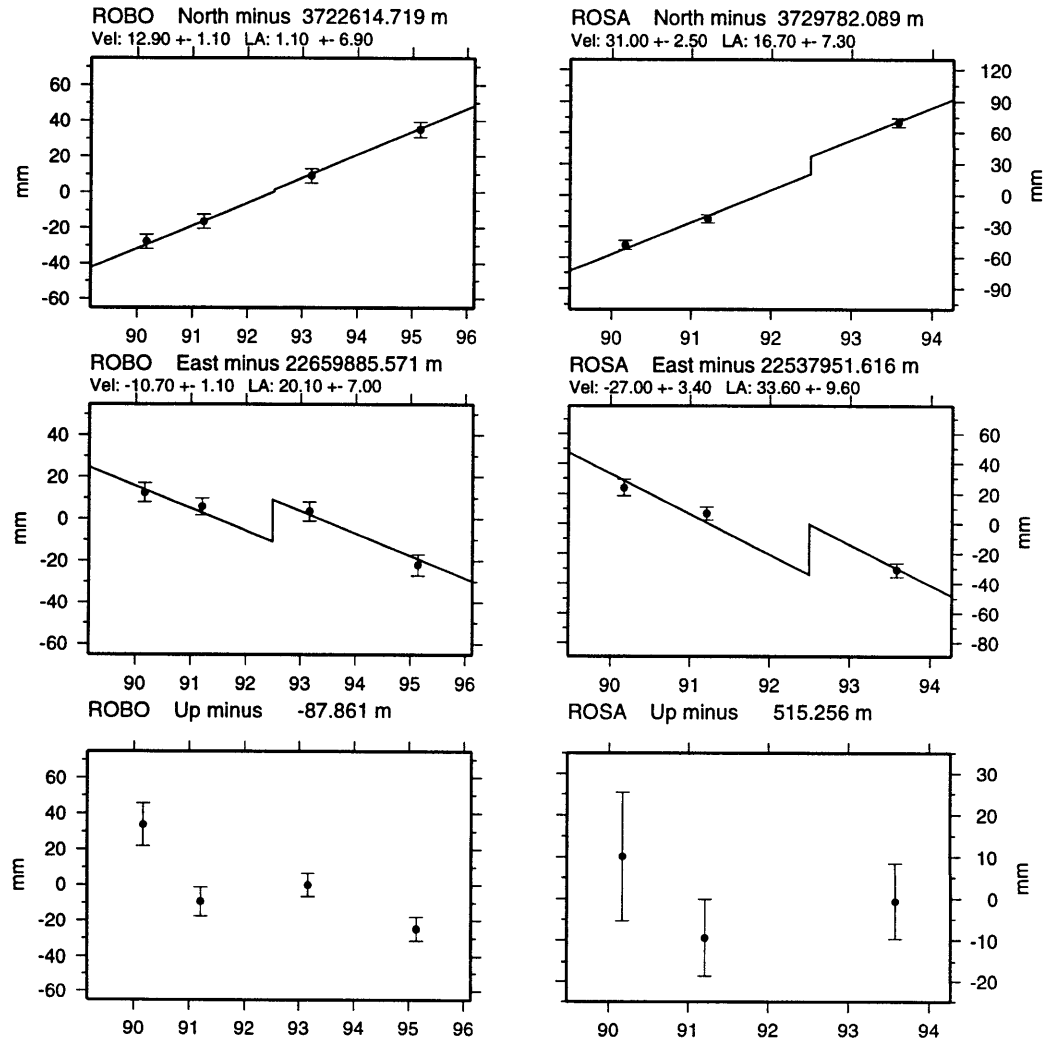

Figure C-21: Time series of GPS coordinate estimates for sites ROBO and ROSA. Our ability to confidently reject significant earthquake related displacements at site ROSA is hampered due to the limited number of observations. There is no evidence for coseismic displacements in the north component of ROBO's coordinate estimate.

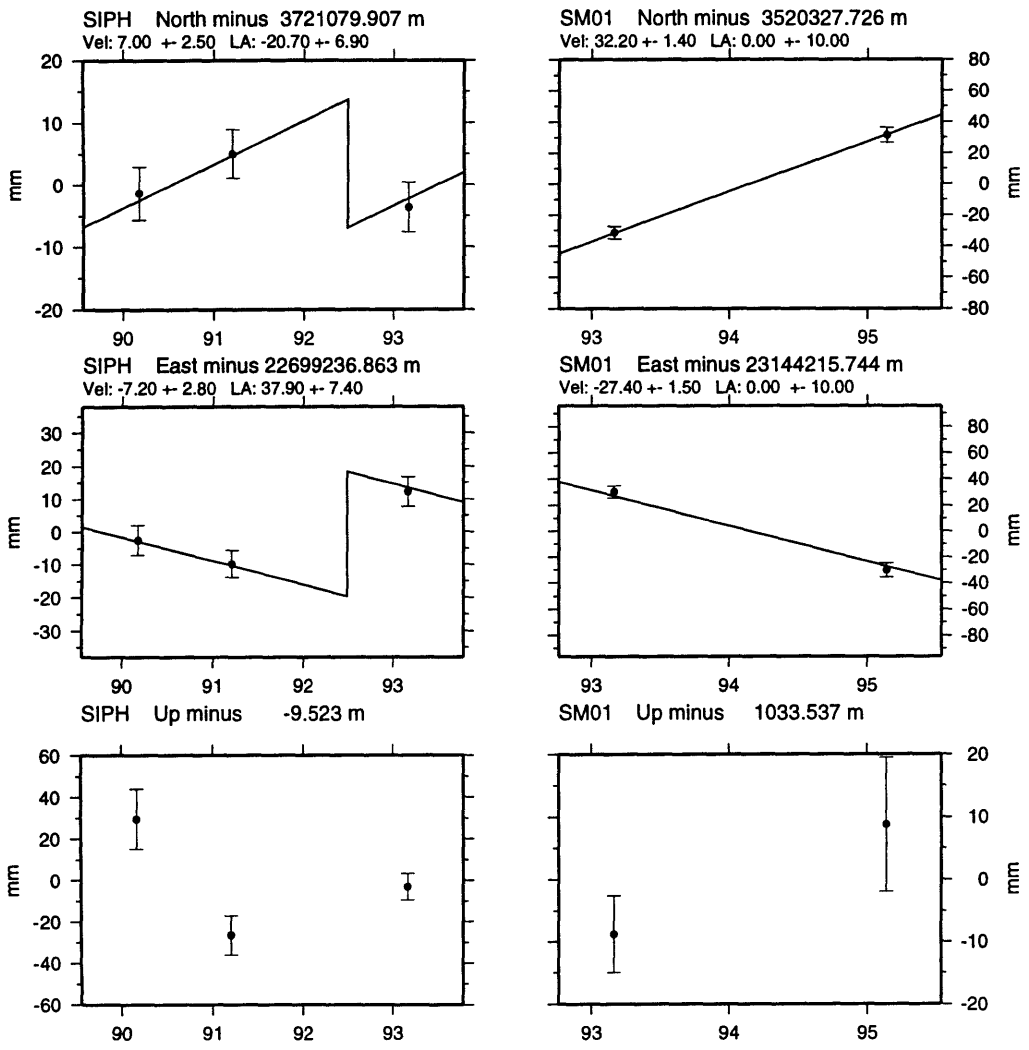

Figure C-22: Time series of GPS coordinate estimates for sites SIPH and SM01. With only three epochs observations from site SIPH, it is difficult to ascertain possible earthquake signals. We cannot estimate earthquake effects at site SM01 from only two epochs of measurement.

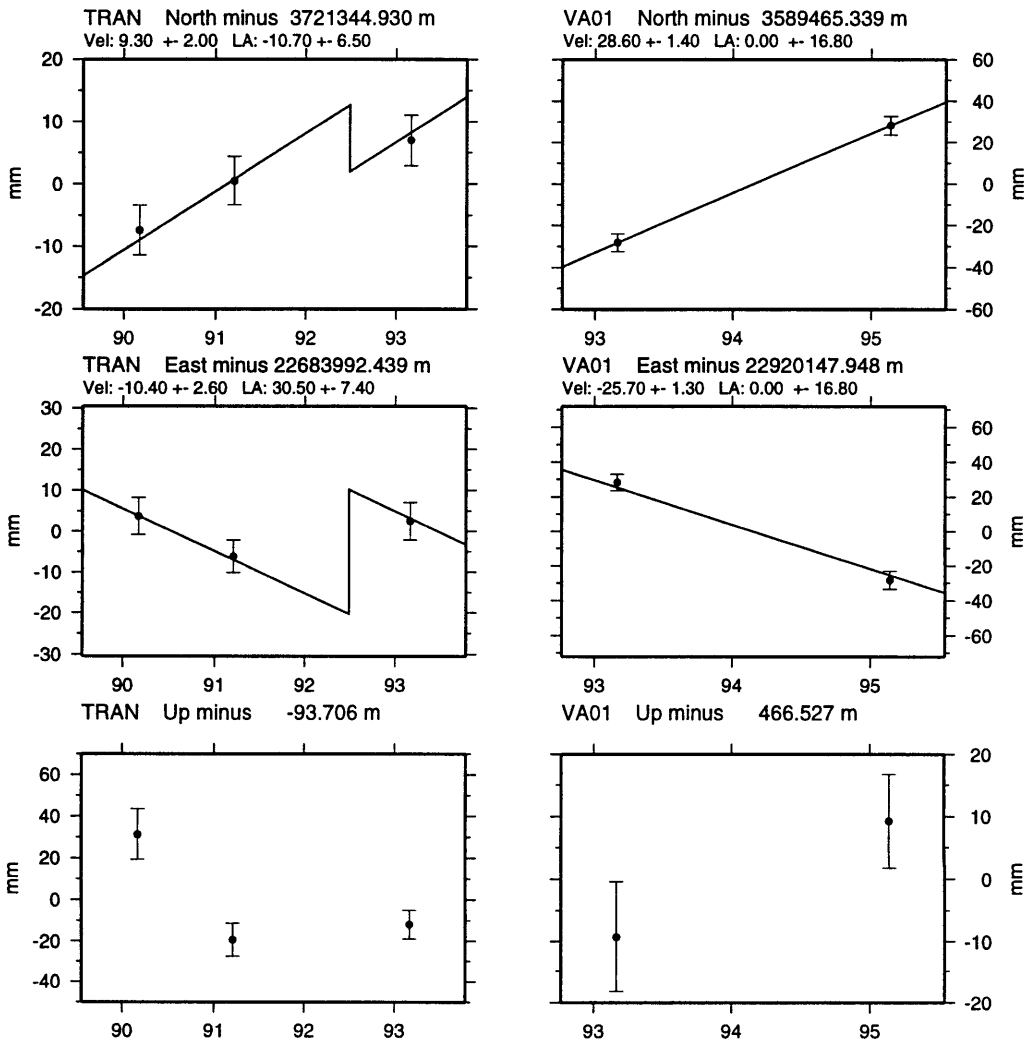

Figure C-23: Time series of GPS coordinate estimates for sites TRAN and VA01. With only three epochs observations from site TRAN, it is difficult to ascertain possible earthquake signals. We cannot estimate earthquake effects at site VA01 from only two epochs of measurement.

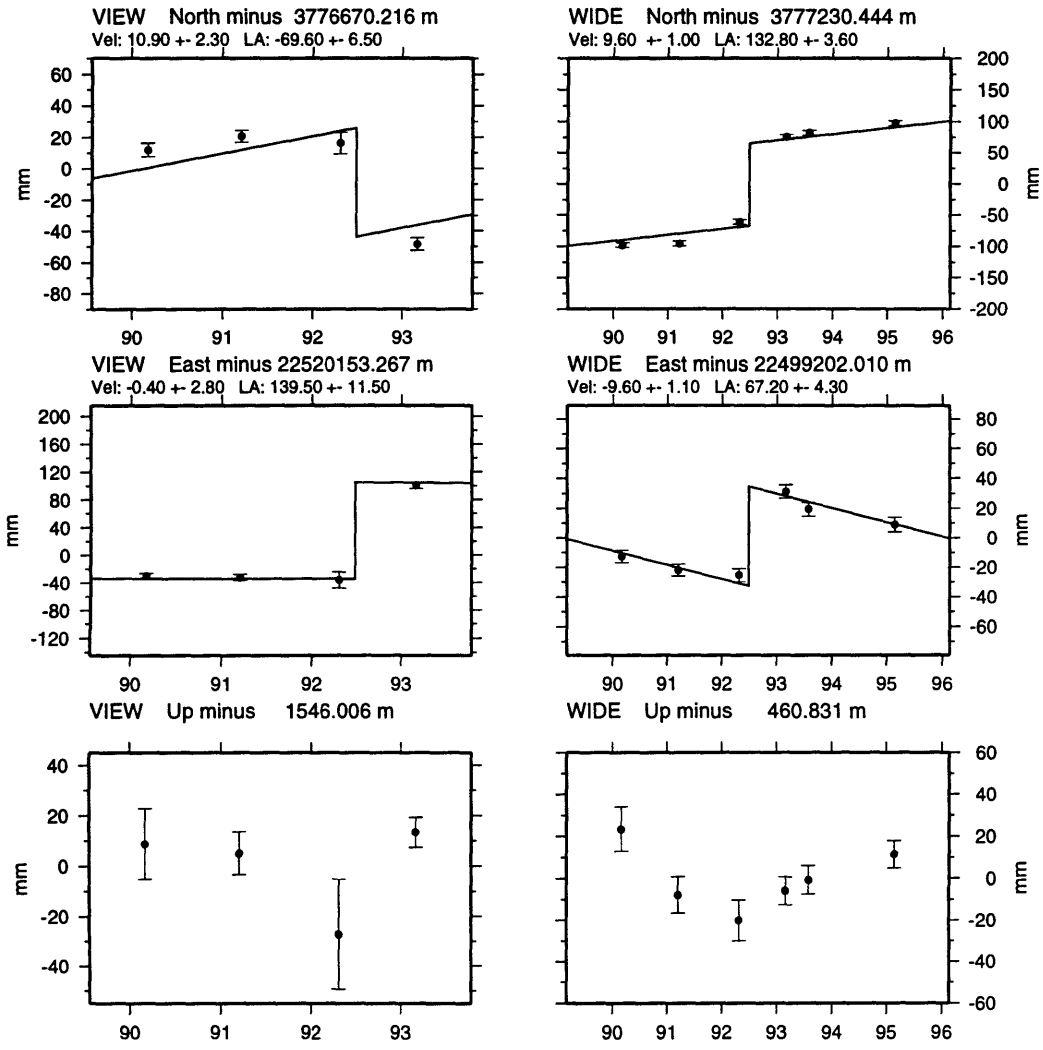

Figure C-24: Time series of GPS coordinate estimates for sites VIEW and WIDE. Horizontal coordinate estimates for both sites provide good examples of secular and episodic displacement signals.

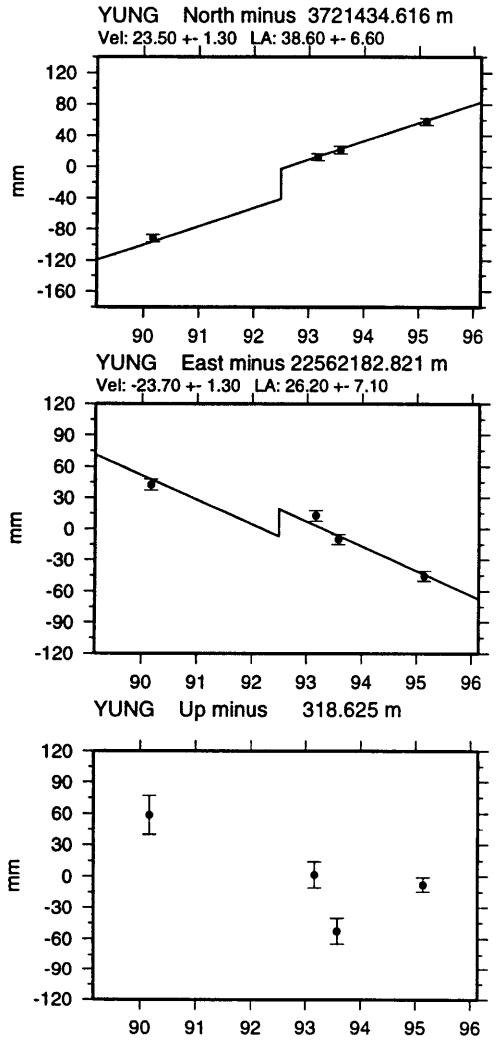

Figure C-25: Time series of GPS coordinate estimates for site YUNG. With only one epoch of measurement before 1992, we must extrapolate the secular trend in the post-1992 observations for site YUNG to estimate coseismic displacements. The data appear to be consistent with a relatively small earthquake disturbance.

Appendix D

Tikhonov regularization with differential operators valid for convex domains

We here present a formulation of Tikhonov regularization with differential operators valid for convex domains. General results are from *Morozov* [1993]. Let $\mathcal{S}$, $\mathcal{D}$, and $\mathcal{F}$ be Hilbert spaces and let $A: \mathcal{S} \to \mathcal{D}$ and $T: \mathcal{S} \to \mathcal{F}$ be linear operators with domains $\mathrm{Dom}\, A$ and $\mathrm{Dom}\, T$, respectively, each dense in $\mathcal{S}$. For $\alpha > 0$, define the functional

$$\Psi_\alpha(s) = \|d - As\|_{\mathcal{D}}^2 + \alpha^2 \|f - Ts\|_{\mathcal{F}}^2, \tag{D.1}$$

where $s \in \mathcal{S}_{AT} \equiv \mathrm{Dom}\, A \cap \mathrm{Dom}\, T$, $d \in \mathcal{D}$ and $f \in \mathcal{F}$. The problem, then, is to minimize Ψ_α over a convex subset $\mathcal{S}_+ \subset \mathcal{S}_{AT}$, i.e.

$$\Psi_\alpha(s_\alpha) = \inf_{s \in \mathcal{S}_+} \Psi_\alpha(s). \tag{D.2}$$

Morozov [1993; Thm 4, p.23] shows that the solution $s_\alpha \in \mathcal{S}_+$ exists uniquely for any $d \in \mathcal{D}$ and $f \in \mathcal{F}$ under the following two conditions on A and T:

(I) A and T are jointly closed on $\mathcal{S}_+$. This means that for every sequence $s_n \in \mathcal{S}_+$ such that

$$\lim_{n\to\infty} \max\left(\|d - As_n\|_{\mathcal{D}}^2, \|f - Ts_n\|_{\mathcal{F}}^2, \|s - s_n\|_{\mathcal{S}}^2\right) = 0, \tag{D.3}$$

relations $s \in \mathcal{S}_+$, $As = d$, and $Ts = f$ hold. Note that if A and T are both closed on $\mathcal{S}_+$, then they are jointly closed on $\mathcal{S}_+$.

(II) A and T are complementary on $\mathcal{S}_+$. This means that there exists a constant $\gamma \neq 0$ such that

$$\|As - Av\|_{\mathcal{D}}^2 + \|Ts - Tv\|_{\mathcal{F}}^2 \geq 1/\gamma^2 \|s - v\|_{\mathcal{S}}^2 \tag{D.4}$$

for any $s, v \in \mathcal{S}_+$. For the case of a linear $\mathcal{S}_+$, this condition states that the operators are jointly bounded from below.

For our problem, we let A and $\mathcal{D}$ be as defined in Chapter 3, and let $\mathcal{S} = L_2(\Sigma)$, the space of square integrable functions on Σ. We let $\mathcal{F}$ be the product space $L_2(\Sigma) \oplus L_2(\partial\Sigma)$ and define T by

$$Ts = \left(\nabla^2 s, s|_{\partial\Sigma}\right) \tag{D.5}$$

where $s|_{\partial\Sigma}$ denotes the restriction of s to the boundary $\partial\Sigma$. We then set $\mathcal{S}_{AT} = W^2(\Sigma)$, the Sobolev space of functions on Σ with square integrable second order derivatives. $\mathcal{S}_+$ is defined as follows. First consider the set of positive functions constructed out of $\mathcal{S}_{AT}$ by

$$\mathcal{X} \equiv \{\max(s, 0) : s \in \mathcal{S}_{AT}\}. \tag{D.6}$$

We then define the convex subset of $\mathcal{S}_{AT}$ as

$$\mathcal{S}_+ \equiv \mathcal{S}_{AT} \cap \mathcal{X} \subset \mathcal{S}. \tag{D.7}$$

It is well known that the Dirichlet problem $Ts = f$ has a unique solution which depends continuously on $f = (\rho, h)$ for every $\rho \in L_2(\Sigma)$, $h \in L_2(\partial\Sigma)$, i.e. T^{-1} exists

and is bounded. Therefore, T is bounded from below on its domain (under the L_2 norm) and its range is closed. From these two facts it follows that T is closed on $\mathcal{S}_{AT}$. *Morozov* [1993; Lemma 1, p.36] implies, then, that operators A and T are jointly closed on $\mathcal{S}_{AT}$ provided that A is bounded under the graph norm, defined as

$$\|s\|_T^2 = \|s\|_{\mathcal{S}}^2 + \|Ts\|_{\mathcal{F}}^2. \tag{D.8}$$

We note that $\|\cdot\|_T$ is an equivalent norm on $W^2(\Sigma)$. Since the data kernels $g_i(\xi)$ are square integrable on Σ, G is bounded under $\|\cdot\|_T$. That the evaluation functionals δ_ξ, are bounded under $\|\cdot\|_T$ follows from the Sobolev imbedding theorems [e.g. *Sobolev,* 1963].

We now address joint closure and complementarity on $\mathcal{S}_+$. First, we show that $\mathcal{X}$ is closed in $\mathcal{S}$. To demonstrate this, assume a sequence $s_n \in \mathcal{X}$ such that $s_n \to s \in \mathcal{S}$. s can be decomposed as $s = s^+ + s^-$ where $s^+ = \max(s, 0)$, and $s^- = \min(s, 0)$. By noticing that $s^+ s^- = 0$, it is clear that $\|s - s_n\|_{\mathcal{S}}^2 \geq \|s^+ - s_n\|_{\mathcal{S}}^2$. Therefore $s_n \to s^+ \in \mathcal{X}$.

Since $\mathcal{X}$ is closed in $\mathcal{S}$, A and T are jointly closed on $\mathcal{S}_+ = \mathcal{S}_{AT} \cap \mathcal{X}$. To show this, assume a sequence $s_n \in \mathcal{S}_{AT} \cap \mathcal{X}$ such that $s_n \to s \in \mathcal{S}$, and such that As_n and Ts_n converge. Since A and T are jointly closed on $\mathcal{S}_{AT}$, $s \in \mathcal{S}_{AT}$. Finally, since $\mathcal{X}$ is closed, $s \in \mathcal{X}$, i.e. $s \in \mathcal{S}_{AT} \cap \mathcal{X}$.

That A and T are complementary on $\mathcal{S}_+$ follows directly from the fact that T is bounded from below on $\mathcal{S}_{AT}$ and hence A and T are jointly bounded from below on $\mathcal{S}_{AT}$.